UNIVERSITY OF CALIFORNIA

Santa Barbara

The Metamorphic and Magmatic History of the Ross Orogen in Southern Victoria Land, Antarctica

A dissertation submitted in partial satisfaction of the

requirements for the degree Doctor of Philosophy

in Geological Sciences

by

Graham Hagen-Peter

Committee in charge:

Professor John Cottle, Chair

Professor Bradley Hacker

Professor Matt Jackson

September 2015

The dissertation of Graham Hagen-Peter is approved.

_____

Bradley R. Hacker

_____

Mathew G. Jackson

_____

John M. Cottle, Committee Chair

July 2015

ACKNOWLEDGEMENTS

I would like to acknowledge the support and mentorship of my supervisor, John Cottle, who made all of this possible. He presented me with many fantastic opportunities during my time at UCSB, and I am truly grateful for those experiences. The other members of my committee, Brad Hacker, Matt Jackson, and Frank Spera, provided valuable guidance over the years. I am also grateful for the excellent teaching and technical support from Gareth Seward and Andrew Kylander-Clark. My housemates at the Continental and other friends in Santa Barbara provided important emotional support throughout the years. I am lucky to have been surrounded by such an outstanding group of people. My partner, Alice Newman, had unwavering belief in me, even when times were difficult. I could not have done this without her support and positivity. Finally, I would like to thank my family—especially my parents—for their love and encouragement. Through them I learned to work hard, be humble, smile, and dance.

VITA OF GRAHAM HAGEN-PETER

Education

Fall 2015 (expected): PhD in Geological Sciences, *UC Santa Barbara*

Spring 2010: Bachelor of Science in geology from the *University of Vermont, Burlington, VT* summa cum laude

Professional Experience

Fall 2010– Present: Graduate student researcher at *UC Santa Barbara*

Winter 2015: Instructor of record at *UC Santa Barbara*

Fall 2010– Spring 2015: Teaching assistant at *UC Santa Barbara*

Summer 2009– 2010: Laboratory assistant at the *University of Vermont, Burlington, VT*

Fall 2007– Fall 2008: Teaching Assistant at the *University of Vermont, Burlington, VT*

2005– 2010: Operating Room Assistant at *Fletcher Allen Health Care, Burlington, VT*

Teaching Experience

As teaching assistant: Dynamic Earth, Dinosaurs, Tectonics, Analytical Methods, Spring Field Camp, Summer Field Camp

As instructor of record: Antarctic Earth Science

Technical Experience

UC Santa Barbara geochronology and geochemistry laboratory

- Mineral separations, SEM, EPMA, LA MC-ICP-MS analysis of U-Pb and Hf isotopes, LA ICP-MS analysis of trace elements, ion-exchange chromatography for Lu-Hf geochronology, high-precision and accuracy solution-MC-ICP-MS isotope analysis

National Taiwan University geochemistry laboratory

- Low-blank clean lab chemistry and ion-exchange chromatography for Sr and Nd isotopes

UC Los Angeles secondary-ion mass spectrometer workshop

- The principles, analytical methods, and applications of SIMS

Stable isotope geochemistry laboratory at the *University of Vermont, Burlington, VT*

- cryogenic gas isolation on vacuum extraction line, measurement of carbon isotopes on V.G. SIRA stable isotope ratio mass spectrometer

Software proficiency

- MATLAB®, Mathematica™, Igpet, Igor Pro, Adobe Creative Suite®, Thermo-Calc, Perple_X

Research Experience

Fall 2012– present: Coupled garnet Lu-Hf and monazite U-Pb geochronology constrain early convergent margin dynamics in the Ross orogen, Antarctica

Fall 2010– present: Source heterogeneity and the relative roles of crustal growth and recycling through continental arc magmatism: A case study from the Ross orogen, Antarctica

Fall 2010– Fall 2015: The source and timing of a short-lived subduction-related magma system in the Dry Valleys area, Antarctica: Insights from U-Pb and Hf isotopes and whole-rock geochemistry

Summer 2009– 2010: Large-scale shear-related folds in the Tavan Har basement block, southeastern Mongolia: Implications for intracontinental deformation; Advisor: Dr. Laura Webb at *UVM, VT*

Spring 2009: Stable carbon isotopes in *Pinus strobus* tree rings, northwestern Vermont: A record of anthropogenic CO_2 in the atmosphere

Presentation of Research

Journal Articles

Hagen-Peter, G., Cottle, J.M., Smit, M., and Cooper, A.F. (In Review). Coupled garnet Lu-Hf and monazite U-Pb geochronology constrain early convergent margin dynamics in the Ross orogen, Antarctica. *Journal of metamorphic geology.*

Hagen-Peter, G., Cottle, J.M., Tulloch, A.J., and Cox, S.C. (2015). Mixing between enriched lithospheric mantle and crustal components in a short-lived subduction-related magma system, Dry Valleys area, Antarctica: Insights from U-Pb geochronology, Hf isotopes, and whole-rock geochemistry. *Lithosphere*, **7**, 174–188.

Published Abstracts

Hagen-Peter, G.A., Webb, L.E., Stypula, M. (2009). *AGU Fall Meeting Abstract* T33C-1921.

Hagen-Peter, G.A., Cottle, J.M., Tulloch, A. (2011). *GSA Abstracts with Programs*, 43(5), 46.

Hagen-Peter, G.A., Smit, M.A., Cottle, J.M., Schmidt, J (2013). *GSA Abstracts with Programs*

Hagen-Peter, G.A., Cottle, J.M. (2013). *AGU Fall Meeting* Abstract T13A-2520

Hagen-Peter, G.A., Cottle, J.M. (2014). *GSA Abstracts with Programs*

Invited Talks

Carleton College (USA), Academia Sinica (Taiwan), and National Taiwan University

Select Grants, Fellowships, and Awards

2015: ScienceLine acknowledgement of constant support in promoting K-12 science education, *UCSB*
2014: NSF EAPSI fellowship, *NSF*
2012 & 2014: ScienceLine Outstanding Contributor, *UC Santa Barbara*
2013: Graduate Opportunity Fellowship, *UC Santa Barbara*
2013: Richard V. Fisher Scholarship for Volcanology, *UC Santa Barbara*
2011: Richard and Eleanor Migues Field Research Prize*, UC Santa Barbara*
2009: Arthur J. and Claire Heiser Joseph B. Tinker Memorial Grant*, University of Vermont*
2009: Hawley Award Research Grant, *University of Vermont*
2008 & 2009: VT-NASA EPSCoR Vermont Space Grant Consortium Undergraduate Scholarship

Outreach Activities

Fall 2014−Present: UCSB Department of Earth Science outreach committee representative
Fall 2011– Present: UCSB ScienceLine scientist
Fall 2010– Present: Numerous outreach visits to grade schools in Santa Barbara, Isla Vista, and Vermont, including guest lectures and participation in "science nights"
Fall 2011– Present: "Geologists On Ice" blog (http://www.antarctica360.net/)
Summer 2012: UCSB Summer Institute in Mathematics and Science mentor
Summer 2011: UCSB Summer Research Mentorship Program Participant

ABSTRACT

The Metamorphic and Magmatic History of the Ross Orogen in Southern Victoria Land, Antarctica

by

Graham Adrian Hagen-Peter

The process of subduction has significant influence on the geochemical evolution of the crust and mantle, and subduction-related magmatism may have been an important mechanism for the growth of continental crust over time. Extensive exposure of the mid-crustal levels of an ancient, exhumed continental arc in the Transantarctic Mountains provides an exceptional opportunity to study the metamorphic and magmatic processes associated with an archetypal subduction zone. The belt of multiply deformed metamorphic rocks and granitoid batholiths records convergence and subduction of paleo-Pacific oceanic lithosphere beneath East Antarctica during the Neoproterozoic–Paleozoic Ross orogeny. These rocks are especially well exposed in the southern Victoria Land (sVL) segment of the Transantarctic Mountains—the largest ice-free area of Antarctica. The metamorphic and igneous rocks in sVL provide insights into the early stages of convergent-margin tectonism, the compositional diversity of subduction-related magmatism, and the relative roles of crustal growth and recycling in continental arcs.

In Chapter 1 of this dissertation, garnet Lu-Hf and monazite U-Pb geochronology—combined with petrography, mineral chemistry, and thermobarometry—reveal a Barrovian-style metamorphic history that predated the dominant

phase of magmatism in sVL. The geochronology data from this study provide one of the oldest records of tectonism along the Ross orogen. The results are consistent with a tectonic model that involves shortening across the margin of East Antarctica prior to the major phase of subduction-related magmatism.

Chapter 2 explores the age and magma sources of a large subduction-related igneous complex in the Dry Valleys area. Zircon U-Pb geochronology demonstrates that the period of magmatism in the Dry Valleys was relatively short-lived compared to other segments of the Ross orogen. Whole-rock geochemistry and Hf isotopes in zircon reveal the assimilation of ancient crust during the differentiation of juvenile magmas that were likely derived from an enriched sub-continental lithospheric mantle source. A compilation of Nd and Sr isotope data from granitoids from along the Ross orogen suggest that enriched lithospheric mantle may have been a common juvenile magma source along the arc.

In Chapter 3, a comprehensive geochemical, geochronologic, and isotopic investigation of the magmatism in sVL explores the conspicuous occurrence of alkaline silicate rocks and carbonatites—most commonly associated with intraplate and continental-rift magmatism—within the continental arc. The alkaline magmatism was partially contemporaneous with the emplacement of large sub-alkaline igneous complexes in adjacent segments of the arc. The isotopic and trace element composition of the alkaline and subalkaline rocks suggests derivation from geochemically enriched sources—potentially metasomatized sub-continental lithospheric mantle. Despite enriched isotopic and trace element compositions that broadly resemble recycled continental crust, binary mixing and assimilation-fractional crystallization models indicate that crustal growth may have been dominant over crustal reworking in the sVL magmatism.

INTRODUCTION

Subduction zones are perhaps the most salient of tectonics settings—where oceanic crust is recycled back into the mantle, the locations of $M_W > 9$ earthquakes, and proximal to extensive chains of explosive volcanism. The trenches that mark the surficial interface between the downgoing and overriding plates, and the chains of volcanoes that form on the overriding plates, are prominent physiographic features that span for many thousands of kilometers across Earth's surface. The process of subduction and associated magmatism have significant influence on the geochemical evolution of the crust and mantle. For example, the process of subduction recycles crust back into the mantle, re-enriching it in incompatible elements (Pearce, 1983; Plank & Langmuir, 1993; Pearce & Peate, 1995). It has also been argued that subduction zone magmatism has been the primary mechanism for growth of the continental crust over earth's history; some arguments for and against this hypothesis are reviewed in Davidson and Arculus (2005). The paradigm for subduction zone magmatism is that dehydration reactions in the downgoing slab flux the overlying mantle wedge with aqueous fluids (and perhaps slab-derived melts), leading to partial melting. The partial melts of mantle peridotite are basaltic, or perhaps andesitic (with high Mg#; e.g., Kelemen, 1995), in composition and buoyantly ascend through the wedge. They may stall at the moho, differentiate and crystallize in the crust, or ascend rapidly through the crust to be erupted as near-primary lavas. A more encompassing view recognizes contributions from the mantle wedge, the downgoing slab (and sediments), and the overlying crust (oceanic or continental). Varying proportions of these different end-member components, as well as significant variability in the compositions of the components themselves, lead to a diversity in subduction zone magmas that is not fully explained by a single, general model. This is

especially poignant in continental arc settings, where magmas ascend through and interact with a thick column of continental lithosphere, the intrusive manifestation of which are extensive granitoid batholiths that generally resemble the composition of the bulk upper continental crust (Rudnick & Gao, 2003). The range of possible scenarios for the source(s) and differentiation of continental arc magmas—and the significance of arc magmatism in models for crustal generation and refinement—warrants further study of subduction tectonics and magmatism.

Extensive exposure of the metamorphic and igneous rocks of an ancient, exhumed continental arc in the Transantarctic Mountains provides an exceptional opportunity to study the metamorphic and magmatic processes associated with an archetypal subduction zone. The Transantarctic Mountains, forming the boundary between East and West Antarctica, are considered an extension-related mountain belt that formed during the latest Mesozoic– early Cenozoic during the opening of the West Antarctic Rift System (Gleadow & Fitzgerald, 1987; Siddoway et al., 2004). Exposed in the uplifted rift shoulder along the extent of the Transantarctic Mountains are multiply deformed metamorphic rocks and granitic batholiths associated with the late Neoproterozoic– early Paleozoic Ross orogeny. Part of the greater Terra-Australis orogen, the Ross orogen is thought to have developed through subduction of paleo-Pacific oceanic lithosphere westward beneath the margin of East Gondwana (Fig. 1). Deformation, metamorphism, and magmatism associated with the Terra-Australis orogeny is recorded over ~18,000 km from southeast Australia and southwest New Zealand, across Antarctica, in southern Africa, and along the western margin of South America (Cawood, 2005). Convergence between the paleo-Pacific ocean and segments of East Gondwana persisted for over 300 million years (summarized in Cawood, 2005), although only the early

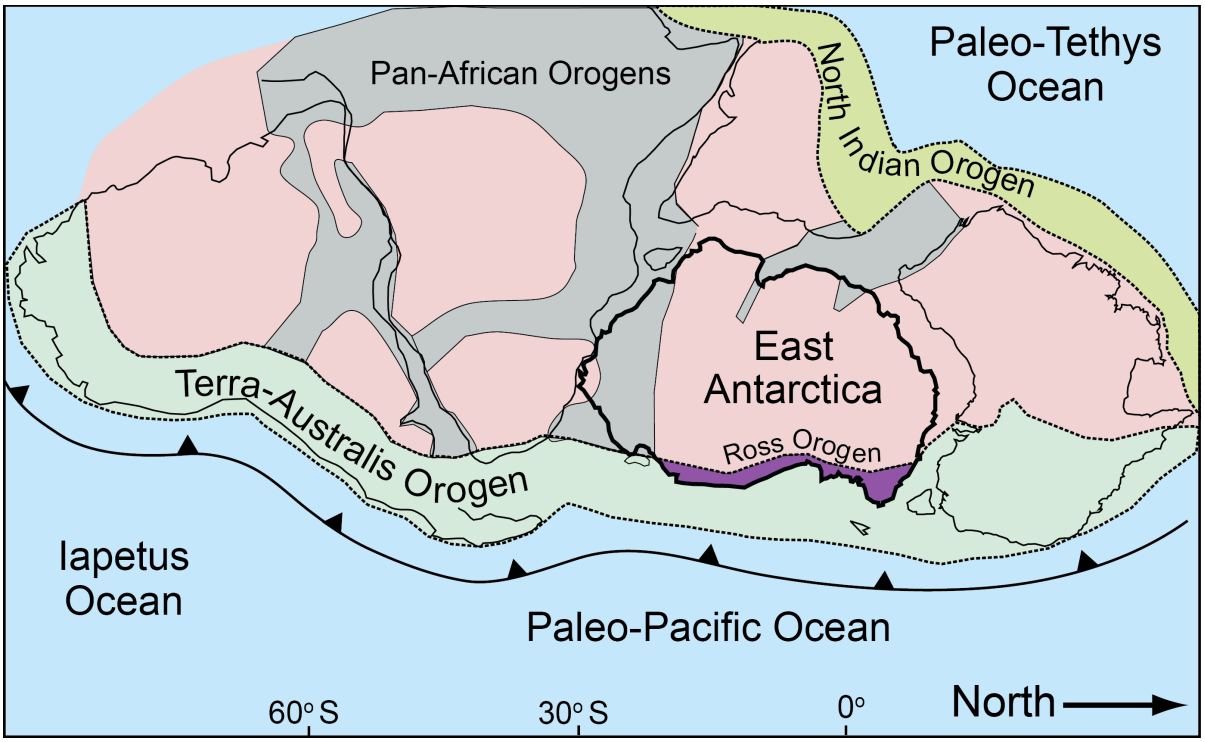

Figure 1 Paleogeographic reconstruction of the supercontinent Gondwana ca. 530 Ma (modified from Cawood, 2005; Cawood et al., 2011). The Ross orogen (purple), part of the extensive Terra-Australis orogen, developed along the margin of East Antarctica through the subduction of paleo-Pacific oceanic lithosphere westward beneath Gondwana. The pink areas are major cratonic blocks sutured together along the collisional Pan-African orogens (grey). The accretionary Terra-Australis and North Indian orogens are shown in shades of green. The position of the trench outboard of the Terra-Australis orogen is not to scale.

phases of this long-lived convergence are recorded in the Ross orogen. Nonetheless, nearly continuous exposure of metamorphic and intrusive igneous rocks—exhumed from mid- to upper-crustal levels—for >2500 km along the Transantarctic mountains provide and excellent opportunity to study the early stages of convergence and the subsequent magmatic arc that developed along this major convergent margin. These rocks are especially well-exposed along the southern Victoria Land (sVL) segment of the Transantarctic Mountains—the largest ice-free area of the continent. The metamorphic and igneous rocks exposed along ~500 km of sVL are the focus of this dissertation.

Chapter 1 is focused on the early history of the Ross orogeny through the study of high-grade metamorphic rocks that host the intrusive igneous rocks in sVL. The questions addressed in this study are: 1) Were metamorphism and magmatism entirely contemporaneous during the Ross orogeny? 2) Do the metamorphic rocks record information about convergent-margin tectonism that is absent in the igneous record? Garnet Lu-Hf and monazite U-Pb geochronology, combined with petrography, mineral chemistry, and thermobarometry, reveal a "Barrovian-style" metamorphic history that predated the dominant phase of magmatism in sVL. Aside from detrital zircons and glacially-transported igneous clasts, the geochronology from this study is the earliest record of tectonism along the entire Ross orogen. The results are consistent with a tectonic model that involves shortening across the margin of East Gondwana prior to the major phase of subduction-related magmatism. In addition to its bearing on Gondwanan tectonics, this study has important implications for the interpretation of accessory mineral (monazite) dates in the context of rock-forming mineral reactions.

Chapter 2 examines the timescale of emplacement and potential magma sources of a

large igneous complex in the iconic Dry Valleys area. The primary questions of this study are: 1) Over what timescale was the relatively large igneous complex constructed, and how did the timing relate to magmatism in other segments of the arc? 2) Do variations in magma source explain the occurrence of three distinct magmatic suites in this area? 3) Does this granitic (*sensu lato*) batholith represent primarily the addition on juvenile continental crust or the reworking and "distillation" of previously existing crust? Three magmatic suites, with different emplacement styles and geochemical characteristics, were emplaced over a relatively short period (ca. 23 million years) compared to magmatism in other segments of the Ross orogen. The rocks have relatively restricted range in Hf isotope composition, although a broadening of the range of isotopic composition in evolved samples records the involvement of crustal reworking in the source or during magmatic differentiation. A broadening of the isotopic composition in younger samples suggests that the degree of crustal reworking increased over time. The isotopically enriched composition of the most primitive samples points toward enriched sub-continental lithospheric mantle (SCLM)—as opposed to depleted mantle—as a primary magma source, and a compilation of Sr and Nd isotope data from igneous rocks from along the orogen suggests that primitive rocks along the entire arc may have been sourced from enriched mantle.

Chapter 3 is a comprehensive geochemical, geochronologic, and isotopic investigation of petrologically- and compositionally- diverse magmatism along ~500 km of the arc in sVL. This is largely motivated by the conspicuous occurrence of alkaline silicate rocks and carbonatites—igneous rocks most commonly associated with intraplate and continental-rift magmatism—within the continental arc. These alkaline rocks of the Koettlitz Glacier Alkaline Suite (KGAS) are adjacent to large complexes of more typical subduction-

related igneous rocks in the Dry Valleys and Byrd Glacier areas. The questions addressed in the study include: 1) Was the alkaline magmatism contemporaneous with subalkaline subduction-related magmatism in sVL? 2) Are the gross petrologic and compositional differences of the igneous rocks in sVL better explained by difference in magma sources or differentiation processes? 3) Can we quantify the proportions of juvenile magmas and reworked crust in the igneous rocks in order to constrain the relative roles of crustal growth and recycling through arc magmatism?

Some of the questions posed above are more tractable than others, and I must admit that the answers to many of them remain elusive. However, I hope that the contributions of this dissertation offer some progress towards addressing these questions, and, ideally, providing ideas and guidelines for future research.

A note concerning Chapters 2 and 3: There is some overlap in the content (both data and ideas) of Chapters 2 and 3. Chapter 2, on the intrusive igneous rocks of the Dry Valleys area, has been published as a self-contained research article (see Hagen-Peter et al., 2015). As a comprehensive study of the magmatism across southern Victoria Land, Chapter 3 necessarily includes the results from the Dry Valleys study. Though most of the data from Dry Valleys study are repeated, they are combined with many new data and are interpreted in a greater regional context with omission of some of the details of Chapter 2.

I. Coupled garnet Lu-Hf and monazite U-Th-Pb geochronology constrain early convergent margin dynamics in the Ross orogen, Antarctica

INTRODUCTION

Uranium- and thorium-bearing accessory minerals, such as zircon, monazite, titanite, and allanite are routinely employed as geochronometers in metamorphic rocks. Zircon and monazite are the most commonly targeted because of their widespread occurrence in a range of rock types. Ideally, the growth or recrystallization of these minerals can be linked to rock-forming mineral reactions or fabric formation during tectono-metamorphic events. Although raising increasing interest, this approach presents many challenges. Zircon in metamorphic rocks is often inherited from the protolith, and, in many cases, the growth of zircon may be strictly mediated by the presence or absence of aqueous fluid (e.g., Young & Kylander-Clark, 2015) or melt (e.g., Rubatto et al., 2001) during peak or retrograde metamorphism. Zircon may grow or recrystallize during prograde metamorphism (Liati & Gebauer, 1999; Liu et al., 2006), and monazite may grow over a range of prograde conditions, from greenschist- through to granulite facies (Rubatto et al., 2001). However, the reactions that form these minerals are not well understood, and it can be difficult to link the dates obtained from them to the paragenesis and P-T path of the rock in which they are found.

Several studies have tied the formation of zircon (Hermann & Rubatto, 2003) and monazite (Hermann & Rubatto, 2003; Kohn & Malloy, 2004; Corrie & Kohn, 2008) directly to the prograde and retrograde breakdown of rock-forming silicate minerals. Using trace element concentrations as indirect proxies for the coexistence of rock-forming minerals provides a valuable complementary approach. For example, low relative abundances of heavy rare earth elements (HREE) in zircon and monazite are commonly interpreted to

represent cogenesis with garnet, and the absence of negative Eu anomalies in normalized REE patterns for zircon and monazite could reflect plagioclase breakdown during eclogite facies metamorphism (e.g., Kylander-Clark et al., 2013; Hacker et al., 2015; Holder et al., 2015). This approach has been successful in elucidating the absolute timing and rates of metamorphic and deformation processes in a variety of tectonic settings. However, relatively few studies have linked dates from accessory phases to the growth of rock-forming minerals by direct chronometry of both.

In this paper, we present garnet Lu-Hf and monazite U-Pb ages from metapelites and an amphibolite from the Ross orogen of Antarctica, a Neoproterozoic–early Paleozoic continental arc. Establishing an absolute chronology of garnet and monazite growth in these rocks, combined with textural information and trace-element compositions for both, allows us to test the validity of common proxies used to link age and trace element data from monazite to the coexistence of rock-forming minerals. The age data are combined with forward and inverse phase equilibria modeling to reveal the tectonic burial of the protolith sediments to mid-crustal depths prior to the onset of widespread arc magmatism in the Ross orogeny.

GEOLOGIC SETTING

Tectonic framework

The Ross orogen is a ~3500 km-long belt of deformed sedimentary, metamorphic, and intrusive igneous rocks of Neoproterozoic to early Paleozoic age. The belt spans the Transantarctic Mountains and continues into southwestern New Zealand and the Delamerian orogen of southeast Australia (Fig. 1.1, Foden et al., 2006). Deformed and metamorphosed

sedimentary rocks and granitic batholiths of the Ross orogen are thought to record convergence and subduction along the margin of East Gondwana (see Stump, 1995 for an overview). Deformation and metamorphism during the Ross orogeny affected marine sediments deposited on the Gondwanan margin during and after the rifting of Rodinia in the Neoproterozoic. The isotope composition of granitoids along the arc also record magmatic reworking of Precambrian crystalline basement (e.g., Goodge et al., 2012; Hagen-Peter et al., 2015), although pre-Ross metamorphic rocks are only exposed in the Miller and Geologist Ranges of the Central Transantarctic Mountains (Fig. 1.1; Goodge, 2007).

The Ross orogen differs from other continental margins involved in a Wilson cycle in that there is no evidence for full closure of the paleo-Pacific ocean through an orogen-scale collision (Cawood, 2005). Several microcontinent collisions have been recognized in northern Victoria Land (nVL; Stump et al., 1983; Weaver et al., 1984; Gibson & Wright, 1985; Borg et al., 1987; Kleinschmidt & Tessensohn, 1987) and postulated for the central Transantarctic Mountains (cTAM; Borg et al., 1990; Goodge et al., 1992; Stump et al., 2006), but were not recognized in intervening southern Victoria Land (sVL; Fig. 1.1). The closure of an oceanic basin and subduction of oceanic and continental crust through collisional orogenesis at ca. 500 Ma resulted in eclogite facies metamorphism in nVL (Ricci et al., 1996; Di Vincenzo et al., 1997; Palmeri et al., 2003). Eclogites in the Nimrod Group in cTAM are not related to this stage; they formed during the ca. 1.7 Ga Nimrod orogeny (Goodge, et al., 1992; 2001).

The onset of magmatism was transient along the Ross orogen (Hagen-Peter et al., 2015), and different segments of the orogen experienced different metamorphic histories at different times (Goodge, 2007). However, a paucity of geochronology for metamorphic rocks

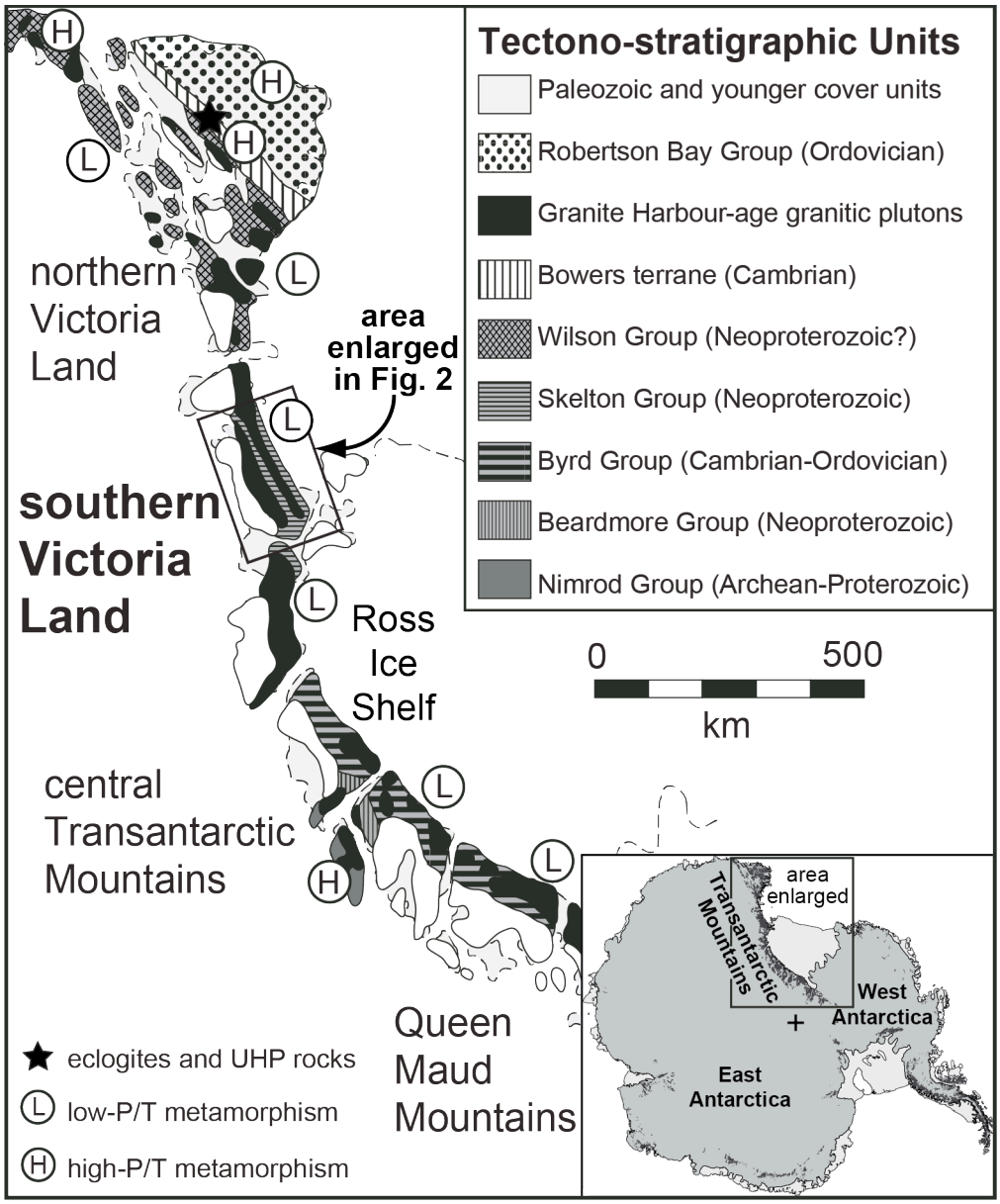

Figure. 1.1 Map of Ross orogen tectono-stratigraphic units exposed in the Transantarctic Mountains (modified from Goodge, 2007). Metasedimentary groups of various age and provenance are exposed along the orogen and host plutonic rocks of the Granite Harbour Intrusives. Circles denote the relative pressure/temperature (P/T) conditions of areas that have been previously studied.

in the Ross orogen makes it difficult to integrate the metamorphic and deformational history with the well-established magmatic history of the arc. The garnet- and monazite-bearing metamorphic rocks from sVL—the subject of this study—provide an opportunity to elucidate the timing of metamorphism in a major segment of the arc with a well-established magmatic chronology.

Geology of southern Victoria Land

Deformed and metamorphosed Neoproterozoic sedimentary rocks in southern Victoria Land are known collectively as the Skelton Group (formerly subdivided into the Koettlitz and Skelton Groups; Cook & Craw, 2001; Cox et al., 2012), which composes ~30% of the exposed basement between the Koettlitz Glacier and Granite Harbour, the largest ice-free area of Antarctica (Fig. 1.2; Cox et al., 2012). The Skelton Group comprises, in order of decreasing areal extent, marble and calc-silicate, pelitic and psammitic schist and paragneiss, metaconglomerate, and amphibolite, with minor felsic orthogneiss layers (Findlay et al., 1984; Cox et al., 2012). A general SW-NE metamorphic gradient has been recognized, with dominantly upper greenschist facies in the Skelton Glacier area, lower- to upper-amphibolite facies in the Walcott Glacier area, and upper amphibolite facies north of the Walcott Glacier (Fig. 1.2; Talarico et al., 2005; Cox et al., 2012). Pelitic and psammitic lithologies were extensively migmatized in the Dry Valleys area (Allibone, 1992; Allibone & Norris, 1992; Cox, 1992). An apparent discontinuity in the metamorphic grade and structural grain in the vicinity of the Walcott Glacier has been attributed to the presence of a major shear zone ("Frio Shear Zone"; Cook, 1997; Cox et al., 2012; Figs. 1.2, 1.3), though direct observations of this structure are lacking.

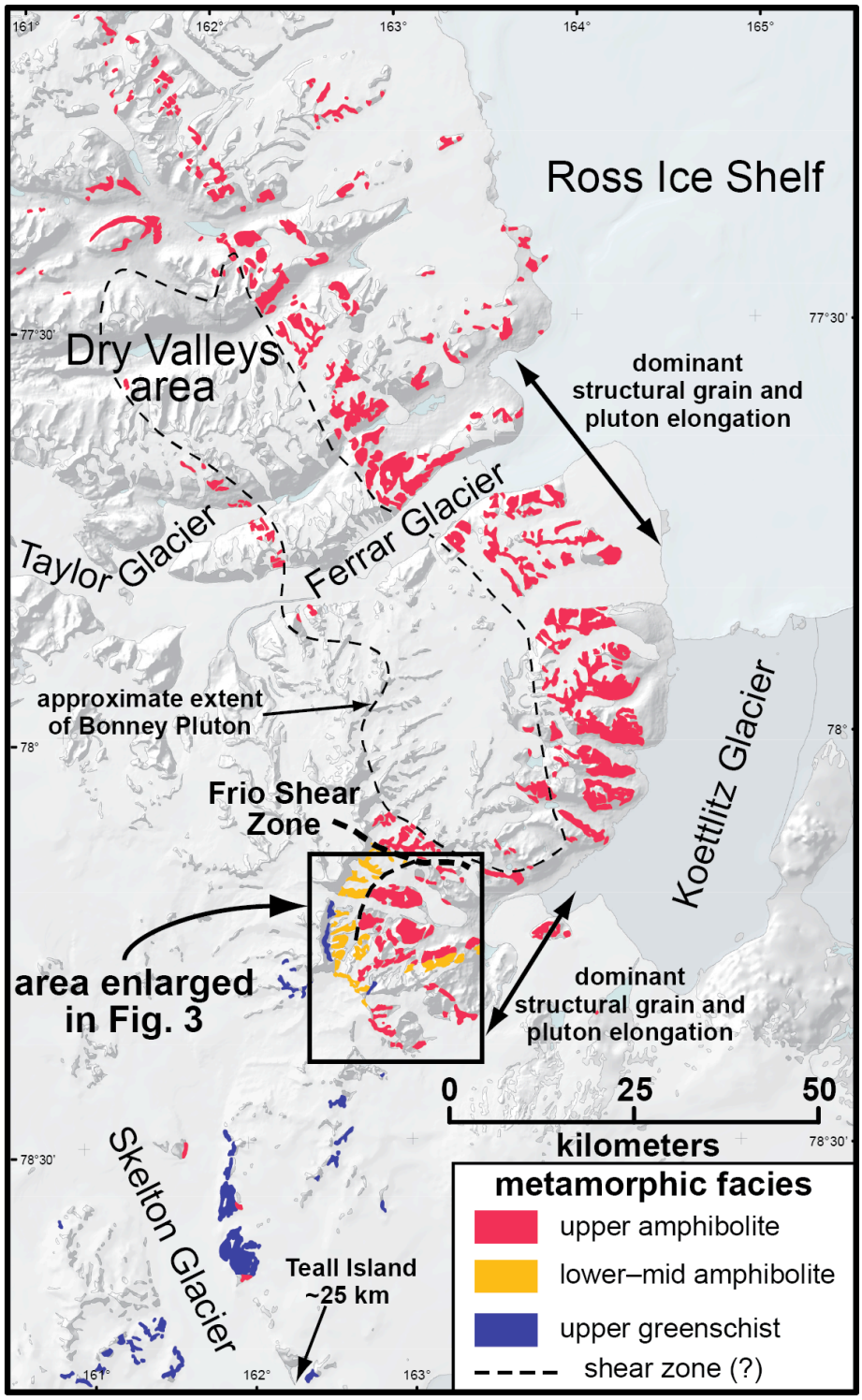

Figure 1.2 Generalized metamorphic grade map of the southern Victoria Land segment of the Transantarctic Mountains (modified from Cox et al., 2012). Only metamorphic rocks are shown to emphasize the distribution and general north to south metamorphic gradient of the Skelton Group in southern Victoria Land. Rocks with upper-greenschist to upper-amphibolite-facies assemblages occur in the area enlarged in Figure 1.3.

The protoliths to the Skelton Group have been generally interpreted to represent a syn-rift to passive margin sequence recording the rift-to-drift transition of the paleo-Pacific margin of East Gondwana following the breakup of Rodinia in the Neoproterozoic (Findlay et al., 1984; Cooper et al., 2011). Metamorphism and intense deformation during the Ross orogeny have precluded a comprehensive synthesis of the original stratigraphy across the region (Findlay et al., 1984), but it has been accomplished locally. Cook (2007) and Cooper et al. (2011) documented a ~120 meter-thick section of relatively low-grade metaconglomerate and metavolcanics rocks exposed on the north side of the Skelton Glacier (Fig. 1.2). Cooper et al. (2011) determined zircon U-Pb ages of ca. 650 Ma for rift-related volcanic clasts in the upper third of the section. Together with a U-Pb age peak of ca. 650 Ma for detrital zircon in a sample from Teall Island (immediately south of the Skelton Glacier; Stump et al., 2007), these data provide the most robust constraint on the maximum age of deposition of *some* sections of the Skelton Group. A slightly younger age is suggested by a small peak (n = 4) at ca. 587 Ma in the age distribution of one detrital zircon sample (Cooper et al. (2011). The minimum age of deposition is constrained by the intrusion of the ca. 546 Ma Mulock A-type granite which cross-cuts deformed Skelton Group rocks (Cottle & Cooper, 2006b). There are few direct constraints on the timing of metamorphism and deformation of the Skelton Group within this 100 Myr time bracket. Wysoczanski and Allibone (2004) dated metamorphic overgrowths on detrital zircons from the north side of the Taylor Glacier (Fig. 1.2). They identified several populations of Cambrian zircon ca. 500–495 Ma, as well as single analyses that yielded 552- and 532-Ma dates. They interpreted these dates to record progressive or punctuated metamorphism beginning as early as 552 Ma and reaching peak (anatectic) conditions at ca. 500 Ma.

Magmatism in southern Victoria Land commenced by ca. 550 Ma with the intrusion of alkaline rocks of the Koettlitz Glacier Alkaline Suite (summarized in Read et al., 2002) and calk-alkaline magmatism south of the Mulock Glacier (Cottle & Cooper, 2006a, b; Stump et al., 2006). The major pulse of arc magmatism, including the emplacement of the ~1000 km^2 Bonney Pluton, in the Dry Valleys area, occurred at ca. 515−490 Ma (Fig. 1.2; summarized in Hagen-Peter et al., 2015).

Structure of Walcott Glacier area

Upper greenschist to upper amphibolite facies rocks are exposed over ~450 km^2 in the Walcott Glacier area (Figs. 1.2; 1.3). Based on geologic mapping, Cook and Craw (2001) suggested that the area could be divided into five distinct crustal sub-blocks with breaks in metamorphic gradient across ductile shear zones. Although some breaks in metamorphic grade were observed, our field observations do not support the division of the area into distinct blocks with different tectono-metamorphic histories. The results of this study are interpreted independent of this framework. The Skelton Group in this area is composed of roughly sub-equal proportions of marble, calc-silicate, and pelitic and psammitic schist with less amphibolite, metaconglomerate, and quartzite (Fig. 1.4). The rocks are multiply deformed, and the dominant structural fabric is northeast-trending (Cook & Craw, 2001), as opposed to the predominant northwest-trending structural fabric north of the Frio Shear Zone (Figs. 1.2; 1.3). Metamorphic rocks were intruded by numerous plutons and smaller bodies belonging to the Koettlitz Glacier Alkaline Suite, including alkaline mafic rocks, nepheline syenites, carbonatites, and A-type granites (Cooper et al., 1997; Cottle & Cooper, 2006b; Read et al., 2002; Cox et al., 2012). The samples in this study vary in proximity to large

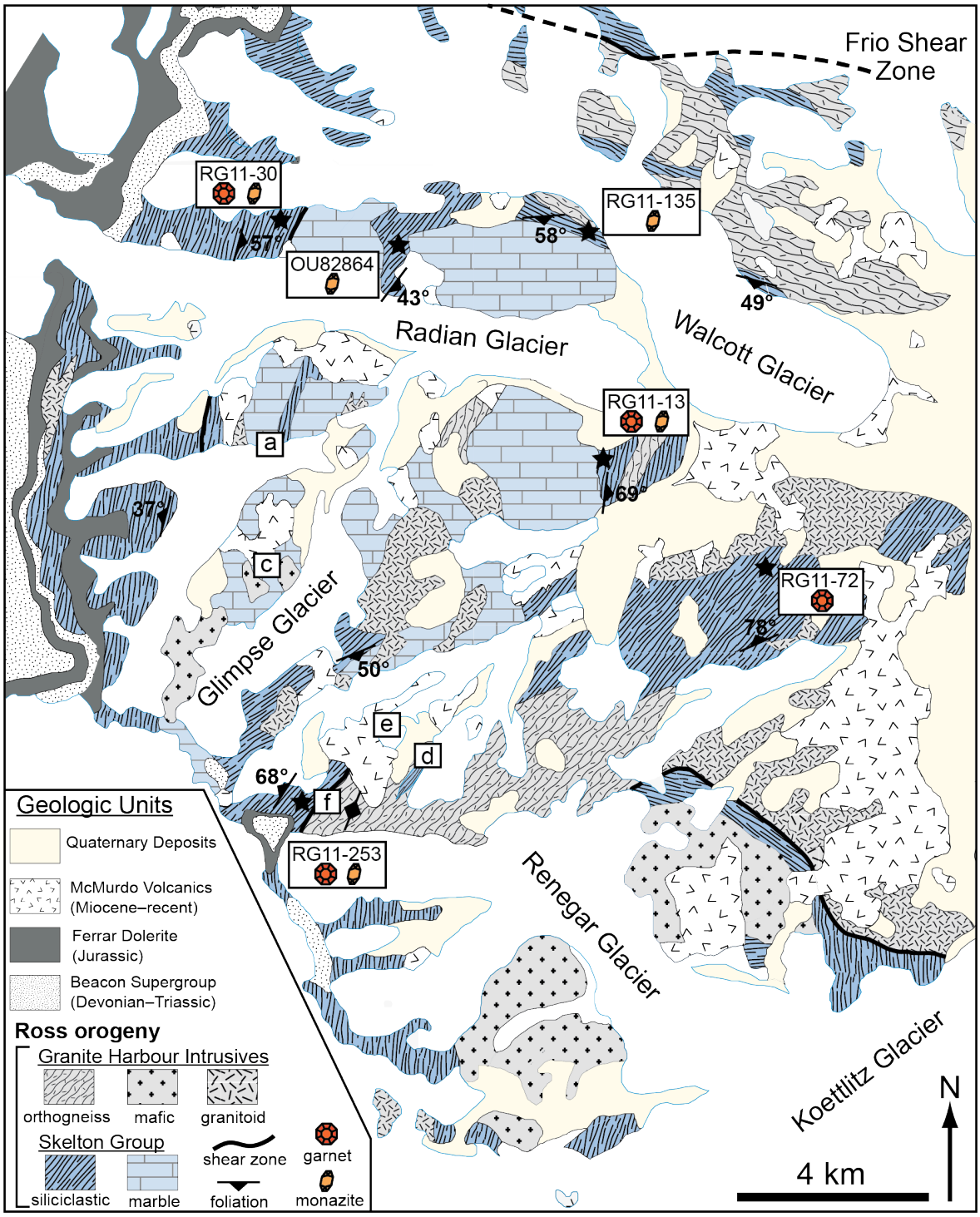

Figure 1.3 Geologic map of the Walcott Glacier area emphasizing the distribution of Skelton Group metasedimentary rocks (modified from Cox et al., 2012). Large shear zones and the dominant foliation in different areas are shown. The locations of the samples from this study are also shown, with icons denoting the type of geochronometer used in each (garnet and/or monazite). Boxes with letters mark the locations of the field photographs shown in Figure 1.4.

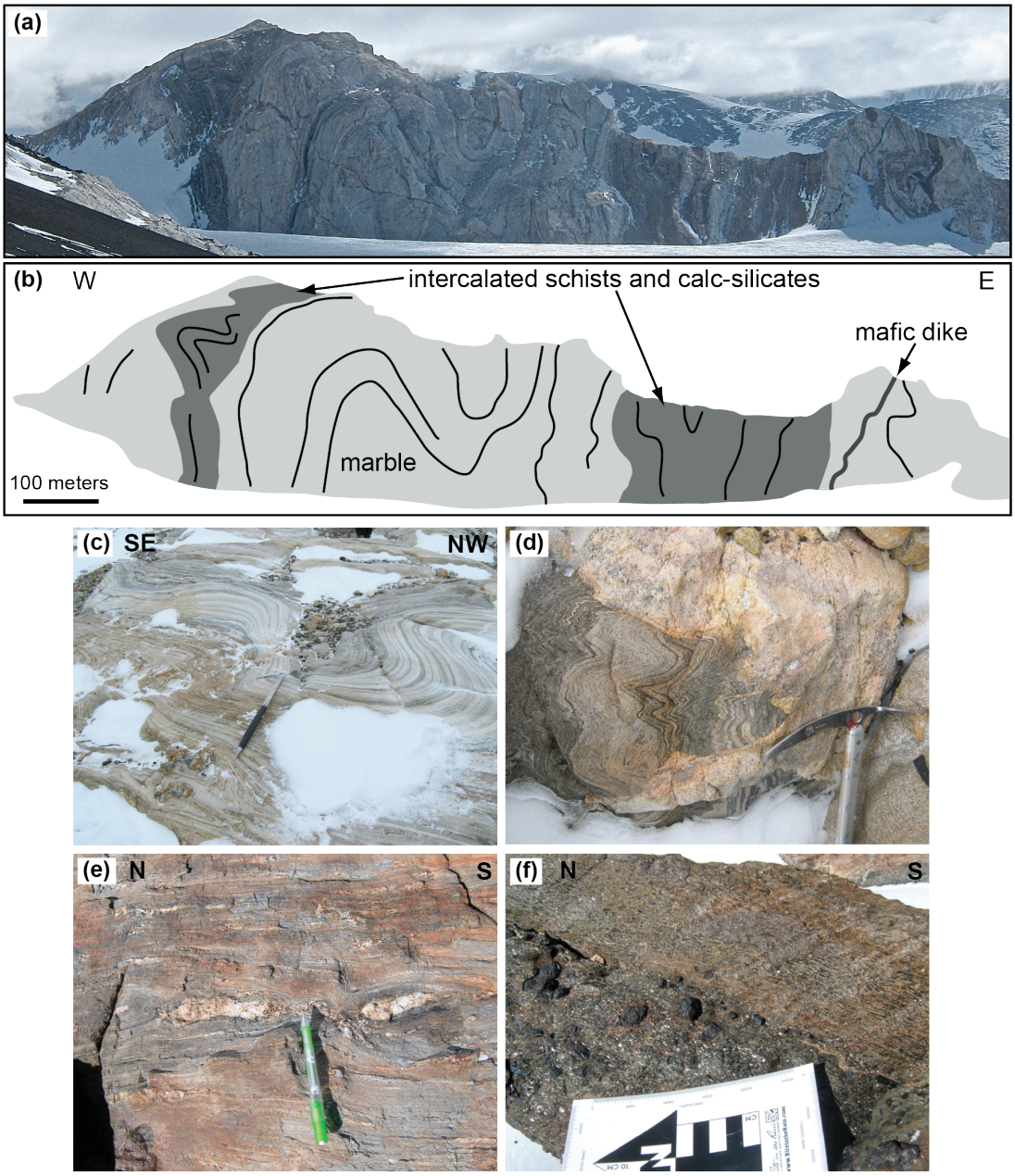

Figure 1.4 Field photographs of Skelton Group outcrops. (a) Large-scale folds in interlayered marble, calc-silicate, and schist on Radian Ridge. (b) Sketch interpretation of the outcrop in a. (c) Multiply-folded marble composes most of the Skelton Group in the study area. (d) Deformed and migmatitic paragneiss hosts granitic intrusions. (e) Migmatitic paragneiss with boudinaged leucosomes. (f) Garnet- tourmaline schist in contact with amphibolite. The orientations of the photographs are given where possible.

igneous bodies (Fig. 1.3) and include five metapelites and one garnet amphibolite.

PETROGRAPHY AND MINERAL CHEMISTRY

Analytical methods

Compositional X-ray maps of garnet and monazite, and quantitative mineral compositions were obtained at UC Santa Barbara using a Cameca SX-100 electron-probe microanalyzer (EPMA) outfitted with five wavelength-dispersive spectrometers. Semi-quantitative X-ray maps were generated for garnet by measuring a grid of spots over the grains, applying 8 μm spacing, 15 kV accelerating voltage, 200 nA beam current, and 120-millisecond dwell time. Monazite grains were mapped with a fully-focused beam across 1 μm-spaced grids applying a 20-kV accelerating voltage, a 200-nA beam current, and 100-millisecond dwell time.

Elemental concentrations in garnet were determined for Al, Ca, Cr, Fe, K, Mg, Mn, Na, Si, and Ti using wavelength-dispersive spectrometry. The accelerating voltage was 15 kV, the beam current 10 nA, and the spot size 2 μm. Synthetic and natural reference materials were used for primary standardization, as well as for drift monitoring and to check accuracy. On- and off-peak counting times were 20 seconds for all elements, and dead-time corrections were applied to all analyses. Each result is the average of seven on-peak measurements. Matrix-effect corrections were done using a ϕρz correction protocol.

Trace element concentrations in garnet were measured in thin section by quadrupole laser-ablation inductively-coupled plasma mass spectrometry (Q-LA-ICP-MS). A Photon Machines 193 nm ArF Excimer laser was used to conduct two traverses on each grain, one parallel- and one perpendicular-to the foliation. These were typically parallel to traverses done by EPMA to enable linking trace- and major-element concentrations across the grains. Traverses consisted of 53 or 65 μm diameter spots with 25–100 μm spacing between spots. A

laser fluence of approximately 2–3 J/cm^2 was used for 25-second ablations at 8 Hz pulse frequency with 10-second washouts in between analyses. Measurements were made with an Agilent 7700S quadrupole ICP-MS. Trace element concentrations were internally normalized to the Al concentrations of the grains previously measured by EPMA and externally normalized using BHVO-2 (USGS; utilizing the GeoReM recommended values as of 2015; Jochum et al., 2005) as a primary reference material. Accuracy was monitored through replicate analysis of an in-house garnet reference and NIST SRM 612 glass after every ~12 unknowns. The reproducibility of the rare earth element (REE) concentrations for the reference materials was within 5% (2σ) of the accepted values. Data reduction was performed using Iolite version 2.31 (Paton et al., 2010; 2011). The one-dimensional Lu concentration data from laser-ablation transects were used in volumetric calculations to determine budgets of Lu (and by proxy, radiogenic ^{176}Hf produced *in-situ*) across grains (e.g., Smit et al., 2010). This was done to examine the potential effect of age bias from the Lu zoning, assuming constant radial or volumetric growth rates.

Petrography and mineral compositions

RG11-13

Sample RG11-13 is a garnet-bearing sillimanite-grade schist collected near the contact with a ~300 m-wide layer of orthogneiss (Fig 3). The rock comprises an assemblage of biotite (X_{Mg} = Mg/[Mg+Fe] = 0.48–0.60) + quartz + plagioclase ($an_{29–35}$) + garnet ($alm_{60–62}$; $sps_{22–27}$; $prp_{8–13}$; $grs_{3–6}$) + sillimanite and contains minor muscovite, tourmaline, and accessory monazite and zircon. There is a prominent crenulated foliation defined by aligned biotite and elongate quartz and plagioclase. Bundles of fibrolitic sillimanite are typically aligned parallel to the

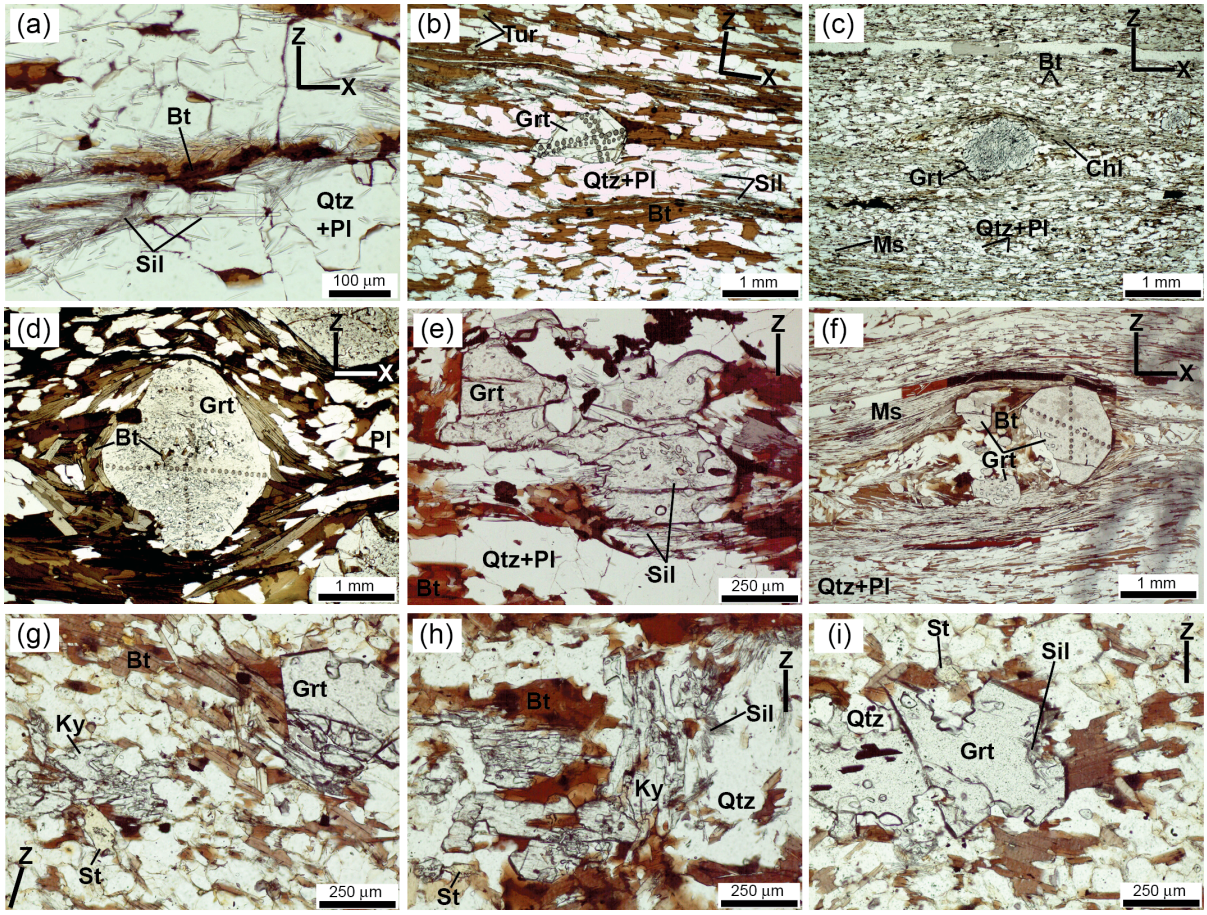

Figure 1.5 Photomicrographs showing some representative assemblages and textures of the samples from this study. (a; RG11-13) Fibrolitic sillimanite with mats aligned parallel to the foliation also with some randomly aligned sillimanite needles. (b; RG11-13) Subhedral inclusion-poor garnet porphyroblast with pits from laser-ablation traverses. (c RG11-30) Garnet porphyroblast with sigmoidal inclusion trails of quartz that are concordant with the external foliation. (d; RG11-72) Garnet amphibolite (hornblende outside the field of view) with euhedral garnet porphyroblasts with randomly-oriented biotite and quartz inclusions. (e; RG11-135) Anhedral garnet porphyroblast with sillimanite inclusions. (f; RG11-253) Inclusion-free garnet porphyroblast that shows evidence for fracturing and disaggregation due to tectonic strain. The shadow on the right side is an etching in the underside of the thin section. (g; OU82854) Ragged kyanite adjacent to a small staurolite grain. The garnet porphyroblast in the upper right has two well formed faces and quartz-filled embayments on other faces. (h; OU82854) Kyanite grains bordered by radiating sillimanite fibers. (i; OU82854) Garnet porphyroblast with sillimanite inclusions. Orientation markers "Z" and "X" correspond to the axes of greatest principle shortening and extension, respectively. Mineral abbreviations after Kretz (1983).

foliation but, in places, form radiating clusters (Fig. 1.5a). Sillimanite is mostly concentrated around grains of biotite. Plagioclase grains have bent deformation twins, and quartz grains show evidence of subgrain development and grain boundary migration. Garnet porphyroblasts are approximately 1 mm in diameter, subidioblastic to idioblastic, and typically free of inclusions (Fig. 1.5b).

RG11-30

Sample RG11-30 is a pelitic schist consisting of muscovite + biotite (X_{Mg} = 0.45–0.47) + quartz + plagioclase ($an_{27–31}$) + garnet ($alm_{65–70}$; $sps_{15–20}$; $prp_{9–11}$; $grs_{3–5}$) + chlorite and contains minor opaques and accessory monazite. The main foliation is defined by layers of aligned micas and chlorite separating quartz + plagioclase segregations. Quartz subgrains exhibit 120° dihedral angles. Garnet occurs as subidioblastic to idioblastic grains, which are typically ~ 1 mm in diameter and poikiloblastic, with bands of quartz inclusions defining an internal foliation. The internal foliation is sigmoidal and the inclusion trails are near-concordant with the matrix foliation (Fig. 1.5c). The quartz inclusions are most abundant in the cores of grains, and most grains have 50−100 μm-wide inclusion-free rims.

RG11-72

Sample RG11-72 is a garnet amphibolite from near the contact with an A-type granite pluton (Fig. 1.3). The assemblage contains hornblende + biotite (X_{Mg} = 0.37–0.49) + garnet ($alm_{71–76}$; $sps_{2–5}$; $prp_{6–11}$; $grs_{12–17}$) + plagioclase ($an_{33–43}$) + quartz with accessory zircon. The main foliation is defined by aligned biotite and hornblende and is wrapped around idioblastic garnet porphyroblasts (Fig. 1.5d). Quartz grains show evidence of subgrain rotation with

subordinate bulging recrystallization and grain boundary migration. Garnet porphyroblasts are subidioblastic or idioblastic, are 2−3 mm in diameter, and contain abundant randomly dispersed inclusions of quartz and biotite (Fig. 1.5d).

RG11-135

Sample RG11-135 is a sillimanite-grade schist containing an assemblage of biotite (X_{Mg} = 0.46–0.48) + muscovite + quartz + plagioclase ($an_{24–37}$) + garnet ($alm_{63–66}$; $sps_{18–24}$; $prp_{8–13}$; $grs_{3–4}$) + sillimanite + opaques with accessory monazite. Sillimanite occurs as fibrolite bundles or small tabular grains aligned parallel to the foliation. Garnet porphyroblasts are sparse, small (<1 mm), and xenoblastic, and contain quartz and sillimanite inclusions (5e). Quartz shows evidence of progressed recrystallization by subgrain rotation and grain boundary migration, partially overprinted by static recovery— evident by 120˚ dihedral angles defined by grain boundaries.

RG11-253

Sample RG11-253 is a sillimanite-grade schist from a section composed of calcareous schist with thinner layers of amphibolite and pelitic schist. The assemblage is biotite (X_{Mg} = 0.33–0.38) + muscovite + quartz + sodic plagioclase ($an_{7–8}$) + garnet ($alm_{84–87}$; $sps_{5–7}$; $prp_{4–8}$; $grs_{1–3}$) with minor sillimanite and accessory monazite + zircon. Xenoblastic to idioblastic garnet porphyroblasts range from ~ 1−5 mm in diameter and show evidence of tectonic strain (Fig. 1.5f). When present, quartz inclusions are more concentrated in the cores of garnet grains.

OU82864

Sample OU82864 is a sillimanite-grade schist. It is distinct in that it contains both kyanite and sillimanite, as well as staurolite and cordierite— phases absent from the other samples in this study. The rock also contains quartz, plagioclase (an_{33-53}), biotite (X_{Mg} = 0.51–0.55), garnet ($alm_{66–69}$; $sps_{12–14}$; $prp_{12–16}$; $grs_{4–5}$), minor tourmaline, and accessory monazite and apatite. It exhibits a weak foliation defined by alignment of small tabular biotite grains. The fabric is absent in domains where biotite is larger, randomly oriented, and interlocking. Tabular kyanite grains are corroded and texturally associated with small staurolite porphyroblasts (Fig. 1.5g; 1.5h). In some areas kyanite is proximal to radiating sillimanite needles, but the phases are not intergrown (Fig. 1.5h). Cordierite occurs in leucocratic zones with quartz and plagioclase. Garnet porphyroblasts are small (0.5−1 mm in diameter), and xenoblastic to subidioblastic, and often show quartz-filled embayments at the grain boundaries (Fig. 1.5g; 1.5i). In some cases, sillimanite fibers extend from embayments into garnet grains (Fig. 1.5i).

Mineral zoning

Garnet X-ray maps and major element quantitative profiles

Element maps of Ca, Fe, Mg, and Mn were generated for garnets from each of the samples targeted for Lu-Hf geochronology. Different grains within single samples show variable degrees of zoning and different zoning patterns, although it is important to note that the grains are not necessarily cut through a median section. In general, garnet show more pronounced zoning in Mn and Ca than in Mg and Fe (Fig. 1.6).

Garnet grains that are zoned in Fe typically show increasing Fe content from core to rim. Where present, Mg zoning is typically opposite of the Fe zoning in the same grain, but is

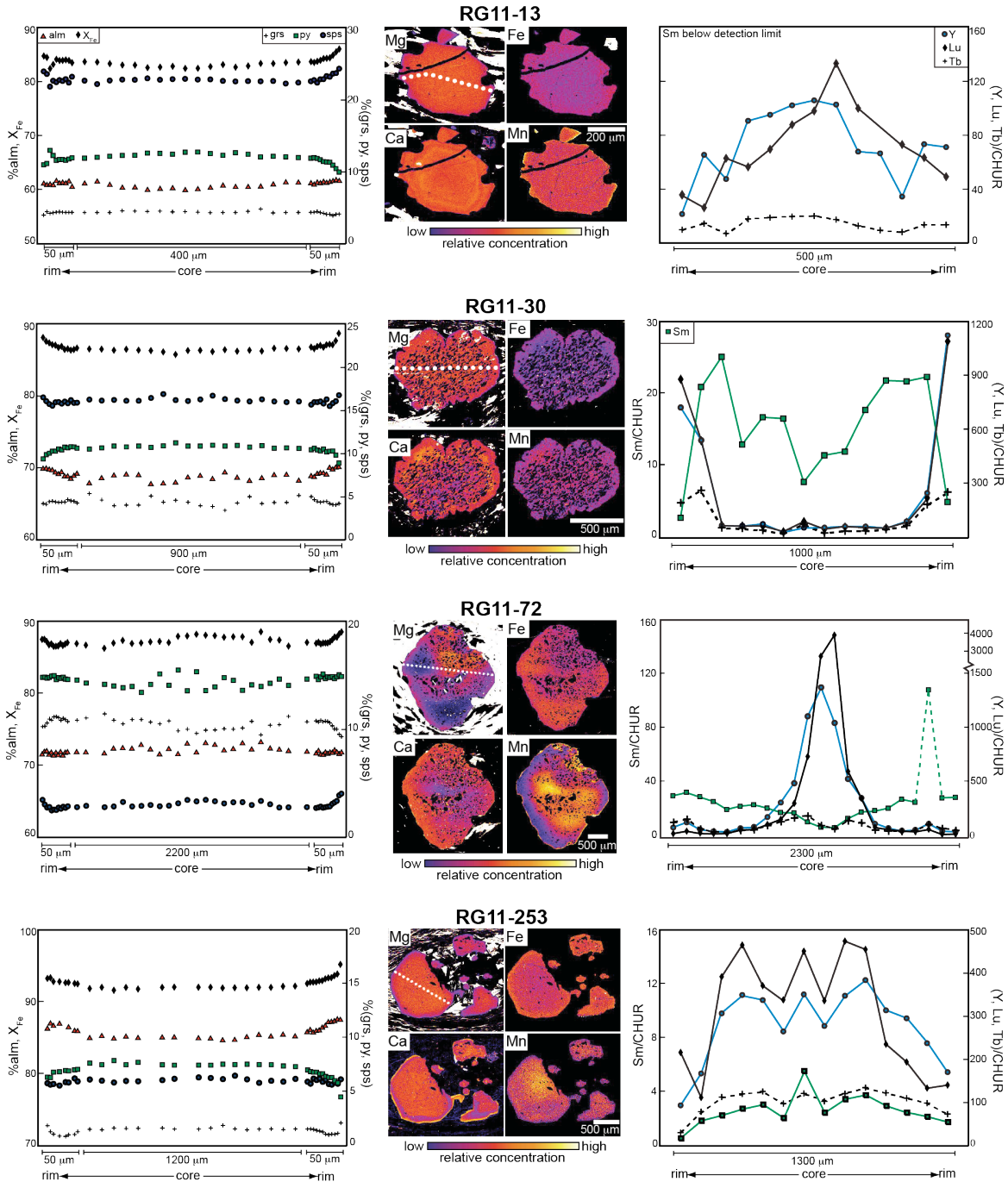

Figure 1.6 Element X-ray maps and composition profiles of garnets from the samples targeted for Lu-Hf dating. Some major element zoning is evident in the element maps, particularly in Ca. Quantitative major element profiles show relatively small variations in composition across the grains. The largest variations are within ~50 μm of the edges of grains. The REE profiles across the same grains show significant zoning, typically with decreasing concentrations of heavy REE from the cores to rims of grains (except in RG11-30). The approximate positions of laser-ablation transects for the REE measurements are shown on the element maps.

usually subtle. Grains that show the most pronounced variation in Mn concentration typically have smooth zoning patterns from high concentrations in cores to low concentrations in rims (Fig. 1.6; RG11-72; 253). Calcium commonly shows sharp to diffuse oscillatory zoning, often with concentration maxima in the mantles of the grains. Some garnet grains, particularly the xenoblastic and highly poikiloblastic grains of samples RG11-72 and RG11-253 (not shown in Fig. 1.6), have irregular or patchy zoning (Appendix Fig. 1). Grains from these samples are often fractured and disaggregated (e.g., Fig. 1.6; RG11-253).

The quantitative EPMA transects show that the greatest compositional ranges in a single garnet are 2–3 mole % for the almandine, spessartine, pyrope, and grossular components. The X_{Fe} (X_{Fe} = Fe/[Mg+Fe]) varies by less than 0.04 in any one grain. In most grains, Fe concentrations increase slightly from core to rim and rise sharply within ~50 μm of the edge of the grains, whereas Mg decreases slightly. Rim-to-rim Ca profiles are slightly "M"-shaped in several samples, reflecting the Ca maxima in the mantles of the grains seen in the X-ray maps. The Ca concentrations generally decrease near the edges of the grains, except for RG11-253, where they increase slightly. The Mn profiles are relatively flat or slightly "M"-shaped and show steep increases of 1–2% near the edges of the grains.

Garnet rare earth element zoning

In most samples, the heavy REE (HREE; represented by Lu in Fig. 1.6) are concentrated in the cores and decrease towards the rims of grains. An exception is RG11-30, which has relatively low concentrations of Lu in the interiors of grains with sharp increases to concentrations of 25–30 ppm (~1,000 × chondrite) within ~150 μm of the edges of grains. The distributions of Y across the grains closely resemble the Lu profiles. The middle REE

(MREE; represented by Tb in Fig. 1.6) commonly show "M"-shaped patterns with maxima in the mantles of the grains. Light REE (LREE; represented by Sm in Fig. 1.6) show variable zoning patterns. Garnet grains from RG11-30 and RG11-72 have lowest Sm concentrations in the cores with increasing concentrations towards the rims. A garnet from RG11-253 shows an "M"-shaped pattern for all REE (Fig. 1.6).

Monazite X-ray maps

Element maps of La, Nd, Th, U, and Y were acquired for monazite targeted for U-Pb geochronology. The Y element maps for representative grains are shown in Figure 1.7; the zoning of all measured elements reflects the Y zoning. A set of element maps for each sample is provided in Appendix Figure 2. Xenoblastic to subidioblastic grains show irregular or patchy zoning of the listed elements. Small, irregular zones in the cores of grains show embayments and cuspate edges (Fig. 1.7). A nearly ubiquitous feature of the grains is low Y concentrations in the core with increasing concentrations towards the rims. Many of the grains from sample RG11-135 (Fig. 1.7) have the highest Y concentrations in the mantles with lower-Y rims. In most grains, compositional zones are apparent in all of the elements. The Y concentrations are typically negatively correlated with La and Nd, and positively with U and Th (Appendix Fig. 2).

PHASE EQUILIBRIA MODELLING

Analytical methods

Phase-equilibria calculations were conducted using THERMOCALC ver. 3.33 (Powell & Holland, 1988) with mineral compositions obtained by EPMA (see above section for

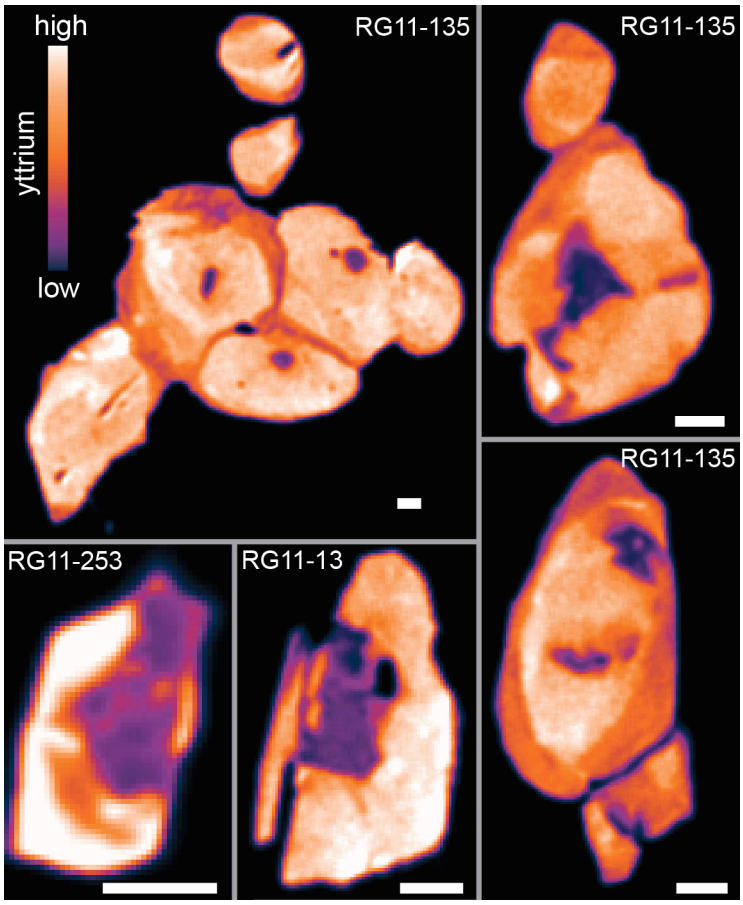

Figure 1.7 Monazite yttrium X-ray maps of representative grains from several samples. Small, irregular, low-Y cores are a common feature in many grains. The highest Y concentrations typically occur in the mantles (e.g., RG11-135) or rims (e.g., RG11-13 and RG11-253) of grains. Scale bars are 10 μm.

analytical details). Whole-rock major element compositions were used for forward modeling with *Perple_X* ver. 6.7.0 (Connolly, 2005; 2009) using the internally-consistent thermodynamic data set of Holland and Powell (2011). Whole-rock major element compositions for the samples with the prefix "RG" were obtained by X-ray fluorescence at Pomona College in Claremont, CA. For sample OU82864 there was no sample available to analyze by XRF. The bulk composition of this sample was estimated by averaging compositions measured by WDS over a rectangular grid of ~620 analyses across a thin section. The analytical setup was similar to that used for the measurement of individual mineral compositions (methods described in the previous section), but with a shorter counting time during each analysis. The results from the WDS "point counting" agree well with a bulk composition for the same thin section estimated by a "semi-quantitative" grid measured by energy-dispersive spectrometry on an FEI Quanta 400f scanning electron microscope. Representative mineral compositions and the bulk composition data used for modeling are given in Table 1.1.

Results

Pressure-temperature calculations were done using the "average P-T" function in THERMOCALC. A summary of the P-T estimates and the equilibria used for each estimate are given in Table 1.2. Multiple calculations were done for each modeled sample to test the assumption of equilibrium among phases and to extract information about the prograde metamorphic path from the composition of zoned minerals. The calculations yielded consistent P-T estimates, and estimates from different zones of minerals are indistinguishable. Temperatures and pressures calculated with THERMOCALC range from

611 ± 74 to 682 ± 31 °C and 4.5 ± 0.8 to 6.0 ± 1.2 kbar, respectively (uncertainties are 1σ). Temperatures were also calculated using the Ti-in-biotite thermometer of Henry et al. (2005). The calculated temperatures range from ~ 530–640 °C (uncertainty on the calibration is estimated to be ~ 12–24 °C; Henry et al., 2005), and are typically lower than the THERMOCALC average P-T temperature for the same sample, except for sample OU82864—for which it is higher.

Pseudosections were calculated for samples RG11-13, RG11-253, and OU82864 in the MnNCKFMASHT ($Mn\text{-}Na_2O\text{-}CaO\text{-}K_2O\text{-}FeO\text{-}MgO\text{-}Al_2O_3\text{-}SiO_2\text{-}H_2O\text{-}TiO_2$) system (Fig. 1.8). Calcium-in-garnet isopleths—as well as independent constraints on peak temperatures and pressures from the inverse modeling results—typically overlap with the field containing the observed paragenesis in each sample (except for RG11-253, in which the Ti-in-biotite records a lower apparent temperature).

Lu-Hf GEOCHRONOLOGY

Analytical methods

For garnet Lu-Hf analysis, rocks were gently broken into chips using a steel pestle. All rock chips and mineral fragments were rinsed with de-ionized water and ethanol. Large unweathered rock chips were selected for bulk-rock Lu-Hf analysis. Garnet grains were hand picked from the crushed material under a binocular microscope with an effort to select only whole-grains, and so to avoid core-rim biasing. Separates were rinsed in de-ionized water and weighed in pre-cleaned Teflon vials. The grains were submerged in 1 M HCl for 1 hour at room temperature, after which they were rinsed twice in de-ionized water. Garnet fractions were admixed with a ^{176}Lu-^{180}Hf tracer solution and dissolved by alternating addition of

Table 1.1 Mineral and whole-rock compositions used for phase equilibria modeling

Sample	Mineral	SiO_2	TiO_2	Al_2O_3	Cr_2O_3	FeO	MnO	MgO	CaO	Na_2O	K_2O	P_2O_5	H_2O*	Total
RG11-13	grt	36.87	0.01	20.58	0.00	26.58	9.88	2.89	1.46	0.01	0.00	-	-	98.28
	bt	35.62	2.48	19.33	0.02	17.03	0.30	9.39	0.02	0.19	8.81	-	-	93.19
	msc	45.70	0.82	35.41	0.02	1.02	0.00	0.64	0.00	0.75	10.13	-	-	94.49
	pl	60.58	0.00	24.94	0.00	0.10	0.01	0.00	6.53	7.91	0.11	-	-	100.18
	w.r.	66.21	0.87	16.66	-	5.81	0.11	3.33	1.08	1.28	3.66	0.11	1.4	99.01
RG11-30	grt	36.99	0.02	20.86	0.00	30.75	7.09	2.64	1.53	0.01	0.00	-	-	99.89
	bt	35.51	1.61	19.33	0.02	19.41	0.17	9.38	0.06	0.11	7.55	-	-	93.15
	msc	45.82	0.39	35.40	0.01	0.92	0.00	0.57	0.03	1.11	9.49	-	-	93.74
	pl	61.20	0.00	24.80	0.01	0.06	0.00	0.00	6.26	7.78	0.62	-	-	100.73
	w.r.	65.88	0.93	18.36	-	5.37	0.17	2.46	0.87	1.10	3.89	0.08	1.9	99.03
RG-72	grt	37.63	0.04	20.84	0.01	32.19	1.30	2.67	5.06	0.01	0.00	-	-	99.75
	bt	36.60	1.06	16.06	0.01	19.83	0.04	10.85	0.02	0.23	8.70	-	-	93.40
	amph	42.70	0.45	12.75	0.02	19.96	0.18	7.23	10.74	1.30	0.57	-	-	95.90
	pl	58.47	0.01	25.80	0.00	0.08	0.00	0.00	7.77	6.83	0.42	-	-	99.38
	w.r.	61.82	0.66	11.49	-	13.07	0.25	4.46	2.88	0.74	2.86	0.12	1.2	98.23
RG-135	grt core	37.52	0.02	20.75	0.05	28.75	8.68	3.03	1.05	0.01	0.00	-	-	99.86
	grt rim	37.64	0.01	20.72	0.02	28.55	9.32	2.56	1.38	0.01	0.01	-	-	100.22
	bt	36.09	2.71	19.06	0.04	18.16	0.29	8.98	0.01	0.25	9.21	-	-	94.80
	msc	46.02	0.86	34.97	0.01	0.93	0.00	0.63	0.00	0.79	10.22	-	-	94.43
	pl	61.36	0.00	24.20	0.00	0.30	0.00	0.00	5.71	8.24	0.23	-	-	100.04
	w.r.	64.13	1.10	18.99	-	5.43	0.10	2.72	0.57	0.98	4.96	0.08	1.3	98.98
RG-253	grt core	37.6	0.02	20.31	0.00	36.85	2.79	1.78	0.56	0.01	0.00	-	-	99.93
	grt rim	37.79	0.01	20.32	0.00	37.15	2.46	1.48	0.66	0.01	0.01	-	-	99.89
	bt	34.79	2.01	18.92	0.00	24.04	0.06	5.95	0.00	0.22	8.95	-	-	94.94
	msc	46.41	0.36	35.55	0.00	1.48	0.00	0.46	0.00	1.29	9.48	-	-	95.03
	pl	67.07	0.00	20.97	0.01	0.06	0.01	0.00	1.71	10.73	0.06	-	-	100.62
	w.r.	66.71	0.40	18.14	-	5.10	0.08	1.11	0.65	3.29	3.55	0.23	1.3	99.03
OU82864	grt core	38.31	0.02	20.66	0.04	30.73	4.99	3.88	1.63	0.01	0.00	-	-	100.26
	grt rim	38.54	0.02	20.70	0.02	30.06	5.86	3.87	1.45	0.01	0.00	-	-	100.52
	bt	36.8	2.28	18.94	0.02	16.25	0.16	11.01	0.00	0.26	9.33	-	-	95.05
	pl	57.7	0.01	27.11	0.00	0.04	0.00	0.00	9.16	6.32	0.07	-	-	100.41
	crd	48.79	0.01	32.38	0.00	6.70	0.36	8.59	0.01	0.35	0.00	-	-	97.18
	w.r.	64.58	0.59	15.69	0.01	5.08	0.06	3.64	2.54	2.07	2.72	-	1.20	96.96

*, H_2O concentrations estimated from the modal proportions of hydrous phases;**, whole-rock totals from XRF calculated on a water-free basis

Table 1.2 Thermobarometry results

Sample	THERMOCALC "average P-T"							Ti in biotite*
	T (°C)	1σ	P (kbar)	1σ	ρ	σ(fit)	n	T (°C)
RG11-13	682	31	5.9	1.1	0.879	0.62	7	626
RG11-30	625	34	6.0	1.2	0.783	1.20	6	530
RG-135	652	30	5.1	1.2	0.916	0.39	5	639
RG-253	635	30	4.7	1.2	0.964	0.65	5	564
OU82864	611	74	4.5	0.8	0.856	0.31	5	629

*, calibration of Henry *et al.* (2005); ρ, error correlation coefficient; n, number of independent reactions

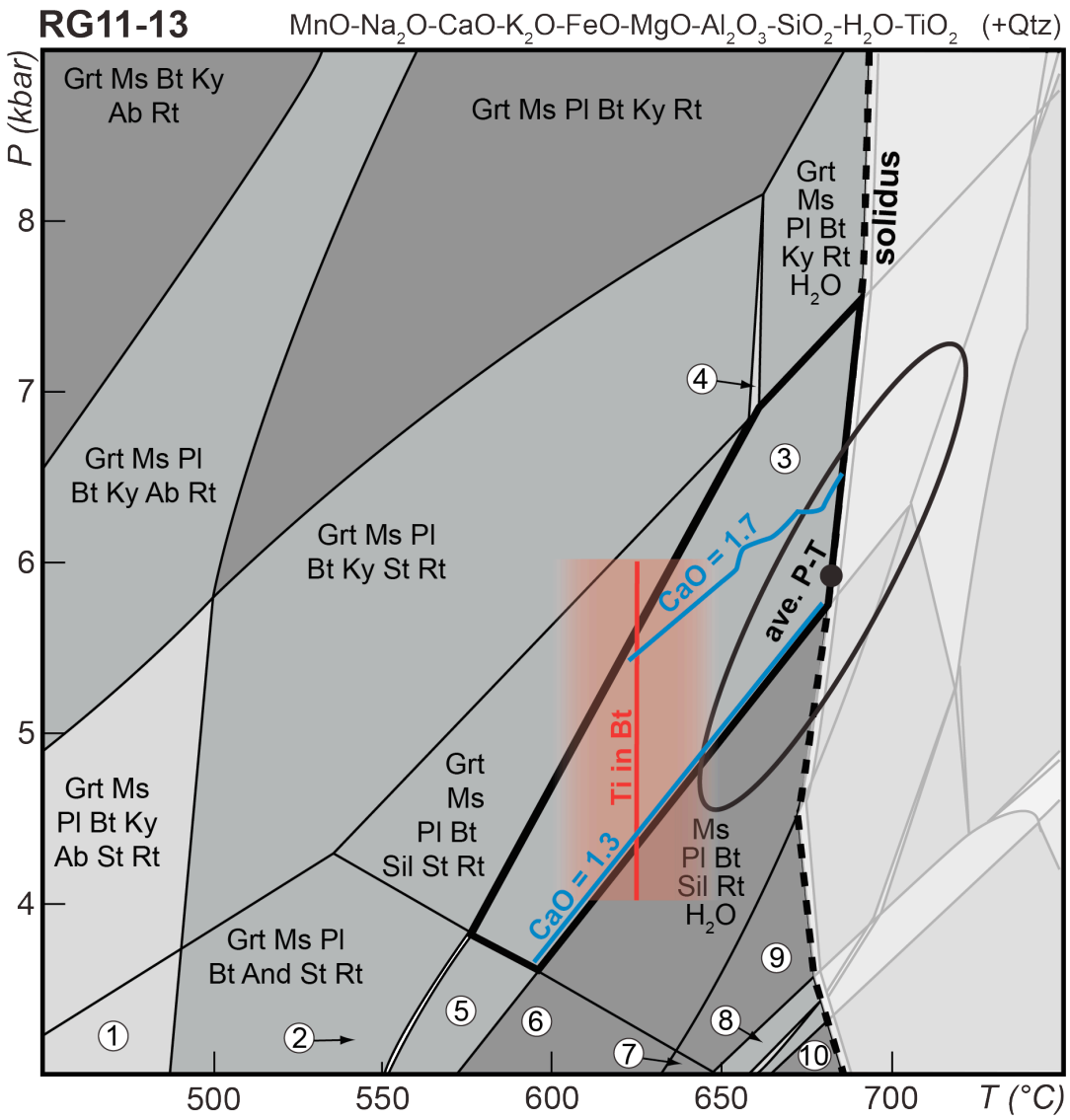

(1) Grt Ms Pl Bt And Ab St Rt
(2) Grt Ms Pl Bt And St Rt H_2O
(3) Grt Ms Pl Bt Sil Rt H_2O
(4) Grt Ms Pl Bt Ky St Rt H_2O
(5) Grt Ms Pl Bt And Rt H_2O
(6) Ms Pl Bt And Rt H_2O
(7) Pl Kfs Bt And Rt H_2O
(8) Pl Kfs Bt Crd Sil Rt H_2O
(9) Pl Kfs Bt Sil Rt H_2O
(10) Pl Kfs Bt Ilm Crd Rt H_2O

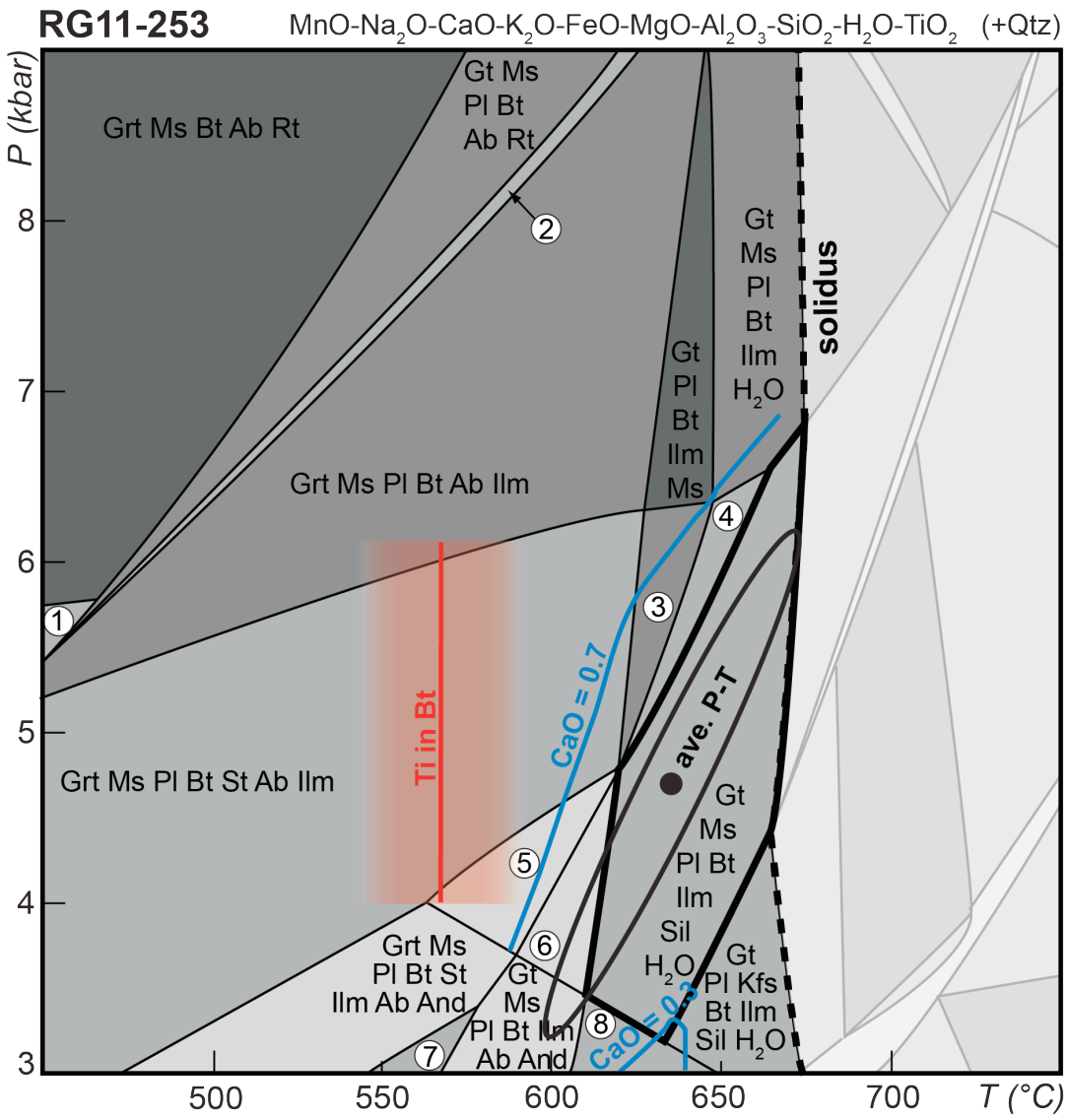

(1) Grt Ms Bt Ab Ilm Rt Ky
(2) Grt Ms Pl Bt Ab Ilm Rt
(3) Grt Ms Pl Bt St Ilm
(4) Grt Ms Pl Bt St Ilm H_2O
(5) Grt Ms Pl Bt St Sil Ab Ilm
(6) Grt Ms Pl Bt And Ab Ilm H_2O
(7) Grt Ms Pl Bt And Ab Ilm
(8) Grt Ms Pl Bt And Ilm H_2O

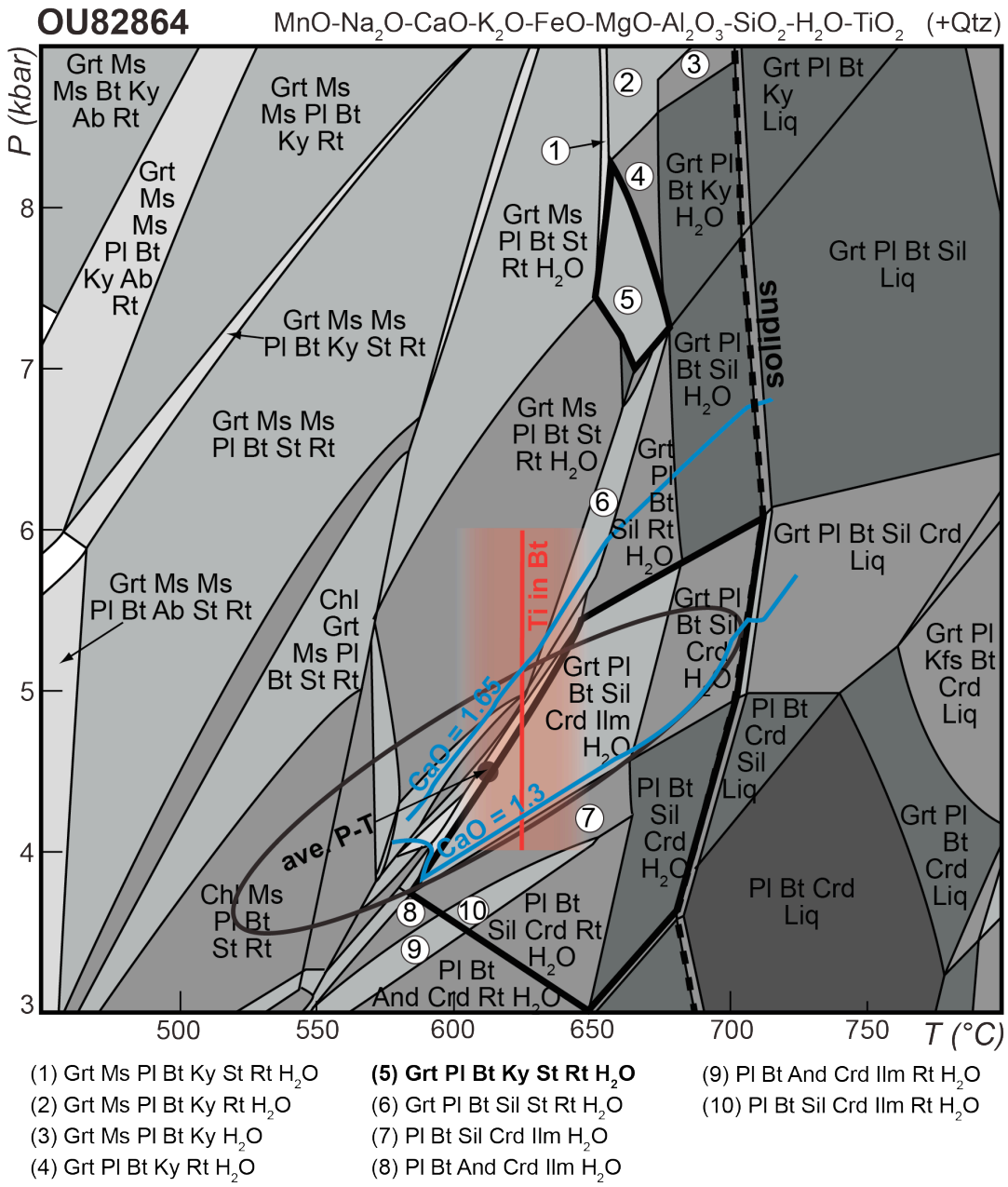

Figure 1.8 Pseudosections for representative samples. Fields containing the observed mineral assemblages are outlined with thick black lines. For OU82864, the multiple outlined fields contain minerals (e.g., kyanite, staurolite, sillimanite, and cordierite) that could not have composed a stable assemblage but could be linked to specific parageneses. Blue curves are Ca-in-garnet isopleths (numbers are wt % CaO) that span most of the range of observed garnet CaO concentrations in the samples. Red lines are Ti-in-biotite apparent temperatures plotted across the pressure range of the thermometer calibration (4–6 kbar); the red bands represent the uncertainty association with the thermometer calibration (~ 24 °C; Henry et al., 2005). The "ave. P-T" are calculated with THERMOCALC, with the ellipses representing the correlated 1σ uncertainties. Mineral abbreviations after Kretz (1983). The abbreviation "Ms" represents white mica—not strictly muscovite.

concentrated HF-HNO_3-$HClO_4$ and HCl with sample dry-downs in between (Lagos et al., 2007). The whole-rock chips were powdered using a ceramic mortar and pestle, and were then weighed, admixed with a ^{176}Lu-^{180}Hf tracer, and dissolved in 6 mL of concentrated HF+HNO_3 using pressure dissolution vessels (PDV) at 180°C for seven days. Table-top and PDV blanks were performed with every group of samples. Separation of Lu and Hf was done by cation exchange chromatography using Eichrom® Ln-Spec resin following the method of Münker et al. (2001) and applying Fe-purification after Sprung et al. (2010). The separation yielded between 30–100 ng Hf.

Lutetium and hafnium samples were oxidized using H_2O_2 and re-dissolved in dilute HNO_3 and HF+HNO_3 solutions, respectively. Isotope measurements were conducted with a Nu Instruments Plasma HR multi-collector ICP-MS at UC Santa Barbara. Mass bias corrections were done using an exponential law and assuming ^{179}Hf/^{177}Hf = 0.7325 (Hf; Patchett and Tatsumoto, 1980a; 1980b) and ^{173}Yb/^{171}Yb = 1.129197 (for Lu and Yb; Vervoort et al., 2004). The samples were bracketed (typically every 3–4 samples) with, and normalized to, measurements of the JMC-475 reference solution (^{176}Hf/^{177}Hf = 0.282163; Blichert-Toft et al., 1997). External reproducibility of ^{176}Hf/^{177}Hf was estimated on the basis of replicate JMC-475 analyses at concentrations bracketing those of our unknowns following the rationale and methodology of Bizzarro et al. (2003). Isochron regression was done using Isoplot version 3.00 (Ludwig, 2003) applying $\lambda^{176}\text{Lu} = 1.867 \times 10^{-11}$ yr^{-1} (Scherer et al., 2001; 2003; Söderlund et al., 2004). The Lu-Hf isotope results are given in Table 1.3 and shown on isochron diagrams in Figure 1.9. Uncertainties on the isochron dates are given at the 95% confidence level of the regressions for comparison of the Lu-Hf dates from this study. Uncertainties in the λ^{176}Lu (Scherer et al., 2001; 2003; Söderlund et al., 2004)

correspond to additional uncertainty of ~5 million years on 550–600 Ma dates, which must be taken into account when comparing the Lu-Hf and U-Pb age results.

Results

The apparent Lu-Hf ages range from 572 ± 4 Ma to 616 ± 7 Ma, with initial $^{176}Hf/^{177}Hf$ values ranging from 0.28212 ± 2 to 0.28245 ± 1 ($\varepsilon Hf_{(i)} \approx -11$ to +1 at 570 Ma). Three of the isochrons have four garnet points and one whole-rock point. The oldest date (RG11-253) is from an isochron with five garnet points only. Two whole-rock fractions were analyzed for this sample, but both fell above the garnet-only isochron.

A plot of cumulative Lu versus the normalized radial distance from core to rim (Fig. 1.10) shows that the majority of the Lu is in the outer 50% of the garnet radii. Sample RG11-72, with the strongest partitioning of Lu in the core, has a nearly one-to-one relationship on this diagram, whereas RG11-30 has over 80% of the cumulative Lu in the outer 20% of the grain radius. The model of cumulative Lu versus the core-to-rim volume percentage shows that in most of the samples, the majority of Lu is partitioned in the inner domains of the grains. The grains from samples RG11-13, RG11-72, and RG11-253 each have ~65% of the total Lu within the inner 50% of the grain volumes. The Lu in the grain from RG11-30 is still biased toward outer domains of the garnet on this plot, with ~80% of the Lu in the outer 40% of the grain volume.

MONAZITE U-Pb AND TRACE ELEMENTS

Analytical procedures

Monazite U-Pb isotopes and trace elements were measured by laser-ablation split-stream

Table 1.3 Lu-Hf isotope data

Sample	Fraction	Lu (ppm)	Hf (ppm)	$^{176}Lu/^{177}Hf$			$^{176}Hf/^{177}Hf$		
RG11-13	grt-1	23.8	3.62	0.9343	±	29	0.292466	±	89
	grt-2	26.5	3.48	1.081	±	4	0.294097	±	14
	grt-3	24.7	2.96	1.184	±	3	0.295206	±	7
	grt-4	25.3	2.95	1.219	±	3	0.295612	±	15
	w.r.-1**	0.487	7.53	0.009179	±	35	0.284651	±	89
	w.r.-2	0.657	8.57	0.01087	±	3	0.282276	±	13
RG11-30	grt-1	6.76	5.77	0.1662	±	4	0.283984	±	53
	grt-2	7.25	5.50	0.1868	±	6	0.284251	±	14
	grt-3	6.56	5.37	0.1732	±	4	0.284097	±	11
	grt-4	6.45	5.00	0.1830	±	5	0.284200	±	8
	w.r.-1	0.386	7.06	0.007564	±	26	0.282318	±	12
	w.r.-2**	0.387	7.23	0.007583	±	19	0.282239	±	15
RG-72	grt-1	1.23	3.63	0.04829	±	12	0.282971	±	6
	grt-2	1.43	5.12	0.03947	±	10	0.282875	±	6
	grt-3	1.6	2.57	0.08833	±	23	0.283408	±	15
	grt-4	0.814	3.33	0.03471	±	9	0.282875	±	78
	w.r.-1**	0.201	6.33	0.004489	±	20	0.282948	±	12
	w.r.-2	0.212	6.47	0.004639	±	12	0.282495	±	17
RG-253	grt-1	5.92	5.16	0.1626	±	4	0.283967	±	48
	grt-2	4.49	6.31	0.1010	±	3	0.283286	±	11
	grt-3	6.12	5.20	0.1671	±	4	0.284066	±	22
	grt-4	8.03	4.68	0.2436	±	6	0.284935	±	12
	grt-5	4.91	5.45	0.1277	±	3	0.283587	±	20
	w.r.-1**	0.914	8.05	0.01610	±	12	0.282643	±	14
	w.r.-2**	0.853	8.16	0.01481	±	5	0.282518	±	25

grt, garnet fraction; w.r., whole-rock fraction; *, universal uncertainty of 0.25% assumed for $^{176}Lu/^{177}Hf$; **, not used in regression

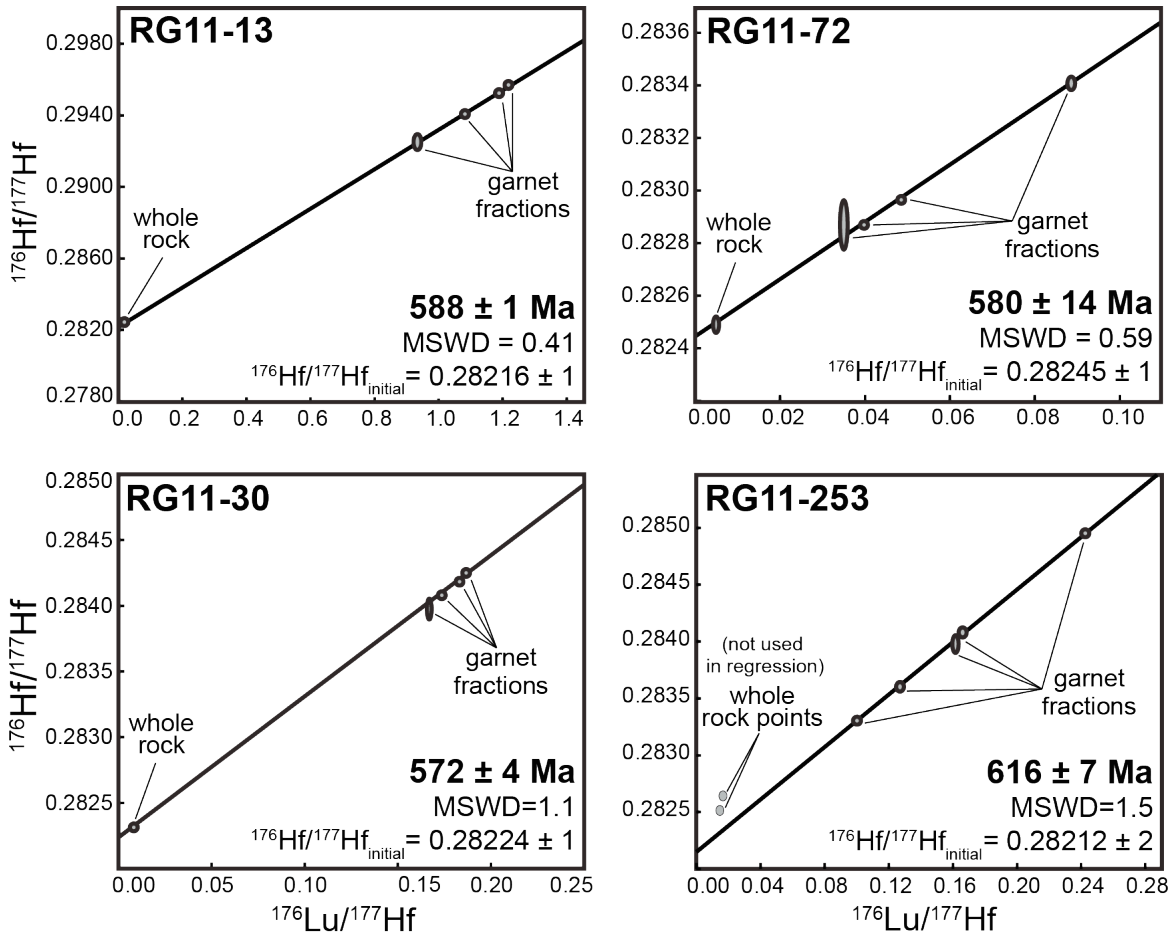

Figure 1.9 Lu-Hf isochron diagrams. Sample RG11-253 has a five-point garnet-only isochron, with the whole-rock points determined to fall above the isochron. The sizes of the error ellipses have been exaggerated for visibility.

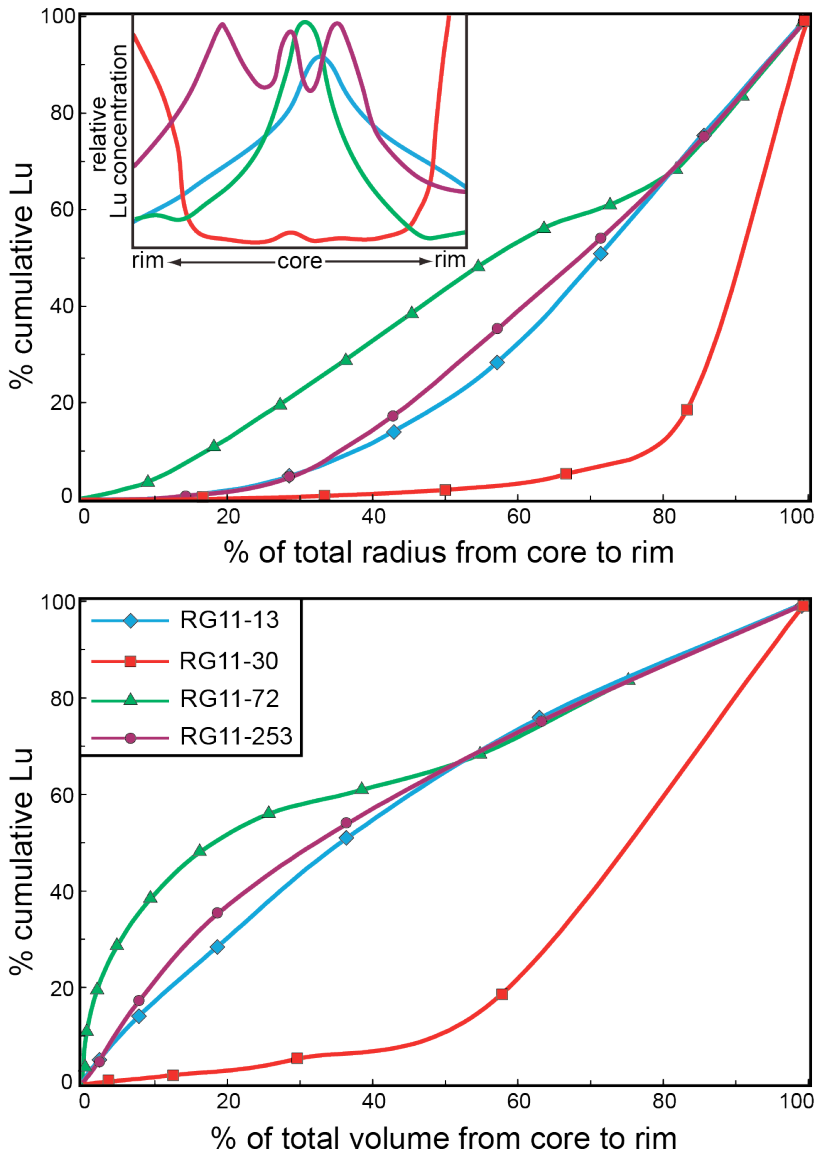

Figure 1.10 Cumulative distributions of Lu from core to rim in garnet from the samples dated with Lu-Hf. The inset shows the Lu zoning patterns of the grains used in the cumulative Lu graphs. The inset Lu rim-to-rim distribution curves are simplified smoothed fits to the data from laser-ablation transects across the grains shown in Figure 1.6 (except for RG11-72, for which a grain with more moderate core Lu concentrations was used). These transects were chosen due to their nearly-symmetric Lu distributions. The point at the axis of symmetry is taken as the core of the grain. The cumulative Lu models use the average Lu concentrations of two adjacent analyses (positions shown by symbols) as the value for the concentric shell between the two points. The garnets are modeled as spheres for simplicity.

ICP-MS (LASS; Kylander-Clark et al., 2013; Cottle et al., *2013*) at UC Santa Barbara. Compositional X-ray maps of monazite grains in thin section (Fig. 1.7) were used to guide the placement of laser-ablation spots in domains of different REE and Y concentrations. A Photon Machines ArF Excimer laser (λ = 193 nm) was used to ablate domains of 7 or 10 μm diameter. Laser fluence was typically 3–4 J/cm^2. After 2 "cleaning" shots to remove any surface Pb contaminant, spots were ablated at 4 Hz repetition rate for 25 seconds with 12-second washout delay in between analyses. The U-Pb isotope analysis was done using a Nu Instruments Plasma HR multi-collector ICP-MS. The m/z corresponding to $^{208}Pb^+$, $^{207}Pb^+$, $^{206}Pb^+$, $^{204}(Pb+Hg)^+$ were measured on secondary electron multipliers, while those of $^{238}U^+$ and $^{232}Th^+$ were measured on Faraday collectors equipped with 10^{11}-Ω resistors. Trace element concentrations were determined using an Agilent 7700S Q-ICP-MS. Data reduction, including corrections for baseline, instrumental drift, mass bias, and down-hole fractionation was carried out using Iolite version 2.31 (Paton et al., 2010; 2011). Trace-element analyses and U-Pb ratios were externally normalized using bracketing analyses of the reference monazites Bananeira (Kylander-Clark et al., 2013) and 44069 (Aleinikoff et al., 2006), respectively. Manangotry and 44069 monazites (Kylander-Clark et al., 2013) were used as secondary reference materials for trace element analyses. To monitor U-Pb data accuracy, Bananeira ($^{206}Pb/^{238}U$ age = 507.8 ± 0.9 Ma; 2 s.e.; Kylander-Clark et al., 2013) and Manangotry ($^{206}Pb/^{238}U$ age = 562.7 ± 3.0 Ma; 2 s.e.; Kylander-Clark et al., 2013) monazites were used as secondary references. Bracketing analyses of Bananeira and Manangotry throughout the analytical sessions yielded weighted mean ages of 510.6 and 565.9 Ma, respectively, with external reproducibility of better than 2% (2 s.d.).

Results

The concordant monazite dates for all of the samples range from ca. 610–500 Ma (Fig. 1.11). Only one concordant analysis is older than 600 Ma, whereas several samples have concordant dates ca. 590–560 Ma. Individual analyses in some samples span 70–80 million years (Fig. 1.11). Individual dates in each sample are dispersed along Concordia, with an absence of discrete populations. In general, the oldest analyses in each sample correspond to low-Y domains and younger analyses to high-Y domains, consistent with the zoning shown in X-ray maps in Figure 1.7. An exception to this is sample RG11-135, which does not show a consistent relationship between age and Y concentration. Older monazite domains are also typically depleted in HREE and have higher Gd/Yb relative to younger domains (Fig. 1.11). Plots of normalized Y concentration and Gd/Yb ratios versus ^{207}Pb-corrected age in Figure 1.12 also demonstrate the enrichment in Y and HREE of younger domains relative to older domains. There is no clear trend in Eu anomalies with time (Fig. 1.12). In all samples, a majority of monazite grains found were in the rock matrix outside of garnet grains. Small monazite inclusions in garnet porphyroblasts (<20 μm in diameter) yield concordant dates that range from ca. 566−499 Ma. One inclusion in RG11-253 has a ^{207}Pb-corrected ^{206}Pb/^{238}U date of 609 Ma, but is reversely discordant (Fig. 1.11).

DISCUSSION

Pressure temperature history of the Skelton Group

Previous studies have proposed contrasting P-T paths for Skelton Group metasedimentary rocks (Fig. 1.13a). Talarico et al. (2005) identified an early stage of metamorphism and deformation at moderate P-T conditions, followed by partial metamorphic re-equilibration at

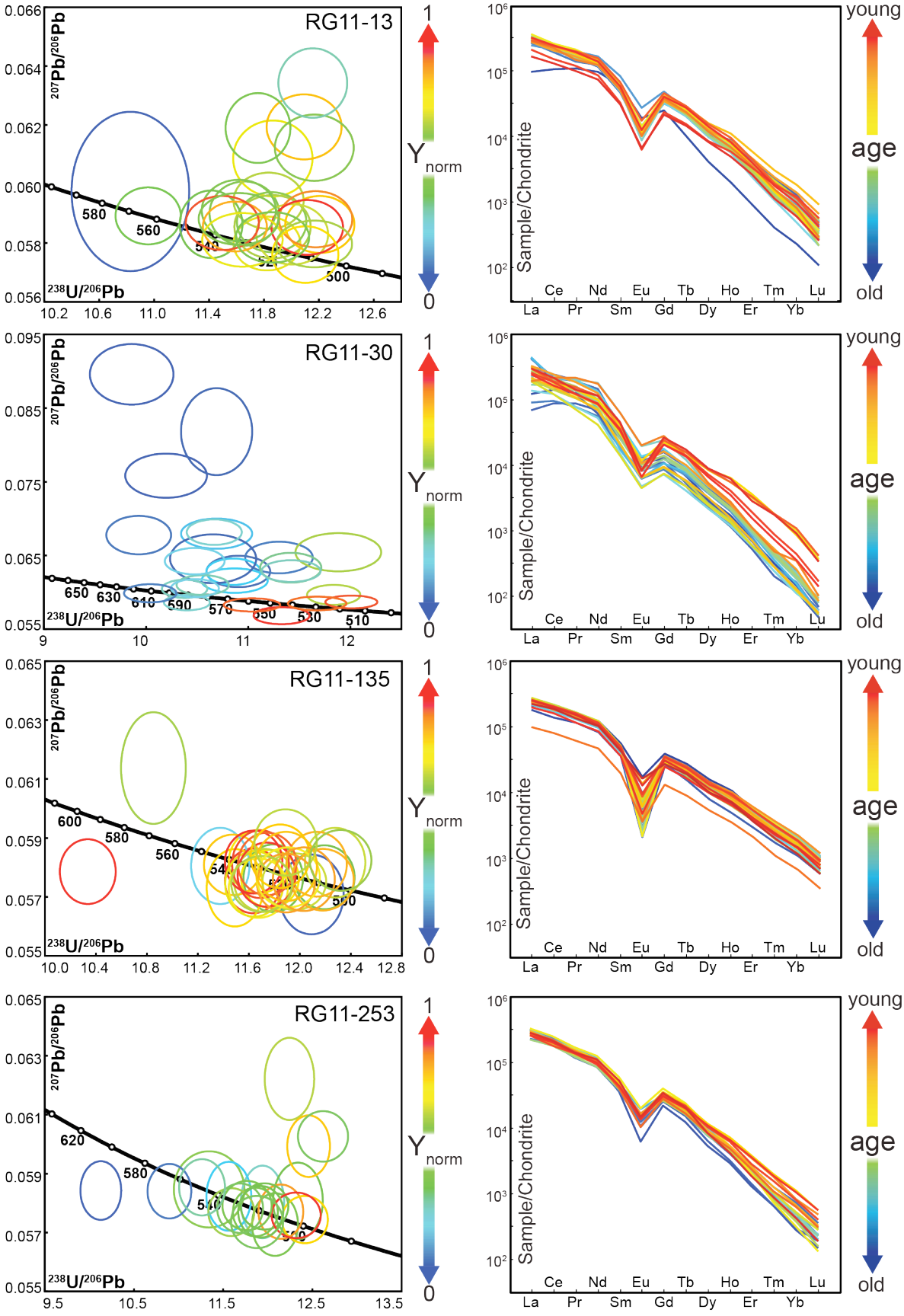
RG11-13
RG11-30
RG11-135
RG11-253
$^{207}Pb/^{206}Pb$
$^{238}U/^{206}Pb$
Y norm
1
0
Sample/Chondrite
young
age
old
Ce Nd Eu Tb Ho Tm Lu
La Pr Sm Gd Dy Er Yb

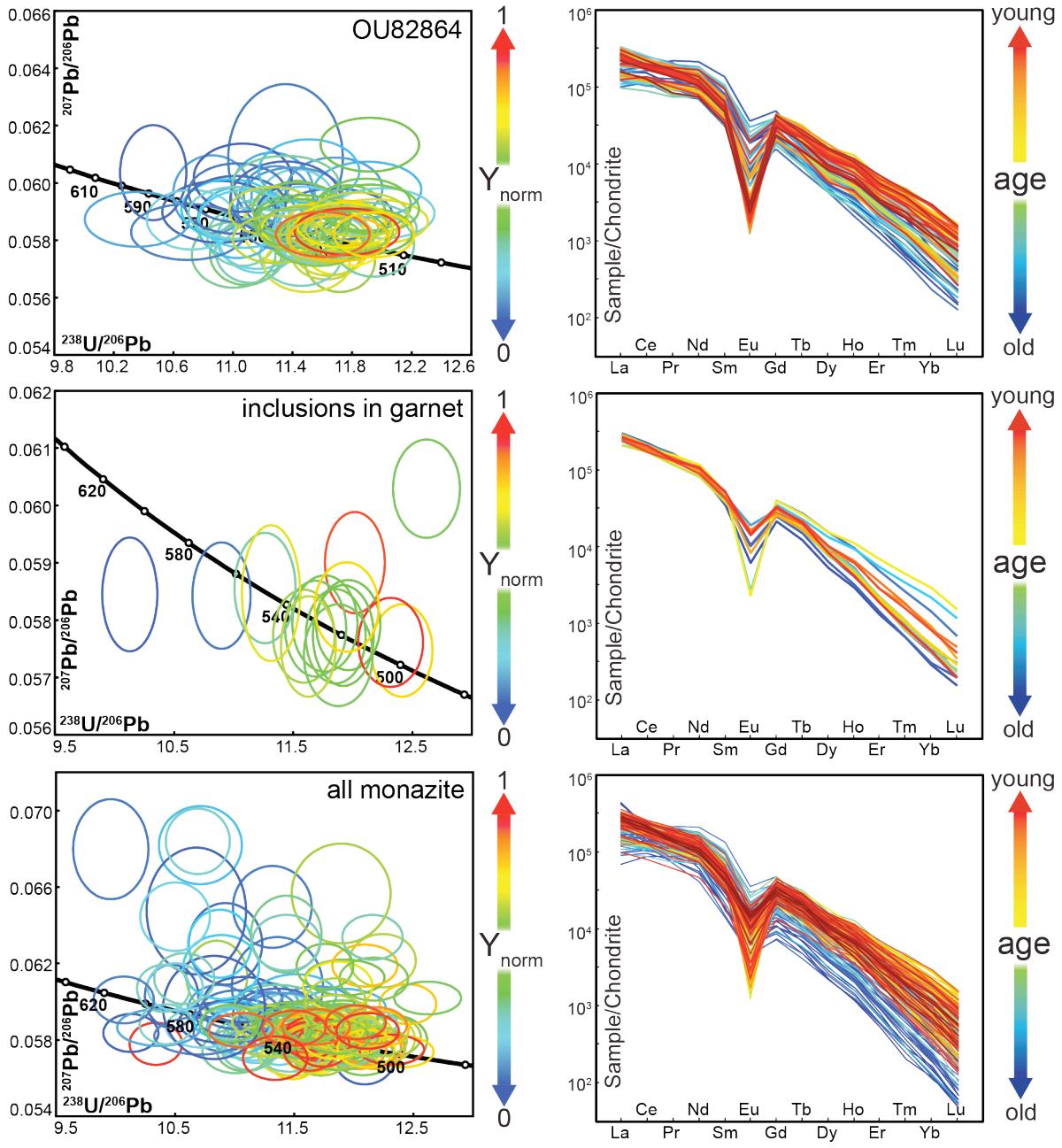

Figure 1.11 Inverse concordia diagrams and chondrite-normalized REE diagrams. Error ellipses on the concordia diagrams are color-coded according to the Y concentration of the analysis normalized to the highest Y analysis from that sample (Y_{norm}). This allows comparison of the relative Y concentrations of monazite between samples that may have different bulk Y concentrations. Chondrite-normalized REE traces for each analysis are color-coded by the corresponding relative ^{207}Pb-corrected $^{206}Pb/^{238}U$ age, from old to young in each sample.

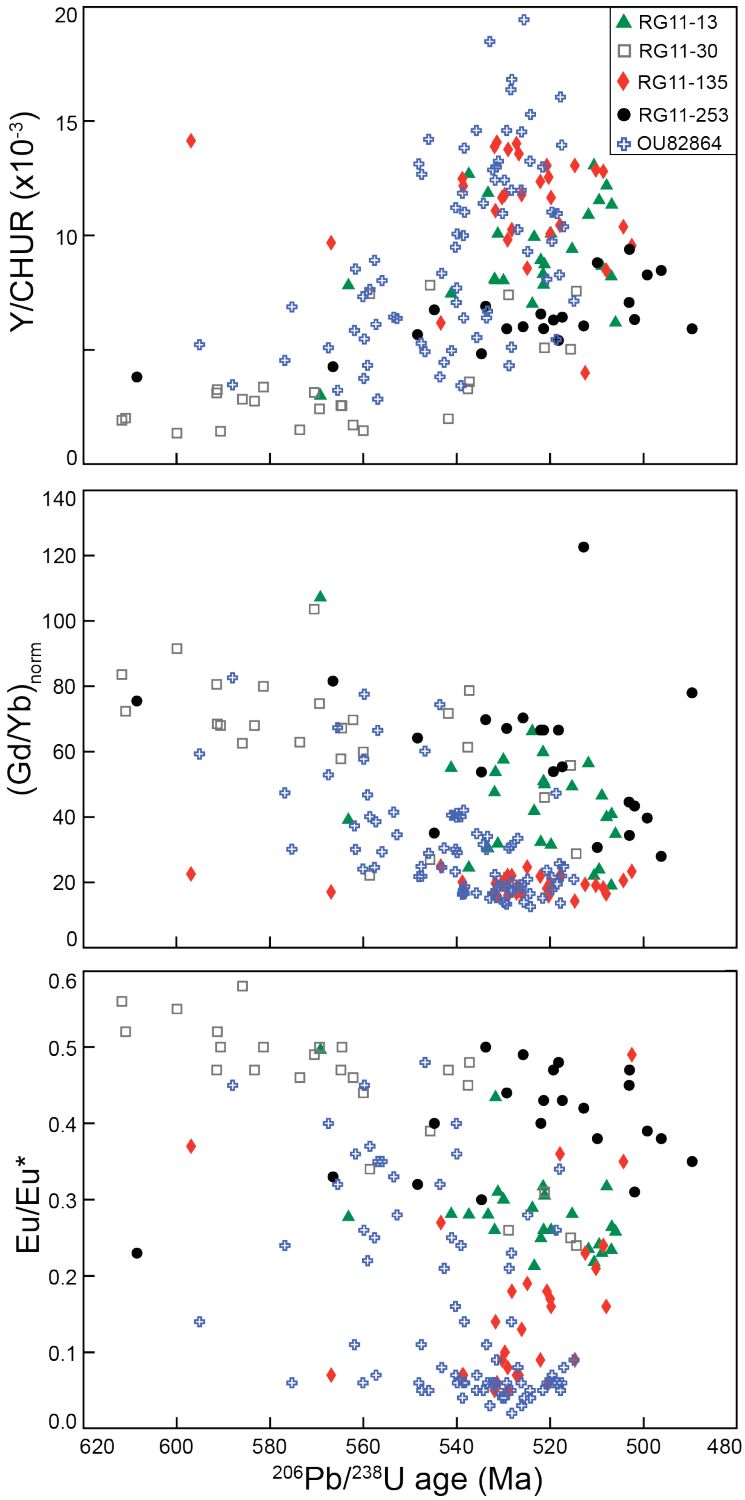

Figure 1.12 Monazite trace element composition versus ^{207}Pb-corrected age. The subscript "norm" indicates chondrite-normalized values. The europium anomaly (Eu/Eu*) = $Eu_{norm}/(Sm_{norm} \times Gd_{norm})$.

lower pressures and temperatures. Though there is incomplete information on the prograde path of these rocks, the interpretation of Talarico et al. (2005) is consistent with a clockwise P-T path through "Barrovian-style" metamorphism (Fig. 1.13a). Goodge (2007) concluded that Skelton Group rocks underwent a counterclockwise P-T path with near-isobaric heating at low pressure followed by isobaric cooling (Fig. 1.13a). This interpretation was based on studies by Allibone (1992) and Cox (1992), who identified sillimanite + cordierite bearing assemblages with relict andalusite, requiring that the rocks were heated to sillimanite-grade conditions at pressures below the Al_2SiO_5 triple point. Time constraints on the peak conditions of this P-T path are provided by ca. 505–480 Ma zircon overgrowths formed during anatexis of Skelton Group rocks near the Taylor Valley (Fig. 1.2; Wysoczanski & Allibone, 2004). The interpretation of a low-pressure counterclockwise P-T path is based primarily on studies of Skelton Group rocks in the Dry Valleys area, ~50 km north of the Walcott Glacier area. Here, voluminous magmatism may have resulted in a "contact metamorphism" thermal overprint at relatively low pressures.

Samples from this study and from Talarico et al. (2005) record an earlier metamorphic history not preserved north of the Ferrar Glacier in the Dry Valleys area. Most of these samples record peak P-T conditions in the sillimanite stability field at moderate temperatures of ~600–700° C and pressures of ~4.5–6 kbar (Fig. 1.13). The kyanite + staurolite bearing assemblage of OU82864 apparently records a higher-pressure lower-temperature event followed by a moderate- to high-temperature event at lower pressure in the stability fields of sillimanite and cordierite. The absence of muscovite, leucocratic segregations of quartz, plagioclase, and cordierite, and leucocratic embayments in garnet, suggest that the low-pressure event was accompanied by incipient partial melting in this

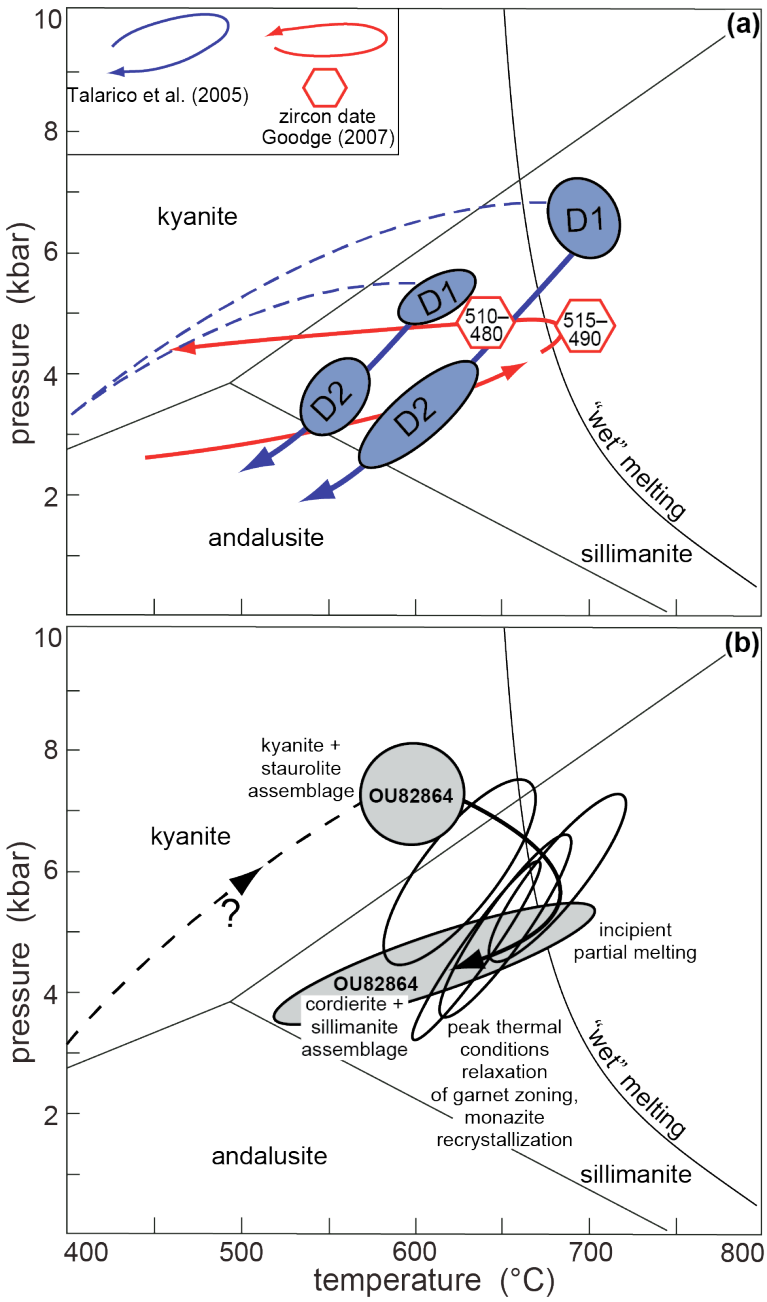

Figure 1.13 (a) Diagram of previously proposed P-T paths for Skelton Group rocks (petrogenetic grid modified from Goodge et al., 2007). The two different paths proposed by Talarico et al. (2005; ellipses and solid blue lines) correspond to samples that achieved different peak metamorphic conditions. The blue ellipses labeled "D1" and "D2" correspond to two different phases of deformation recognized by Talarico et al. (2005). The dashed blue lines are inferred prograde paths added to the paths from Talarico et al. (2005). (b) Inferred P-T evolution of the samples from this study. Black ellipses show the "average P-T" results from THERMOCALC, interpreted as peak or near-peak conditions. All of the average P-T results fall in the sillimanite stability field, but sample OU82864 contains remnants an earlier paragenesis including kyanite and staurolite.

sample. Mineral compositions were apparently reset under the low-pressure conditions, evidenced by the overlap of the calculated "average P-T", Ti-in-biotite apparent temperature, and Ca-in-garnet isopleths in cordierite- and sillimanite-bearing fields on the pseudosection in Figure 1.8. It is difficult ascertain nature of the prograde path for the other samples, but pressures of ~4.5–6 kbar require burial to depths of ~15–20 km. Based on the early kyanite + staurolite assemblage of OU82864, and the pressures recorded by the other samples, our preferred interpretation is that the samples underwent a clockwise P-T with burial to ≥20 km depth accompanied by heating. The peak temperatures achieved may have been related to a thermal pulse during arc magmatism, but low-pressure contact metamorphism does not characterize the entire metamorphic history of the Skelton Group in the Walcott Glacier area.

Age interpretation

Garnet Lu-Hf geochronology

Grains from several samples show prominent smooth or abrupt concentric zoning in Mn, Mg, Fe, and Ca, whereas those from other samples are unzoned in Mn, Mg, and Fe and zoned in Ca. Whereas zoning is in places evident in X-ray element maps, the quantitative major element compositional profiles reveal only minor variations across the grains (maximum range of 3 mole %), with the most significant variations within ~50 μm of the grain boundaries (Fig. 1.6). Several interpretations potentially explain the lack of significant major element zoning in these garnet grains: 1) Growth zoning was not established due to open-system chemical buffering (e.g., influx of a fluid; Caddick et al., 2010); 2) Divalent cation diffusion within the grains outpaced porphyroblast growth; 3) Zoning developed but was relaxed through grain-scale re-equilibration. Thermal relaxation of the growth zoning

(interpretations 2 and 3), as opposed to chemical buffering (interpretation 1), is supported by the observation that several of the garnets are essentially unzoned in Mn, Mg, and Fe but retain zoning in Ca (e.g., RG11-30 in Fig. 1.6), the slowest-diffusing major divalent cation in garnet (Carlson, 2006; Ague & Carlson, 2013). The retention of strong REE zoning in all of the grains (Fig. 1.6) further supports the interpretation that the garnets were diffusively reset during or after growth. Diffusive re-equilibration indicates protracted residence at high temperature, either as a result of slow heating or cooling, long-lived residence at peak temperature, or both. This being the case, the susceptibility of the Lu-Hf chronometer to diffusive re-equilibration must be considered.

Scherer et al. (2000) determined that the effective closure temperature of the Lu-Hf system in garnet is greater than or equal to that of the Sm-Nd system. Smit et al. (2013) empirically constrained the effective closure temperature of the Lu-Hf system for a range of garnet grain sizes and cooling rates. They demonstrated that even grains smaller than ~ 1 mm in diameter preserved the timing of prograde garnet growth and were not completely reset at peak temperatures of ~ 760°C or subsequent cooling at a very slow rate (< 2° C/Myr). Our data corroborate the implied robustness of the Lu-Hf system in recording information about the prograde history of metamorphic rocks that have experienced subsequent thermal perturbation. Although thermal relaxation of the divalent cation zoning is evident, strong REE zoning is preserved in the Skelton Group garnet. This is most likely due to the comparatively slow diffusion rates of the trivalent REE relative to divalent cations in garnet (Carlson, 2012). Lutetium is significantly more mobile than Hf in garnet (Bloch et al., 2015), and therefore preservation of Lu zoning implies strong retention of Hf, which controls the robustness of the Lu-Hf chronometer (Scherer et al., 2000).

Several studies have extracted geochronologic records of individual garnet growth domains through microsampling techniques (e.g., Ducea et al., 2003; Pollington & Baxter, 2010; Pollington & Baxter, 2011). More commonly, isochron dates represent one or several bulk grains, providing a mixture of all domains within the grains weighted by their Lu/Hf (Lapen et al., 2003; Smit et al., 2010; Baxter & Scherer, 2013). Strong partitioning of Lu in cores relative to rims of grains as a result of Rayleigh fractionation often leads to these ages being biased toward early garnet growth (Lapen et al., 2003; Kellett et al., 2014). The cumulative Lu distribution models in Figure 1.10 are used to assess this effect. Garnet grains from RG11-13, RG11-72, and RG11-253 show strong enrichment of Lu in the cores relative to the rims (Fig. 1.6; inset in Fig. 1.10). This is especially pronounced in RG11-72, with a core/rim Lu concentration ratio of ~20 in the modeled grain. Despite core partitioning revealed by the 1-D profiles, most of the Lu— and thus *in situ* radiogenic ^{176}Hf— resides in the outer 50% of the total radius in each of the modeled grains. This means that the Lu-Hf ages are unbiased or biased toward the younger garnet growth for constant radial growth rate. Bias toward younger growth domains is greatest in sample RG11-30, with over 80% of the cumulative Lu (and therefore radiogenic ^{176}Hf) in the outer 20% radial increment. In contrast, when cumulative Lu is plotted versus core-to-rim volume %, it is evident that a majority of Lu resides within the inner 50 % of the total volume of the grains modeled for samples RG11-13, -72, and -253. This indicates that these ages are unbiased or biased toward the earlier garnet growth for a constant volumetric growth rate. However, RG11-30 is still biased toward the younger garnet domains, with ~80% of Lu residing in the outer 40 % of the volume of the modeled grain.

The samples with the strongest partitioning of Lu into the core (RG11-72) and the rim

(RG11-30) have indistinguishable ages. However, the isochron age for RG11-72 has a large uncertainty due to the very low spread in $^{176}Lu/^{177}Hf$. The isochron ages for RG11-13 and RG11-30 are well outside uncertainty. This could potentially reflect protracted garnet growth over a period of >10 million years, with the RG11-13 bulk age biased toward the older garnet interiors and the RG11-30 bulk age biased toward the younger rims as expected on the basis of Lu zoning. Alternatively, garnet growth could have occurred in short spurts (e.g., Ague & Baxter, 2007), and the range in isochron dates record variability in the timing of garnet-grade metamorphism across the study area. The coincident results for RG11-72 and -30— with the strongest core- and rim- Lu partitioning, respectively— lead us to favor the latter explanation.

Sample RG11-253 yielded a five-point garnet-only isochron age of 616 ± 7 Ma, significantly older than the other samples from this study (Fig. 1.9). It is possible that this rock underwent garnet-grade metamorphism prior to the other samples, though this is difficult to reconcile given the consistency of the isochron ages of all the other samples and the absence of an older monazite population in this sample (Fig. 1.11). Kohn (2009) showed that regressions through garnet points only could result in erroneously steep (old) "isochrons" in the case of strong Lu/Hf fractionation during protracted grain growth. As predicted in this model, the whole-rock analysis does not form an isochron together with the garnet analyses. Two-point whole-rock-garnet "isochrons" for this sample span from ca. 563–404 Ma. The oldest of these is consistent with the ages of the other samples, whereas most are considered to be erroneously young in the context of the established chronology of the Ross orogeny. In addition, if the slope of the garnet-only isochron were severely steepened due to the effect of protracted garnet nucleation, the lower intercept would be at extremely low $^{176}Hf/^{177}Hf$ (e.g.,

εHf ≈ –300 in Fig. 1.10d of Kohn, 2009). The lower intercept of the garnet-only isochron for RG11-253 is $^{176}Hf/^{177}Hf = 0.28212 \pm 2$, corresponding to an $\varepsilon Hf_{(i)} \approx -10$ at 616 Ma and a depleted-mantle model age of 1.6 Ga (single-stage) or 2.1 Ga (two-stage), reasonable for the Skelton Group protolith sediments which contain significant Archean and Proterozoic peaks in detrital zircon age spectra (Wysoczanski & Allibone, 2004; Stump et al., 2007; Cooper et al., 2011). The whole-rock points for this sample are therefore interpreted to record isotopic re-equilibration of the rock matrix outside of its garnet reservoir, and the garnet-only isochron of 616 ± 7 Ma is therefore taken as our best estimate for the initiation of garnet-grade metamorphism in RG11-253.

Monazite U-Pb geochronology

The monazite U-Pb data record more-complicated age spectra than the garnet Lu-Hf isochrons, with concordant ages that span ca. 610–500 Ma (Fig. 1.11). The ca. 110 million-year dispersion along concordia does not necessarily indicate that crystallization and recrystallization processes were continuous over this period; it is possible that the continuous age spectrum in Figure 1.11 reflects mixing of distinct age domains during laser ablation, either as a result of spot overlap or progressive sample excavation. Indeed, at least three domains with discrete Y concentrations are apparent in several of the monazite grains shown in Figure 1.7, and the extent of these domains with depth in the grains cannot be assessed. Whether the age dispersion represents continuous or punctuated recrystallization, the monazite age data record either a protracted or polyphase metamorphic history of the Skelton Group.

Several prominent observations arise from the monazite LASS data shown in Figures

1.11 and 1.12: 1) There is a general correlation between age and Y concentration, with older monazite domains typically depleted in Y relative to younger domains. 2) The normalized Gd/Yb ratios, representing the magnitude of the slope of the HREE on chondrite-normalized diagrams, generally decrease over time. 3) There is a wide range in Eu anomalies over time, but large negative Eu anomalies are more common in younger monazite domains (< 550 Ma). Depletions in Y and the HREE in monazite have been correlated with synchronous garnet growth (e.g., Rubatto et al., 2006; Kylander-Clark et al., 2013), as garnet strongly partitions these elements and depletes the surrounding rock matrix. Many of the low-Y and high-Gd/Yb monazite domains span the range of the garnet Lu-Hf ages, consistent with competition for Y and the heavy REE between these phases during synchronous growth. The trace-element composition of these old monazite grains thus supports the notion that they crystallized in the presence of growing garnet, and the age records from both minerals are mutually consistent.

The monazite show textural evidence for resorption, with small rounded or cuspate low-Y cores surrounded by high-Y mantles and rims (Fig. 1.7, Appendix Fig. 2). Kelsey et al. (2008) and Yakymchuk and Brown (2014) modeled monazite dissolution and growth at suprasolidus conditions and showed that monazite (and zircon) in metapelites should progressively dissolve during continued heating above the solidus and re-precipitate upon cooling. However, most of our samples do not show evidence of partial melting (e.g., they lack K-feldspar). In fact, the one sample that shows evidence for partial melting (OU82864) contains the most abundant record of old low-Y monazite. These observations lead us to conclude that pre-existing low-Y monazite was partially dissolved and grew high-Y mantles and rims during progressive subsolidus reactions.

Higher Y and lower Gd/Yb in younger monazites could be due to the breakdown of garnet or another HREE-bearing phase, or to open-system behavior with an influx of HREE. The major element transects across the garnets show slight upturns in Mn and Fe near the edges of grains, consistent with minor resorption. Sample OU82864, which exhibits leucocratic segregations and pervasive embayment of garnet (Fig. 1.5), shows the most pronounced shifts toward higher Y, lower Gd/Yb, and lower Eu/Eu* in younger monazite (Fig. 1.11; 1.12). This indicates that garnet breakdown during partial melting could have caused increased Y and HREE in monazite, and that crystallization of plagioclase from the melt phase may have caused the pronounced Eu anomalies. The monazite in this sample therefore most likely record garnet-stable growth along the prograde path *and* melt crystallization and minor garnet resorption near peak conditions or during decompression.

To investigate the partitioning of HREE among garnet and monazite, we calculated ratios of REE in monazite and garnet (here referred to as $D_{mnz/grt}$; Fig. 1.14). To account for REE zoning in the garnet, these ratios were calculated for each monazite analysis separately relative to the core and rim composition of representative garnet from the same sample. The garnet "core" and "rim" compositions are averages of 3−4 analyses from each domain to avoid selecting an outlier analysis as a representative composition. In samples RG-13 and RG30, none of the monazite age domains correspond to the $D_{mnz/grt}$ determined by Hermann and Rubatto (2003; $D_{mnz/grt,HR}$), with discrepancies up to an order of magnitude. In RG11-13, apparent $D_{mnz/grt}^{LREE}$ using garnet cores are higher than $D_{mnz/grt,HR}^{LREE}$, whereas $D_{mnz/grt}^{HREE}$ are broadly similar to $D_{mnz/grt,HR}^{HREE}$. The $D_{mnz/grt}^{LREE}$ using garnet rims are lower than $D_{mnz/grt,HR}^{LREE}$, whereas $D_{mnz/grt,HR}^{HREE}$ are apparently too high. The one monazite analysis from this sample which overlaps with the Lu-Hf age is more depleted in the HREE, but still

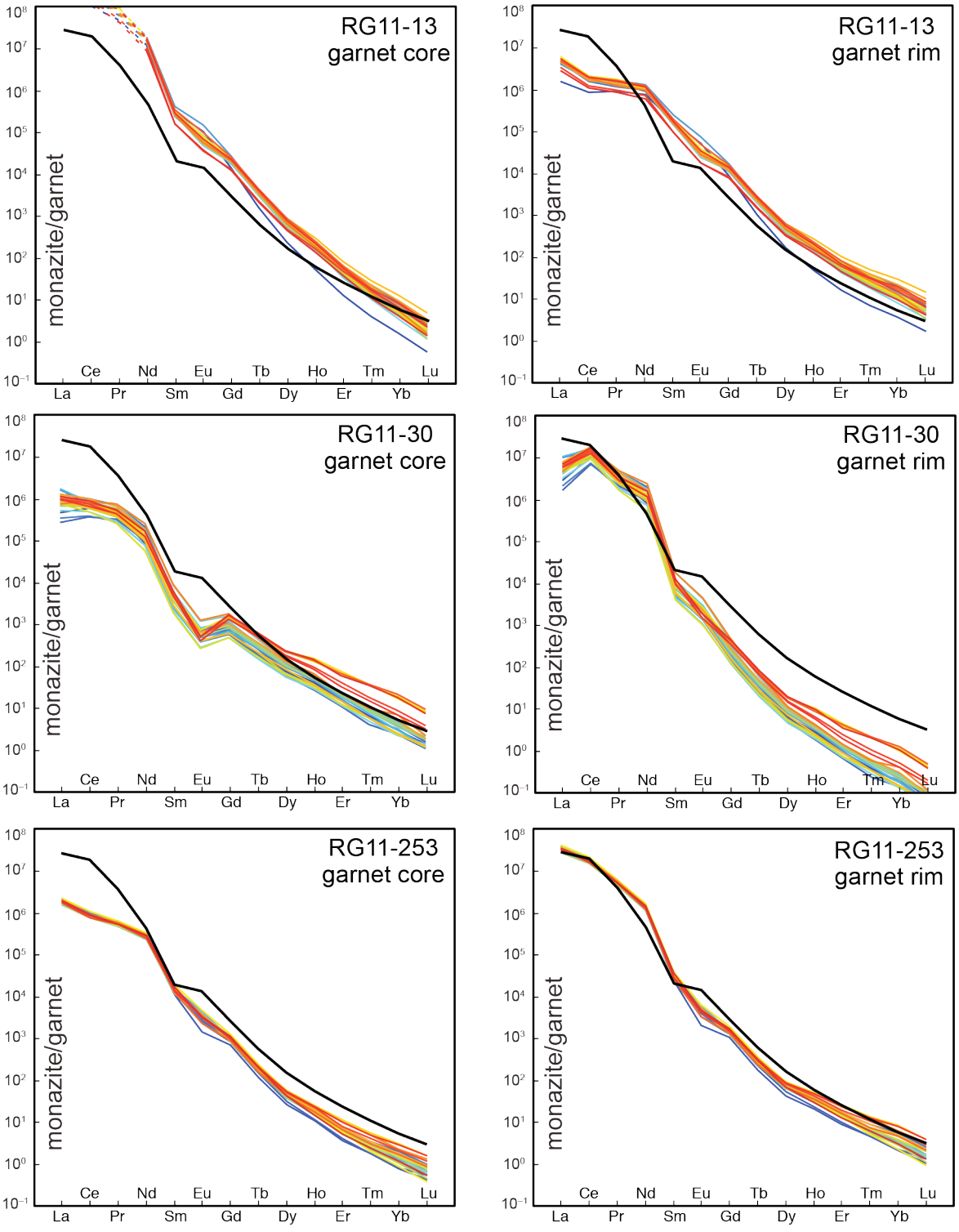
RG11-13
garnet core
RG11-13
garnet rim
RG11-30
garnet core
RG11-30
garnet rim
RG11-253
garnet core
RG11-253
garnet rim
monazite/garnet
La Ce Pr Nd Sm Eu Gd Tb Dy Ho Er Tm Yb Lu

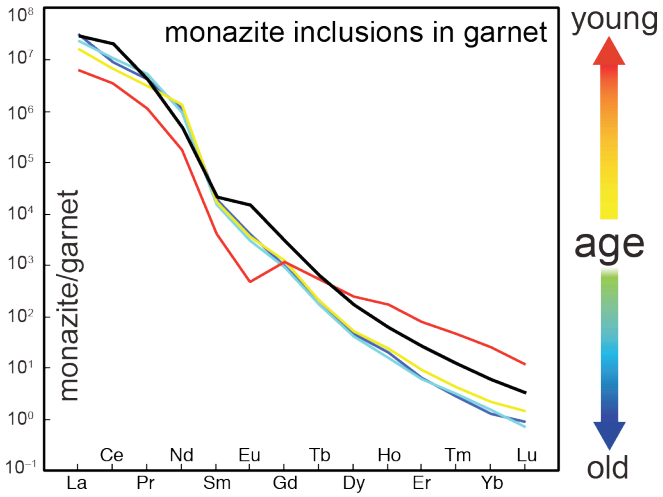

Figure 1.14 Monazite/garnet REE distributions calculated for each sample with both monazite and garnet REE data. Because the garnet are zoned in REE, average concentrations of REE in different domains of representative garnets were used in separate calculations. The garnet "core" and "rim" concentrations were taken as the average of 3–4 analyses (to avoid using an outlier) in the center and ends, respectively, of a symmetric zoning profile (the same profiles shown in Figure 6). The partition coefficients were calculated between a particular garnet domain and each monazite analyzed in the sample, and the patterns are color coded by the relative age (old to young) of the monazite analysis. The thick black line on each diagram represents the monazite/garnet partition coefficients reported by Hermann and Rubatto. Dashed lines are used where the garnet REE measurements are questionable due to low REE concentrations.

does not correspond to $D_{mnz/grt,HR}^{HREE}$. Likewise, monazite analyses from RG11-30 which overlap the Lu-Hf age for that sample do not correspond to $D_{mnz/grt,HR}$ for all of the REE. In RG11-253, the $D_{mnz/grt}$ using garnet rims are broadly similar to $D_{mnz/grt,HR}$. The discrepancies between apparent and experimentally constrained $D_{mnz/grt}$ for monazite domains consistent with the garnet Lu-Hf ages, suggests that the $D_{mnz/grt,HR}$ reported by Hermann and Rubatto (2003) may not be universally applicable in metapelites. Our garnet and monazite ages support the notion that Y+REE compositions of monazite can be used circumstantially to trace garnet stability, but additionally show that garnet geochronology is required to reliably date garnet growth.

Monazite inclusions in garnet

The first-order interpretation that mineral inclusions are younger than their host is called into question by comparing the ages of monazite inclusions in garnet to the Lu-Hf garnet ages for the same samples. Monazite inclusions in garnet are few in our samples, yet in two different samples (RG11-13 and RG11-253), monazite inclusions in garnets are significantly younger than the Lu-Hf ages for the same rocks (Fig. 1.15). There are no Lu-Hf data for sample OU82864, but the rim of a garnet porphyroblast in this rock contains a ca. 518 Ma monazite inclusion—one of the youngest monazite analyses from this sample (Figs. 1.10; 1.11). Our observations resemble those made by Yakymchuk et al. (2014), who identified monazite inclusions that were younger than the Lu-Hf ages of their host garnets, always associated with fractures that may have connected to the edge of the garnet. They attributed the young ages of the inclusions to monazite growth during suprasolidus breakdown of garnet coupled with a light REE source from pre-existing monazite or an influx through fracture networks.

In our samples, however, many of the monazite inclusions are within apparently pristine garnet, not obviously connected to any fractures (Fig. 1.15), nor annealed fractures, which might be visible in the X-ray maps (Fig. 1.6, Appendix Fig. 1).

Several interpretations potentially explain the presence of monazite inclusions that are younger than the Lu-Hf ages of their host: 1) The monazite inclusions grew within their host garnets through reactions involving the garnet and some light REE source (e.g., apatite); 2) The monazite inclusions were recrystallized or diffusionally reset, whereas the Lu-Hf system in garnet was not. Several monazite grains formed on the fringes of what appears to be an apatite inclusion within a garnet in Figure 1.15b, consistent with interpretation 1. However, this relationship between apatite and monazite was not seen in any of the other inclusions. It is unlikely that the monazite inclusions have completely replaced apatite grains, as the concentration of the light REE in metamorphic apatite (500–2500 ppm; Kohn & Malloy, 2004, and references therein) is far too low to account for the concentration of light REE in monazite (~50 wt. %; Kohn & Malloy, 2004). Also, unaltered apatite inclusions close to monazites are present within other garnet grains (e.g., Fig. 1.15d). We thus prefer interpretation 2—that monazite inclusions were recrystallized or isotopically reset within the host garnets. Isotopic resetting can be excluded on the basis of diffusive systematics of Pb in monazite. Cherniak et al. (2004) demonstrated that Pb diffusivity in monazite is relatively slow, with 10 μm-size monazite effectively closed to Pb diffusion at temperatures below 900°C for a cooling rate of 10 °C/Myr Although the inferred metamorphic history of the Skelton Group rocks does include a prolonged thermal event following prograde garnet growth, the temperatures and durations of peak conditions and cooling, were not such that significant diffusive Pb loss can be expected. Monazite grains from multiple samples show

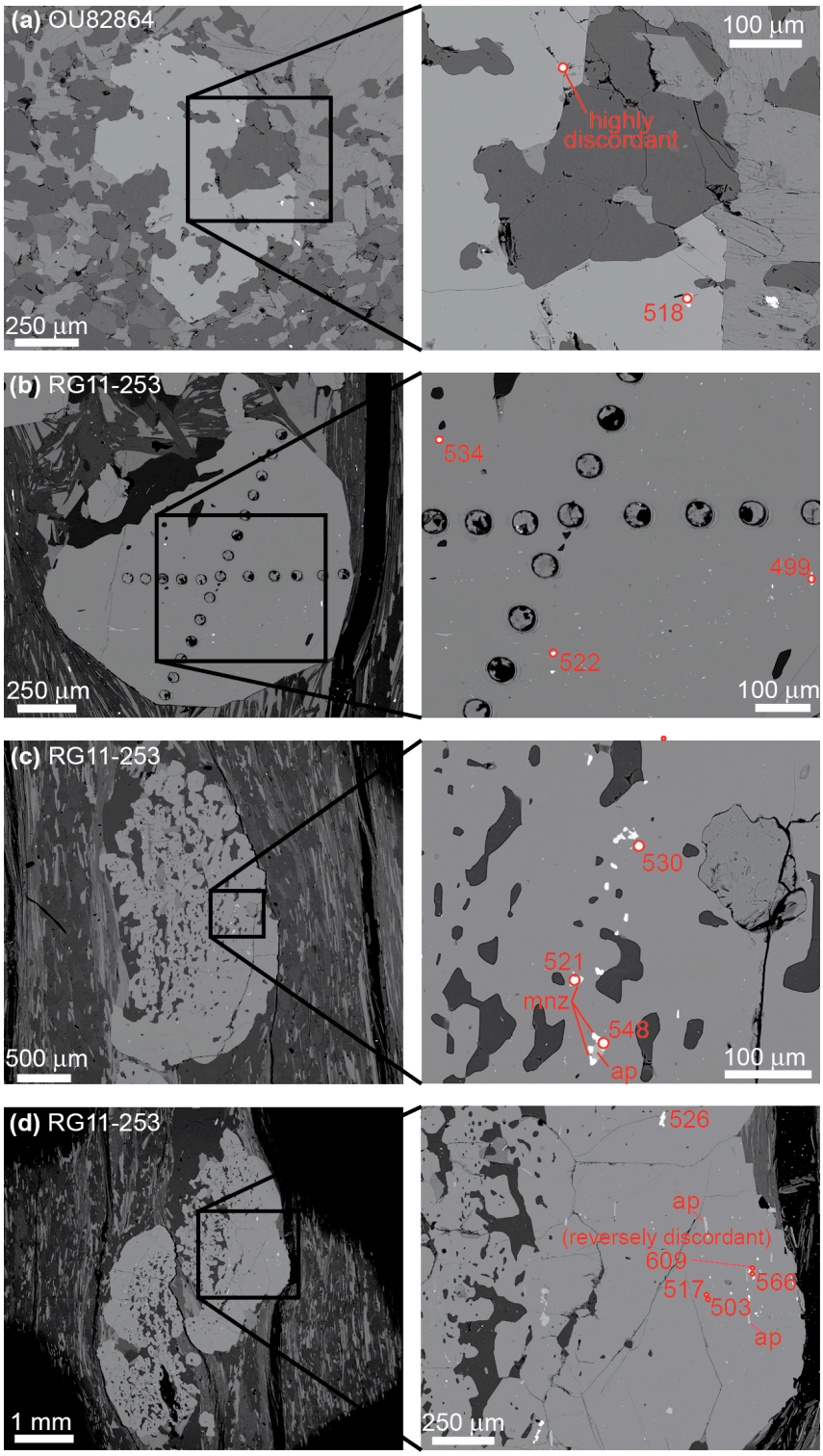

Figure 1.15 Backscatter electron images (BSE) of garnet porphyroblasts containing monazite inclusions. The inclusions (bright in BSE) are commonly found within pristine, crack-free garnet and are typically small (< 20 µm). The grains in images c and d also contain inclusions of apatite (ap). The dark shadows at the edges of image d are from an aperture in the column of the SEM.

textural evidence for resorption or recrystallization of early monazite, with irregular rounded or cuspate low-Y cores surrounded by relatively wide domains of different composition (Fig. 1.7, Appendix Fig. 2). This process may have affected primary monazite inclusions within garnet and reset the U-Pb system. Likewise, strain could have facilitated or promoted inclusion modification. Many of the young monazite inclusions in RG11-253 are within garnet porphyroblasts that show evidence of strain. For example, the garnet in Figure 1.15c (the same shown in Figs. 1.5f and 1.6) is fragmented and disaggregated parallel to the foliation in the rock, with biotite, muscovite, and quartz between the fragments. Read (2010) reported ages of 515 ± 4 Ma and 511 ± 3 Ma for undeformed granitoids in the Walcott Glacier area, placing a younger age bracket on regional deformation at ca. 515 Ma. Ductile deformation in the Dry Valleys area, immediately north of the Walcott Glacier area, had also ended by 500 Ma, with subsequent intrusions interpreted as "post-tectonic" (summarized in Allibone & Wysoczanski, 2002). Tectonic strain may therefore not account for concordant ca. 500 Ma ages from monazite inclusions in garnet, but provides a viable mechanism to explain inclusion modification before 515-510 Ma. Our data demonstrate the possible complexity of interpreting inclusion records in polyphase metamorphosed and deformed rocks, and underscore the efficacy of combining U-Pb analysis of accessory minerals with garnet geochronology in such cases.

Tectonic synthesis

Figure 1.16 shows a timeline summarizing the existing geochronology on magmatism and metamorphism associated with the Ross orogeny. Published U-Pb ages for igneous rocks in southern Victoria Land span ca. 550−485 Ma (summarized in Hagen-Peter et al., 2015).

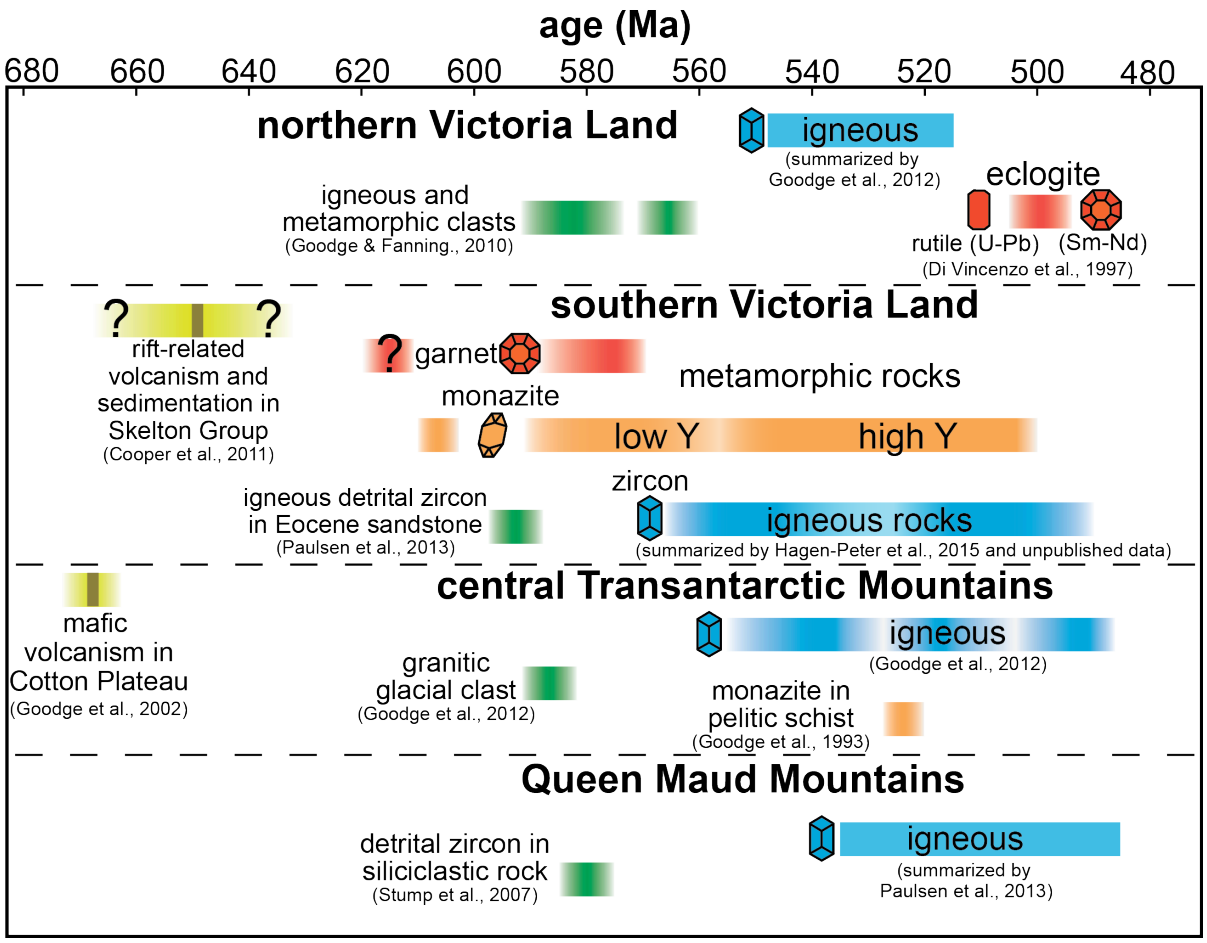

Figure 1.16 Timeline summarizing existing geochronology on metamorphic and igneous rocks spanning over 1500 km along the Ross orogen. Detrital zircons and trachytic volcanic clasts constrain a maximum age of ca. 650 Ma for sections of the Skelton Group metasedimentary sequence (Cooper et al., 2011). Skelton Group rocks underwent garnet-grade metamorphism and early, low-Y monazite growth prior to magmatism in sVL, also prior to most magmatism along the entire orogen. Only one age from an igneous rock (a ca. 590 Ma granitic glacial clast; Goodge et al., 2012) in the central Transantarctic Mountains predates the garnet-grade metamorphism in sVL. Monazite growth/recrystallization in Skelton Group rocks occurred over nearly the entire timespan of magmatism in sVL, and may have been due to relatively low P/T contact metamorphism that developed the sillimanite ± cordierite assemblages.

Read (2010) reported an age of 557 ± 5 Ma for an alkaline gabbroic pluton in the Walcott Glacier area, and unpublished zircon U-Pb data (Hagen-Peter, unpublished data) confirm that magmatism commenced by 565 ± 7 Ma in this area. The character of igneous activity in the Walcott Glacier area was distinct from that of the rest of the Ross orogen, with relatively small-volume alkaline magmatism of the Koettlitz Glacier Alkaline Suite (KGAS) interpreted to represent "anorogenic"-type magmatism in an extensional jog within the Ross orogen (Cooper et al., 1997; Read et al., 2002; Cottle & Cooper, 2006b). Magmatism to the north and south of the KGAS is characterized by large calc-alkaline intrusions, including the ~1000 km^2 Bonney Pluton in the Dry Valleys area (Fig. 1.2).

Magmatism in northern Victoria Land (nVL) spanned ca. 545–495 Ma (summarized in Hagen-Peter et al., 2015). Eclogite facies metamorphism occurred in this region at ca. 500 Ma, related to the collision of the Bowers Terrane with the Antarctic margin (Ricci et al., 1996; Di Vincenzo et al., 1997; Palmeri et al., 2003). In the central Transantarctic Mountains (cTAM), in-place granitoid intrusions span ca. 545–485 Ma (Goodge et al., 2002). Magmatism in the Queen Maude Mountains spanned ca. 535–485 (summarized in Paulsen et al., 2013). The oldest record of Ross magmatism comes from a glacially transported granitic clast from the cTAM with a ca. 590 Ma zircon population (Goodge et al., 2012). Other potential records of early Ross magmatism include a 581 Ma detrital zircon age peak in a siliciclastic rock from the Queen Maud Mountains (Stump et al., 2007), a 587 Ma detrital zircon age peak in southern Victoria Land (Cooper et al. 2011), and a 595 Ma detrital zircon age peak from a sandstone glacial erratic from southern Victoria Land (Paulsen et al., 2011). Goodge and Fanning (2010) analyzed glaciogenic clasts from dredges off the Wilkes Land coast, including an igneous clast with a ca. 584 Ma zircon population and metamorphic clasts

with ca. 583 and 568 Ma zircons. According to their tectonic reconstruction, these rocks may have formed in a zone of collision between southern Australia and Antarctica, perpendicular to the Ross orogen (Fig. 16 in Goodge & Fanning, 2010). These data are shown on Figure 1.16 but should perhaps be considered separately, as they likely represent suturing of Australia and Antarctica in the Neoproterozoic, as opposed to the long-lived convergence between paleo-Pacific lithosphere and the East Antarctic Craton during the Ross orogeny. The new Lu-Hf and U-Pb data represent the oldest definitive record of orogenesis in southern Victoria Land, and provide a new reference frame for the 595 Ma detrital zircon age peak observed from a glacial erratic (Paulsen et al., 2011). The garnet + whole-rock Lu-Hf ages of RG11-30 and -72 are within uncertainty of the timing of the earliest definitive magmatism in this area (565 ± 7 Ma; Hagen-Peter, unpublished data). The Lu-Hf ages of RG11-13 and -253 and monazite U-Pb ages from multiple samples predate any in-place igneous rocks in this area. The ages are also older than any in-place igneous rocks dated along the entire orogen (Fig. 1.16). If the garnet-only Lu-Hf age (616 ± 6 Ma; RG11-253) and the oldest concordant monazite date (611 ± 9 Ma; RG11-30) are considered, these ages are older than any other record of orogenesis along the entire arc, including detrital zircons and glacial clasts (Fig. 1.16).

To explain these observations, we developed a generalized tectonic model (Fig. 1.17). Stage 1 of the model (ca. 675 Ma) involves rifting of the East Antarctic Craton from a conjugate continental block and the beginning of deposition of the Skelton Group protolith sediments. This would provide a context for the 650-Ma rift-related volcanic clasts in a Skelton Group metaconglomerate (Cooper et al., 2011) and detrital zircon age peaks at 673 Ma and 665 Ma (Cooper et al., 2011) and 650 Ma (Stump et al., 2007) in Skelton Group

rocks. In Stage 2, the edge of the East Antarctic Craton evolved into a passive margin, with the deposition of the lower-energy facies protoliths to the marbles and pelitic schists of the Skelton Group. The age brackets on this stage are poorly defined, with an upper limit constrained by the 650 Ma rifting and a lower limit *tentatively* constrained at ca. 615–610 Ma— the garnet-only Lu-Hf and oldest monazite dates. A more definitive lower bracket is ca. 590 Ma, with the oldest garnet + whole-rock Lu-Hf age, numerous monazite ages, and detrital zircon age peaks summarized above. Stage 3 involved shortening across the margin and burial of Skelton Group sediments to garnet-grade conditions. This stage of Barrovian-style metamorphism is recorded in the prograde growth of garnet, the crystallization of low-Y monazite, the development of early fabrics retained in rotated garnet porphyroblasts (e.g., Fig. 1.5c), and the relatively high-pressure low-temperature kyanite + staurolite assemblage of OU82864. The paucity of an igneous record at this time (ca. 590–570 Ma) suggests that this stage of metamorphism represents pre-magmatic shortening and thickening, at least in the immediate Walcott Glacier area. Our data and model corroborate the model Goodge (1997) with pre-magmatic basin inversion and shortening, which explains contractional deformation accommodated by sediments in cTAM at ca. 600–550 Ma, prior to pluton emplacement. Stage 4 (ca. 565–500 Ma) involved steady-state subduction and magmatism. The alkaline magmatism in the Walcott Glacier area may have been due to local lithospheric thinning in an extensional jog (Cooper et al., 1997; Read et al., 2002; Cottle & Cooper, 2006b). Lithospheric thinning and high-temperature alkaline magmatism in the Walcott Glacier area likely caused the late-stage thermal metamorphism that affected the Skelton Group. This process resulted in relaxation of major element zoning in garnet porphyroblasts, protracted recrystallization of high-Y monazite, and growth of the sillimanite ± cordierite

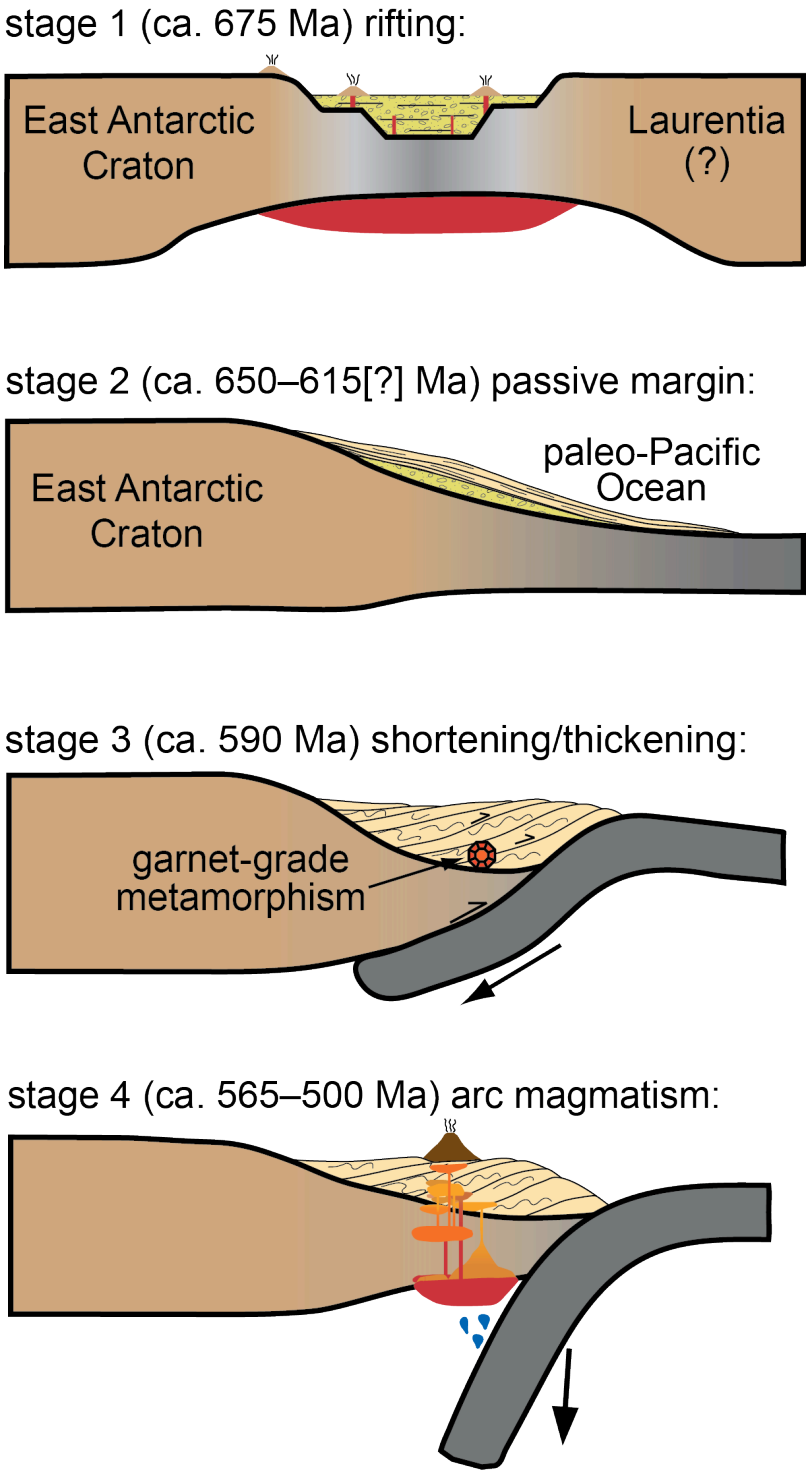

Figure 1.17 A Simplified tectonic model (not-to-scale) for the evolution of the Ross orogen that explains the observation from this study. The different stages of the model are explained in the text.

assemblages that typify the Skelton Group in this area. Late high-T overprinting is also recorded by extensive migmatization of the Skelton Group in the Dry Valleys area at ca. 500 Ma (Allibone, 1992; Allibone & Norris, 1992; Cox, 1992; Wysoczanski & Allibone, 2004).

Various studies have linked the initiation of the Ross orogeny to global-scale plate reorganization associated with the assembly of Gondwana (e.g., Goodge, 1997; Foden et al., 2006; Paulsen et al., 2007). Final closure of ocean basins (perhaps the Mozambique Ocean) and the collisional Pan-African orogenies may have caused convergence to transfer to the eastern margin of Gondwana, initiating subduction along the extensive Terra-Australis orogen (Cawood, 2005; Cawood & Buchan, 2007). Relating our geochronology data from the Ross orogen to Pan-African orogenesis and the assembly of Gondwana is beyond the scope of this study. However, the new evidence for shortening across the margin of East Gondwana (the Ross orogen) at ca. 590 Ma, and perhaps as early as 615–610 Ma, provides valuable new information for the development of more comprehensive models of Gondwana assembly and the initiation of convergence along the Terra-Australis orogen.

CONCLUSIONS

Garnet and monazite record a protracted metamorphic history of the Skelton Group, spanning ca. 100 million years. As such, our data provide the oldest in-place record of the Ross orogeny. They reveal pre-magmatic shortening in the southern Victoria Land region, which may have occurred in response to the assembly of Gondwana through the Pan-African orogenies. The garnet Lu-Hf geochronometer robustly retained the timing of prograde garnet growth despite subsequent high-T metamorphism and modification of major element zoning

in garnet. The monazite age and trace element data record garnet-stable prograde growth as well as high-T metamorphism associated with alkaline magmatism in the area. The garnet Lu-Hf ages are consistent with the oldest monazite U-Pb ages, which correspond to monazite domains that are depleted in Y and heavy REE, consistent with contemporaneous garnet growth. Younger monazite domains are enriched in Y and heavy REE, even in samples that contain idioblastic non-resorbed garnets, requiring an influx of REE or a change in the REE partitioning between monazite and other minerals in the rocks. Monazite/garnet REE ratios do not closely match previously reported partition coefficients for these minerals, even for monazites that are the same age as the garnets and for monazite inclusions and surrounding garnets. As such, our data show the potential, as well as shortcomings, of using REE systematics to obtain meaningful information on phase relations and the age of garnet growth. In several samples, monazite inclusions in garnet yield concordant U-Pb dates significantly younger than the garnet Lu-Hf ages for the same rocks. These monazites were apparently recrystallized within their host garnet, calling into question assumptions about the "shielding" of accessory mineral inclusions from resetting and interpreting ages of rock-forming minerals based on accessory mineral inclusions.

ACKNOWLEDGMENTS

Funding for this work was provided by National Science Foundation grant ANT-1043152 to J.M. Cottle and Deutsche Forschungsgemeinschaft grant SM 308/1 to M.A. Smit. We thank the University of Otago Geology Department Rock Catalogue for providing one of the samples, collected during field work supported by Antarctica New Zealand. We thank Jade Star Lackey at Pomona College for providing XRF analyses.

II. Mixing between enriched lithospheric mantle and crustal components in a short-lived subduction-related magma system, Dry Valleys area, Antarctica: Insights from U-Pb geochronology, Hf isotopes, and whole-rock geochemistry

INTRODUCTION

Subduction zones control the generation and recycling of much of Earth's crust. Petrogenetic and geochronologic studies of magmatism at convergent margins play an important role in understanding the rates and relative importance of such processes. The structure of active continental arcs can be studied using geophysical techniques, and igneous processes through volcanism, but information about the dynamics of magmatic processes at deeper crustal levels is largely absent. It is also impossible to study the entire sequence of magmatism, from initiation to termination, in active systems. Extensively exposed mid-crustal igneous rocks in the Dry Valleys area of southern Victoria Land, Antarctica yield insights into the timing, duration, and source of an exhumed subduction-related magmatic system.

The Ross orogen in the Transantarctic Mountains forms the boundary between the Proterozoic and Archean East Antarctic Craton and the amalgamated terranes of West Antarctica (Fig. 2.1; Dalziel & Elliot, 1982; Borg & DePaolo, 1991; Goodge et al., 1993b; Stump, 1995). A geochemically diverse suite of igneous rocks in the southern Victoria Land segment of the orogen records a history of magmatism that resulted from westward subduction of paleo-Pacific oceanic lithosphere beneath the East Gondwanan margin during the Neoproterozoic–Ordovician (Borg et al., 1987; Borg & DePaolo, 1991; Dalziel, 1992; Smillie, 1992; Allibone et al., 1993a,b; Stump, 1995; Encarnación & Grunow, 1996 Cox et al., 2000; Stump et al., 2006). Large volumes of plutonic rocks are especially well exposed in

the Dry Valleys area of southern Victoria Land, which is the largest ice-free area on the continent.

Magmatism in the Dry Valleys is thought to have spanned ca. 45 Myr, from 530 to 485 Ma (summarized in Allibone & Wysoczanski, 2002), but with few broad geochronology studies, ages for plutons are currently limited and thus our understanding of the timing and duration of magmatism in the Dry Valleys remains incomplete. Here we present zircon uranium-lead ages, hafnium isotope compositions and model ages, and whole-rock major- and trace-element geochemistry for 31 samples spanning 150 km along- and 50 km across-strike of the Ross orogen (Fig. 2.1), including the ~1000 km^2 Bonney Pluton. Specifically, we aim to place further constraints on the timing and duration of magmatism as well as potential magma source(s) and their evolution through time. Our new data indicate that most of this batholith-scale intrusive system was constructed in only ca. 23 million years from 515–492 Ma. An enriched sub-continental lithospheric mantle (SCLM) may have been the primary source of the mafic intrusions, but recycling of Proterozoic continental crust played a significant role in the evolution of the larger granitic plutons.

GEOLOGIC BACKGROUND

The Ross orogen is a continental arc that is thought to have been constructed on the attenuated margin of the Archean and Proterozoic East Antarctic Craton (Grindley & McDougall, 1969; Borg et al., 1990; Finn et al., 2006; Goodge & Finn, 2010), though cratonic rocks crop out only in the Miller and Geologist ranges of the central Transantarctic Mountains (Borg et al., 1990; Goodge & Fanning, 1999; Goodge et al., 1991; 1992). Along the orogen, syn-rift and passive-margin sedimentary rocks deposited during and after the

breakup of Rodinia are deformed and metamorphosed and host granitic (*sensu lato*) batholiths known collectively as the Granite Harbour Intrusives (Gunn & Warren, 1962). Metamorphic and igneous rocks associated with the Ross orogen are unconformably overlain by clastic sedimentary rocks of the Devonian− Triassic Beacon Supergroup (McKelvey et al., 1970; summarized in Barrett, 1981), and both are intruded by Ferrar dolerite sills associated with the breakup of Gondwana in the Jurassic (Heimann et al., 1994; Encarnación et al., 1996). Ross-age crystalline basement is now exposed in the rift-shoulder of the Cenozoic extension-related Transantarctic Mountains (Gleadow & Fitzgerald, 1987).

Extensive geochronologic and isotopic studies of granitoids from northern Victoria Land and central Transantarctic Mountains have resulted in various tectonic models for the evolution of the Gondwanan margin in the Neoproterozoic and early Paleozoic (e.g., Borg et al., 1990; Borg & DePaolo, 1991; Rocchi et al., 1998; Goodge et al., 2012). The Sr-and Nd isotopic composition of plutonic rocks and their host metasedimentary rocks in southern Victoria Land have been reported by various workers (Borg & DePaolo, 1994; Hall et al., 1995; Cooper et al., 1997; Cox et al., 2000; Read et al., 2002; Mellish et al., 2002; Cottle & Cooper, 2006a,b). Extensive exposures of metamorphic and granitic basement in southern Victoria Land provide an opportunity for a more detailed geochronologic and isotopic study.

Within the Dry Valleys area of southern Victoria Land, plutonic rocks of the Granite Harbour Intrusives are hosted in metamorphic rocks of the Skelton Group. The Skelton Group in the Dry Valleys consists of multiply-deformed marble, psammitic schist, calc-silicate, and lesser amounts of pelitic schist and amphibolite intercalated with layers of granitic orthogneiss (Findlay et al., 1984). These rocks were metamorphosed to uppermost amphibolite conditions, and psammitic and pelitic schists are migmatitic (Allibone, 1992;

Allibone & Norris, 1992; Cox, 1992). Allibone and Norris (1992) concluded that relatively small volumes of anatectic melt ('microplutons' ≤ 50 m across) could not have contributed significantly to the larger-scale Granite Harbour plutons, however it is possible that assimilation of anatectic melt(s) occurred at deeper, unexposed crustal levels.

Plutonic rocks compose approximately 70% of exposed pre-Devonian basement in the Dry Valleys (Fig. 2.1). The granitoids, consisting of approximately 40–50 plutons over an area greater than 5,000 km^2 (Fig. 2.1, Forsyth et al., 2002; Cox et al., 2012), have been divided into three magmatic suites based on intrusion characteristics, deformation style, and composition (Smillie, 1992; Allibone et al., 1993b). Based on field relationships and whole-rock geochemistry, these workers interpreted the DV1a and DV1b suites as subduction-related, with the subsequent DV2 suite generated in an extensional regime after the cessation of subduction. Though the classification of all of the plutonic rocks in the Dry Valleys into three suites may be a simplification, the DV1a, DV1b, and DV2 suite divisions are a useful framework for the discussion of the samples from this study.

Limited geochronology suggests that the DV1a and DV1b suites overlap in age and were emplaced between ca. 530 Ma and 490 Ma, whereas the DV2 intrusions largely post-date the DV1 suites, with the youngest U-Pb zircon age of ca. 485 Ma (Encarnación and Grunow, 1996; Allibone & Wysoczanski, 2002). The largest DV1a pluton (Bonney Pluton) was emplaced at a mid-crustal level (4.2 kbar or ~15 km depth), synchronous with contraction across the arc and amphibolite-facies metamorphism of the Skelton Group host metasediments (Allibone et al., 1993a; Cox, 1993). Subsequent emplacement of the DV2 suite occurred at progressively shallower crustal levels during extension and exhumation, with late stage porphyry dikes recording pressures as low as 1.2 kbar (~4 km depth; Allibone

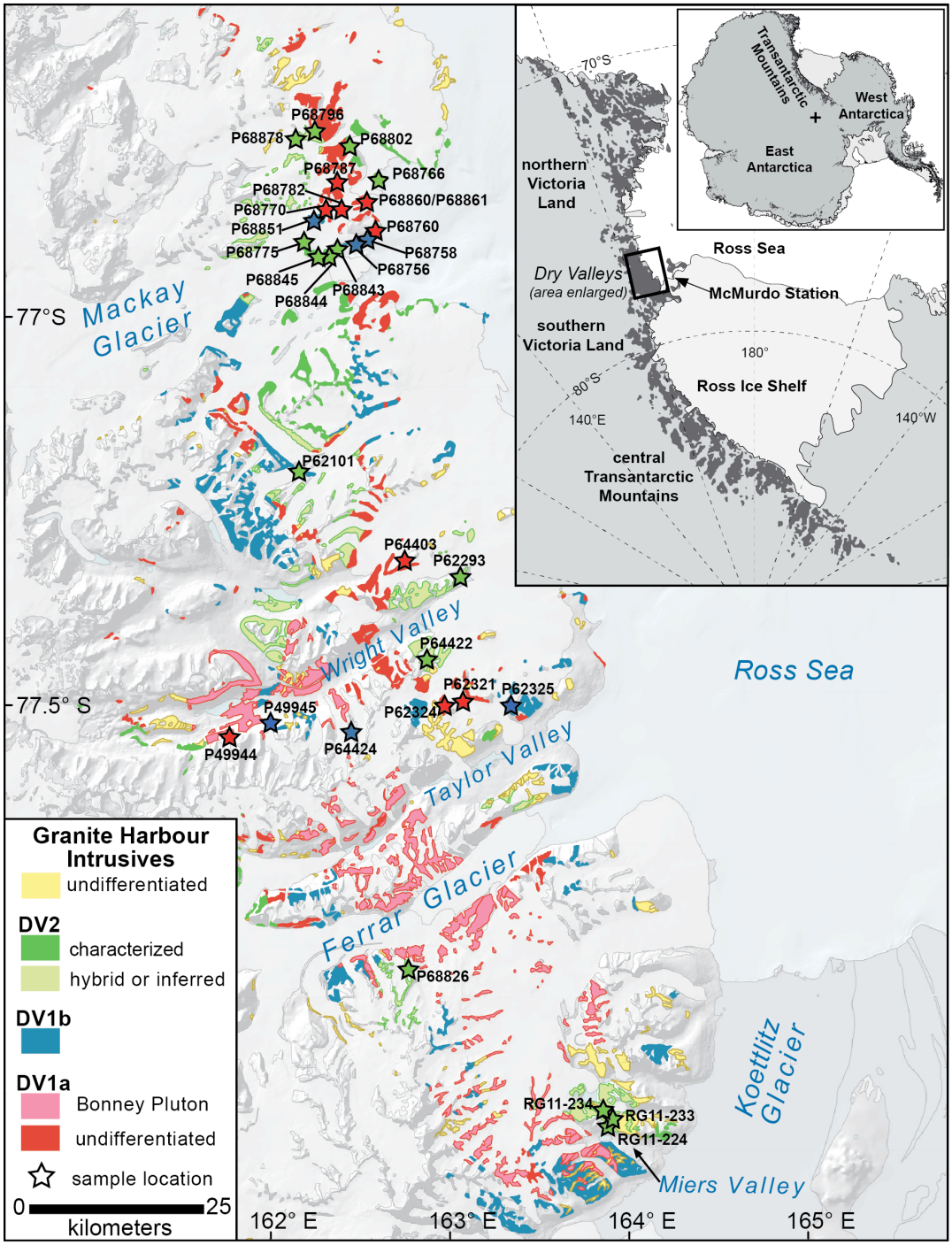

Figure 2.1 Location map of the Transantarctic Mountains (inset) showing the different physiographic segments and the study area. The box surrounding the Dry Valleys area is enlarged in a geologic map modified from Cox et al. (2012). The geologic map shows the distribution of the three Dry Valleys igneous suites, with the metamorphic country rock and younger sedimentary and volcanic rocks omitted to emphasize the distribution of intrusive rocks. The locations of samples from this study are marked by stars, color-coded according to DV suite.

et al., 1993a). The distinctive compositions and contrasting styles of deformation of various units in the Dry Valleys suggest that the Ross orogen probably developed through several distinct tectono-magmatic phases during the Neoproterozoic through Early Ordovician (Encarnación & Grunow, 1996).

METHODS

Thirty-one samples ranging from gabbro to granite were selected with an effort to target representative rock types for each suite and to sample the largest-scale intrusions. Here we offer an abbreviated explanation of the methods employed in this study. A thorough description of the analytical details is provided in Appendix Text 1.

Whole-rock major- and trace-element geochemistry were measured by X-ray fluorescence (XRF) and inductively-coupled plasma mass spectrometry (ICP-MS) and used to distinguish samples based on composition and to correlate samples to the specific DV igneous suites of Smillie (1992) and Allibone et al. (1993b).

We employed zircon U-Pb geochronology by laser-ablation multi-collector (MC)-ICP-MS to determine the crystallization ages of individual bodies and constrain the duration of magmatism in the Dry Valleys area during the Ross orogeny. Zircon separates were mounted in epoxy disks, polished to reveal medial sections, and imaged by scanning electron microscope with a cathodoluminescence (CL) detector (Fig. 2.2). Images were used to guide the placement of spots for laser-ablation, with care taken to avoid overlapping multiple growth domains or inherited cores, though in some cases it was impossible to avoid overlapping distinct CL domains (e.g., sample 49944 in Fig. 2.2). A Photon Machines short pulse width (~4ns) 193 nm wavelength excimer laser was used to ablate spots of 24–30 μm

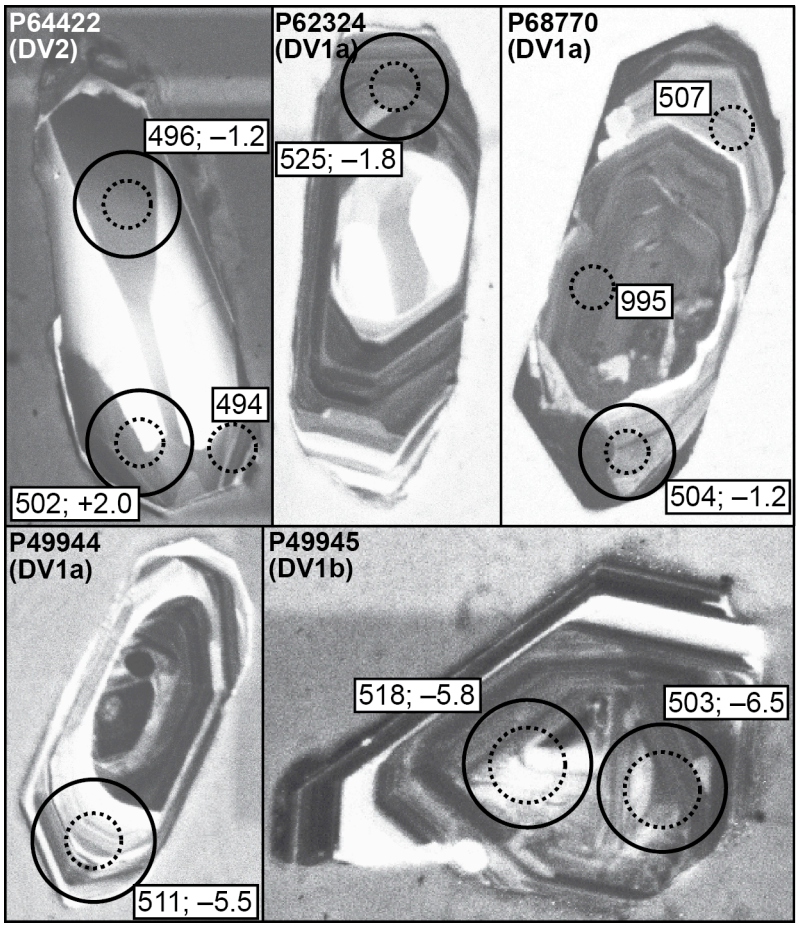

Figure 2.2 Cathodoluminescence (CL) images of zircon grains from representative samples showing a range of internal zoning characteristics, including sector- (upper left) and concentric oscillatory-zoning and inherited cores (upper right). The dashed- and solid-circles show the locations of laser-ablation pits for U-Pb (measured first) and Hf isotope analyses, respectively. The diameter of the Hf pits is 53 μm for scale. The boxes adjacent to the circles show the $^{206}Pb/^{238}U$ age (Ma) and $\varepsilon Hf_{(i)}$ measured from those spots. Uncertainties are typically 1% on individual $^{206}Pb/^{238}U$ ages and ~3 $\varepsilon Hf_{(i)}$ units (1s) on individual Hf measurements. Representative CL images of grains from all the samples in this study are provided in the supplementary material of Hagen-Peter et al. (2015).

diameter, and ^{238}U, ^{232}Th, ^{208}Pb, ^{207}Pb, ^{206}Pb, and ^{204}(Pb+Hg) were measured with a Nu Instruments Nu Plasma High Resolution MC-ICP-MS at the University of California, Santa Barbara. The Lu-Hf-Yb isotope compositions of the same zircons were measured by MC-ICP-MS in later analytical sessions. Laser-ablation spots for Lu-Hf-Yb measurements were 53 μm in diameter and overlapped those used in the U-Pb age determinations (Fig. 2.2). Age data were coupled to Hf isotopes and whole-rock geochemistry to identify temporal shifts in magma sources and evolutionary trends.

The Hf isotope system has become an important tracer for crustal evolution and magma source studies. Due to the stronger partitioning of Lu relative to Hf in the mantle during differentiation processes and the radioactive decay of ^{176}Lu to ^{176}Hf, over time the $^{176}Hf/^{177}Hf$ of the depleted mantle increases relative to the crust (Patchett & Tatsumoto, 1980a,b; Patchett et al., 1981; Patchett, 1983). In a way this system is analogous to the Sm-Nd system. However, *in situ* analyses of Hf isotopes in individual growth zones of zircons may record processes such as magma mixing or country rock assimilation that changed the isotopic composition of the reservoir from which the zircons crystallized (e.g., Griffin et al., 2002; Hawkesworth & Kemp, 2006). Additionally, the physical robustness of zircon makes it less susceptible to the open-system behavior sometimes observed in whole-rock Sm-Nd (e.g., Moorbath et al., 1997), and commonly in Rb-Sr (e.g., Field & Råheim, 1979; Ramos et al., 2005).

Zircon readily incorporates Hf into its structure (routinely >1 wt%) and has a low Lu/Hf ratio (Ahrens & Erlank, 1969; Hoskin & Schaltegger, 2003; Hawkesworth & Kemp, 2006); thus (assuming no fractionation of Hf isotopes during crystallization), the Hf composition of a zircon approximates that of the reservoir from which it crystallized. Unlike

trace element patterns, which are affected by fractional crystallization/melting processes, Hf isotopes in zircon may reflect the composition of the source if open-system processes such as contamination and magma mixing are minimal during the evolution of the magma. In a gross sense, large positive $\varepsilon Hf_{(i)}$ (the $^{176}Hf/^{177}Hf$ in the sample at the time of crystallization relative to the chondritic uniform reservoir) indicates a depleted-mantle source for the sample, while a negative $\varepsilon Hf_{(i)}$ suggests a significant recycled crust component (Vervoort & Blichert-Toft, 1999; Belousova et al., 2005; Belousova et al., 2010).

Depleted-mantle model ages (T_{DM}) provide an estimated time of separation of a crustal magma source from a depleted-mantle reservoir. Details of the principles behind the calculation of depleted-mantle model ages (T_{DM}) and two-stage depleted-mantle model ages (T_{DM}^{C}) are described thoroughly in DePaolo et al. (1991), and, as applies to Hf isotopes, in Griffin et al. (2000; 2002). It is important to note that model ages involve several untestable assumptions that may significantly affect the calculated "crustal separation age". Two fundamental assumptions are: 1) that the crustal source of a melt separated from a reservoir that followed the $^{176}Hf/^{177}Hf$ evolution curve defined by the depleted-mantle model parameters (present day $^{176}Hf/^{177}Hf$= 0.28325; $^{176}Lu/^{177}Lu$= 0.0384; Griffin et al., 2000; 2002) and that; 2) the crustal source evolved along the $^{176}Hf/^{177}Hf$ trajectory of "average crust", with $^{176}Lu/^{177}Hf$ = 0.015 (Griffin et al., 2002). The latter assumption is specific to T_{DM}^{C}. Model ages are often interpreted to represent a minimum age because any contamination from a more radiogenic (higher $^{176}Hf/^{177}Hf$) mantle component or younger crustal component would drive the resulting isotope composition toward a younger model age. Because of the major assumptions explained above, the model ages presented in this study are considered only *very general* estimates of the age of crust underlying the Ross

orogen.

RESULTS

Major- and trace- element geochemistry

The XRF geochemical data for each dated sample (except for two, for which there was no additional material to analyze) are given in Appendix Table 4 and displayed on discriminant diagrams in Figure 2.3. The whole-rock composition data presented here are a combination of those from Allibone et al. (1993b), Forsyth et al. (2002), and from this study. See Allibone et al. (1993b) for a comprehensive geochemical dataset for Dry Valleys samples. Sample locations and brief descriptions of the rock types can be found in Table 2.1. Additional information on the samples from this study is available in the New Zealand Institute of Geological and Nuclear Science (GNS) rock and mineral database (www.pet.gns.cri.nz).

Considerable scatter on the Harker diagrams in Figure 2.3 precludes a simple cogenetic relationship of samples assigned to each suite, while there is also considerable overlap between the different suites. This demonstrates the need for caution when interpreting the samples in the framework of magmatic suites with distinct sources and evolutionary trends. It should also be noted that the original DV suite subdivision of Allibone et al. (1993b) was primarily for samples with > 60 wt% SiO_2, therefore, the suite assignment of mafic (< 60 wt% SiO_2) samples from this study should be considered tentative. However, the major conclusions drawn in this study do not change significantly when the data are interpreted independently of the suite framework.

DV1a

The DV1a samples from this study range in SiO_2 content from ~50–70 wt%. On Harker diagrams, DV1a samples display steep negative slopes for Al_2O_3, MgO (not shown in Fig. 2.3), and CaO. The Na_2O contents are relatively constant, while K_2O increases with increasing SiO_2 content. The DV1a suite generally has higher Na_2O and lower K_2O than the DV1b and DV2 suites. There is a wide range in the concentration of the trace elements Y, Sr, Rb, Zr, and Ba, with no strong correlation to SiO_2 content (except in Sr). DV1a samples have Sr/Y ratios (not shown in Fig. 2.3) similar to DV2 samples and lower than most DV1b samples. The evolved DV1a samples typically plot near the boundary of the metaluminous and peraluminous fields, within the continental arc granitoid field (Fig. 2.3; Maniar & Piccoli, 1989). On tectonic discrimination diagrams (Fig. 2.3), the samples overlap the boundary of I&S-type and A-type granitoids on the diagram of Whalen et al. (1987), and plot within the "volcanic arc granitoids" (VAG) field on the diagram of Pearce et al. (1984).

DV1b

The DV1b samples from this study are all highly evolved, with a restricted range in SiO_2 from ~70–75 wt% and major element oxides that largely overlap with the evolved DV1a and DV2 samples. These samples have greater K_2O/Na_2O ratios than most DV1a samples and are distinguished from evolved DV2 samples by generally higher Ba and Sr and low Zr and Y. The DV1b samples are weakly peraluminous and primarily plot within the I&S-type granitoid and VAG fields on tectonic discrimination diagrams (Fig. 2.3)

DV2

The DV2 suite samples range in SiO_2 content from ~48–75 wt%, with major oxides that

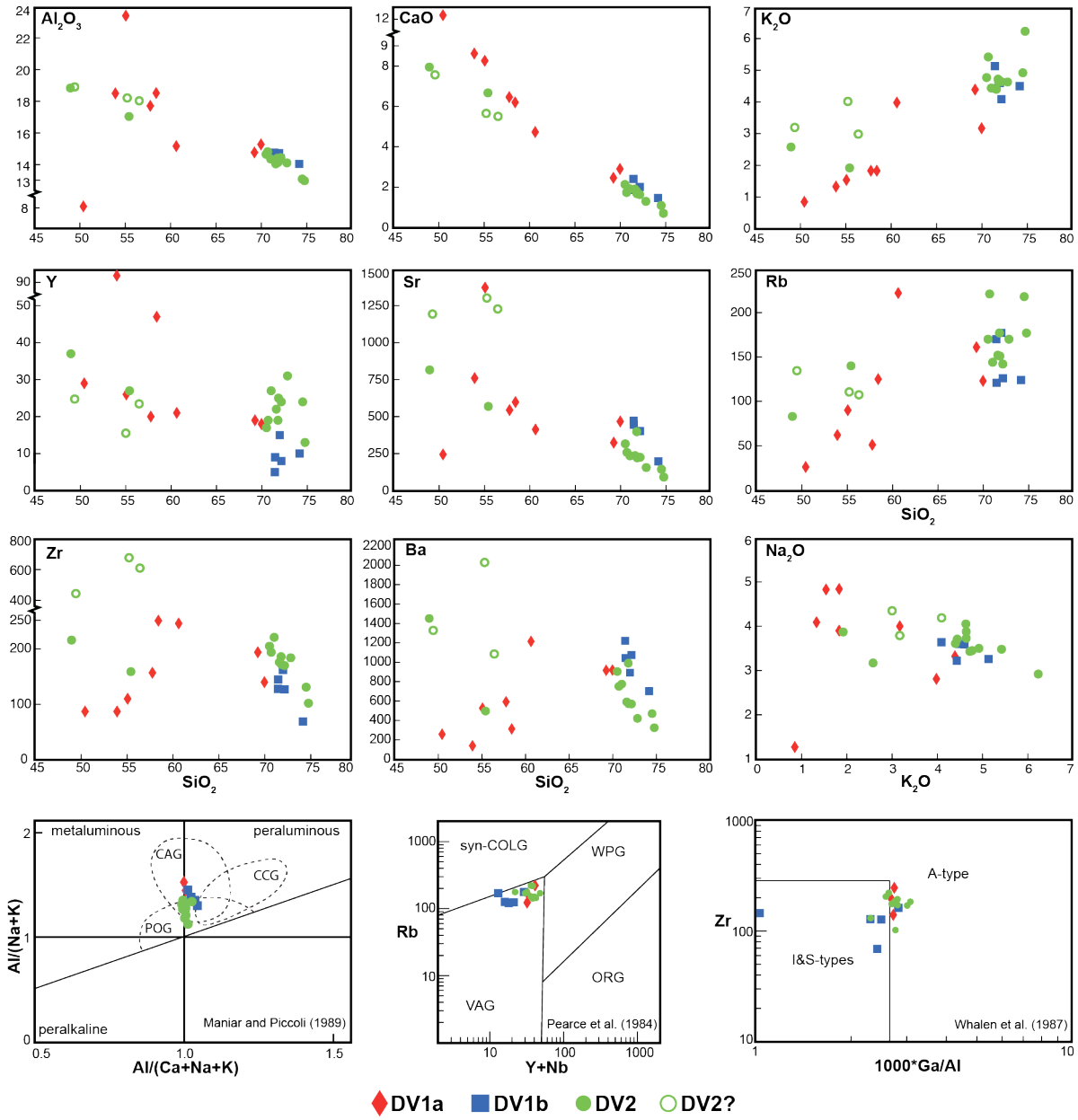

Figure 2.3 Composition data for the dated samples on variation diagrams compare and contrast the chemical characteristics of the DV igneous suites. On some discrimination diagrams samples show coherent trends (e.g., CaO vs. SiO_2), suggesting cogenetic relationships, but significant dispersion on others precludes a simple liquid-line of descent for the evolution of the suites. Remelting, mixing of source components, and contamination are more viable mechanisms for the geochemical diversity of the suites. Only samples with greater than 60 wt% SiO_2 are plotted on tectonic discrimination diagrams of Maniar and Piccoli (1989), Pearce et al. (1984), and Whalen et al. (1987). Abbreviations for different fields are as follows: post-orogenic granitoids (POG), continental arc granitoids (CAG), continental collision granitoids (CCG), syn-collisional granites (syn-COLG), within-plate granites (WPG), volcanic arc granites (VAG), and ocean ridge granites (ORG). Major oxide concentrations are in wt%; trace elements are in ppm.

largely overlap with DV1a and DV1b samples at high SiO_2 content. Two primitive DV2 samples have lower Al_2O_3 and CaO and slightly higher K_2O and Rb than DV1a samples of comparable SiO_2 content. Evolved DV2 samples are enriched in Y and Zr and depleted in Sr and Ba relative to most other samples. They typically have high K_2O/Na_2O and low Sr/Y (not shown in Fig. 2.3) ratios relative to DV1a and DV1b samples, respectively. Evolved samples plot near the boundary of the metaluminous and peraluminous fields, within the overlapping continental arc granitoid and post-orogenic granitoid fields (Fig. 2.3). They plot near the boundary between the I&S-type and A-type fields and within the VAG field on tectonic discrimination diagrams.

Tentative DV2

Three samples from the Miers Valley, in the southern end of the study area (Fig. 2.1) are tentatively assigned to the DV2 suite based on composition and field characteristics (Simpson & Aslund, 1996; Cox et al., 2012). These samples are relatively primitive (49–56 wt% SiO_2), Ca-poor, and alkali-rich. They have high Ba, Sr, and Zr and low Y concentrations. They have some chemical characteristics similar to the DV1b suite, most notably very high Sr/Y ratios. These samples are all relatively primitive (< 57 wt% SiO_2) and are not plotted on the tectonic discrimination diagrams that were devised for granitoids. However, the alkali-rich nature of these samples is consistent with the other DV2 samples and the interpretation of Smillie (1992) and Allibone et al. (1993b) that the DV2 suite represents post-tectonic magmatism in the Dry Valleys area.

U-Pb geochronology

The U-Pb ages and Hf isotope populations for all of the samples from this study are summarized in Table 2.1. The ages are presented as $^{206}Pb/^{238}U$ weighted mean ages. They are categorized by suite to emphasize the timing and duration of magmatism. For several samples, the mean square of weighted deviates (MSWD) of the analyses used in the age calculation is greater than that expected for a single population given the sample size. This indicates that either the uncertainties assigned to each individual data point are under-estimated, or that the data used in the weighted mean may not be representative of a single population, that is, there is geologic significance to the scatter in the data (Wendt & Carl, 1991). Given that repeated measurements of secondary reference materials returned a mean age within uncertainty of the reference isotope dilution-thermal ionization mass spectrometry (ID-TIMS) age and an MSWD of near 1 (Fig. 2.4), we are confident that the uncertainty assigned to each data point is appropriate, and therefore sample MSWDs >1 likely represent minor inheritance and/or Pb-loss. We take the weighted mean $^{206}Pb/^{238}U$ ages reported in Table 2.1 as the best estimates of the crystallization ages of the samples.

The samples range in age from 515.4 ± 6.6 Ma to 492.2 ± 6.1 Ma. Ages from the DV1a suite range between 515.4 ± 6.6 Ma and 500.1 ± 6.6 Ma (10 samples). Only one reliable age of 508.9 ± 6.4 Ma was obtained for a sample from the regionally extensive Bonney Pluton. Four of six DV1b samples yielded robust ages, ranging from 515.3 ± 6.4 Ma and 500.6 ± 6.6 Ma. Sixteen samples from the DV2 suite range between 505.0 ± 6.5 Ma and 492.2 ± 6.1 Ma. Concordia diagrams and $^{206}Pb/^{238}U$ age distributions of several samples are shown in Figure 2.5. These examples demonstrate the issue of Proterozoic and "young" (ca. 550 Ma) inheritance present in some samples, the origin of which is discussed further in a following section.

Table 2.1 Summary of U-Pb, Hf, and Nd isotope results

Sample name	Rock description	Location		U-Pb age*	± †	*n*	MSWD	$\varepsilon Hf_{(i)}$ §	± †	*n*	MSWD	T_{DM}^{Hf}	$\varepsilon Nd_{(i)}$	T_{DM}^{Nd}
		Lat (°S)	Long (°E)	(Ma)	(Ma)							(Ga)		(Ga)
RG11-233	Hbl diorite	-78.073	163.895	492.2	6.1	27	1.9	–4.0	0.6	8	1.4	1.7	–	–
P64422#	Hbl diorite	-77.482	162.821	493.2	6.1	35	0.8	–1.8	1.2	12	1.5	1.5	–	–
P68826	pink granite	-77.877	162.636	495.5	6.1	25	1.2	–5.9	1.1	12	0.5	1.8	–	–
P62101	granite	-77.231	162.067	495.6	6.1	20	1.3	–2.2	1.5	10	1.0	1.6	–	–
P68775	granite	-76.943	162.161	495.9	6.2	30	2.0	–4.6	1.2	12	0.9	1.7	–	–
P68845	Hbl granite	-76.953	162.247	496.1	6.1	26	1.2	–4.5	1.3	12	0.8	1.7	–	–
P68844	Hbl granite	-76.952	162.267	496.8	6.1	28	1.0	–5.6	1.3	10	1.3	1.8	–	–
P62293	megacrystic granite	-77.369	163.007	496.9	6.2	22	1.7	–4.2	1.5	12	0.7	1.7	–	–
P68802	pink granite	-76.810	162.443	497.1	6.2	29	1.4	–2.4	1.1	10	1.3	1.6	–	–
RG11-234	cpx-bt gabbro-diorite	-78.060	163.849	498.6	6.5	13	2.6	–2.7	0.7	8	1.2	1.6	–6.1	1.7
P68760	granite	-76.934	162.473	500.1	6.6	18	1.6	–3.7	1.4	10	0.8	1.7	–	–
RG11-224	Bl diorite	-78.078	163.867	500.2	6.1	26	1.4	–3.3	0.5	10	0.8	1.6	–	–
P49945	Bt granodiorite	-77.556	161.858	500.6	6.6	17	2.1	–5.9	1.4	9	0.6	1.8	–	–
P64403	Hbl gabbro	-77.329	162.815	501.9	6.4	20	1.6	–0.6	1.5	10	0.5	1.5	–	–
P68796	pink granite	-76.802	162.157	502.1	6.6	23	2.0	–4.0	1.1	12	1.3	1.7	–	–
P68766	granite	-76.861	162.551	502.6	6.6	10	0.5	–2.1	1.4	8	0.5	1.6	–	–
P68843	porphyritic granite	-76.950	162.292	504.2	6.4	19	0.9	–3.6	1.2	10	0.7	1.7	–	–
P68770	weakly-foliated granite	-76.892	162.248	504.8	7.0	14	2.8	–3.2	1.4	9	0.5	1.7	–	–
P68878	porphyritic diorite dike	-76.804	162.135	505	6.5	18	1.5	–2.1	1.5	8	1.4	1.6	–	–
P68851	megacrystic Hbl granite	-76.903	162.196	505.5	6.5	16	1.5	–1.4	1.5	10	0.4	1.5	–	–
P68782	weakly-foliated granite	-76.895	162.395	506.4	6.4	16	1.0	–3.5	1.7	8	1.2	1.7	–	–
P68861	massive Hbl diorite	-76.884	162.485	507.8	6.4	20	1.5	–0.3	1.5	12	0.8	1.5	–	–
P49944	Qtz monzodiorite	-77.569	161.628	508.9	6.4	23	1.3	–2.0	1.3	10	1.2	1.6	–	–
P68860	foliated Hbl tonalite	-76.884	162.485	509.4	6.6	17	1.9	–3.5	1.6	8	1.2	1.7	–	–
P62321	foliated diorite	-77.533	162.962	509.5	6.3	20	1.1	–1.1	1.2	12	0.4	1.5	–	–
P68787	Hbl monzodiorite	-76.866	162.349	511	6.4	28	2.2	–2.4	1.4	12	0.9	1.6	–	–
P68756	megacrystic granite	-76.944	162.335	514.5	6.7	10	0.7	–1.5	1.2	10	1.6	1.6	–	–
P68758	granite	-76.939	162.396	515.3	6.4	11	1.0	–2.9	1.7	10	0.8	1.6	–	–
P62324	foliated diorite	-77.535	162.900	515.4	6.6	28	1.3	–1.7	1.1	12	0.9	1.6	–	–
P64424	megacrystic granite	-77.578	162.385	–	–	–	–	–7.2††	1.9	5	1.1	1.9	–	–

Note: MSWD—mean square of weighted deviates; T_{DM}^{Hf}—two-stage depleted-mantle Hf model age; T_{DM}^{Nd}—two-stage depleted-mantle Nd model age.

* "U-Pb ages" with a corresponding uncertainty are weighted-mean $^{206}Pb/^{238}U$ mean ages. Ages preceded by a "~" are estimated ages of samples for which mean ages were not calculated.

† Uncertainties on mean ages are quadriatic additions of the internal 2 S.E. and external uncertainty estimated from the reproducibility of the GJ-1 and Plešovice reference zircons. Uncertainties on $\varepsilon_{Hf(i)}$ are reported as the 2 standard error (S.E.) of the population of analyses used in the calculation.

§ $\varepsilon_{Hf(i)}$ are weighted mean values of multiple measurements of a population from each sample.

Samples with prefix "P" are housed in the New Zealand Institute of Geological and Nuclear Science (GNS) PETLAB database (www.pet.gns.cri.nz).

†† A mean age could not be calculated for sample P64424, but individual spot ages were used to calculate $\varepsilon Hf_{(i)}$.

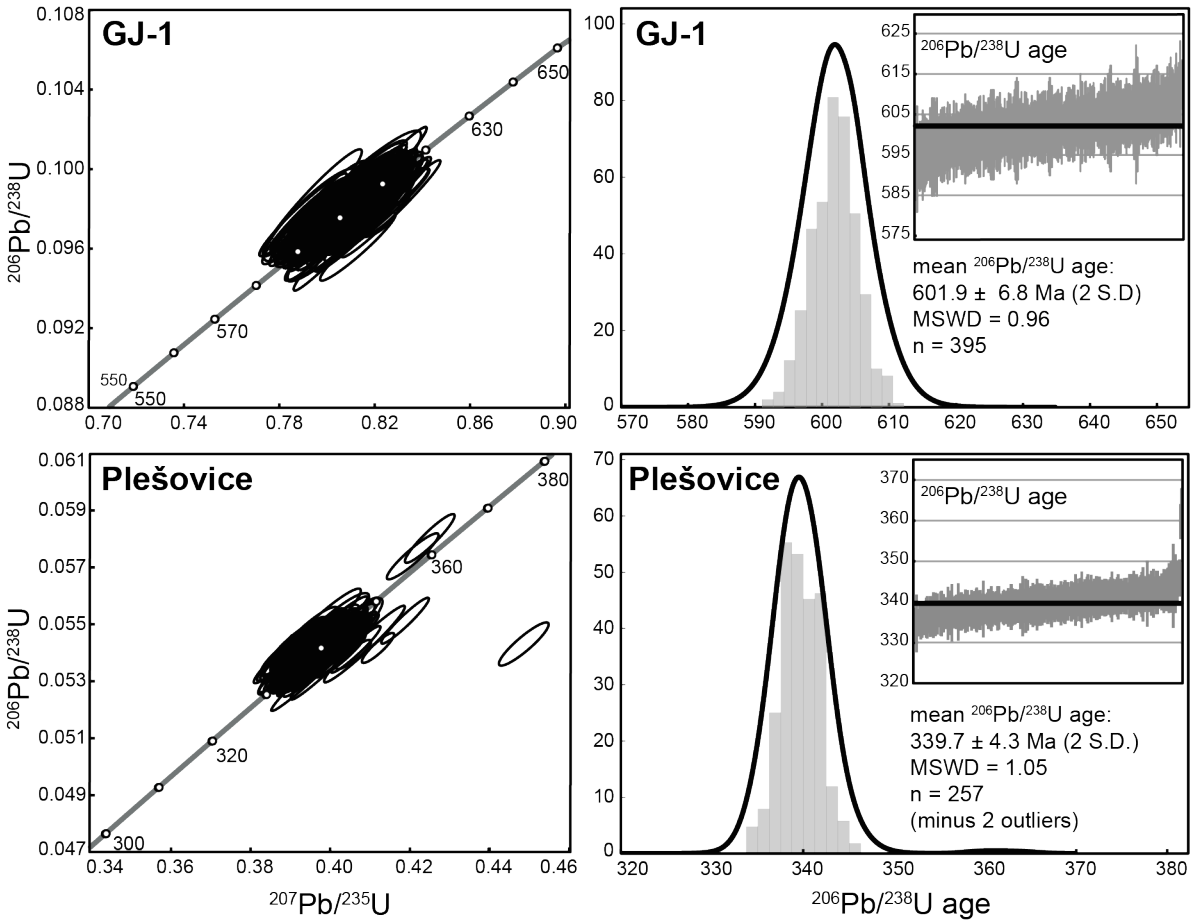

Figure 2.4 Results of the secondary reference zircons analyzed throughout the sessions when the Dry Valleys (DV) samples were measured (spanning many months) on concordia diagrams (left) and $^{206}Pb/^{238}U$ age distributions (right). These data provide estimates for the accuracy and external precision of our analyses. Both reference zircons were reproduced very accurately, within <1% of the "true" ages (GJ-1 = 601.7 Ma: Condon, personal communication; Plešovice = 337.1 Ma: Sláma et al., 2008). The external reproducibility was 1.1–1.3% (2 S.D.); this was propagated into the uncertainty of the final $^{206}Pb/^{238}U$ weighted-mean ages for the DV samples. MSWD—mean square of weighted deviates.

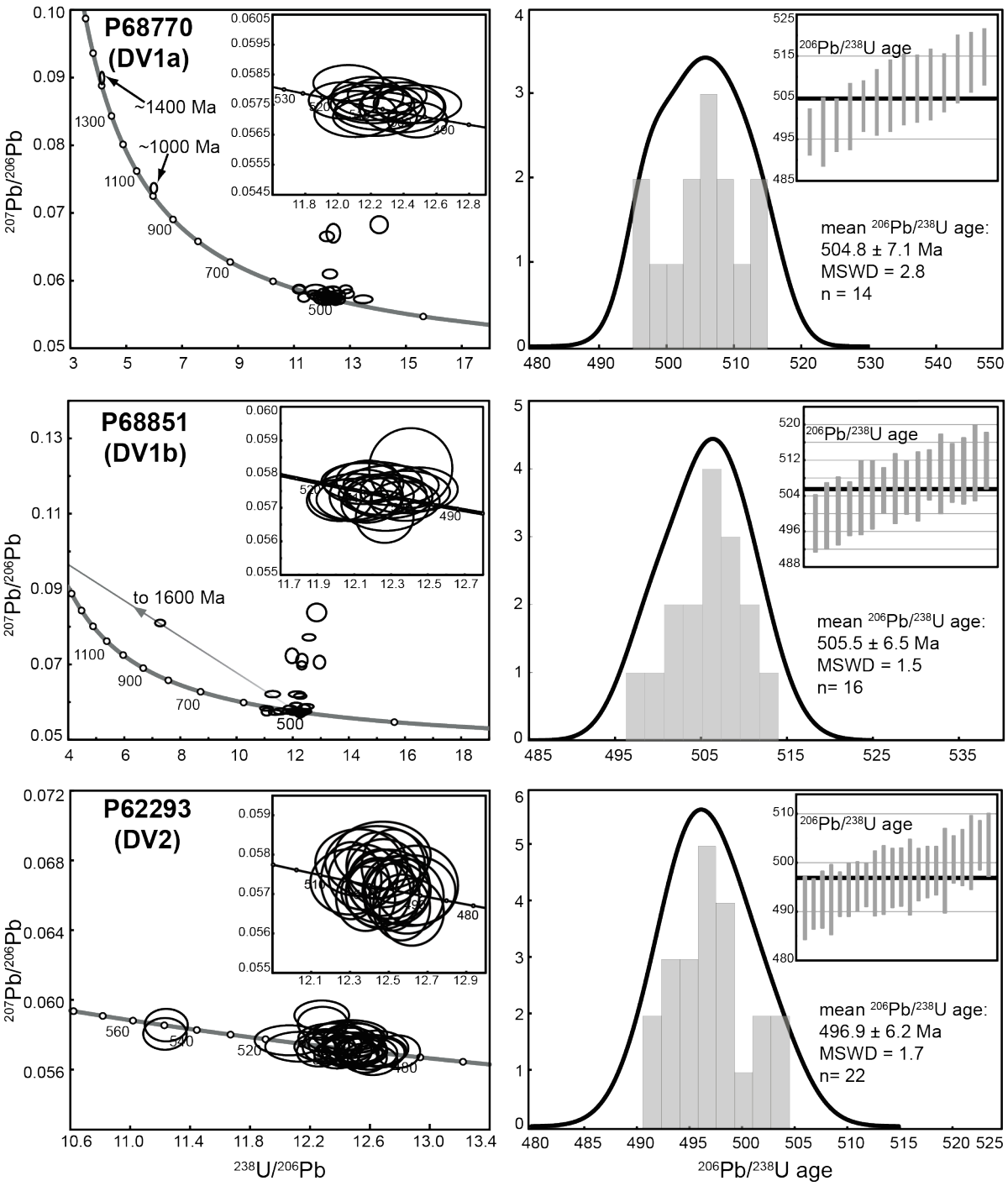
P68770
(DV1a)
~1400 Ma
~1000 Ma
1300
1100
900
700
500
530
520
490
480
mean 206Pb/238U age:
504.8 ± 7.1 Ma
MSWD = 2.8
n = 14
206Pb/238U age
P68851
(DV1b)
to 1600 Ma
1100
900
700
500
490
mean 206Pb/238U age:
505.5 ± 6.5 Ma
MSWD = 1.5
n= 16
206Pb/238U age
P62293
(DV2)
560
540
520
500
480
mean 206Pb/238U age:
496.9 ± 6.2 Ma
MSWD = 1.7
n= 22
206Pb/238U age
207Pb/206Pb
238U/206Pb
206Pb/238U age

Figure 2.5 Examples of the U-Pb data from several representative Dry Valleys (DV) samples. The inverse concordia diagrams on the left show all of the analyses for each sample. The inverse concordia insets and $^{206}Pb/^{238}U$ age distributions on the right show the analyses used in the calculation of the weighted-mean ages reported in Table 1. The "n" are the number of analyses used in the age calculations (out of a total of 30–40 spots per sample). These examples are meant to demonstrate the occurrence of clear Proterozoic (P68770 and P68851) and likely "young" (P62293 and P68851) inheritance in some of the samples. There is also some evidence of common-Pb and Pb-loss in the first two samples. Note that inheritance is not ubiquitous among the samples from this study, though zircon CL domains that appeared to be inherited were generally avoided. Similar diagrams for all samples can be found in the supplementary material of Hagen-Peter et al. (2015). MSWD—mean square of weighted deviates.

Hf isotopes

The samples from this study have a restricted range of $\varepsilon Hf_{(i)}$ values between −0.3 and –7.2 (Table 2.1; Fig. 2.6), with values overlapping for all of the suites. The DV1a suite ranges from −0.3 to –3.7. The DV1b suite ranges between –1.4 and –7.2. The DV2 samples range from –1.8 to –5.9. The oldest DV1a and DV1b samples have a restricted range of ~3 $\varepsilon Hf_{(i)}$ units, and younger samples, including the DV2 suite display a wider range (Fig. 2.6b). There is a broadening of the range of $\varepsilon Hf_{(i)}$ and lower $\varepsilon Hf_{(i)}$ values with increasing silica content (Fig. 2.6a) and decreasing age (Fig. 2.6b) of the samples. Depleted-mantle model ages range between 1.1 Ga and 1.4 Ga, and two-stage depleted-mantle model ages range between 1.5 and 1.9 Ga (Table 2.1).

DISCUSSION

Here we discuss the interpretation of the U-Pb and Hf isotope data with respect to the timing and duration of magmatism and the potential source(s) for the Dry Valleys granitoids.

Timing and duration of magmatism in the Dry Valleys

Previously reported U-Pb zircon ages for intrusive rocks from the Dry Valleys area suggest that magmatism spanned ca. 530–485 Ma (Encarnación & Grunow, 1996; Cox et al., 2000; Allibone & Wysoczanski, 2002). On Mount Morning, approximately 70 km southeast of the Ferrar Glacier (Fig. 2.1), Martin et al. (2014) identified felsic granulite xenoliths (hosted in Cenozoic volcanic rocks) with DV suite geochemical affinities. They reported an age of ca. 545 Ma for one granulite xenolith with DV1b geochemical affinity, suggesting that subduction-related magmatism commenced by this time in southern Victoria Land (Martin et

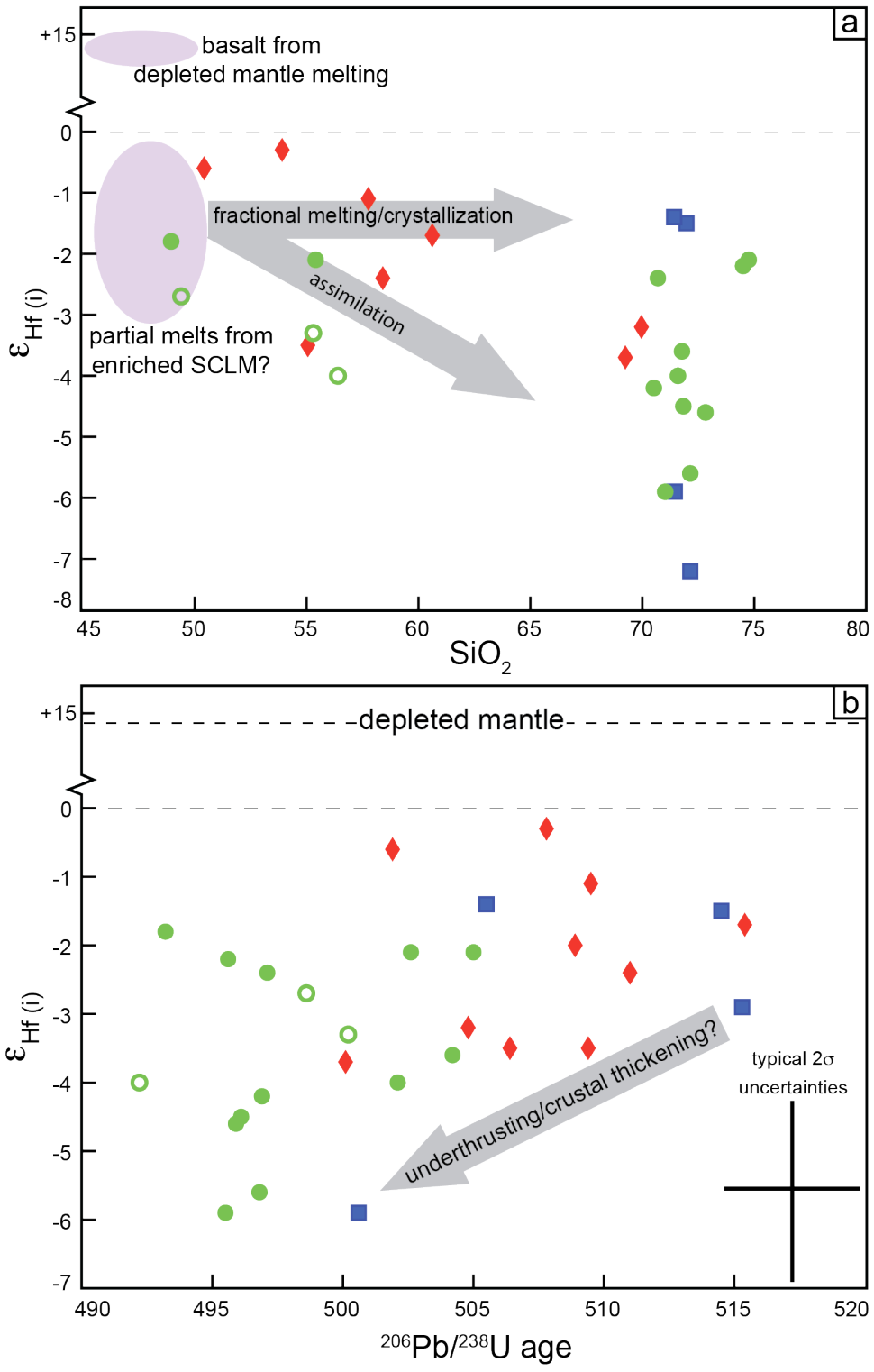
a
basalt from
depleted mantle melting
fractional melting/crystallization
assimilation
partial melts from
enriched SCLM?
εHf (i)
SiO2
b
depleted mantle
underthrusting/crustal thickening?
typical 2σ
uncertainties
206Pb/238U age

Figure 2.6 (a) Diagram of $\varepsilon Hf_{(i)}$ versus SiO_2 (wt%) for the Dry Valleys (DV) samples with the expected field for melts sourced from DM for reference. The thin dashed line is at the chondritic uniform reservoir (CHUR) reference value. The light grey arrows show the different trajectories expected to arise from evolution through fractional melting/crystallization and crustal assimilation ("contamination"). The low $\varepsilon Hf_{(i)}$ of some of the evolved samples can be explained by contamination by old high-silica crust. SCLM—sub-continental lithospheric mantle. (b) Diagram of $\varepsilon Hf_{(i)}$ versus age shows a broadening and lower $\varepsilon Hf_{(i)}$ values in younger samples. This trend may reflect contamination of later magmas during ascent through thickened arc crust or underthrusting of supracrustal material into the source region. There is a discrepancy in the number of points on Figure 6b and Figure 6B because not every sample has complementary U-Pb, Hf, and geochemistry data. For example, the DV1b sample with the lowest $\varepsilon Hf_{(i)}$ did not yield a reliable mean age ($\varepsilon Hf_{(i)}$ was calculated at 500 Ma) and so it does not appear in Figure 6b. Symbols as in Figure 3.

al., 2014). Our samples do not represent the entire range of magmatism in this area during the Ross orogeny, with an oldest and youngest age of ca. 515 Ma and 492 Ma, respectively (Fig. 2.7). Allibone and Wysoczanski (2002) reported ages of 531 ± 10 Ma and 516 ± 10 for small orthogneiss bodies with DV1b suite affinity. Encarnación and Grunow (1996) reported an age of 484 ± 7 Ma age for a DV2 plagioclase-porphyry dike. These bodies are inferred to be volumetrically insignificant, composing <<1% of the area of exposed basement rocks mapped in southern Victoria Land (Cox et al., 2012). All other U-Pb zircon ages for DV suite granitoids (summarized in Allibone & Wysoczanski, 2002) fall within the 515–492 Ma range represented by the samples from this study. One sample from the large Bonney Pluton yielded a robust age of 508.9 ± 6.4 Ma, which is consistent with ages of samples from other parts of the pluton, including ca. 505 Ma ages reported by Encarnación and Grunow (1996) and Cox et al. (2000) and an age of 499 ± 6 Ma from Allibone and Wysoczanski (2002). The four ages from this pluton agree within uncertainty, but the dispersion in the mean ages may reflect its composite emplacement. Our samples are not distributed evenly across the entire Dry Valleys area (Fig. 2.1), however we targeted the largest plutons, including the Bonney and Discovery plutons, and all the units dated in this study collectively represent over 40% of the exposed Granite Harbour Intrusives in this area (Cox et al., 2012). We therefore interpret our data to record the largest pulse of subduction-related magmatism in the Dry Valleys area during the Ross orogeny.

Transient initiation and synchronous cessation of magmatism

In the northern Victoria Land (nVL) segment intrusions spanned ca. 545–485 Ma (Black & Sheraton, 1990; Tonarini & Rocchi, 1994; Rocchi et al., 1998; Fioretti et al., 2005;

Bomparola et al., 2006; Tiepolo & Tribuzio, 2008). In the central Transantarctic Mountains (cTAM) calc-alkaline magmatism may have initiated as early as 590 Ma, and persisted for over 100 million years (Goodge et al., 2012). Immediately to the south of the Dry Valleys, alkaline intrusive rocks of the Koettlitz Glacier Alkaline Suite (KGAS; Read et al., 2002; Cox et al., 2012) were emplaced ca. 557–517 Ma (Rowell, et al., 1993; Encarnación & Grunow, 1996; Cooper et al., 1997; Mellish et al., 2002; Read et al., 2002; Cottle & Cooper, 2006a; Read, 2010). Although magmatism in the Dry Valleys area may have persisted for ~45 million years during the early Paleozoic (based on the ca. 530 Ma age from Allibone and Wysoczanski, 2002 and the ca. 485 Ma age of Encarnación & Grunow, 1996), the majority of granites were likely emplaced between ca. 515–492 Ma. This period was significantly abbreviated compared to other segments of the orogen, and coincides almost exactly with the short period of deformation and magmatism recorded in the Delamerian orogen of southeast Australia (ca. 514−487 Ma; Foden et al., 2006). These results, compared with data from nVL and cTAM, highlight the transient nature of continental arc magmatism and deformation along the paleo-Pacific margin of Gondwana, with no clear trend of younging in one direction along the margin (Fig. 2.7).

Overlap in the ages of the subduction-related DV1 suites and the post-tectonic DV2 suite record a transitional shift in tectonic regime. Post-tectonic magmatism occurred within a relatively short period (ca. 495−485 Ma) along at least 1500 km of the arc from southeast Australia through southern Victoria Land with the emplacement of mafic complexes and A-type granites in southeast Australia (Foden et al., 2006 and references therein), potassic Irizar granites and associated Vegetation lamprophyres in central Victoria Land (Rocchi et al., 2009), and late, alkalic DV2 granites and the Vanda dike swarm in southern Victoria Land

(this study; Allibone et al., 1993a,b; Encarnación & Grunow, 1996). In the cTAM the magmatic arc broadened from ~80 km wide to over 160 km wide by ca. 510 Ma, and post-kinematic intrusions persisted until ca. 485 Ma (Goodge et al., 2012). Despite its transient initiation, magmatism seems to have ceased nearly synchronously along the entire arc (Fig. 2.7). Various mechanisms have been proposed to explain the synchronous late-stage magmatism and extension across the orogen. Foden et al. (2006) suggested that the subducting slab beneath southeast Australia may have reached the base of the mantle transition zone (~660 km depth), resulting in hinge rollback, decoupling of the subducting and overriding plates, and exhumation of the upper plate. Hinge rollback, coupled with lithospheric delamination, was proposed to explain the late-stage lamprophyres and extensional collapse in Victoria Land (Di Vincenzo & Rocchi, 1999; Rocchi et al., 2009; Rocchi et al., 2011). There is also evidence for the suturing of discrete continental fragments in nVL, though there is some debate over whether the fragments are exotic terranes (e.g., Borg et al., 1987; Kleinschmidt & Tessensohn, 1987; Borg & DePaolo, 1991) or autochthonous mobile belts (e.g., Rocchi et al., 2011). Allibone et al. (1993a) postulated that there could have been a similar collisional event in sVL at approximately the same time, with remnants of the colliding terrane composing part of the Ross seafloor east of the sVL coast.

The short period of subduction-related magmatism also contrasts with other well-studied continental arcs, for example the Sierra Nevada batholith, in which Ca-alkaline magmatism persisted for over 160 million years (Saleeby et al., 2008, and references therein), albeit through high-flux episodes separated by relative magmatic quiescence (Barton et al., 1988; Barton, 1996; Ducea, 2001; Ducea & Barton, 2007). However, a picture of periodic magmatism in the Ross orogen emerges if the entire arc is considered (Fig. 2.7);

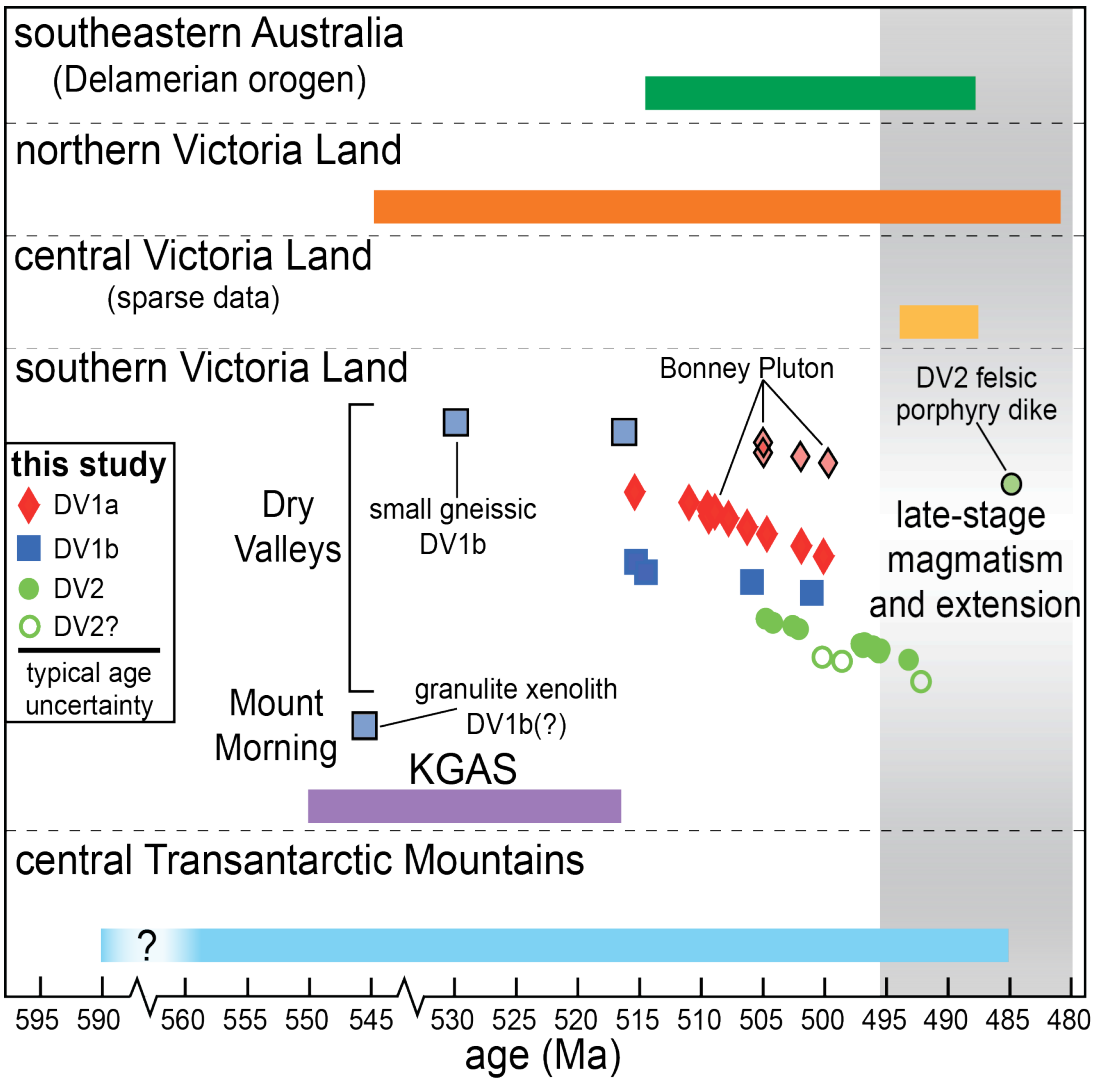

Figure 2.7 Summary diagram of published U-Pb zircon ages from different segments of the Ross-Delamerian orogen, spanning over 1800 km along-strike, emphasizing the short duration of magmatism in the Dry Valleys relative to other areas. Note the breaks in the horizontal scale. Samples from the Bonney Pluton range in age from ca. 509–499 Ma, demonstrating its composite nature. Lightly-shaded symbols with black outlines are from Encarnación and Grunow (1996), Cox et al. (2000), Allibone and Wysoczanski (2002), and Martin et al. (2014). Colored bars summarize U-Pb geochronology from the other segments of the orogen. Data are from the following sources: southeastern Australia—Foden et al. (2006, and references therein); northern Victoria Land—Black and Sheraton (1990) Fioretti et al. (2005), Bomparola et al. (2007), Tiepolo and Tribuzio (2008); central Victoria Land—Rocchi et al. (2009); Koettlitz Glacier Alkaline Suite (KGAS)—Rowell et al. (1993), Hall et al. (1995), Encarnación and Grunow (1996), Cooper et al. (1997), Mellish et al. (2002), Read et al. (2002), Cottle and Cooper (2006a, 2006b); central Transantarctic Mountains—Goodge et al. (1993a, 2004, 2012).

the abbreviated magmatism in the Dry Valleys records only one major high-flux episode.

Inheritance of ca. 550 Ma components (Fig. 2.5) records Ross-stage (magmatic?) zircon growth and/or recrystallization in the Dry Valleys area several tens of millions of years before the emplacement of the voluminous DV igneous suites. Several samples contain a range in concordant $^{206}Pb/^{238}U$ individual spot ages (>50 million years for some samples; see supplementary material of Hagen-Peter et al., 2015). Some dispersion of ages may be attributable to protracted zircon crystallization from a melt, but 50 million years is an unreasonably long period of time to support such a hypothesis. We interpret the spectra to represent inheritance of zircon grains from slightly older (tens of millions of years) sources. This indicates a complex intrusive history, with partial assimilation of the earliest emplaced plutons and/or juvenile lower crust into later magmas.

Potential magma sources

Several prominent observations arise from the zircon Hf data in Figure 2.6: 1) $\varepsilon Hf_{(i)}$ values of all samples from this study are negative (−0.3 to –7.2); 2) more felsic samples have a wider range and lower $\varepsilon Hf_{(i)}$ than mafic samples; 3) the range of $\varepsilon Hf_{(i)}$ broadens with decreasing age. Several scenarios potentially explain the negative $\varepsilon Hf_{(i)}$ values: 1) low-$\varepsilon Hf_{(i)}$ crustal reservoirs, which separated from the mantle at times indicated by the model ages of the samples, were the direct magma sources for the DV suites; 2) the DV suites were sourced from depleted mantle (DM), with a relatively radiogenic Hf isotopic composition, and subsequently assimilated a significant proportion of low-$\varepsilon Hf_{(i)}$ crust; 3) melts sourced from an enriched (or primitive) sub-continental lithospheric mantle (SCLM), with a sub-chondritic Hf isotopic composition, were contaminated by a subordinate amount of crust during magma

differentiation. There are essentially three end-member components involved in these hypotheses: DM, SCLM, and recycled crust (Proterozoic or older in this case), all of which are feasible constituents in the source of arc magmas. The contrasting hypotheses have bearing on the composition of the mantle wedge beneath the arc and on the relative roles of crustal growth versus recycling in the Dry Valleys area during the Ross orogeny. However, the Hf isotope data alone do not uniquely fit any of these potential scenarios.

The presence of enriched SCLM beneath the Ross orogen

The most mafic samples (~49–50 wt% SiO_2) have negative $\varepsilon Hf_{(i)}$ from –0.6 to –2.7. A viable interpretation is that the gabbroic (*sensu lato*) rocks were derived from partial melting in the mantle wedge beneath the arc. Alternatively, they could have been sourced from mafic lower crust with 1.5–1.6 Ga depleted-mantle model ages, however this would require *total fusion* of a gabbroic source. It is also possible that the gabbros are cumulates or the residuum of partial melting of an intermediate crustal source, and that the intermediate and felsic samples represent the extracted differentiates/partial melts. The most mafic DV1a sample (50 wt% SiO_2) has a high Mg# (74; not shown in Fig. 2.3) and very high Ni (120 ppm) and Cr (825 ppm) contents (not shown in Fig. 2.3; Appendix Table 4) suggesting a cumulate origin. However, the two DV2 suite samples with SiO_2 < 50 wt% have relatively low Mg# (~44; not shown in Fig. 2.3) and are relatively enriched in incompatible elements, such as Rb, Zr, and Ba (Fig. 2.3), and it is unlikely that they are cumulates. All of the mafic to intermediate samples (< 60 wt% SiO_2) range in $\varepsilon Hf_{(i)}$ from −0.3 to −4.0.

The composition of the mafic samples is consistent with derivation from an isotopically enriched SCLM beneath the arc. A depleted-mantle (DM) component would

have a radiogenic Hf composition ($\varepsilon Hf_{(i)}$ of +14.9 at 500 Ma, according to the model parameters of Griffin et al., 2000) that is not observed in any of the DV samples. The introduction of old crustal material (with low $\varepsilon Hf_{(i)}$) into the source region, perhaps through underthrusting of pelagic sediments or subduction erosion of the overriding plate, could have "contaminated" the Hf isotope composition of the resulting melts, potentially driving a DM-sourced melt toward a negative $\varepsilon Hf_{(i)}$.

To evaluate this effect, Figure 2.8 shows a binary mixing model between a basalt sourced from partial melting of DM and Proterozoic crustal material with low $\varepsilon Hf_{(i)}$. A binary mixing is perhaps oversimplified, as the heat budget in an isolated system would require fractional crystallization to accompany melting of assimilated crustal material (i.e., AFC mixing; DePaolo, 1981). However, the purpose of the model is to derive a first-order estimate of the proportion of old crust in the source necessary to drive a DM-derived melt to the Hf isotope composition observed in the most mafic DV samples. The $\varepsilon Hf_{(i)}$ of DM in the model was fixed at +14.9 (the value at 500 Ma based on the parameters of Griffin et al., 2000) and Hf concentration of a melt sourced from the DM is fixed at 2 ppm, based on the average of 12 samples of island arc basalts from White and Patchett (1984). The conditions, and therefore derivatives, of partial melting beneath island arcs may be different from those produced in continental arcs, but these island arc basalts, with highly radiogenic Hf (εHf ranging from +9.1 to +15.1; White & Patchett, 1984), are demonstrably sourced from the DM and are therefore an appropriate analog for this end-member. The Hf concentration and isotope composition of the "old crust" end-member are difficult to estimate because Precambrian cratonic rocks are not exposed in southern Victoria Land. The Hf isotope composition of the crustal component was estimated from the Nd isotope composition of

Skelton Group metasedimentary rocks reported by Cox et al. (2000). The least radiogenic sample from that study has $\varepsilon Nd_{(i)} = -10.2$, which corresponds to an $\varepsilon Hf_{(i)} = -10.9$ (T_{DM}^{C} = 2.1 Ga) when converted using the regression of the Hf-Nd "terrestrial array" of Vervoort and Blichert-Toft (1999; $\varepsilon Hf = 1.36\varepsilon Nd + 3$). We chose the lowest-$\varepsilon Hf_{(i)}$ value in order to estimate a *minimum* amount of Proterozoic crust necessary to drive a DM-sourced melt to the negative $\varepsilon Hf_{(i)}$ values of the mafic DV samples. The Hf concentration of the crustal end member was set at values of 1.9, 3.7, and 5.3 ppm, estimates for mafic lower crust, intermediate "bulk" continental crust, and upper crust, respectively (Rudnick & Gao, 2003).

The model demonstrates that ~35% by mass of Proterozoic crust in the source would be required to depress the Hf composition of a DM-derived melt to the negative $\varepsilon Hf_{(i)}$ values observed in the DV samples (Fig. 2.8). An even greater proportion of crust would be required if mixing involved crust with a lower Hf concentration (~60% of crust with 1.9 ppm Hf; Fig. 2.8). Such a large proportion of crustal material in the source would have significantly affected the bulk composition of the resulting melt, and, accompanied by fractional crystallization, would have shifted the melts to higher SiO_2 concentrations.

A qualitative assessment of Nd-Sr isotope data from along the Ross orogen supports the presence of an enriched SCLM beneath the arc (Fig. 2.9). Parabolic trends of the GHI samples suggest mixing between old crust with low $\varepsilon Nd_{(i)}$ and high $^{87}Sr/^{86}Sr$ and a juvenile component with higher $\varepsilon Nd_{(i)}$ and low $^{87}Sr/^{86}Sr$. However, the juvenile component in each segment of the orogen only extends to moderately high $\varepsilon Nd_{(i)}$ and low $^{87}Sr/^{86}Sr$, far from the composition of depleted mantle sources. This is consistent with the interpretation of Rocchi et al. (2009), that late-stage lamprophyres with low $\varepsilon Nd_{(i)}$ in central Victoria Land were sourced from enriched SCLM. The Vanda dike swarm (including lamprophyres and felsic

porphyries) and DV2 suite in the Dry Valleys may be the equivalent the Vegetation lamprophyres and Irizar granites of Rocchi et al. (2009).

Figure 2.10 shows Hf isotope evolution trajectories for several hypothetical mechanisms for the enrichment of the SCLM beneath the Ross orogen. The metasomatism may have occurred at some time (or progressively) prior to the Ross orogeny, decreasing the Lu/Hf ratio of the SCLM beneath the edge of the East Antarctic craton. Over time, this reservoir, with a low Lu/Hf ratio, could develop a low-εHf composition that is indistinguishable from old crust in terms of radiogenic isotopes. Alternatively, "young" metasomatism may have occurred during the Ross orogeny, decreasing the εHf of the SCLM through the introduction of crust-derived Hf through fluid metasomatism, subduction of pelagic sediments, or subduction erosion of the overriding continental plate. Zircon oxygen isotope data could provide useful information about the nature of the mantle source but are currently unavailable.

Crustal recycling and temporal trends

If the felsic DV samples were direct differentiates of the mafic samples, the data should fall on horizontal trajectories on the $\varepsilon Hf_{(i)}$ versus SiO_2 diagram in Figure 2.6a (e.g., Fig. 2.9 of Rocchi et al., 2009), as fractionation of heavy Hf isotopes would be negligible during partial melting and fractional crystallization processes. The wider range and lower $\varepsilon Hf_{(i)}$ in the more evolved samples (Fig. 2.6a) suggests some involvement of old (low-$\varepsilon Hf_{(i)}$) crust in the evolution of the DV magmas – crustal assimilation increased the silica-content and "contaminated" the Hf isotope composition of the melts.

Archean and Proterozoic cratonic rocks are exposed only in the Miller and Geologist

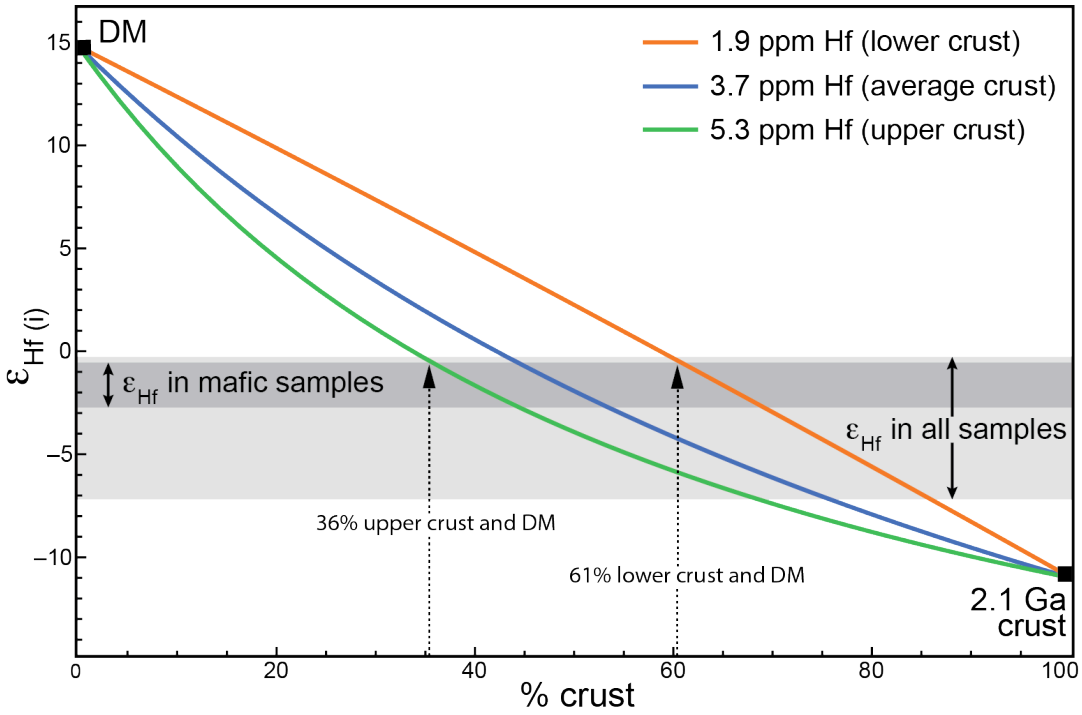

Figure 2.8 Binary mixing models between depleted-mantle (DM) and crustal source components illustrate a wide range of mixing scenarios that could produce the Hf isotope values measured in the DV samples. The parameters of the end members are explained in the text. Two hypothetical mixing scenarios that could explain the range of $\varepsilon Hf_{(i)}$ in the mafic (< 50 wt% SiO_2) DV samples are annotated and discussed in the text. The models demonstrate that a significant proportion of low-$\varepsilon Hf_{(i)}$ crust in the source region would be necessary to "contaminate" the Hf isotope composition of a DM-derived melt to the values observed in the DV samples.

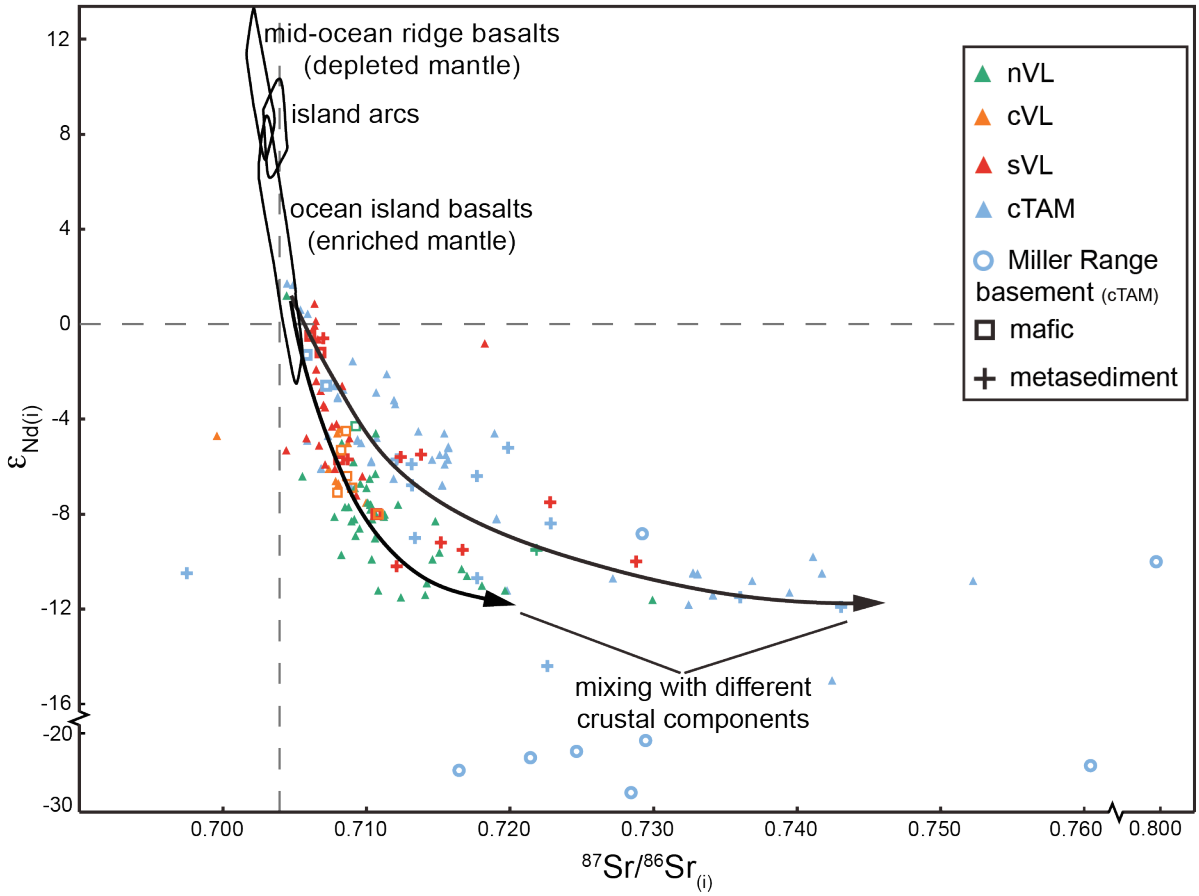

Figure 2.9 A compilation of published Nd and Sr isotope data for Granite Harbour Intrusives from different segments of the Ross orogen. The dashed reference lines are at the isotopic values of bulk earth at the time of crystallization of the intrusives (ca. 500 Ma). The ellipses show simplified fields of several common igneous rock types for reference (from Jacobsen and Wasserburg, 1979). The arrows show qualitative mixing trajectories between an isotopically-enriched mantle source and crustal components with distinct isotopic compositions. Note the breaks and changes in scale in order to display the samples of the Miller Range (central Transantarctic Mountains) basement. The data are from the following sources: northern Victoria Land (nVL)—Borg et al. (1987), Armienti et al. (1990), Tonarini and Rocchi (1994), Rocchi et al. (1998), central Victoria Land (cVL)—Rocchi et al. (2009) southern Victoria Land (sVL)—Borg and DePaolo (1994), Hall et al. (1995), Cooper et al. (1997), Cox et al. (2000), Mellish et al. (2002), Cottle and Cooper (2006a, 2006b); central Transantarctic Mountains (cTAM)—Borg et al. (1990), Borg and DePaolo (1994), Goodge et al. (2008, 2012).

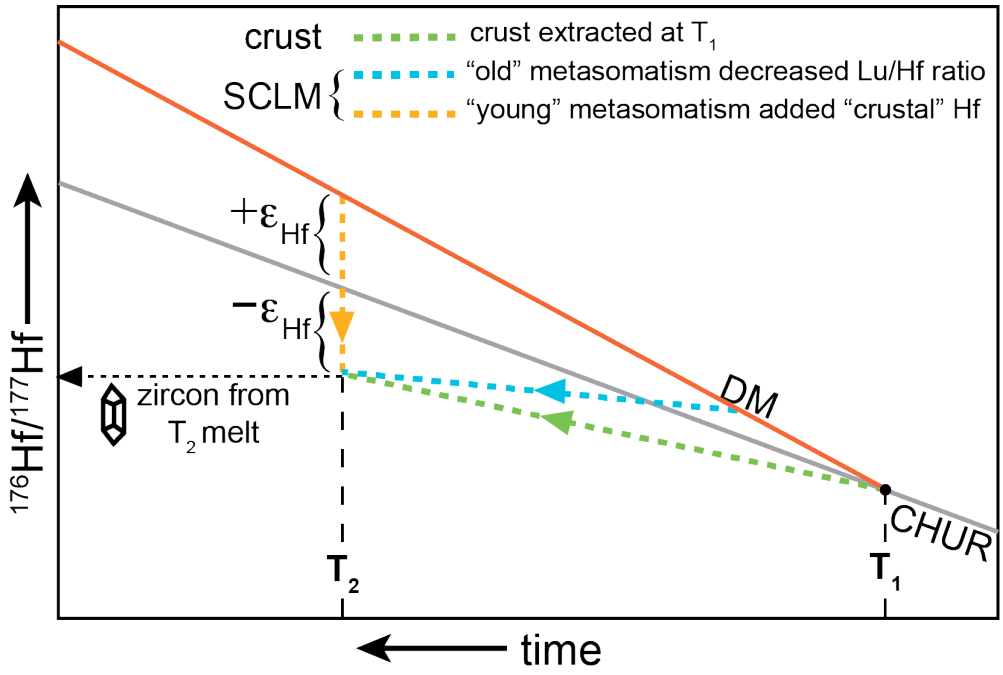

Figure 2.10 A diagram showing the hypothetical Hf isotope evolution of several reservoirs with different Lu/Hf ratios. Time T_1 represents the extraction of continental crust from a primitive mantle, at which time the depleted mantle (DM) and continental crust trajectories diverge. Time T_2 represents a second event of melt generation during continental arc magmatism, analogous to the Ross orogeny. These trends demonstrate two scenarios by which the sub-continental lithospheric mantle (SCLM) may develop a Hf isotope composition that may be interpreted as old crust. One scenario involves a decrease in the Lu/Hf ratio of the SCLM through "old" metasomatism prior to T_2. Note that enrichment of the SCLM may be a continuous process; it is portrayed here as a discrete event for simplicity. The other scenario involves the introduction of low-εHf crustal material into the source region at T_2 through metasomatic fluids, sediment subduction, or subduction erosion of the overriding plate. CHUR—chondritic uniform reservoir.

ranges in cTAM (Goodge & Fanning, 1999). The nature of the crust underlying the metasedimentary rocks and granitoids of the Ross orogen in sVL is known only indirectly through detrital zircon and isotopic studies. Skelton Group metasedimentary rocks have detrital zircon age spectra with strong Grenville (ca. 1050 Ma) and subordinate Mesoproterozoic and Archean peaks (Wysoczanski & Allibone, 2004). However, the provenance of the Skelton Group sediments is not well constrained and the detrital zircons may represent distal sources. Neodymium depleted-mantle model ages for the GHI in the Dry Valleys range from 1.1–2 Ga (Cox et al., 2000), but should only be loosely interpreted as the age range of underlying crust. The presence of Proterozoic zircon xenocrysts in some samples (Figs. 2.2, 2.5), particularly those of granitic composition, is direct evidence of the assimilation of old crust during the evolution of the DV suites. The assimilated material may have been some combination of cratonic rocks in the lower crust and Skelton Group rocks near the level of pluton emplacement.

The broadening of the array of $\varepsilon Hf_{(i)}$ in younger samples (Fig. 2.6b) may reflect a thickening of the crustal column through which the magmas ascended or underplating of supracrustal (low-$\varepsilon Hf_{(i)}$) material into the source region. Refertilization of the source region beneath continental arcs by periodic underthrusting of evolved continental material has been demonstrated in the North American Cordillera (e.g., DeCelles et al., 2009) and in the Australian Tasmanides (Kemp et al., 2009). Those periods were associated with negative excursions in εNd and εHf in concomitant intrusions. The pattern in Figure 2.6b seems to reflect a portion of one cycle of thickening and source refertilization. The conundrum here is that the earlier gneissic plutons in the Dry Valleys (including the Bonney pluton), which have a more restricted range and higher $\varepsilon Hf_{(i)}$ (Fig. 2.6b), were likely emplaced during contraction

across the arc (Cox, 1993). The younger, non-foliated DV2, were interpreted to have been emplaced in a post-subduction extensional regime (Smillie, 1992; Allibone et al., 1993b). However, Allibone et al. (1993b) suggested that the DV2 suite plutons had various sources, and this suite has a wide range of $\varepsilon Hf_{(i)}$. The mafic samples with higher $\varepsilon Hf_{(i)}$ (Fig. 2.6a) may have been sourced from the lithospheric mantle, while the evolved samples with lower $\varepsilon Hf_{(i)}$ may have been sourced primarily from fertile lower crust.

CONCLUSIONS

Whole-rock geochemistry, U-Pb zircon geochronology, and Hf isotopic data for 31 samples from across the Dry Valleys area yield new insights into the magmatic processes that operated in the southern Victoria Land segment of the Ross orogen during the early Paleozoic. Geochronology reveals that the Dry Valleys segment of the arc was predominantly constructed in a relatively short pulse (ca. 23 million years) of magmatism from 515–492 Ma. The style of magmatism transitioned from subduction-related to post-tectonic at ca. 505 Ma, which we interpret as a response to the cessation of subduction. Age spectra for individual samples suggest complex intrusion dynamics and inheritance within individual plutons. Mafic samples show geochemical and isotopic evidence for derivation from an enriched SCLM source. Large granitic bodies may have had a similar source but involved crustal assimilation during their evolution. The crustal component in the DV suites increased over time, perhaps reflecting crustal thickening or the underthrusting of fertile continental crust into the source region. The isotopic composition of the GHI along the Ross orogen suggests the presence of enriched SCLM beneath the entire arc. Melts derived from this source may be incorrectly interpreted as derivatives of crustal melting based on isotopic

composition alone.

ACKNOWLEDGEMENTS

Funding for this work was provided by National Science Foundation grant ANT-1043152 to J.M. Cottle. We thank the New Zealand Institute of Geological and Nuclear Science (GNS) for providing samples for this study. We also thank Michael Flowerdew, Alan Cooper, two anonymous reviewers, and the editor, John Goodge, for providing many useful suggestions that significantly improved this article.

III. Geochronologic, isotopic, and geochemical insights into compositionally diverse continental arc magmatism in the Ross orogen, Antarctica

INTRODUCTION

The processes of subduction and associated magmatism have significant influence on the geochemical evolution of the crust and mantle. Subduction recycles crust back into the mantle, re-enriching it in incompatible elements (Pearce, 1983; Plank & Langmuir, 1993; Pearce & Peate, 1995). Island arcs above subduction zones are important areas of crustal generation from mantle-derived melts (e.g., Gill, 1981). Continental arcs are settings of "distillation" of pre-existing continental crust (e.g., Ducea & Barton, 2007) and may also be important settings of crustal growth (e.g., Rogers & Hawkesworth, 1989). Classic models for the source of arc magmas invoke an H_2O-fluxed mantle wedge (Gill, 1981; Davies & Bickle, 1991) with variable contribution from the subducted slab and sediments. The magmas then evolve along calc-alkaline or tholeiitic trends with products ranging from basalt to rhyolite. As Ducea & Barton (2007) noted, such models are fundamentally based on island arcs. Processes are complicated in continental settings due to the ascent of magmas through a thick column of continental lithosphere, accompanied by stalling, fractionation, and assimilation. The result is compositional and isotopic variability that is not adequately explained by traditional models for subduction-related magmatism.

Extensive exposure of continental arc granitoids associated with the Neoproterozoic–early Paleozoic Ross orogeny of Antarctica (Fig. 3.1) provides an exceptional opportunity to study variations in the character of magmatism along a major continental arc. Along a ~500 km-long segment of the arc in southern Victoria Land (sVL), igneous rocks display gross

petrologic and geochemical differences, with the conspicuous occurrence of a suite of alkaline rocks adjacent to large complexes of sub-alkaline, subduction-related granitoids. Zircon U-Pb and Hf data from ~70 samples from sVL provide the densest geochronologic and isotopic dataset to-date for igneous rocks in the Ross orogen. In this study, we explore: 1) the variability in the timing and composition of magmatism across southern Victoria Land, 2) potential differences in magma source that can explain the compositional variability, 3) the relative roles of crustal growth and reworking through arc magmatism.

GEOLOGIC BACKGROUND

The Ross orogen is a belt of deformed and metamorphosed sedimentary rocks and granitic plutons exposed along the Transantarctic Mountains (Fig. 3.1). The orogen spans ~3500 km across Antarctica and extends into southeastern Australia and southwestern New Zealand (Foden et al., 2006). Deformation, metamorphism, and magmatism in the Ross orogen occurred in response to the subduction of paleo-Pacific oceanic lithosphere beneath the margin of the East Antarctic Craton during the late Neoproterozoic– early Paleozoic (summarized in Stump, 1995). Igneous rocks exposed along the orogen are collectively referred to as the Granite Harbour Intrusive Complex (Fig. 3.1; Gunn & Warren, 1962). Hagen-Peter et al. (2015) summarized the existing geochronology on the Granite Harbour Intrusive Complex in three major physiographic segments of the orogen— northern Victoria Land, southern Victoria Land, and the central Transantarctic Mountains, spanning over 1800 km.

In the southern Victoria Land segment (sVL) of the Ross orogen, the largest ice-free area of Antarctica, metasedimentary rocks of the Skelton Group host plutonic rocks of the

Granite Harbour Intrusive Complex (Fig. 3.1; Cox et al., 2012). The igneous and metamorphic basement is unconformably overlain by Devonian− Triassic siliciclastic sedimentary rocks of the Beacon Supergroup (summarized in Barrett, 1981), and both the basement and cover rocks were intruded by the extensive Ferrar dolerite sills in the Jurassic (Heimann et al., 1994; Encarnación et al., 1996). The composition of the Granite Harbour Intrusives in sVL is highly variable, both in terms of petrology and geochemistry. In this study, we divide these igneous rocks into three groups based on their general petrologic character and geographic distribution: 1) the Dry Valleys area, north of the Walcott Glacier, 2) the Koettlitz Glacier Alkaline Suite, between the Walcott and Mulock Glaciers, and 3) the Byrd and Darwin Glacier areas, between the Mulock and Byrd Glaciers (Fig. 3.2). It should be noted that these broad areas do not perfectly delineate the differences in magmatic character across sVL, but they generally envelope magmatic rocks of particular character. More detailed descriptions of the magmatic character and variability within each area are given below.

Dry Valleys Area

The Dry Valleys area (DV) is defined here as the area between the Fry and Walcott Glaciers (Figs. 3.2, 3.3). Areally extensive plutonic rocks in this area, emplaced into migmatitic metasediments of the Skelton Group (Fig. 3.4a), have been divided into three magmatic suites based on field characteristics (e.g., pluton elongation, contacts with country rock, internal fabrics, etc.; Fig. 3.4), age, petrology, and geochemistry (Smillie, 1992; Allibone et al., 1993a,b). The DV1a, including the ~1000 km^2 Bonney Pluton, and DV1b suite plutons are typically elongate in the NW-SE direction and are interpreted as subduction-related

granitoids emplaced in a regime of contraction across the arc (Smillie, 1992; Allibone et al., 1993a,b). The DV2 suite rocks are have been interpreted as "post-tectonic" granitoids, emplaced at pressures as low as 1.2 kbars (~4 km) after the cessation of subduction (Smillie, 1992; Allibone et al., 1993a,b). Magmatism in this area was relatively short-lived, with a vast majority of the exposed plutonic rocks emplaced from 515−492 Ma (Hagen-Peter et al., 2015).

Koettlitz Glacier Alkaline Suite

The Koettlitz Glacier Alkaline Province (KGAS) is defined here as magmatic rocks within the area between the Walcott and Mulock Glaciers (Figs. 3.2, 3.5). Igneous rocks of the KGAS differ from those in adjacent regions owing to their distinctly alkaline composition (Read et al., 2002; Read, 2010). These rocks include calcite-bearing nepheline syenites, carbonatites, alkaline gabbros, and A-type granites, as well as sub-alkaline rocks (Figs. 3.6, 3.7). The igneous rocks are variably deformed, ranging from undeformed (e.g., Fig. 3.7; RG11-180; 234; 259) to orthogneiss with strong fabrics defined by aligned micas and extensively recrystallized quartz (e.g., Fig. 3.7; RG11-24; 212). The intrusions in the KGAS are relatively small (typically < 10 km^2) compared to the dominantly sub-alkaline DV plutons. The southern extent of the KGAS is currently defined by an A-type granite that crops out on the north side of the Mulock Glacier (Fig. 3.2; Cottle & Cooper, 2006a). Published geochronology data suggest that magmatism in the KGAS occurred ca. 551−517 Ma (Rowell et al., 1993; Encarnación & Grunow, 1996; Cooper et al., 1997; Mellish et al., 2002; Read et al., 2002; Cottle & Cooper, 2006a). In an unpublished PhD thesis, Read (2010) determined that magmatism started slightly earlier at ca. 557 Ma and persisted until ca. 511

Ma.

Byrd and Darwin Glacier Areas

The Byrd and Darwin Glaciers area (BG) is defined here as the area between the Mulock and Byrd Glaciers (Figs. 3.2, 3.8, 3.9). The Ross-age basement in BG consist of granitoids, mafic, and minor ultramafic rocks hosted in the migmatitic metasedimentary rocks of the Horney Formation (Borg et al., 1989; Stump et al., 2006; Carosi et al., 2007). Large granitoid bodies are variably strained, from relatively undeformed with magmatic alignment of K feldspars (Fig. 3.10c) to highly strained orthogneisses (Figs. 3.11a–g, Fig. 12; DG12-118; 230; 182), and cut by deformed and undeformed leucocratic dikes as well as lamprophyres (Figs. 3.11j–l). The granitoids have been variably divided into different magmatic suites (Encarnación & Grunow, 1996; Simpson & Cooper, 2002), though the interpretations of BG area samples in this study are largely independent of this framework. Mafic plugs and small plutons, including the ~ 0.5 km^2 layered Fontaine Pluton (Cottle & Cooper, 2006b), are common (Figs. 3.9, 3.10). Sparse geochronology on igneous rocks in the BG area suggests that magmatism spanned ca. 547–507 Ma (Encarnación & Grunow, 1996; Cottle & Cooper, 2006b; Stump et al., 2006; Carosi et al., 2007).

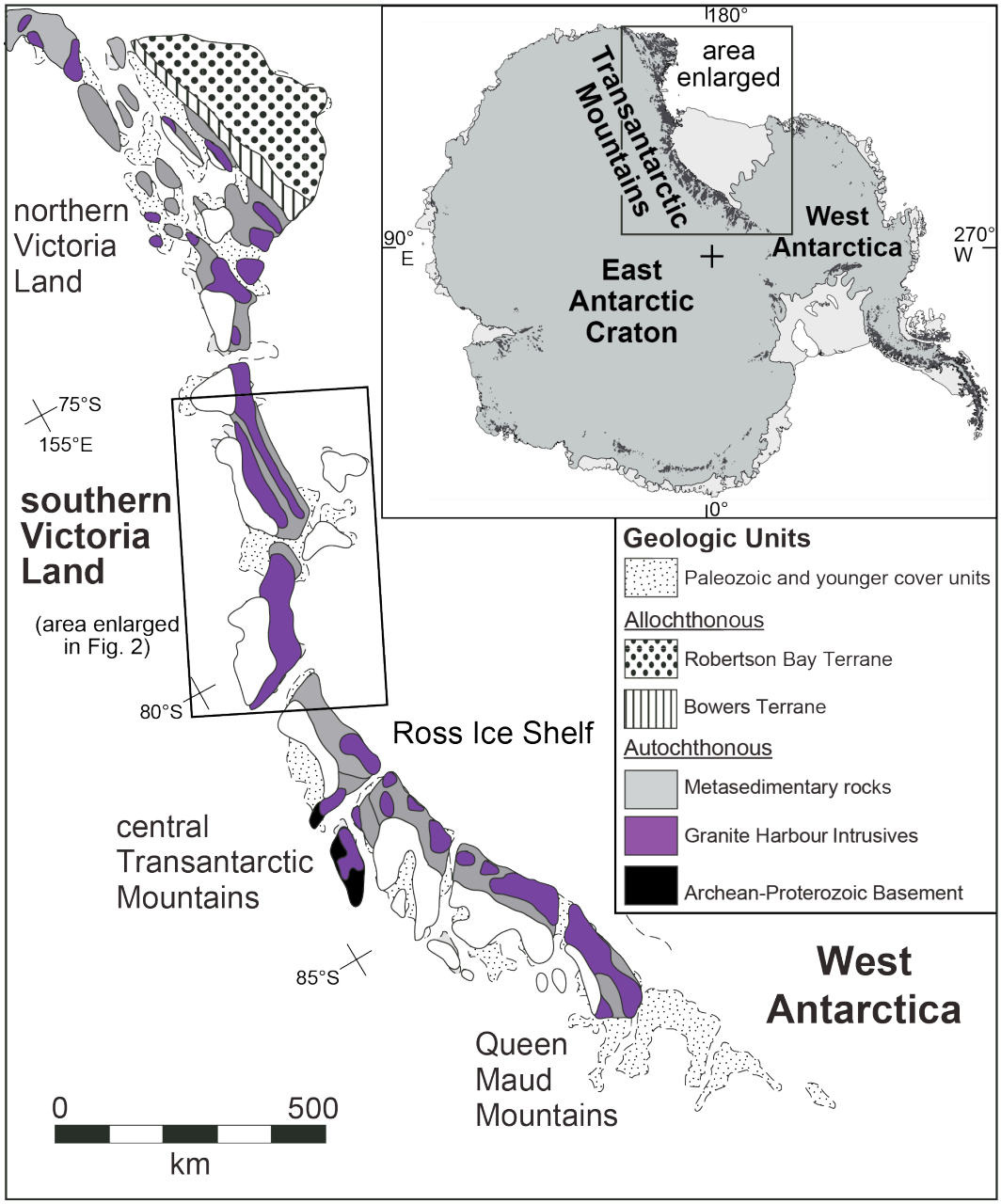

Figure 3.1 Simplified geologic map of metamorphic and igneous rocks of Ross orogen, exposed in the Transantarctic mountains (modified from Goodge, 2007). Igneous rocks of the Granite Harbour Intrusives (GHI) were emplaced into supracrustal metasedimentary rocks along the Antarctic margin. The only exposed contacts between GHI and Archean and Proterozoic basement rocks are in the central Transantarctic Mountains.

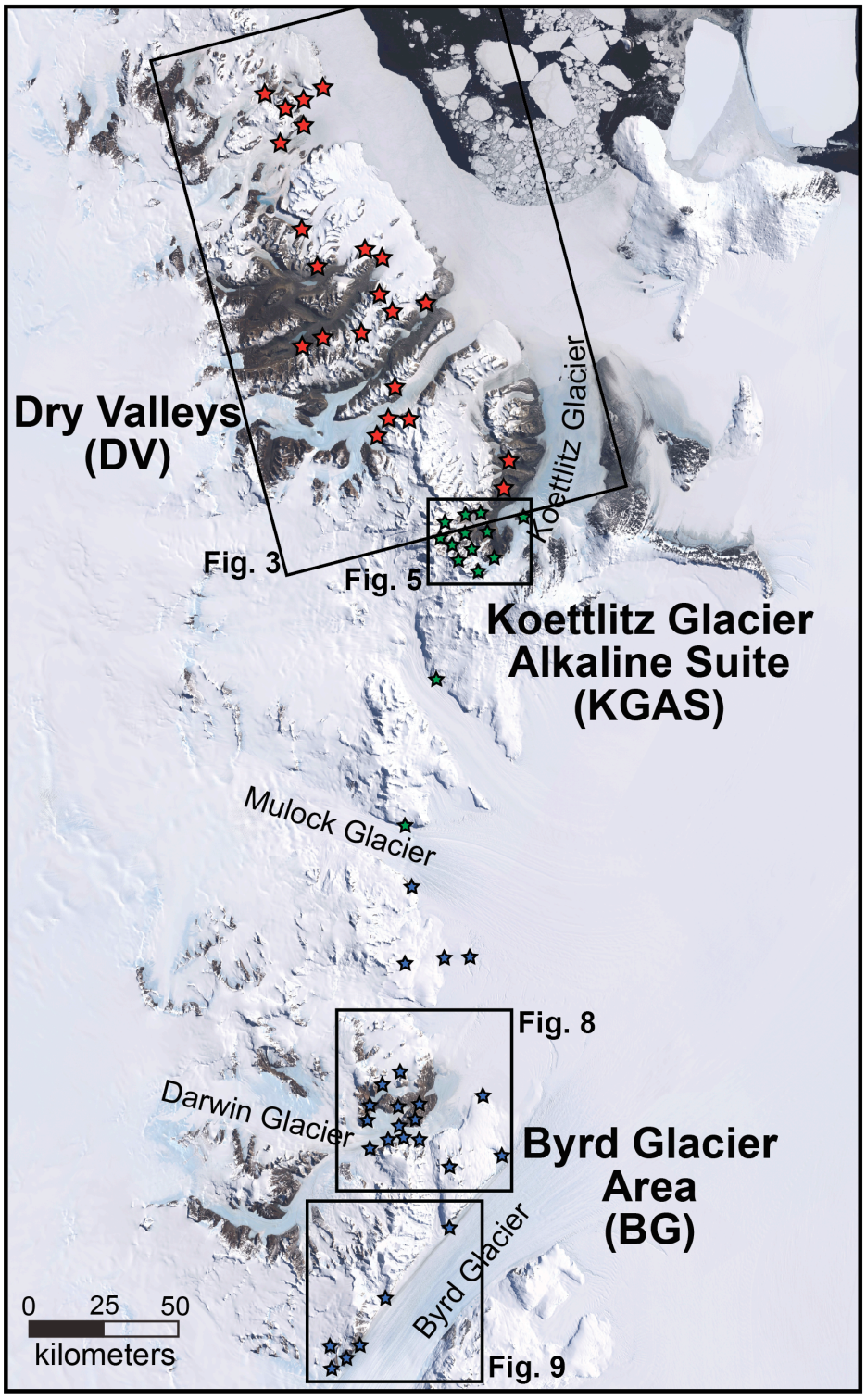

Figure 3.2 Satellite image of southern Victoria Land showing the division of the DV, KGAS, and BG areas. The distribution of samples from this study are shown by stars of different colors. Multiple samples were collected at many of the sites, and so the actual number of samples exceeds the number of stars. Four outlined areas show the areas enlarged in geologic maps in Figures 3.3, 3.5, 3.8 and 3.9.

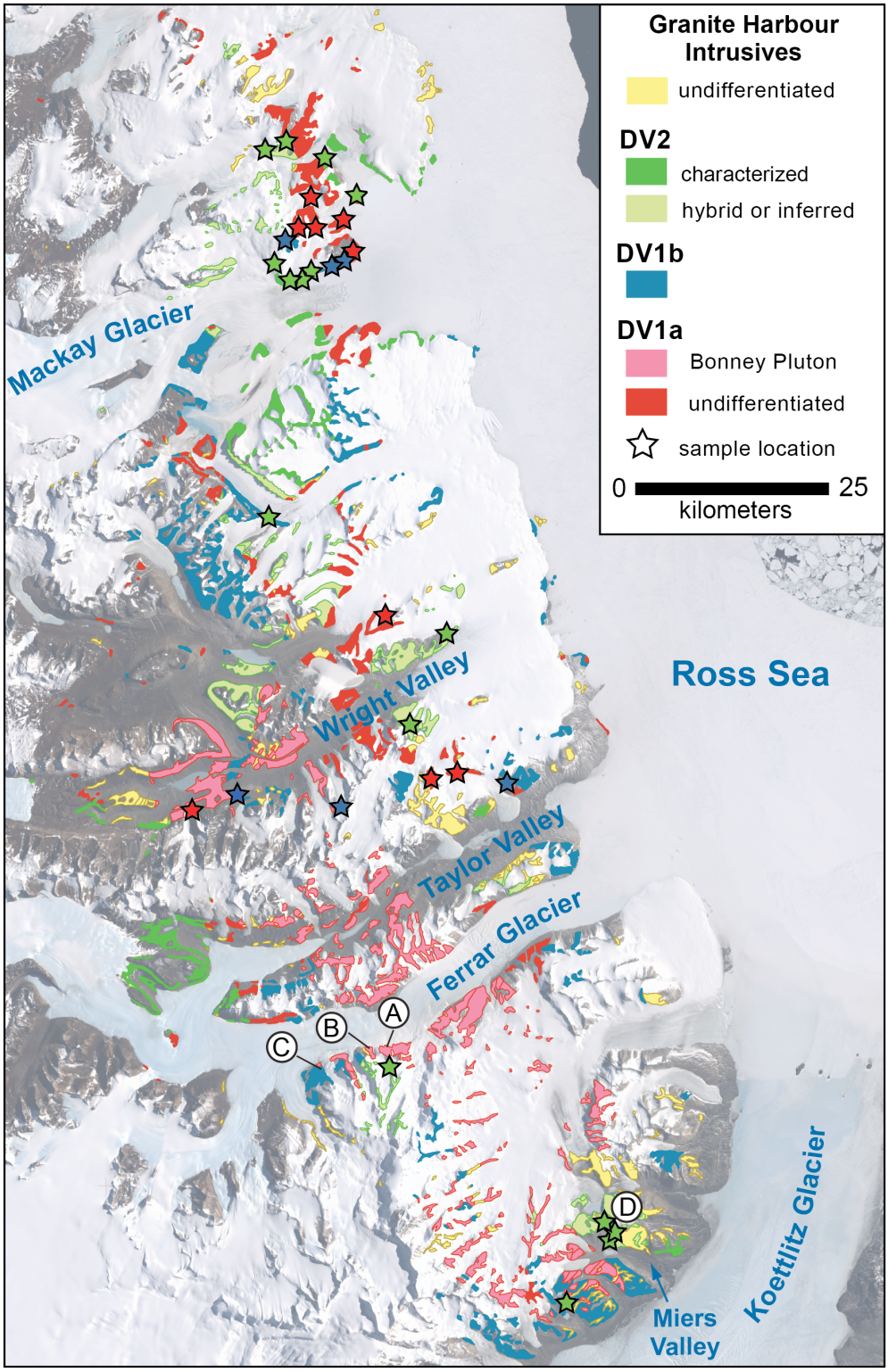

Figure 3.3 Simplified geologic map of the Granite Harbour Intrusives in the Dry Valleys area (modified from Cox et al., 2012). Metamorphic and cover units are removed to emphasize the distribution of igneous rocks. The colors correspond to different magmatic suites.

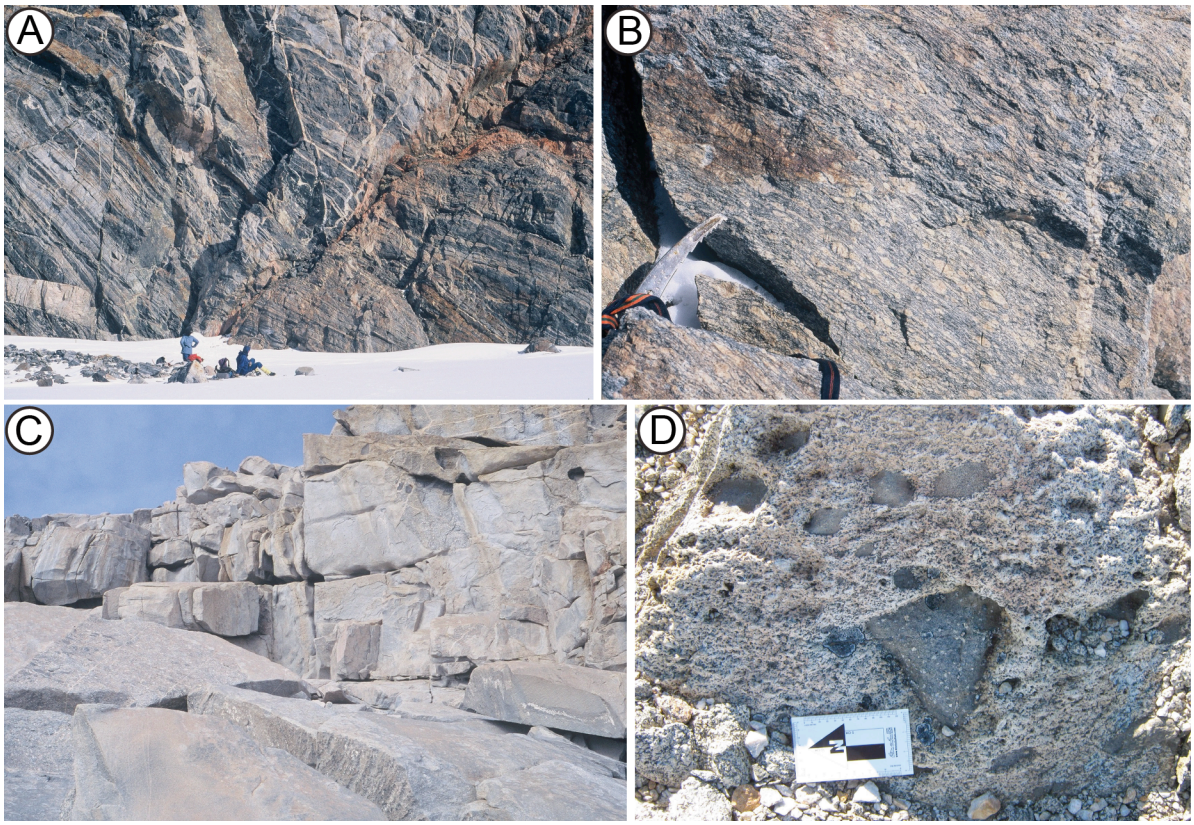

Figure 3.4 Field photos of different rock types in the Dry Valleys area. (A) Migmatitic paragneiss of the Skelton Group pervasively intruded by leucogranite dikes and sills. (B) Augen gneiss fabric in a texturally-old component of the Bonney Pluton. (C) Massive equigranular granite of the Hedley Pluton with xenoliths of more-coarse, gneissic granite from the Bonney Pluton. (D) Porphyritic diorite enclaves within an undeformed granite.

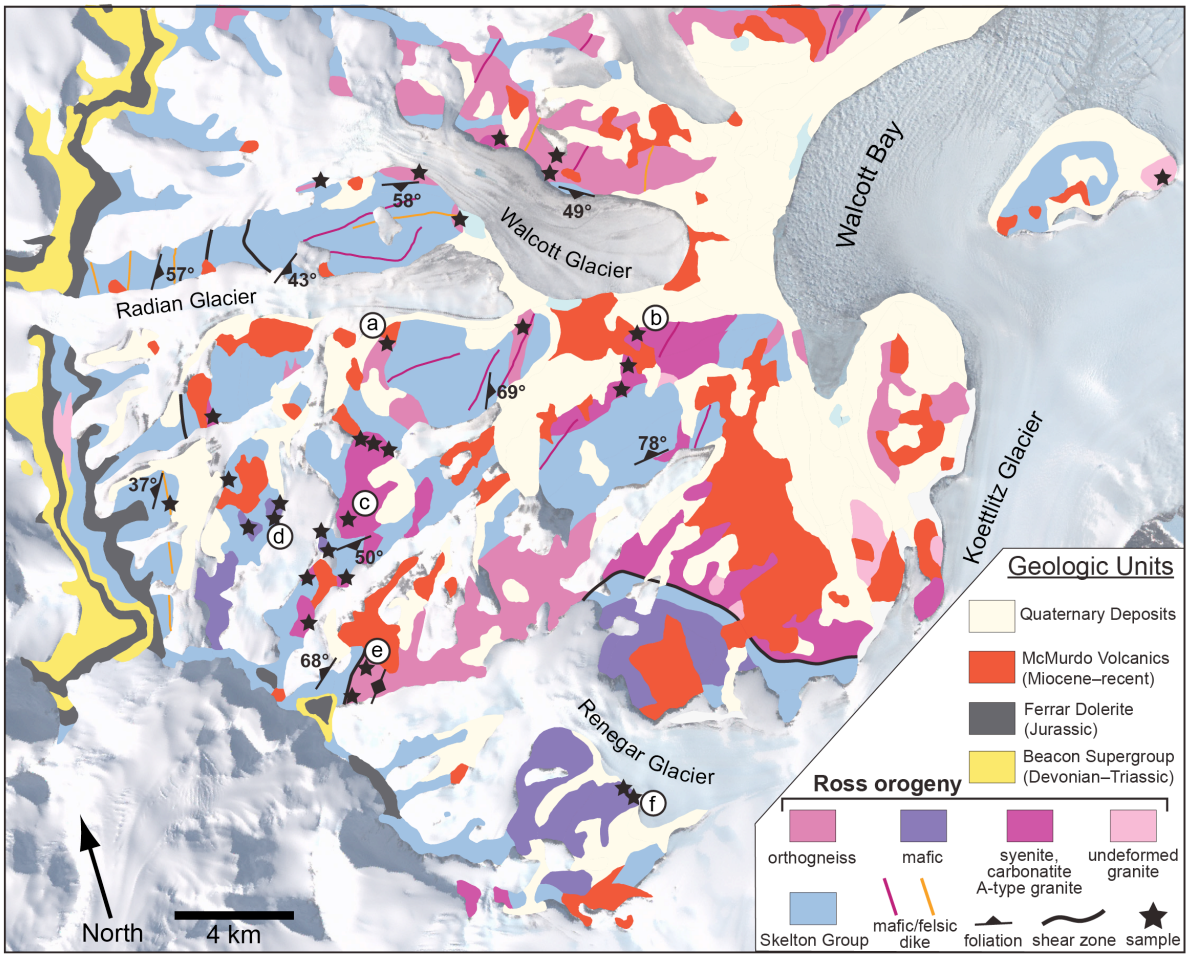

Figure 3.5 Geologic map of the KGAS in the Walcott Glacier area (modified from Cox et al., 2012). Alkaline mafic rocks, syenite, A-type granite, and carbonatite, as well as sub-alkaline orthogneiss and granite, were emplaced into metasedimentary rocks of the Skelton Group. Approximately 250 samples were collected in this area; the stars mark locations of samples for which geochemical, geochronologic, and/or isotopic data are presented. The circles with letters show the locations of the field photographs shown in Figure 3.6.

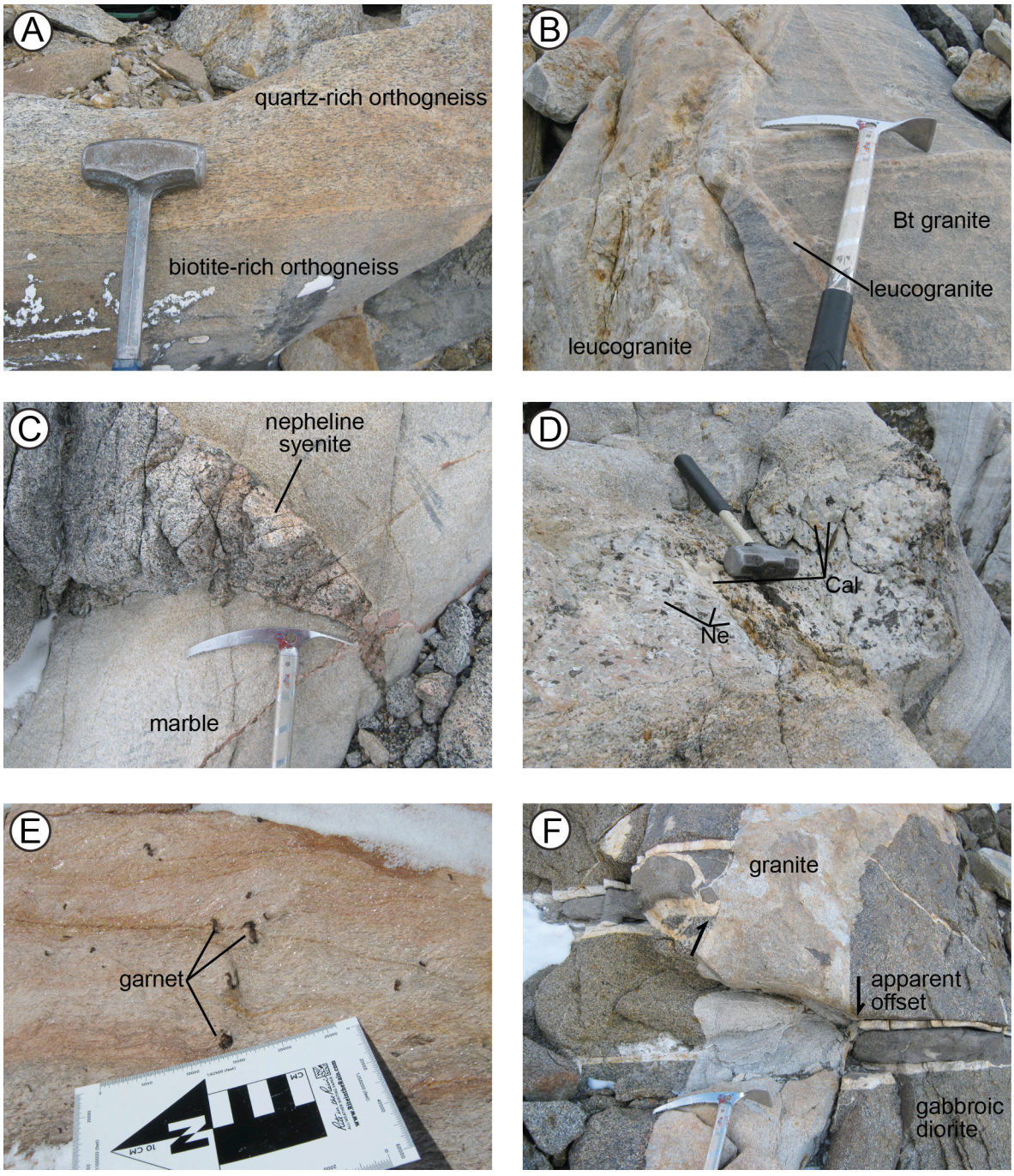

Figure 3.6 Field photos of different igneous rock types in the KGAS. (A) Compositional layering in a biotite orthogneiss. (B) Gneissic banding in an A-type granite cut by a several generations of leucocratic dikes. (C) Tapered nepheline syenite dike cutting marble. (D) Very coarse-grained carbonatite dike with large calcite (Cal) and nepheline (Ne) grains cutting marble. (E) Two-mica orthogneiss with strained Z-shaped garnets. (F) Coarse-grained gabbroic diorite cut 2–3 cm-wide leucogranite sills and ~30 cm-wide granite dike. A ~10 cm-wide layer of fine-grained diorite in between two leucogranite sills is apparently offset across the granite dike.

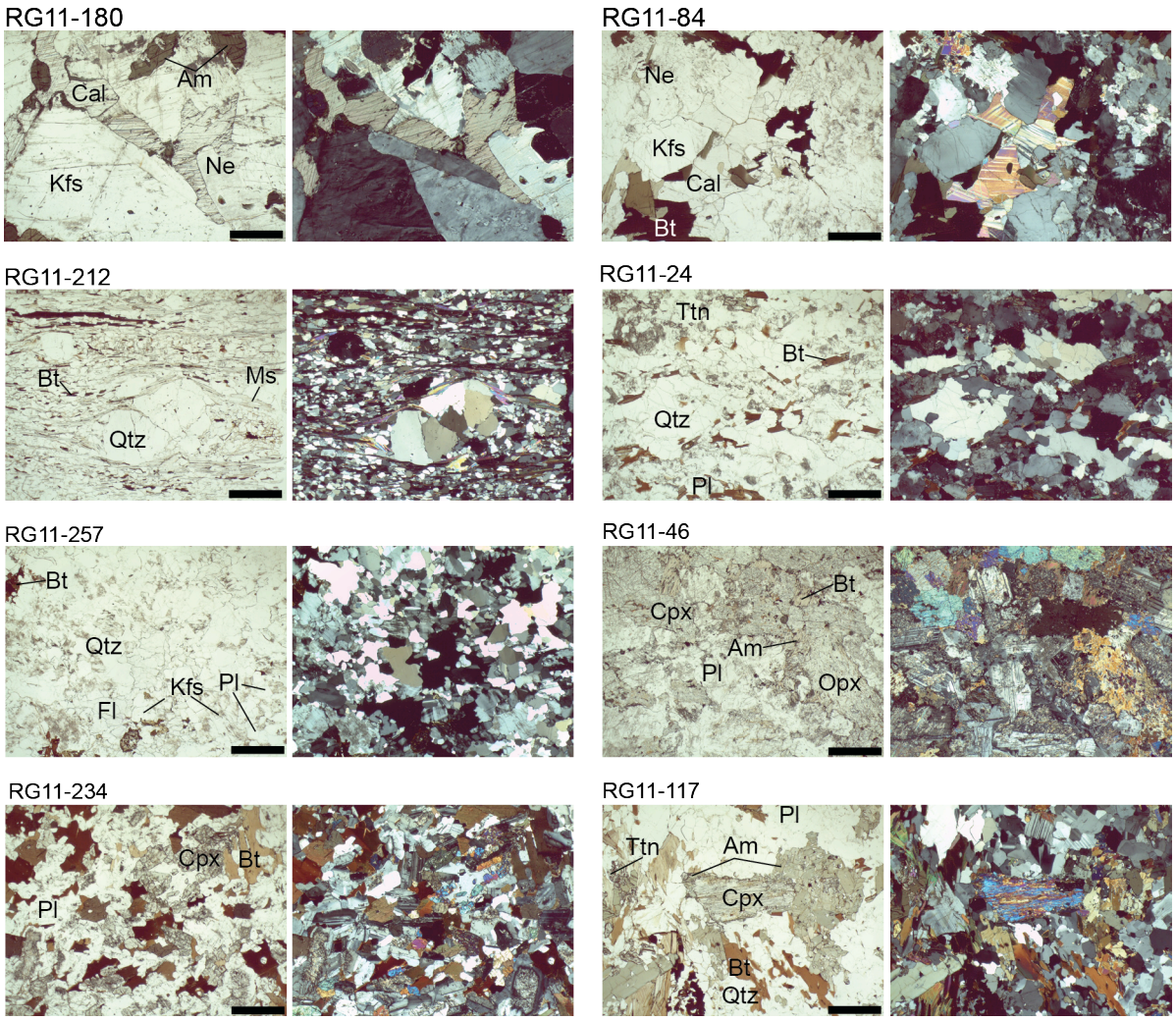

Figure 3.7 Photomicrographs of igneous rocks from the KGAS area. RG11-180: Calcite (Cal) intergrown with potassium feldspar (Kfs) and nepheline (Ne) in a Cal-bearing Ne syenite; RG11-84: Cal intergrown with Kfs, Ne, and biotite (Bt) in a Cal-bearing Ne syenite; RG11-212: Sigmoidal quartz (Qtz) porphyroclasts in an extensively recrystallized Bt + garnet + muscovite (Ms) orthogneiss; RG11-24: Recrystallized Qtz and plagioclase (Pl) in a granitic orthogneiss; RG11-257: Igneous flourite in a leucogranite; RG11-46: Altered clinopyroxene (Cpx) and orthopyroxene (Opx) intergrown with Pl and minor amphibole; RG11-234: Cpx intergrown with Pl and Bt; RG11-117: Cpx grain with an Am corona in a diorite. All scale bars are 1 mm.

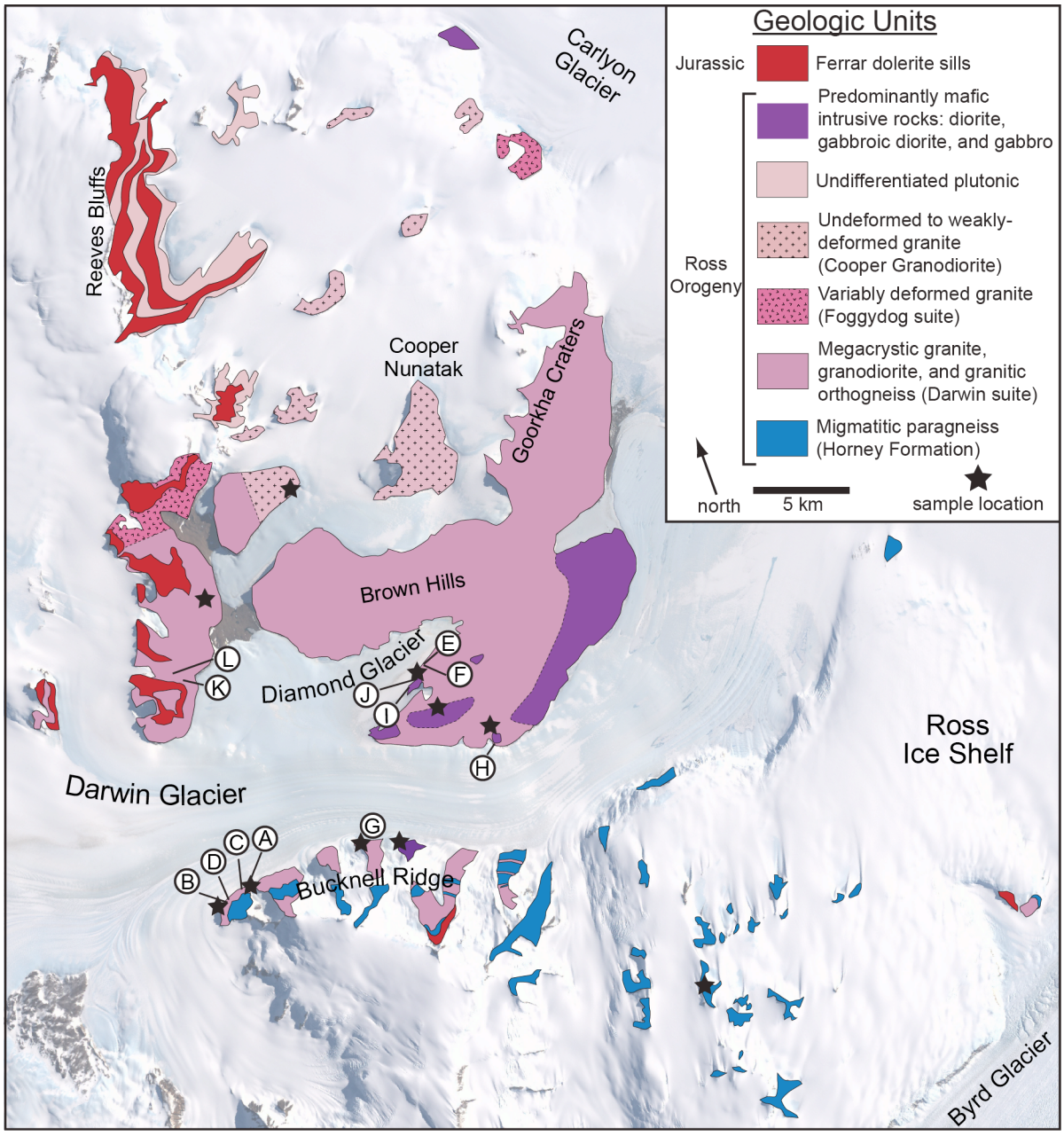

Figure 3.8 Simplified geologic map of the Darwin Glacier area (modified from Cottle, 2002; Simpson & Cooper, 2002; Carosi et al., 2007). Granitic and granodiorite rocks, including orthogneisses with variable fabric development are grouped together. Large areas of diorite and gabbroic diorite are mapped as separate, predominantly-mafic units. Stars show the locations of samples with geochemistry, geochronologic, and/or isotopic data from this study. Multiple samples were collected in the vicinity of the stars on the map, but only a single star is plotted for clarity. Letters show the locations of corresponding field photographs shown in Figure 3.11.

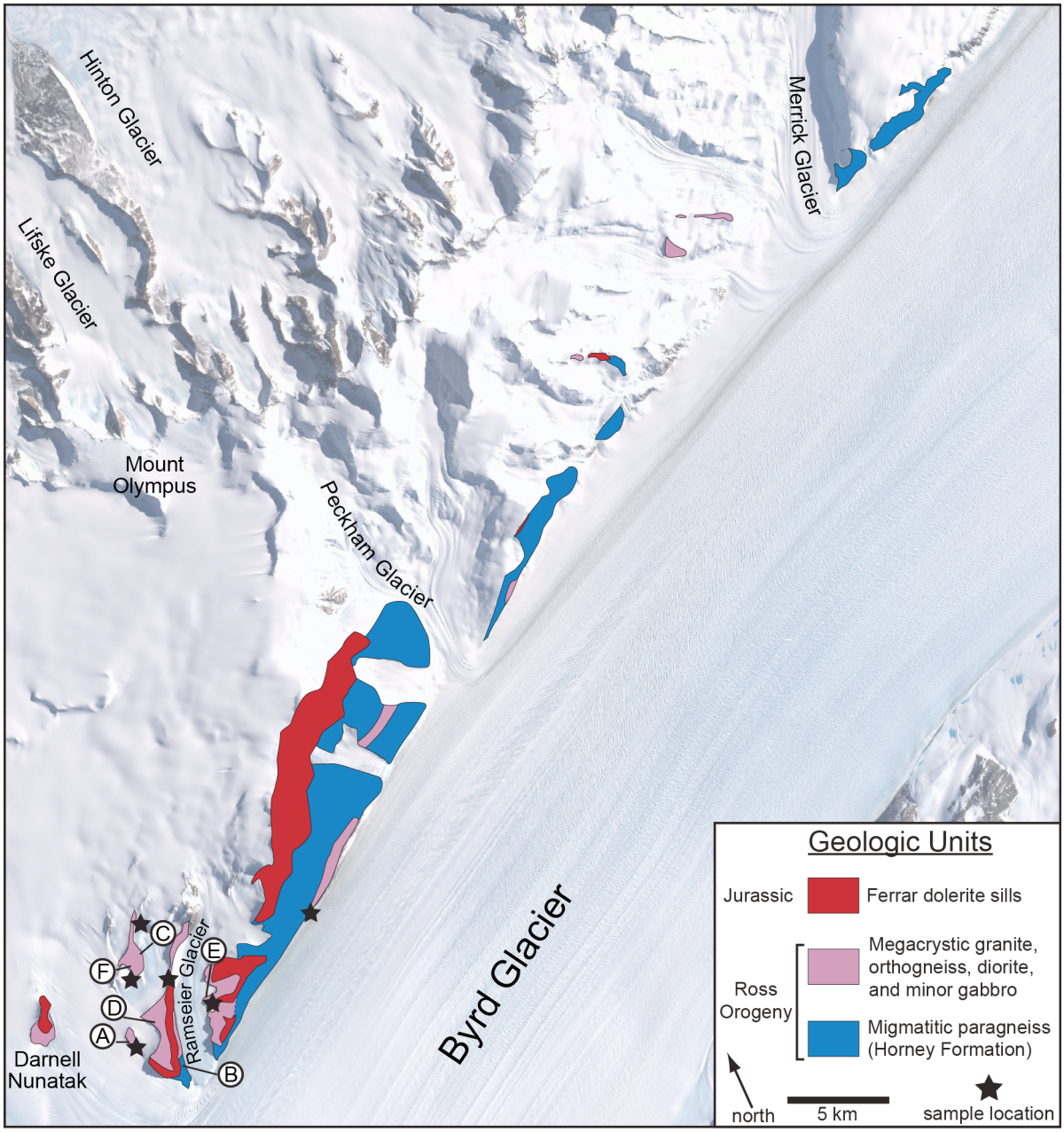

Figure 3.9 Simplified geologic map of the Byrd Glacier area (modified from Carosi et al., 2007). All plutonic rocks, including megacrystic granites, orthogneisses, and mafic rocks are grouped together at the scale of this map. Stars show the locations of samples with geochemistry, geochronologic, and/or isotopic data from this study. Multiple samples were collected in the vicinity of the stars on the map, but only a single star is plotted for clarity. Letters show the locations of corresponding field photographs shown in Figure 3.10.

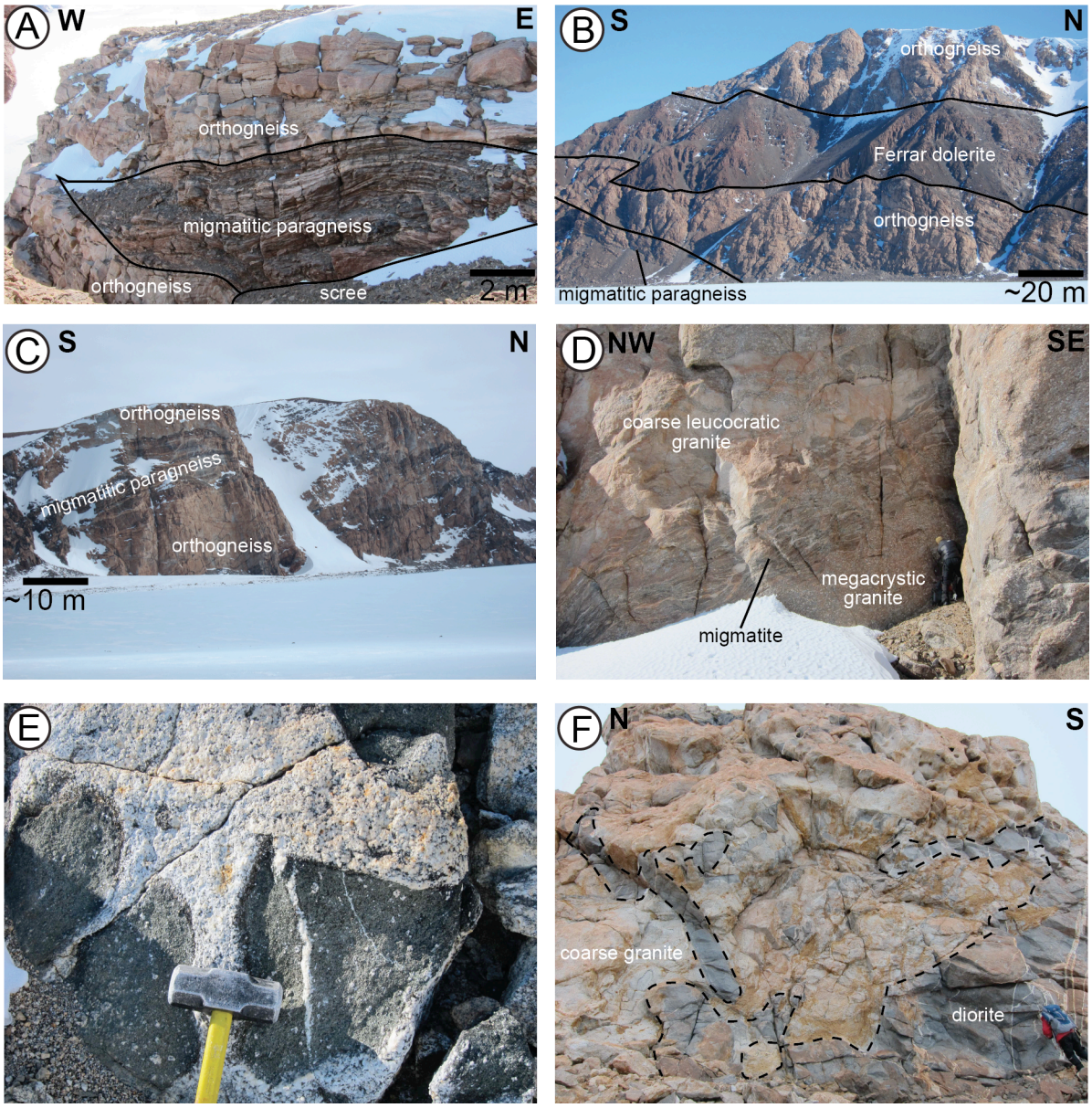

Figure 3.10 Field photos of different rock types in the Byrd Glacier area. (A) Boudinaged lens of migmatitic paragneiss (Horney Formation) enveloped in granitic orthogneiss. (B) Large body of granitic orthogneiss intruded by a Ferrar dolerite sill. (C) Interlayering of orthogneiss and migmatitic paragneiss. (D) Megacrystic K-feldspar granite intermingled with a coarse leucocratic granite with a layer of migmatite. (E) Pyroxene-biotite enclaves within a coarse granite. (F) Intermingling of coarse granite and diorite.

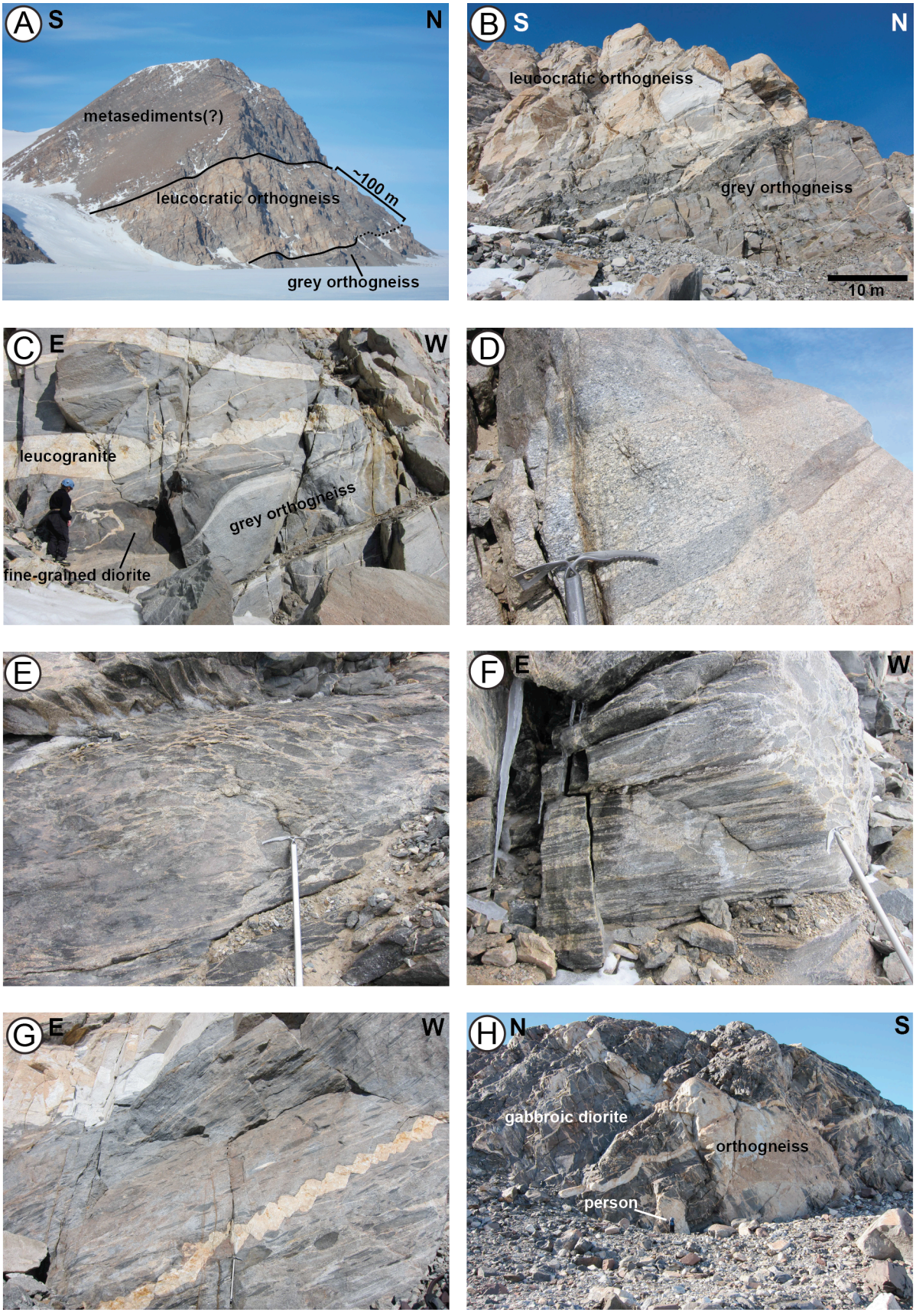
A
S
N
metasediments(?)
~100 m
leucocratic orthogneiss
grey orthogneiss
B
S
N
leucocratic orthogneiss
grey orthogneiss
10 m
C
E
W
leucogranite
grey orthogneiss
fine-grained diorite
D
E
E
F
E
W
G
E
W
H
N
S
gabbroic diorite
orthogneiss
person

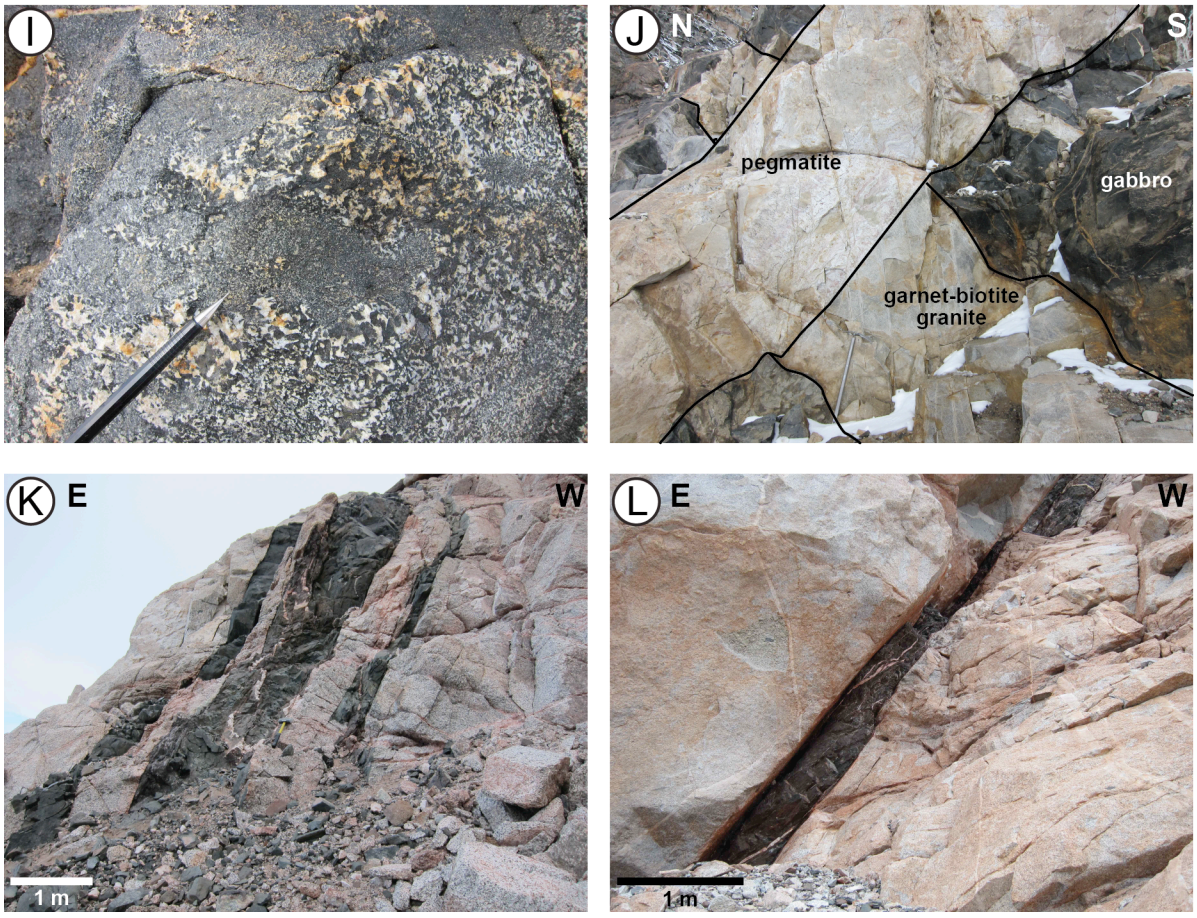

Figure 3.11 Field photos of different igneous rock types in the Darwin Glacier area. (A) Approximately 100 meter-thick sill of granitic orthogneiss beneath layered gneisses of the Horney Formation. (B) Contact between leucocratic and grey hornblende (Hbl) orthogneisses, both cross-cut by leucogranite dikes. (C) Boudinaged pod of fine-grained Hbl diorite within grey orthogneiss. Both contain leucogranite dikes and sills. (D) Centimeter- to meter-scale compositional zoning in an orthogneiss with feldspar augen. (E) High density of strained mafic enclaves in coarse-grained granite. (F) Strained mafic enclaves showing stretching > flattening strain. (G) Grey Hbl orthogneiss with abundant strained mafic enclaves in contact with a leucocratic orthogneiss cut by a domino-boudinaged leucogranite dike. (H) Large pod of gabbroic-diorite cross-cut by a sub-vertical dike of granitic orthogneiss and networks of leucogranite dikes. (I) Variation of grain size within a gabbro. (J) Gabbro cross-cut by a ~1.5 meter-wide dike of biotite-garnet granite, in-turn cross-cut by a garnet-bearing pegmatitic leucogranite. (K) Three parallel lamprophyre dikes cross-cutting a very-coarse-grained biotite orthogneiss. (L) Pyroxenite dike cross-cutting biotite orthogneiss.

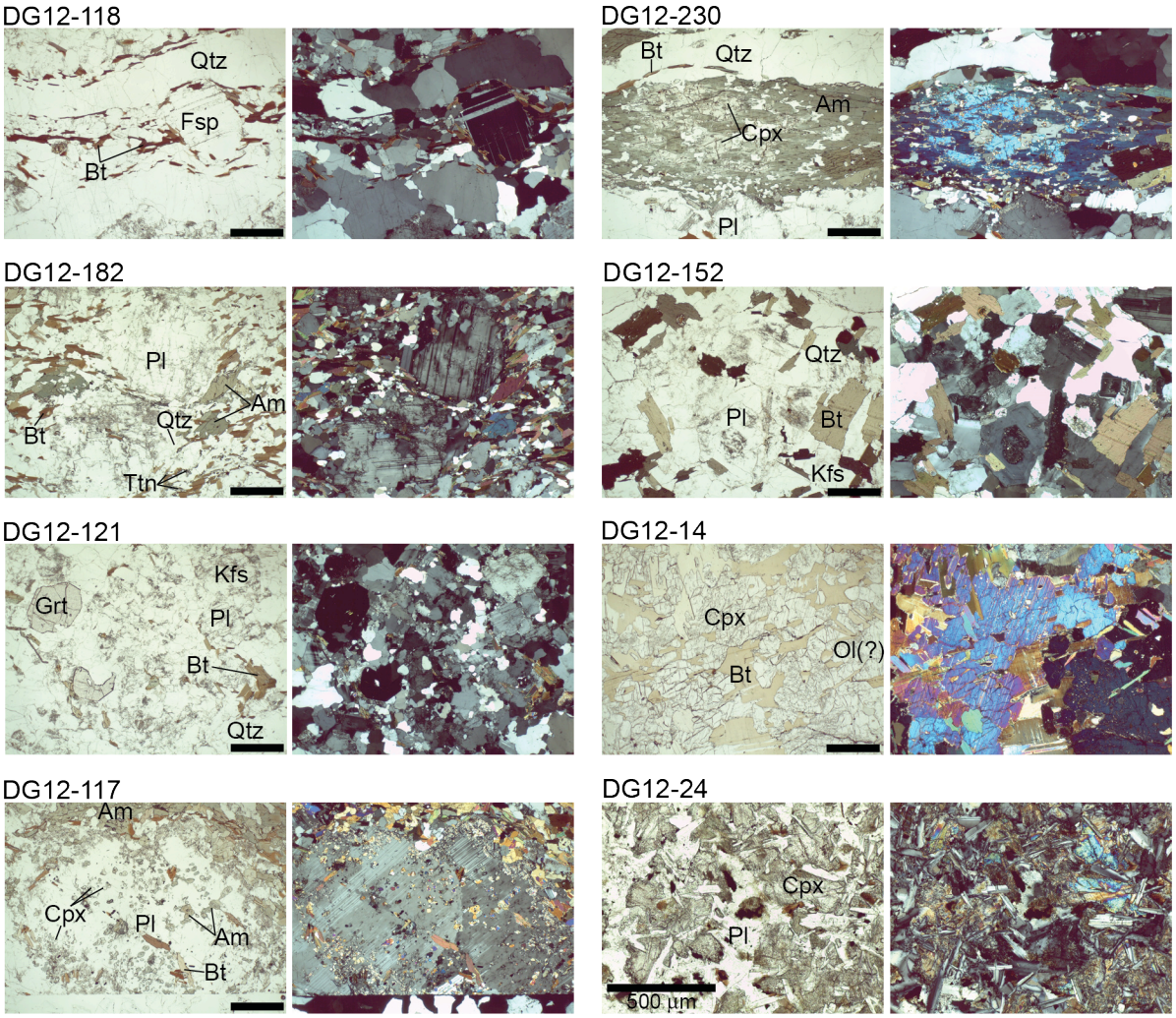

Figure 3.12 Photomicrographs of igneous rocks from the Darwin and Byrd Glacier areas. DG12-118: granitic orthogneiss with feldspar (Fsp) augen, recrystallized quartz (Qtz) bands, and aligned biotite (Bt); DG12-230: Clinopyroxene (Cpx) partially replaced by an elongate amphibole (Am) grain in an orthogneiss; DG12-182: Rounded plagioclase (Pl) porphyroclast surrounded by aligned Bt, Am, recrystallized Qtz, and titanite (Ttn); DG12-152: Undeformed equigranular granite with zoned Pl; DG12-121: Garnet (Gt)-bearing leucogranite; DG12-14: Crystallographically-coherent Cpx crystal surrounding Bt in a gabbro (Ol = olivine); DG12-117: Large plagioclase porphyroclast with inclusions of Cpx, Am, and Bt; DG12-24: Altered Cpx intergrown with randomly-oriented Pl blades in a gabbroic diorite. All scale bars are 1 mm unless otherwise noted.

METHODS

Whole-Rock Geochemistry

Whole-rock geochemistry data for samples with the prefix "P" were reported in Hagen-Peter et al. (2015), and were acquired by the methods described therein. Whole-rock geochemical analyses for samples with prefixes "RG" and "DG" were done at ALS Minerals (alsglobal.com; Reno, NV, USA). Rock chips were crushed and sieved to < 75 μm. Approximately 0.2 g of the pulverized sample was added to 0.9 g of lithium-metaborate flux. The mixture was fused at 1000°C and weighed for loss-on-ignition. The resulting glass bead was dissolved in 100 mL of 4% HNO_3 plus 2% HCl. Major- and trace-elements were then measured by solution inductively-coupled plasma atomic emission spectrometry (ICP-AES) and inductively-coupled plasma mass spectrometry (ICP-MS), respectively. Standard reference solutions, duplicate analyses, and blanks were included in the measurement routines.

Whole-Rock Nd-Sr Isotopes

Whole-rock Nd isotope analyses was done at National Taiwan University (Taipei, Taiwan). The sample preparation and analytical methods are similar to those described by Lee et al. (2012) and are briefly described here. Rocks were gently broken into chips using a steel hammer. The chips were sonicated in water for 20 minutes and allowed to dry. Clean chips were crushed in a steel jaw crusher and then powdered in agate ball mills for 40 minutes. Powders were dried at 105°C for 20 hours.

For trace element concentration measurements, 0.5000 ± 1 g of rock powders were gently mixed with 5.0000 ± 3 g of lithium-metaborate flux, and the mixtures were fused

while being agitated for 5 minutes to achieve complete mixing. The resulting glass beads were fragmented, and the fragments (~40 mg) were added to Teflon beakers and weighed. The glass fragments were dissolved over night in a 1:1 mixture of ultra-pure HF and HNO_3 at 145°C. The resulting solutions were dried down, re-dissolved over three days in HNO_3 at 145°C, and diluted with 2% HNO_3. A solution of Bi + Rh was added as an internal standard. Measurements were done using an Agilent 7500cx quadrupole ICP-MS using USGS AGV-2, BCR-2, BHVO-2, and DNC-1 as secondary reference standards to monitor precision and accuracy. The concentrations of Sm and Nd for the secondary references were typically within the margin of uncertainty of the recommended values.

For Nd isotopes, ~ 150 mg of rock powders were weighed in cleaned Teflon beakers. A 1:1 mixture of HF and HNO_3 was added to each beaker, and the beakers were placed on hot plates at 140°C for six to twelve days. Samples were sequentially dried down and re-dissolved in 4 M HCl (two steps) and 1 M HCl (one step). The 1 M HCl solutions were centrifuged and the supernatant removed from the residue into new clean Teflon beakers. Additional 1:1 HF and HNO_3 mixture was added to the undissolved residue, and the same six-to-twelve-day digestion and dry down process was repeated twice more. After the final dry down, samples were dissolved in 1 mL of 2 M HCl, centrifuged, and loaded onto ion-exchange columns. The ion-exchange chemistry was according to the procedure outlined by Lee et al. (2012). Purified Nd was collected in 2 mL of 3 M HNO_3. Neodymium isotope measurements were done on a Nu Plasma II HR multi-collector ICP-MS. The $^{143}Nd/^{144}Nd$ was corrected for mass bias using $^{146}Nd/^{144}Nd = 0.7129$. Solutions of 50 ppb JNdi-1 ($^{143}Nd/^{144}Nd = 0.512115 \pm 7$; Tanaka et al., 2000 were measured throughout the analytical sessions and used to normalize the $^{143}Nd/^{144}Nd$ of the samples, as well as precision. Solutions

of 50 ppb JNdi-1 measured throughout the session yielded an average $^{143}Nd/^{144}Nd$ = 0.512115 ± 22 (2 s.d.; n=7). The $\varepsilon Nd_{(i)}$ values were calculated relative to the chondritic uniform reservoir (CHUR) with present day $^{147}Sm/^{144}Nd$ = 0.1960 and $^{143}Nd/^{144}Nd$ = 0.512630 (Bouvier et al., 2008). Two-stage depleted mantle model ages (T_{DM}^{Nd}) were calculated using the approach outlined in DePaolo et al. (1991). Internal uncertainties on Nd isotope measurements were on the order of ± 0.000005 (~0.1 εNd units). The largest source of uncertainty in the calculated $\varepsilon Nd_{(i)}$ values is the determination of the Sm/Nd (and therefore $^{147}Sm/^{144}Nd$) of the sample. One measurement of the BHVO-2 reference (USGS) yielded Sm and Nd concentrations that were 6.1% lower than the accepted values, although these values are within uncertainty of the accepted values for BHVO-2. For the samples in this study, a 6.1% error in the Sm and Nd concentrations would cause errors of 0.8–1.8 εNd units for ca. 500 Ma samples in the worst-case scenario (i.e., if the Sm concentration were erroneously low and the Nd concentration were erroneously high).

Zircon U-Th-Pb Geochronology and Trace Elements

Zircon separation, imaging, and isotope analyses were done at University of California, Santa Barbara. Zircons were separated from rock samples using standard crushing, sieving, density separation, and magnetic separation techniques. Grains were hand-selected using a binocular microscope, with care taken to select crack- and inclusion-free grains, and mounted in epoxy resin. The disks were polished to expose median sections of the zircon grains and carbon coated. Zircons were imaged using an FEI Quanta 400f secondary electron microscope (SEM) with a cathodoluminescence (CL) detector. The CL images were used to guide the placement of laser-ablation pits.

Zircons were ablated in a He environment using a Photon Machines 193 nm ArF excimer laser and HelEx cell. Laser energy of 3–4 mJ and 4 Hz repetition rate were used to ablate pits 24 or 31 μm in diameter. Ablation periods were 15–20 seconds (0.2 or 0.4 second integration periods), preceded by two "cleaning" shots (to removed common lead from the surface of the sample) and 12–15 second washout periods for the signal to return to baseline. The ablated sample was transported in a He+Ar mixture to a Nu Plasma multi-collector ICP-MS for the measurement of U-Th-Pb isotopes. Isotopes ^{238}U and ^{232}Th were measured with Faraday cups equipped with 10^{11}-ohm resistors, while ^{208}Pb, ^{207}Pb, ^{206}Pb, and $^{204}(Pb+Hg)$ were measured on secondary electron multipliers. Data reduction and age calculations were done using Iolite version 2.31 (Paton et al., 2010; 2011) and Isoplot version 3.00 (Ludwig, 2003).

Every six to eight analyses were bracketed by analyses of reference zircons. The '91500' reference zircon (1065.4 ± 0.3 Ma $^{207}Pb/^{206}Pb$ ID-TIMS age and 1062.4 ±0.4 Ma $^{206}Pb/^{238}U$ ID-TIMS age; Wiedenbeck et al., 1995; 2004) was used as a primary reference to correct for mass bias, Pb/U and Pb/Th fractionation, and instrumental drift over the analytical sessions. Reference zircons 'GJ-1' (608.5 ± 0.4 Ma $^{207}Pb/^{206}Pb$ ID-TIMS age; Jackson et al., 2004 and 601.7 ± 1.3 Ma $^{206}Pb/^{238}U$ ID-TIMS age; Condon, personal communication) and 'Plešovice' (337.13 ± 0.37 Ma $^{206}Pb/^{238}U$ ID-TIMS age Sláma et al., 2008) were used to assess data accuracy and external reproducibility. Throughout all of the analytical sessions, 'GJ-1' yielded a weighted-mean $^{206}Pb/^{238}U$ age of 602.4 ± 7.3 (2 s.d.; n = 454; MSWD = 1.1, and 'Plešovice' yielded a weighted-mean $^{206}Pb/^{238}U$ age of 339.2 ± 4.2 (2 s.d.; n = 313; MSWD = 1.1).

Zircon Hf Isotopes

Zircon Hf isotope measurements were done by laser-ablation multi-collector ICP-MS on the same grains targeted for U-Th-Pb and trace element analyses. Laser energy of 4 mJ and a repetition rate of 6 or 8 Hz were used to ablate 50 μm-diameter pits, which overlapped the pre-existing U-Th-Pb pits. Data were collected in time resolved mode (1.2 or 1.6 second integration periods) during 50–60-second ablations with 20–30-second washout periods in between each analysis. Masses 171–180 (inclusive) were measured simultaneously on an array of 10 adjacent Faraday cups. An Yb mass bias factor, calculated using $^{173}Yb/^{171}Yb$ = 1.123575 (Thirlwall & Anczkiewicz), was used to correct for Yb and Lu mass bias. A Hf mass bias factor, calculated using $^{179}Hf/^{177}Hf = 0.7325$ (Patchett & Tatsumoto, 1980a,b), was used to correct for Hf mass bias. The natural isotope ratios $^{176}Yb/^{173}Yb$ = 0.786847 (Thirlwall & Anczkiewicz) and $^{176}Lu/^{175}Lu$ = 0.02656 (Chu et al., 2002) were used to subtract isobaric interferences (^{176}Lu and ^{176}Yb) on ^{176}Hf.

Natural zircons 'GJ-1' ($^{176}Hf/^{177}Hf = 0.282000 \pm 5$; Morel et al., 2008), 'Plešovice' ($^{176}Hf/^{177}Hf = 0.282482 \pm 13$; Sláma et al., 2008), and '91500' ($^{176}Hf/^{177}Hf = 0.282308 \pm 6$; Blichert-Toft, 2008), and synthetic 'MUNZirc-1', 'MUNZirc-3', and 'MUNZirc-4' zircons (0.282135 ± 7; Fisher et al., 2011) were measured throughout the analytical sessions and used to assess data accuracy and precision. Throughout the analytical sessions for the samples with prefixes "RG" and "DG", 'GJ-1' yielded a weighted-mean $^{176}Hf/^{177}Hf$ = 0.282035 ± 69 (2 s.d.; n = 60), 'Plešovice' yielded a weighted-mean $^{176}Hf/^{177}Hf = 0.282510 \pm$ 40 (2 s.d.; n = 46), and '91500' yielded a weighted-mean $^{176}Hf/^{177}Hf = 0.282301 \pm 62$ (2 s.d.; n = 22). The synthetic zircons of Fisher et al. (2011), with $^{176}Yb/^{177}Hf$ ranging from ~0.02−0.3, yielded a weighted-mean $^{176}Hf/^{177}Hf = 0.282162 \pm 62$ (2 s.d.; n = 69). During the

analytical sessions for the samples with prefix "P", the reproducibility of reference zircons was less precise (3.5–4.5 εHf units; 2 s.d.). The treatment of these data is described in Hagen-Peter et al. (2015).

The $\varepsilon Hf_{(i)}$ values are reported relative to the chondritic uniform reservoir (CHUR; present-day $^{176}Hf/^{177}Hf = 0.282785$ and $^{176}Lu/^{177}Hf = 0.0336$; Bouvier et al., 2008) using the corresponding $^{206}Pb/^{238}U$ age for the same zircon domain and $\lambda^{176}Lu = 1.867 \times 10^{-11}$ yr^{-1} (Scherer et al., 2001; 2003; Söderlund et al., 2004). Two-stage depleted-mantle model ages (T_{DM}^{Hf}) were calculated using present-day $^{176}Hf/^{177}Hf = 0.282785$ (Nowell et al., 1998; Griffin et al., 2000; Griffin et al., 2002) and $^{176}Lu/^{177}Hf = 0.0336$ (Griffin et al., 2002) for the depleted mantle reservoir and the crustal average $^{176}Lu/^{177}Hf = 0.015$ for the Hf isotope evolution of crustal magma sources after separation from the depleted mantle (Griffin et al., 2002).

RESULTS

Whole-Rock Geochemistry

Major- and trace-element geochemistry for representative samples from the DV, KGAS, and BG areas are shown in Figures 3.13–3.16. Samples from the KGAS and BG areas span a range of SiO_2 content from ~45–78 wt%, whereas there is a gap from ~60–69 wt% for DV samples. On a total alkalis versus silica (TAS) diagram, most DV and BG samples plot within the subalkaline field, whereas many samples from the KGAS plot well within the alkaline field (Fig. 3.13a). Several low-SiO_2 samples from the DV and BG areas also plot within the alkaline field. On modified alkaline lime index (MALI; Frost et al., 2001), DV samples plot primarily in the calc-alkalic and alkali-calcic fields, BG samples plot primarily

in the calcic and calc-alkalic fields, and KGAS samples span the calcic through alkalic fields (Fig. 3.13b). Most samples from each area plot near the boundary of the metaluminous and peraluminous fields in terms of Shand's index, though several samples from the KGAS extend far into the peraluminous and peralkaline fields (Fig. 3.13c). The samples from each area do not plot along simple trends on Harker diagrams (Fig. 3.14). There is generally more dispersion in major oxide and trace element concentrations at lower SiO_2 contents. The dispersion is especially pronounced in KGAS samples, with ranges of approximately 16, 18, 10, and 14 wt% for Al_2SiO_3, CaO, Fe_2O_3, and MgO, respectively, in samples with < 60 wt% SiO_2. The arrays of major element concentrations (Al2SiO3, CaO, Fe2O3, and MgO shown in Fig. 3.14) generally converge at high SiO_2 contents for samples from each area. Nepheline ± calcite syenites from the KGAS have very low MgO contents and correspondingly low Mg# < 10 (molar Mg/[Mg+Fe]). Several KGAS samples have very high CaO concentrations (> 16 wt%) coupled with high MgO and low Fe_2O_3 concentrations and correspondingly high Mg# > 70. Samples from each area have widely variable trace element concentrations. The Zr concentrations of samples show a generally arched pattern with the lowest concentrations in the most mafic and most felsic samples and the highest concentrations in intermediate samples. Samples from the DV and KGAS areas are much more strongly enriched in Sr, with high Sr/Y values in the "HiSY" range (Sr/Y > 40) of Tulloch and Kimbrough (2003).

On the discrimination diagram of Whalen et al. (1987), DV and BG samples plot within or near the boundary of the I- and S-type granite fields, whereas many KGAS samples extend well into the A-type granite field (Fig. 3.15). On tectonic discrimination diagrams of Pearce et al. (1984), DV and BG samples plot primarily in the volcanic arc granite fields, whereas several KGAS samples extend into the within-plate granite fields.

Normalized trace- and rare earth-element (REE) diagrams for the most-primitive samples (SiO_2 < 52 wt%; Mg# > 69) are shown in Figure 3.16. All of the primitive samples show enriched trace element patterns with high concentrations of the large-ion lithophile elements (LILE) relative to the more-compatible high-field strength elements (HFSE), the latter less than 10 times primitive mantle concentrations. The patterns typically show negative Nb, P, and Ti anomalies and positive K and Pb anomalies. The samples show enriched patterns on REE diagrams, with light REE concentrations up to ~100 times chondrite and normalized La/Yb ratios of 3.7−5.8. Most of the patterns display only minor Eu anomalies, although one RG sample has a strong positive Eu anomaly and one BG sample has a strong negative Eu anomaly.

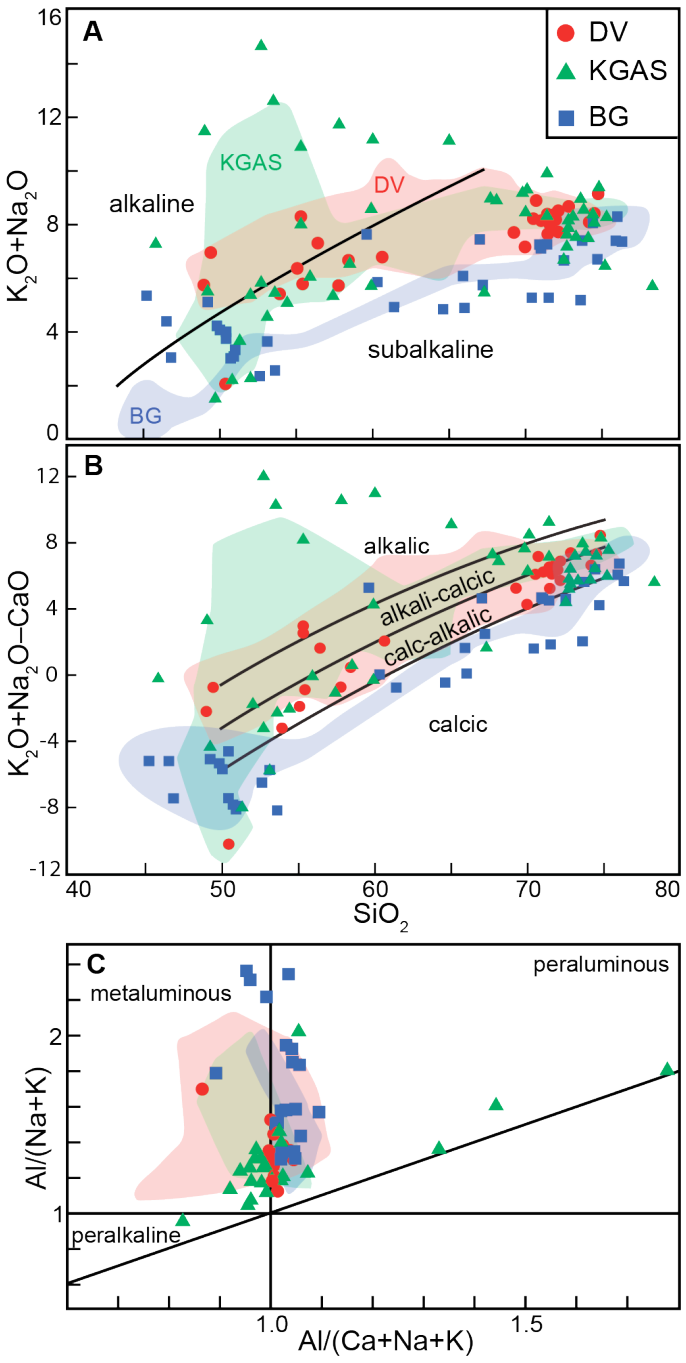

Figure 3.13 (A) Total alkalis versus silica (TAS) and (B) modified alkali-lime index (MALI; Frost et al., 2001) diagrams demonstrate the strong alkali enrichment in some rocks from the KGAS. Rocks from the DV and BG areas are dominantly subalkaline and calc-alkalic or calcic. (C) Discrimination of samples with >60 wt% SiO_2 based on Shand's index. Color-filled fields outline previously published data for the different areas from the following references: DV: Smillie, 1992; Allibone et al., 1993b; Cox et al., 2000; Forsyth et al., 2002; KGAS: Aslund, 1990; Rowell et al., 1993; Hall et al., 1995; Mellish et al., 2002; Read et al., 2002; Cottle & Cooper, 2006a; BG: Simpson & Cooper, 2002; Cottle & Cooper, 2006b.

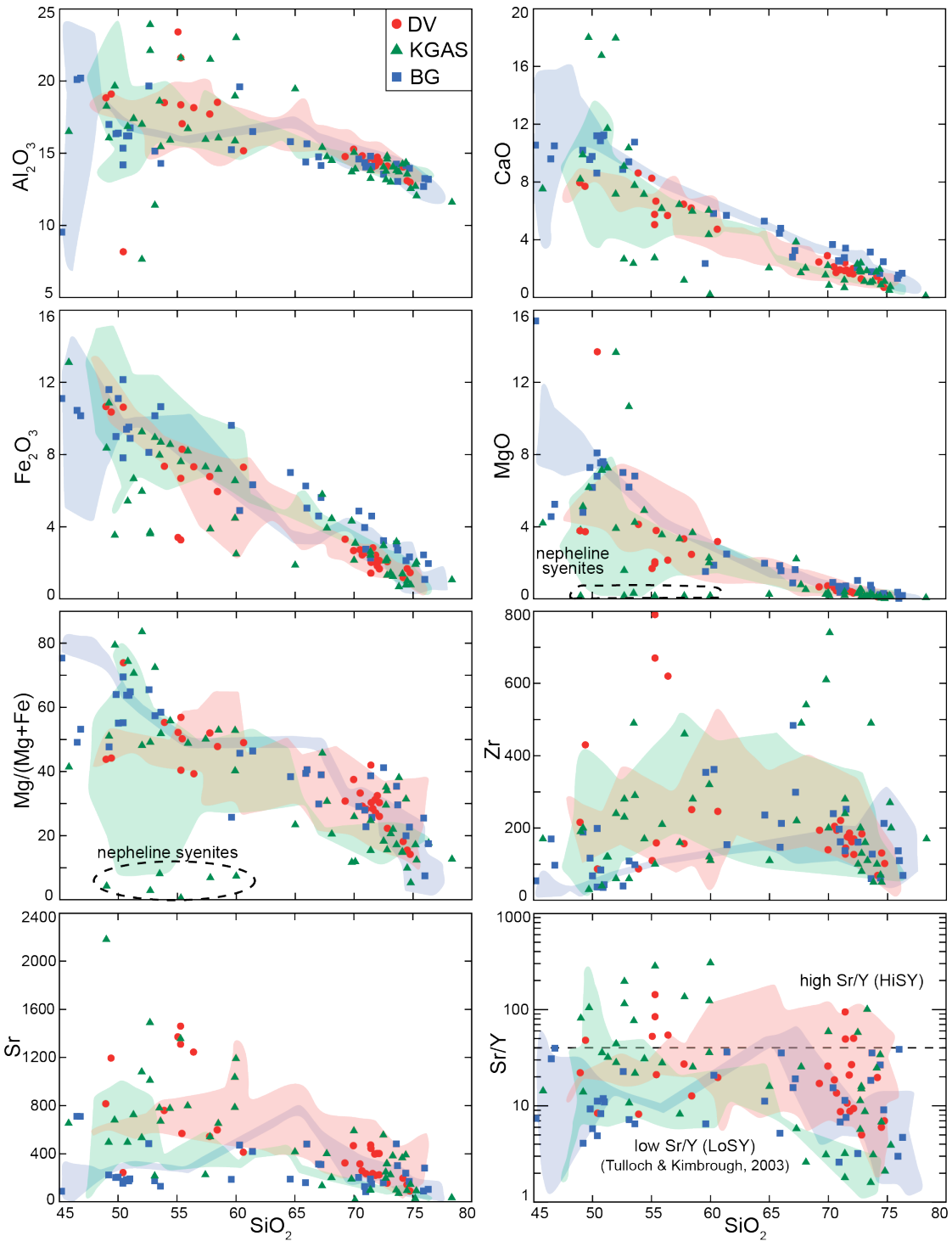

Figure 3.14 Geochemical discrimination diagrams for samples from the DV, KGAS, and BG areas. Igneous rocks from each area span a the range from gabbro to granite (*sensu lato*). Significant dispersion of major- and trace-element concentrations at a given SiO_2 preclude simple fractional crystallization/melting cogenetic relationships for the igneous rocks in each area. Major oxide concentrations are in wt%, and trace element concentrations are in ppm. Symbols as in Figure 3.13.

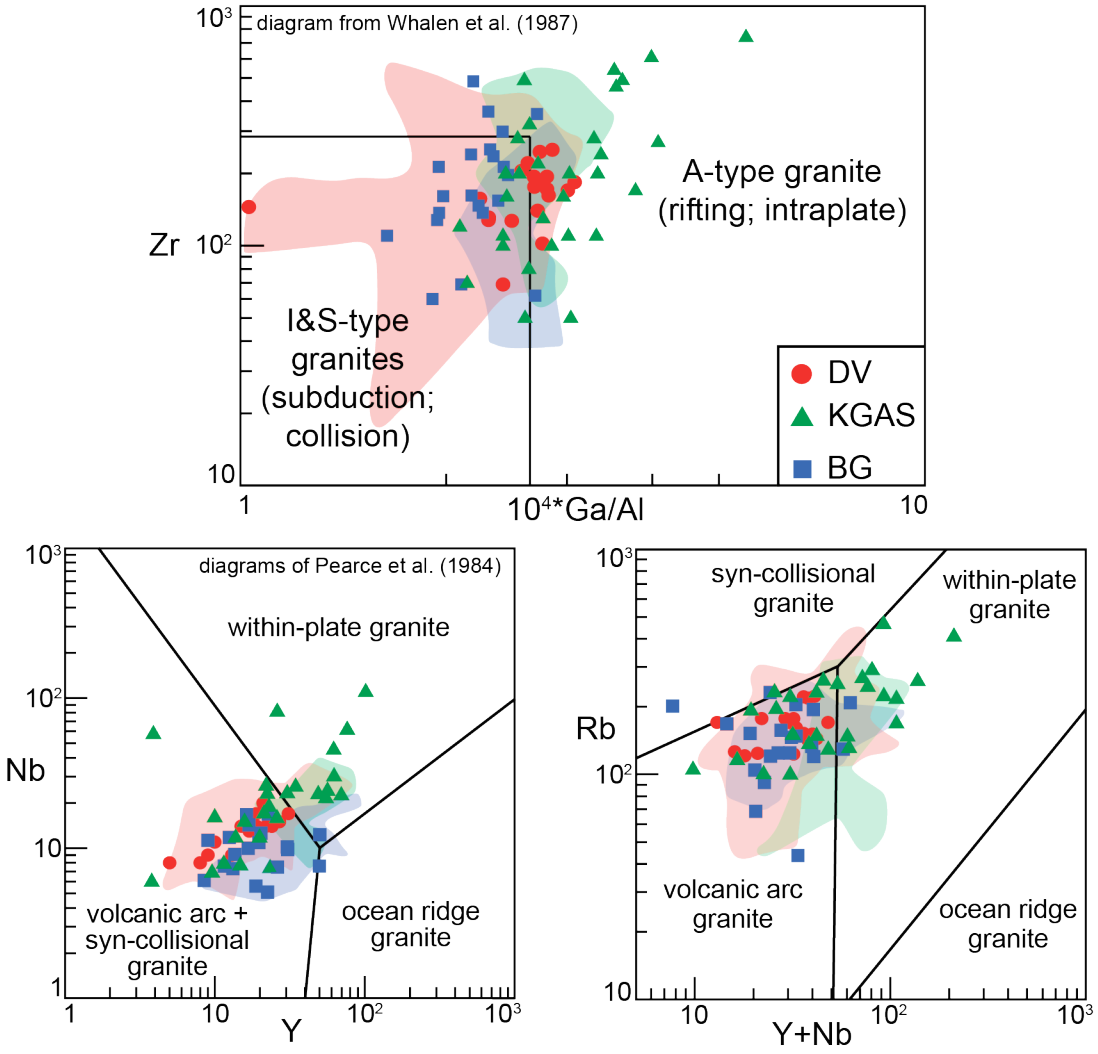

Figure 3.15 Tectonic discrimination diagrams for rocks with >57 wt% SiO_2. Igneous rocks from the KGAS commonly fall within the A-type granite and within-plate granite fields. Most samples from the DV and BG areas fall within or near the boundaries of the I- and S-type granites and volcanic arc granite fields. Symbols as in Figure 3.13.

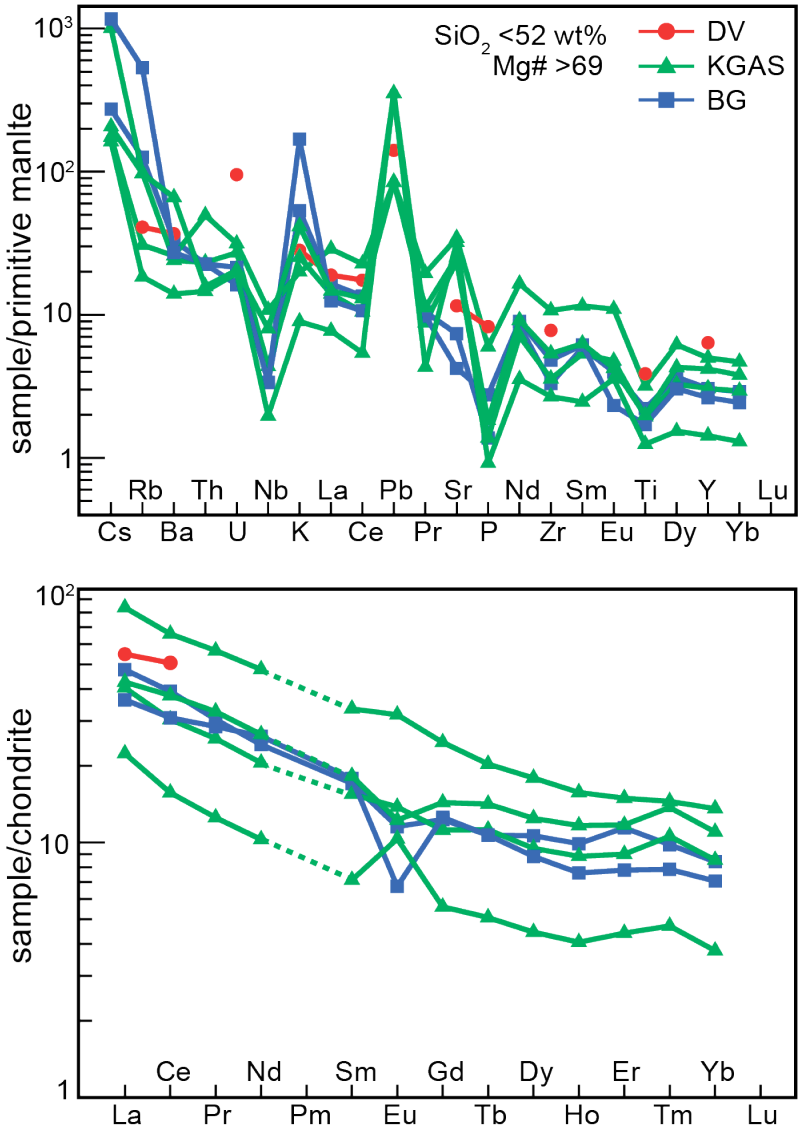

Figure 3.16 Trace-element and rare earth-element (REE) patterns of the most primitive igneous rocks from this study (SiO_2 <52 wt%; Mg# >69) normalized to primitive mantle and the chondritic uniform reservoir, respectively (McDonough & Sun, 1995). All of the primitive samples show strong enrichments in the large ion lithophile elements (LILE) relative to high field strength elements and light REE relative to heavy REE.

Zircon U-Th-Pb Geochronology

Representative CL images of zircons and concordia diagram examples are shown in Figures 3.17 and 3.18, respectively. Geochronology results are reported in Table 3.1. Weighted-mean $^{206}Pb/^{238}U$ dates were calculated for most samples. Some samples have mean-square of weighted deviates (MSWD) greater than expected for a statistically homogeneous normally-distributed population (Wendt & Carl, 1991). This excess dispersion in some samples may be due to a number of factors, including the presence of small amounts of common lead in the zircons when they crystallized and/or minor degrees of lead loss, though the exact cause of the excess dispersion is typically irresolvable by our data. We take the dates reported in Table 3.1 as the best estimates of the crystallization ages of the rocks in which the zircons were hosted. The uncertainties on the reported dates take into account both the internal uncertainty of the U-Pb isotope ratio measurements and the long-term reproducibility of secondary reference zircons, resulting in uncertainties of approximately ± 6−7 Ma for most samples.

Samples from the DV area range from ca. 515−492 Ma. Samples from the KGAS area range from ca. 565−499 Ma. Samples from the BG area range from ca. 550−503 Ma. Near-concordant (<10% difference between $^{206}Pb/^{238}U$ and $^{207}Pb/^{235}U$ ages) inherited zircon ages range from ca. 600–2040 Ma.

Table 3.1 Summary of U-Pb, Hf, and Nd isotope results

Sample name	Rock description	Location		U-Pb age*	± †	*n*	MSWD	$\varepsilon Hf_{(i)}$ §	± †	*n*	MSWD	T_{DM}^{Hf}	$\varepsilon Nd_{(i)}$	T_{DM}^{Nd}
		Lat (°S)	Long (°E)	(Ma)	(Ma)							(Ga)		(Ga)
Dry Valleys area														
RG11-233	Hbl diorite	-78.073	163.895	492.2	6.1	27	1.9	–4.0	0.6	8	1.4	1.7	–	–
P64422#	Hbl diorite	-77.482	162.821	493.2	6.1	35	0.8	–1.8	1.2	12	1.5	1.5	–	–
P68826	pink granite	-77.877	162.636	495.5	6.1	25	1.2	–5.9	1.1	12	0.5	1.8	–	–
P62101	granite	-77.231	162.067	495.6	6.1	20	1.3	–2.2	1.5	10	1.0	1.6	–	–
RG11-241	diorite	-78.161	163.647	495.9	6.1	23	1.5	-5.4	0.7	8	0.7	1.7	–	–
P68775	granite	-76.943	162.161	495.9	6.2	30	2.0	–4.6	1.2	12	0.9	1.7	–	–
P68845	Hbl granite	-76.953	162.247	496.1	6.1	26	1.2	–4.5	1.3	12	0.8	1.7	–	–
P68844	Hbl granite	-76.952	162.267	496.8	6.1	28	1.0	–5.6	1.3	10	1.3	1.8	–	–
P62293	megacrystic granite	-77.369	163.007	496.9	6.2	22	1.7	–4.2	1.5	12	0.7	1.7	–	–
P68802	pink granite	-76.810	162.443	497.1	6.2	29	1.4	–2.4	1.1	10	1.3	1.6	–	–
RG11-234	cpx-bt gabbro-diorite	-78.060	163.849	498.6	6.5	13	2.6	–2.7	0.7	8	1.2	1.6	–6.1	1.7
P68760	granite	-76.934	162.473	500.1	6.6	18	1.6	–3.7	1.4	10	0.8	1.7	–	–
RG11-224	Bl diorite	-78.078	163.867	500.2	6.1	26	1.4	–3.3	0.5	10	0.8	1.6	–	–
P49945	Bt granodiorite	-77.556	161.858	500.6	6.6	17	2.1	–5.9	1.4	9	0.6	1.8	–	–
P64403	Hbl gabbro	-77.329	162.815	501.9	6.4	20	1.6	–0.6	1.5	10	0.5	1.5	–	–
P68796	pink granite	-76.802	162.157	502.1	6.6	23	2.0	–4.0	1.1	12	1.3	1.7	–	–
P68766	granite	-76.861	162.551	502.6	6.6	10	0.5	–2.1	1.4	8	0.5	1.6	–	–
P68843	porphyritic granite	-76.950	162.292	504.2	6.4	19	0.9	–3.6	1.2	10	0.7	1.7	–	–
P68770	weakly-foliated granite	-76.892	162.248	504.8	7.0	14	2.8	–3.2	1.4	9	0.5	1.7	–	–
P68878	porphyritic diorite dike	-76.804	162.135	505	6.5	18	1.5	–2.1	1.5	8	1.4	1.6	–	–
P68851	megacrystic Hbl granite	-76.903	162.196	505.5	6.5	16	1.5	–1.4	1.5	10	0.4	1.5	–	–
P68782	weakly-foliated granite	-76.895	162.395	506.4	6.4	16	1.0	–3.5	1.7	8	1.2	1.7	–	–
P68861	massive Hbl diorite	-76.884	162.485	507.8	6.4	20	1.5	–0.3	1.5	12	0.8	1.5	–	–
P49944	Qtz monzodiorite	-77.569	161.628	508.9	6.4	23	1.3	–2.0	1.3	10	1.2	1.6	–	–
P68860	foliated Hbl tonalite	-76.884	162.485	509.4	6.6	17	1.9	–3.5	1.6	8	1.2	1.7	–	–
P62321	foliated diorite	-77.533	162.962	509.5	6.3	20	1.1	–1.1	1.2	12	0.4	1.5	–	–
P68787	Hbl monzodiorite	-76.866	162.349	511	6.4	28	2.2	–2.4	1.4	12	0.9	1.6	–	–
P68756	megacrystic granite	-76.944	162.335	514.5	6.7	10	0.7	–1.5	1.2	10	1.6	1.6	–	–
P68758	granite	-76.939	162.396	515.3	6.4	11	1.0	–2.9	1.7	10	0.8	1.6	–	–
P62324	foliated diorite	-77.535	162.900	515.4	6.6	28	1.3	–1.7	1.1	12	0.9	1.6	–	–
P64424	megacrystic granite	-77.578	162.385	–	–	–	–	–7.2††	1.9	5	1.1	1.9	–	–

Sample name	Rock description	Location		U-Pb age* (Ma)	± † (Ma)	*n*	MSWD	$\varepsilon Hf_{(i)}$ §	± †	*n*	MSWD	T_{DM}^{Hf} (Ga)	$\varepsilon Nd_{(i)}$	T_{DM}^{Nd} (Ga)
		Lat (°S)	Long (°E)											
Koettiltz Glacier area														
RG11-51	zoned dike edge	-78.256	162.880	499.4	6.4	16	1.9	–11.3	0.7	8	1.2	2.1	–	–
RG11-44	gabbro/diorite	-78.255	162.877	500.3	6.2	20	2.5	–10.3	0.7	8	0.8	2.1	–	–
RG11-222	felsic porphyry sill	-78.266	162.598	500.5	6.6	5	1.2	–4.1	0.9	4	0.8	1.7	–	–
RG11-85	Ne + Cal syenite	-78.198	163.143	509.1	6.4	16	1.6	2.2	0.9	8	0.9	1.3	0.1	1.2
RG11-50	zoned dike core	-78.256	162.880	510.1	8.8	4	2.4	–	–	–	–	–	–	–
RG11-70	granite	-78.255	163.237	518.2	6.4	16	1.3	–9.8	1.3	8	2.8	2.1	–8.2	1.9
RG11-71	granite	-78.255	163.237	522.3	6.7	11	1.2	–9.4	1.5	8	3.7	2.0	–	–
RG11-121	Bt granite	-78.255	163.942	528.4	6.8	13	1.2	–4	0.8	9	1.6	1.7	–	–
RG11-160	gabbro/diorite	-78.273	162.711	541.7	6.7	24	2.3	0.8	0.5	9	1.1	1.4	–	–
RG11-141	Hbl granodiorite	-78.283	162.792	543.7	7.1	8	0.6	–0.3	0.8	4	0.7	1.5	–	–
RG11-183	granitoid	-78.270	162.755	544.3	6.7	9	0.9	1.6	1.1	7	1.8	1.4	–	–
RG11-202	Qtz syenite	-78.300	162.739	549.5	7.1	15	1.3	3.0	0.6	11	1.0	1.3	–0.8	1.3
RG11-117	Hbl diorite	-78.372	163.066	551	6.7	27	1.1	–6	0.6	8	0.9	1.9	–	–
RG11-24	orthogneiss	-78.217	163.067	552	7.0	7	0.9	3.5	0.8	6	1.0	1.3	–1.1	1.3
RG11-119	leucogranite dike	-78.372	163.066	553.2	8.1	7	2.3	–2.7	1.3	8	2.9	1.6	–	–
RG11-146	gabbro	-78.284	162.795	561.9	6.8	24	1.4	–4	1.1	8	1.7	1.7	–6.2	1.7
RG11-212	2-mica + Grt orthogneiss	-78.315	162.799	564.7	7.0	12	1.6	–3	0.6	9	0.7	–	–	–
RG11-180	Ne syenite	-78.281	162.825	~545	–	–	–	–	–	–	–	–	–1.4	1.4
RG11-137	orthogneiss	-78.199	163.005	~540	–	–	–	4.3	1.3	2	0.6	1.2	–	–
RG11-84	leucogranite	-78.198	163.143	N.D.	–	–	–	~ -8	–	–	–	–	–	–
Byrd Glacier area														
DG12-112	Grt granite dike	-80.469	156.142	502.8	6.2	23	2.2	–9.8	0.7	13	2.2	2.1	–	–
DG12-25	leucogranite dike	-80.452	156.321	~510	–	–	–	–5.9	1.9	5	3.3	1.8	–	–
DG12-23	gabbroic diorite	-80.452	156.321	524.9	6.9	16	1.6	–7.3	2.2	7	2.7	1.9	–8.7	1.9
DG12-72	Bt granite dike	-80.442	156.239	529.9	6.9	9	0.7	–7.6	1.6	6	3.6	1.9	–	–
DG12-210	leucogranite sill	-80.049	159.448	531.4	8.0	3	0.3	~ –5	–	–	–	~1.8	–	–
DG12-199	Hbl granodiorite	-80.449	156.730	531.7	8.6	4	1.3	–5.4	0.7	5	0.4	1.8	–	–
DG12-77	massive granite	-80.442	156.244	535.5	7.4	3	0.9	–5.2	0.7	4	0.8	1.8	–	–
DG12-117	gabbro	-79.874	159.040	537.4	6.6	27	1.1	1.6	0.6	12	1.4	1.6	–7.2	1.8
DG12-118	orthogneiss	-79.874	159.040	539.2	6.7	27	1.6	–3.4	0.7	12	1.8	1.7	–6.8	1.8

Sample name	Rock description	Location		U-Pb age* (Ma)	± † (Ma)	*n*	MSWD	$\varepsilon Hf_{(i)}$ §	± †	*n*	MSWD	T_{DM}^{Hf} (Ga)	$\varepsilon Nd_{(i)}$	T_{DM}^{Nd} (Ga)
		Lat (°S)	Long (°E)											
DG12-13	megacrystic granitoid	-80.479	156.371	~540	6.5	–	–	–12.3	1.2	5	1.4	2.2	–10.3	2.0
DG12-182	Hbl orthogneiss	-79.923	158.325	540.6	6.9	26	3.1	–4.4	1.7	14	1.8	1.8	–3.7	1.5
DG12-178	gabbro	-79.931	158.791	541.4	6.7	32	0.6	2.7	0.5	12	0.8	1.3	–4.8	1.6
DG12-127	gabbro	-79.862	158.976	541.6	6.6	29	0.7	bimodal	–	–	–	0.0	–	–
DG12-228	orthogneiss	-79.899	159.131	542.6	7.2	24	2.1	–4.4	0.7	11	1.9	1.7	–5.8	1.7
DG12-152	granitoid	-79.478	160.971	543.8	7.2	5	0.7	1.6	0.7	9	1.3	1.4	–	–
DG12-230	gabbroic diorite	-79.899	159.131	544.8	7.0	14	1.9	–0.2	0.7	9	1.3	1.5	–3.1	1.5
DG12-156	orthogneiss	-79.754	158.879	545.7	7.2	5	0.2	–3.9	1.4	5	2.3	1.7	–	–
CM-1	orthogneiss	-79.575	160.150	546.0	6.9	12	0.7	–3.7	0.7	6	0.8	1.7	–	–
DG12-160	orthogneiss	-79.922	158.694	547.9	6.7	23	0.8	–4.2	0.5	11	1.1	1.7	–	–
DG12-257	gabbro	-79.862	158.984	548.3	7.0	10	0.7	–1.6	0.8	10	1.5	1.6	–	–
DG12-145	orthogneiss	-79.185	160.406	549.7	7.5	5	1.0	–2.9	0.7	7	0.9	1.7	–5.1	1.7
DG12-132	orthogneiss	-79.787	158.536	~550	–	–	–	–2.6	0.8	4	0.9	1.6	–	–

Note: MSWD—mean square of weighted deviates; T_{DM}^{Hf}—two-stage depleted-mantle Hf model age; T_{DM}^{Nd}—two-stage depleted-mantle Nd model age.

* "U-Pb ages" with a corresponding uncertainty are weighted-mean $^{206}Pb/^{238}U$ mean ages. Ages preceded by a "~" are estimated ages of samples for which mean ages were not calculated.

† Uncertainties on mean ages are quadriatic additions of the internal 2 S.E. and external uncertainty estimated from the reproducibility of the GJ-1 and Plešovice reference zircons. Uncertainties on $\varepsilon_{Hf\,(i)}$ are reported as the 2 standard error (S.E.) of the population of analyses used in the calculation.

§ $\varepsilon_{Hf(i)}$ are weighted mean values of multiple measurements of a population from each sample.

Samples with prefix "P" are housed in the New Zealand Institute of Geological and Nuclear Science (GNS) PETLAB database (www.pet.gns.cri.nz).

†† A mean age could not be calculated for sample P64424, but individual spot ages were used to calculate $\varepsilon Hf_{(i)}$.

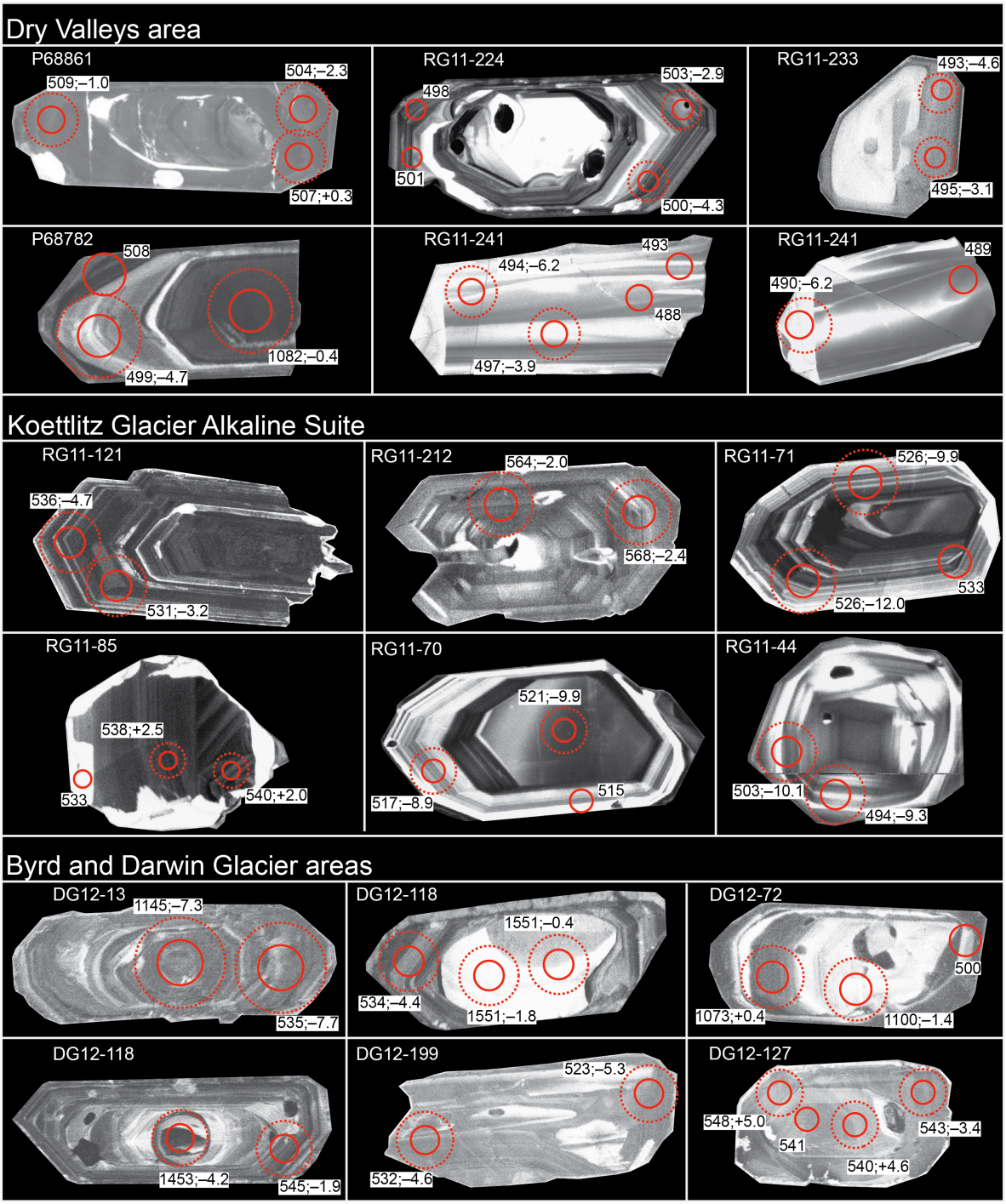

Figure 3.17 Cathodoluminescence (CL) images of representative zircons from different areas. Solid and dashed circles show the locations of laser pits for U-Pb and Hf isotope analyses, respectively. For scale, the Hf laser pits are ~50 mm in diameter. The numbers next to the circles correspond to the $^{206}Pb/^{238}U$ date (first number) and $\varepsilon Hf_{(i)}$ (second number). Propagated uncertainties are typically ± 7 Myr for the $^{206}Pb/^{238}U$ dates and ± 2 for $\varepsilon Hf_{(i)}$.

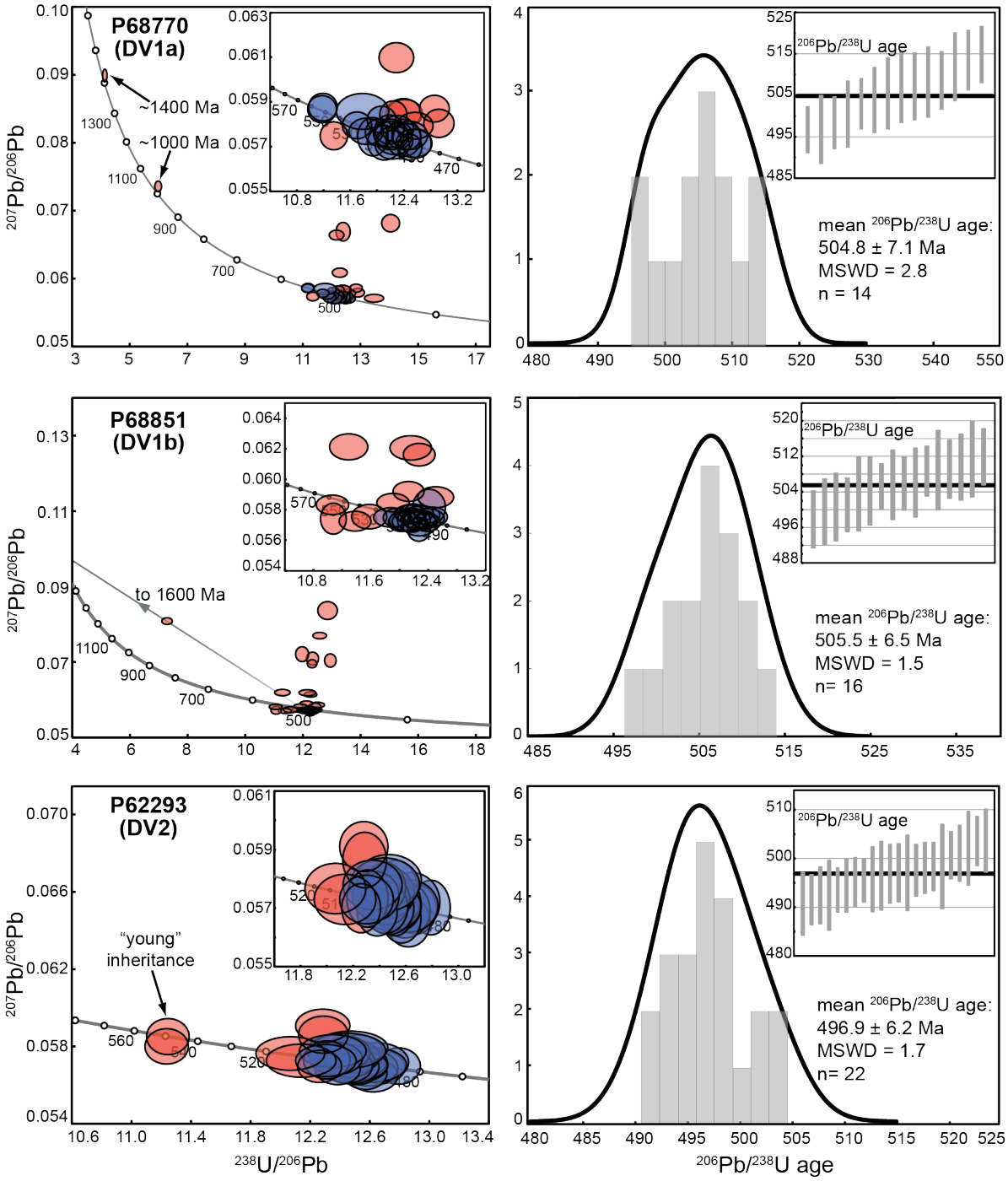
P68770
(DV1a)
~1400 Ma
~1000 Ma
mean 206Pb/238U age:
504.8 ± 7.1 Ma
MSWD = 2.8
n = 14
P68851
(DV1b)
to 1600 Ma
mean 206Pb/238U age:
505.5 ± 6.5 Ma
MSWD = 1.5
n= 16
P62293
(DV2)
"young"
inheritance
mean 206Pb/238U age:
496.9 ± 6.2 Ma
MSWD = 1.7
n= 22
207Pb/206Pb
238U/206Pb
206Pb/238U age

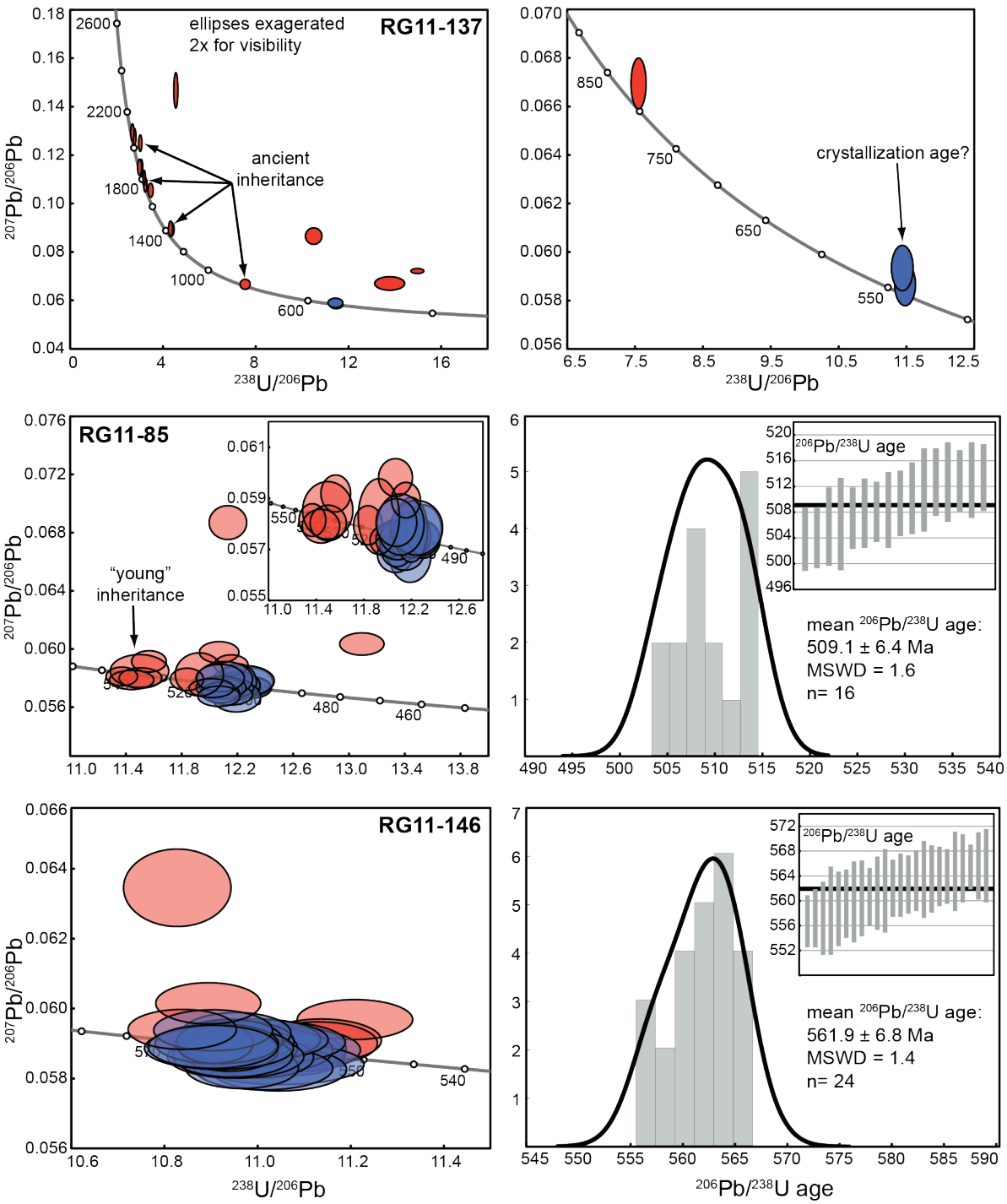
RG11-137
ellipses exagerated
2x for visibility
ancient
inheritance
crystallization age?
RG11-85
"young"
inheritance
mean 206Pb/238U age:
509.1 ± 6.4 Ma
MSWD = 1.6
n= 16
RG11-146
mean 206Pb/238U age:
561.9 ± 6.8 Ma
MSWD = 1.4
n= 24
207Pb/206Pb
238U/206Pb
206Pb/238U age

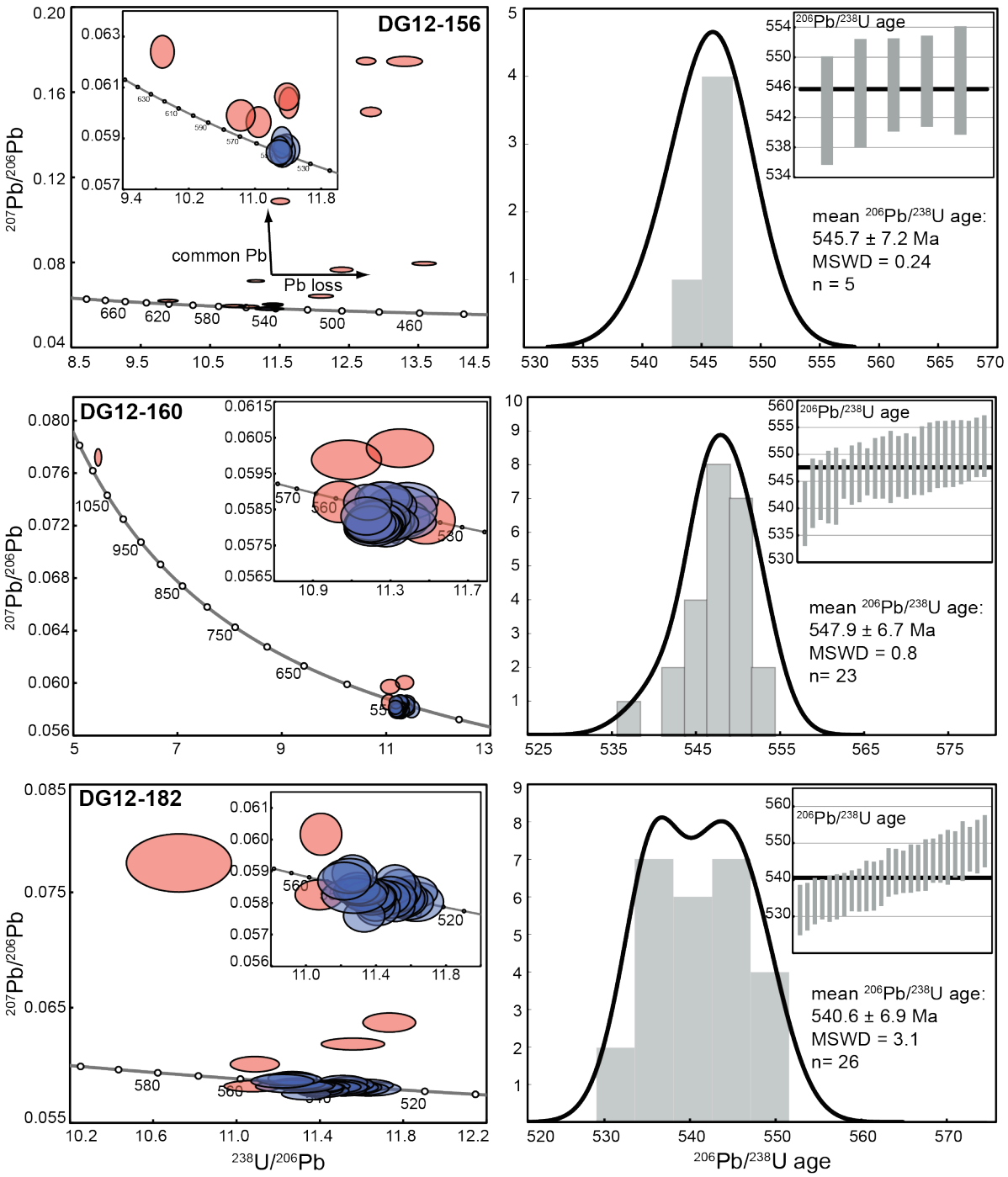

Figure 3.18. Example inverse concordia diagrams and $^{206}Pb/^{238}U$ date distributions for representative samples from each area. These examples demonstrate the effects of ancient (P68770, P68851, RG11-137, DG12-160) and "young" (P68851, P62293, RG11-85) inheritance, the presence of common Pb, and Pb loss. The effects of these processes on the U-Pb systematics are annotated on several of the diagrams. Blue ellipses represent used in the calculation of weighted-mean $^{206}Pb/^{238}U$ dates. Red ellipses represent analyses omitted from the weighted-mean dates.

Zircon Hf Isotopes

One advantage of measuring Hf isotopes in zircon, as opposed to Hf, Nd, or Sr in whole-rock samples is that individual zircon domains may record isotopic evidence of processes such as magma mixing or crustal assimilation (e.g., Griffin et al., 2002; Belousova et al., 2006). However, if a set of zircon Hf analyses from a sample form a statistical population (MSWD = 1), treating the analyses individually could lead to over-interpretation of the range of a statistically predicted distribution. In this study, 8−12 zircon Hf isotope measurements were typically done for each sample, and the Hf isotope compositions typically formed a single population. Therefore, the Hf isotope results from this study are reported as weighted-mean $\varepsilon Hf_{(i)}$ for each sample, unless otherwise noted. For this reason, the Hf isotope results here are interpreted similarly to whole-rock Nd and Sr results. That is, we take the weighted-mean $\varepsilon Hf_{(i)}$ of the zircons to represent the Hf isotope composition of the melt from which they crystallized, and therefore the rock from which they were extracted. Inherited zircon domains were identified using CL images and the U/Pb age of the laser pit that the Hf analysis overlapped (Fig. 3.17). The $\varepsilon Hf_{(i)}$ of inherited zircon domains were not used in the weighted-mean $\varepsilon Hf_{(i)}$ calculations and are reported separately.

The Hf isotope results are reported in Table 3.1. Samples from the DV area span a restricted range of $\varepsilon Hf_{(i)}$ from −7.2 to −0.3, with T_{DM}^{Hf} that range from 1.5 Ga to 1.9 Ga. Samples from the KGAS range in $\varepsilon Hf_{(i)}$ from −11.3 to +3.5, with T_{DM}^{Hf} that range from 1.3 Ga to 2.1 Ga. Samples from the BG area range in $\varepsilon Hf_{(i)}$ from −12.3 to +2.7, with T_{DM}^{Hf} that range from 1.3 Ga to 2.2 Ga. Inherited zircon domains range in $\varepsilon Hf_{(i)}$ from –10.0 to + 9.1, with T_{DM}^{Hf} from 1.3–2.9 Ga.

Whole-Rock Nd-Sr Isotopes

The Nd isotope results are reported in Table 3.1. One sample from the DV area has an $\varepsilon Nd_{(i)}$ = –6.1. Six samples from the KGAS area range in $\varepsilon Nd_{(i)}$ from –8.2 to +0.1. Nine samples from the BG area range in $\varepsilon Nd_{(i)}$ from –10.3 to –3.1. The T_{DM}^{Nd} range from 1.2 to 2.0 Ga. Samples fall close to the εHf-εNd "Terrestrial Array" of Vervoort et al. (1999; Fig. 3.19).

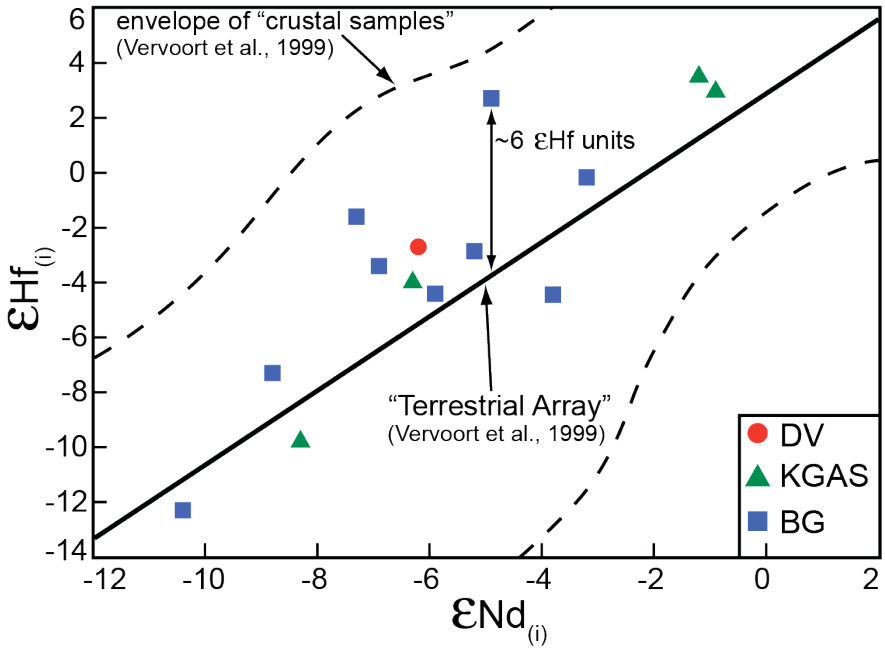

Figure 19. Diagram of $\varepsilon Hf_{(i)}$ versus $\varepsilon Nd_{(i)}$ with the terrestrial array of Vervoort et al. (1999) for reference. Samples generally follow the terrestrial array with deviations of up to 6 εHf units. Most deviations from the array are toward positive $\varepsilon Hf_{(i)}$.

DISCUSSION

Petrologic and Geochemical Variations in Magmatism

There is significant petrological and geochemical variability in the igneous rocks from along a ~500 km segment of the Ross orogen in southern Victoria Land (sVL). Large complexes of orthogneiss, granitoids, and mafic rocks were emplaced in the DV and BG areas, whereas relatively small bodies of alkaline silicates and carbonatites were emplaced in the KGAS. Although the igneous rocks from both the DV and BG areas are dominantly subalkaline and plot primarily in the "volcanic arc granite" fields on tectonic discrimination diagrams (Fig. 3.15), these complexes are compositionally distinct. Some of the igneous rocks in the KGAS have distinctly alkaline compositions and plot in the "within-plate granite" fields on tectonic discrimination diagrams (Fig. 3.15). These rock types, including carbonatites, nepheline syenites, alkaline gabbros, and A-type granites, are much more commonly associated within intraplate tectonic environments (e.g., Sørensen, 1974; Fitton & Upton, 1987; Wooley, 1989) or post-orogenic (e.g., Bonin, 1990; Bonin et al., 1998) magmatism than the continental arc setting inferred for the KGAS.

The geochemical variability of the igneous rocks within each area also rules out a common genetic relationship among the samples within each complex. On Harker diagrams, the samples from each complex do not form coherent arrays, and there is significant dispersion in major- and trace-element concentrations at a given SiO_2 content (Fig. 3.14). These geochemical features could not have developed through simple fractional crystallization/melting processes. Instead, they require variability in magma sources and/or magma evolution processes—for example, different degrees of partial melting, partial melting under different P-T conditions, or different degrees of crustal assimilation.

Despite significant differences in major- and trace-element concentrations, the most primitive rocks from each area, which presumably most closely reflect the primary magma source(s), have remarkably similar normalized trace- and rare earth-element patterns, with similar LILE/HFSE and light REE/heavy REE ratios, negative Nb, P, and Ti anomalies, and positive K and Pb anomalies (Fig. 3.16). These similarities suggest that there are some common features in the magma source(s) in each area, despite the gross petrologic and compositional range of the igneous rocks.

One prominent difference in trace element composition is the variable Sr/Y ratios of samples from each area. Samples from the DV and KGAS areas plot in both the "HiSY" (Sr/Y > 40; Tulloch & Kimbrough, 2003) and "LoSY" fields on a Sr/Y versus SiO_2 diagram (Fig. 3.14), whereas BG samples from this study plot exclusively in the LoSY field. In the KGAS samples, there appears to be a weak negative correlation between Sr/Y and SiO_2, but there is no obvious correlation in the DV and BG samples, suggesting that this ratio is not significantly affected by assimilation–fractional crystallization (AFC) processes. Therefore, the Sr/Y ratio of the samples is taken to reflect the trace element composition of the magma source, or the conditions of melting in the source region. Tulloch and Kimbrough (2003) interpreted HiSY igneous rocks in the Median Batholith of New Zealand and the Peninsular Range of North America to reflect high-pressure melting at the base of the crust during shallow-slab subduction and underthrusting of outboard arc segments. It is therefore inferred that the BG samples represent relatively shallow melting (above the garnet stability field in the lithospheric mantle), whereas the HiSY DV and KGAS samples record higher-pressure melting conditions.

Variability in the Timing and Duration of Magmatism in southern Victoria Land

The timing of magmatism was variable along the sVL segment of the Ross orogen (Fig. 3.20). Martin et al. (2014) dated a ca. 545 Ma xenolith with geochemical affinity to DV granites, and Allibone and Wysoczanski (2002) determined an age of ca. 530 Ma for a small body of orthogneiss. However, the major pulse of magmatism in the DV area was restricted to ca. 23 million years, from 515–492 Ma (Fig. 3.20; Hagen-Peter et al., 2015). A significant volume (inferred from areal exposure) of primarily calc-alkalic plutonic rocks was emplaced during this period, including the ~1000 km^2 Bonney Pluton (Encarnación & Grunow, 1996; Cox et al., 2000; Allibone & Wysoczanski, 2002; Hagen-Peter et al., 2015).

Large calcic and calc-alkalic plutons were apparently emplaced over a similarly short period in the BG area. Most of the BG samples from this study fall within the 550–525 Ma range. The two ages outside of this range (ca. 510 Ma and 502.8 ± 6.2 Ma) are from small leucocratic dikes that crosscut older diorite and orthogneiss. Other age data for the BG area are sparse. Cottle and Cooper (2006b) determined an age of 546 ± 10 Ma for a composite mafic pluton at Fontaine Bluff (Fig. 3.8). Stump et al. (2006) reported ages of 546 ± 7 and 531 ± 8 for a strained granite and a diorite, respectively, from near the Ramseier Glacier (Fig. 3.9). Encarnación and Grunow (1996) reported an age of 515 ± 8 Ma for a biotite-hornblende granite at Cooper Nunatak (Fig. 3.8). Based on a single titanite fraction measured by thermal-ionization mass spectrometry, this date may represent a crystallization age or the timing of closure to lead diffusion during cooling. Nonetheless, most of the large bodies of megacrystic granite, granitic orthogneiss, and diorite/gabbro were emplace over ca. 25 million years, from 550–525 Ma.

In contrast to the DV and BG areas, relatively small volumes of compositionally

diverse igneous rocks were emplaced in the KGAS area over a longer period, ca. 565–500 Ma. The oldest sample (RG11-212; 564.7 ± 7.0 Ma) is a two-mica garnet-bearing orthogneiss. A sub-alkaline gabbro (RG11-146; 561.9 ± 6.8 Ma) is of similar age. Other alkaline mafic rocks, A-type granites, and syenites from this study span ca. 550−542 Ma. A calcite-bearing nepheline syenite from the north side of the Walcott Glacier was emplaced ca. 509 Ma. Previously published zircon U-Pb ages for carbonatites, nepheline syenites, A-type granites, and alkaline mafic rocks range from ca. 557−531 Ma (Hall et al., 1995; Cooper et al., 1997; Mellish et al., 2002; Cottle & Cooper, 2006a; Read, 2010). Subalkaline granitic orthogneiss, granitoids, and mafic rocks were emplaced over the period of ca. 562–499 Ma, partially overlapping the period of alkaline magmatism. It is possible that magmatism in the KGAS was episodic—with pulses of alkaline and subalkaline intrusions separated by millions of years. However, uncertainties of ± 6–7 million years on weighted-mean $^{206}Pb/^{238}U$ dates—interpreted as emplacement ages—preclude discerning between episodic and continuous magmatism.

Large bodies of sub-alkaline orthogneiss and granite (*sensu lato*) were emplaced over similar time intervals (ca. 25 million years) in the DV and BG areas, although the major pulse of magmatism in the DV area initiated ca. 35 million years later than in the BG area. The new geochronology data from this study confirm that alkaline and subalkaline magmatism occurred over similar periods in the KGAS and were contemporaneous with dominantly subalkaline magmatism in both the DV and BG areas.

The Timing of Magmatism Along the Ross Orogen

The 564.7 ± 7.0 Ma two-mica granite (RG11-212) from the KGAS area is the oldest in-place

igneous rock of the Granite Harbour Intrusive Complex (GHI) yet identified (Fig. 3.20) and therefore places constraints on the initiation of Ross-age magmatism in this region. Goodge et al. (2012) identified peaks at 559 ± 5 Ma and 589 ± 5 Ma in a multi-modal zircon U-Pb age distribution from a granitic glacial clast from the central Transantarctic Mountains (cTAM), interpreting the older peak to represent the crystallization age of the rock. Other records of early magmatism during the Ross orogen include ca. 581 Ma and 595 Ma detrital zircon age peaks in sedimentary rocks from the Queen Maud Mountains (QMM; Stump et al., 2007) and sVL (Paulsen et al., 2011), respectively, and a ca. 584 Ma glacially transported igneous clast dredged off the Wilkes Land coast (Goodge & Fanning, 2010). However, the exact provenance, and therefore the context, of these detrital samples is unknown.

Based on the geochronology of in-place igneous rocks, the onset of magmatism appears to have been transient along the Ross orogen (Fig. 3.16). Magmatism commenced in the KGAS ca. 565 Ma. The oldest in-place igneous rocks dated in the cTAM (Goodge et al., 2012), BG area, and northern Victoria Land (nVL; Black & Sheraton, 1990; Fioretti et al., 2005; Bomparola et al., 2006; Tiepolo & Tribuzio, 2008) are all ca. 545–550 Ma. Magmatism in the Queen Maud Mountains appears to have commenced ca. 535 (Paulsen et al., 2013), nearly contemporaneous with the emplacement of small bodies of orthogneiss in the DV area (Allibone & Wysoczanski, 2002). However, if the ca. 545 Ma xenolith with DV granite geochemical affinity (Martin et al., 2014) is taken into account, the early magmatic phase (ca. 550–545) is recorded in the cTAM, BG and DV areas, and nVL. It is possible that early magmatism in the DV area occurred at a deeper crustal level than is presently exposed, and that a younger magmatic complex was emplaced at shallower crustal levels, i.e., an older magmatic complex underlies the complex that is presently exposed at the surface. Further

evidence for his is the presence of "young" inheritance—zircon domains that are tens-of-millions of years older than the apparent crystallization age of the host rock— in samples from the DV area (e.g., Fig. 3.18; P68851; P62293).

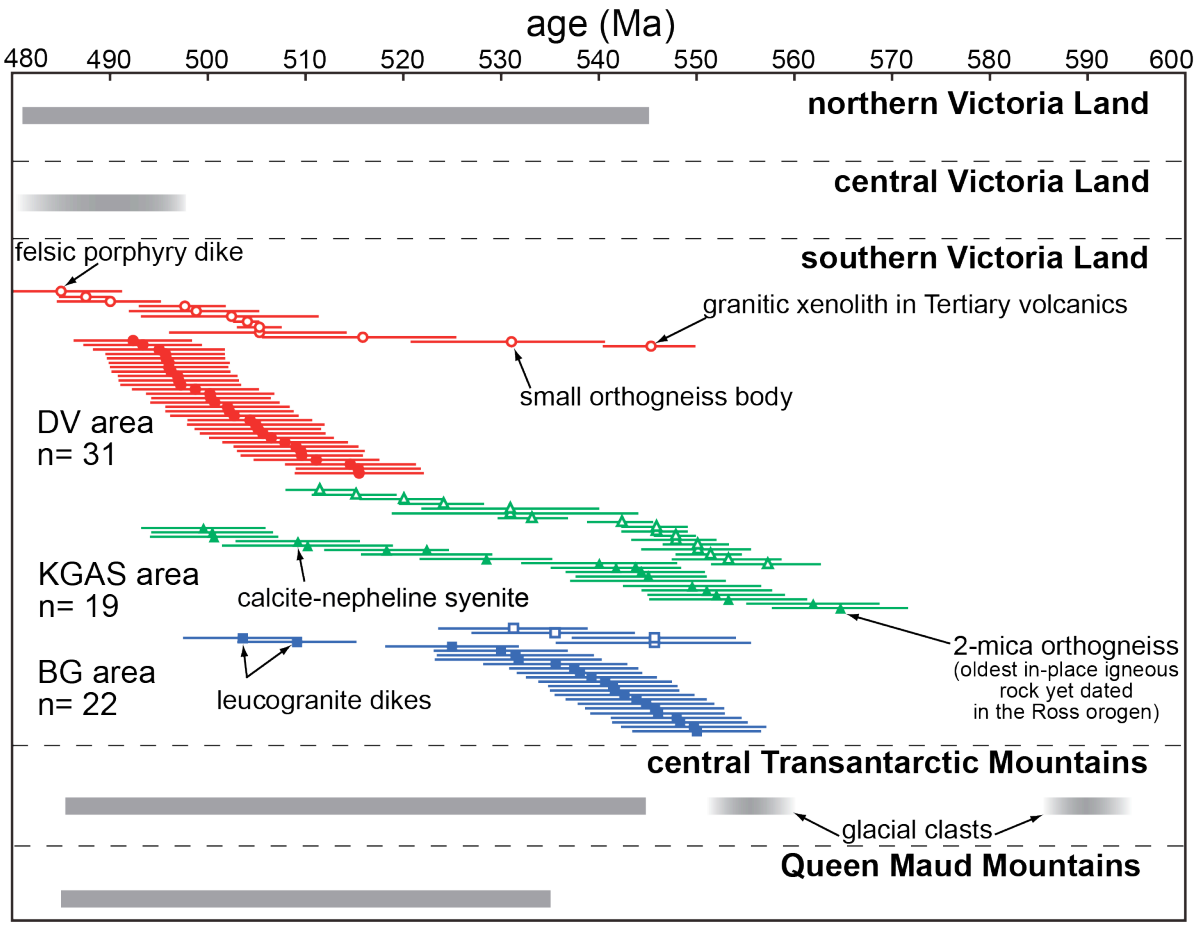

Figure 3.20 Timeline summarizing the zircon U-Pb age data for the Granite Harbour Intrusives along the Ross orogen. Closed symbols are from this study. Open symbols and grey bars are previously published data from the following sources: northern Victoria Land: Black & Sheraton, 1990; Fioretti et al., 2005; Bomparola et al., 2007; Tiepolo & Tribuzio, 2008; central Victoria Land: Rocchi et al., 2009; southern Victoria Land: Rowell et al., 1993; Hall et al., 1995; Encarnación & Grunow, 1996; Cooper et al., 1997; Cox et al., 2000; Allibone & Wysoczanski, 2002; Mellish et al., 2002; Read et al., 2002; Simpson, 2002; Cottle & Cooper, 2006a,b; Read, 2010; Martin et al., 2014; central Transantarctic Mountains: summarized in Goodge et al., 2012; Queen Maud Mountains: Paulsen et at., 2013.

Tectonic Controls on Alkaline Magmatism in a Continental Arc

Alkaline magmatism at convergent margins is typically associated with post-orogenic (PO) stages. The distinction of the alkaline PO magmatism from the preceding subduction- and/or collision-related magmatism may be due to relatively high-temperature melting of lithospheric mantle metasomatically enriched during subduction, followed by increasing primitive mantle components (Bonin et al., 1998). However, there are an increasing number of accounts of alkaline and carbonatitic magmatism within active subduction zone settings (e.g., Carmichael et al., 1996; Abratis & Wörner, 2001; Petrone et al. 2003; D' Orazio et al., 2007).

Cooper et al (1997), Mellish et al. (2002), Read et al. (2002), and Cottle and Cooper (2006a) suggested that the alkaline magmatism in the KGAS was confined to an extensional or transtensional jog along the convergent margin and predated widespread calc-alkaline magmatism in southern Victoria Land. The new geochronology and geochemistry data presented in this study confirm that the alkaline and carbonatitic magmatism within the KGAS was long-lived (at least ca. 562–509 Ma) and contemporaneous with dominantly sub-alkaline magmatism in the adjacent DV and BG areas. Formation of the alkaline magmas in an extensional jog remains a viable hypothesis, although the occurrence of subalkaline magmatism within the KGAS and A-type granitoids in the vicinity of Darwin Glacier (Fig. 3.8; Foggydog suite of Simpson & Cooper, 2002) preclude a clearly delineated extensional province with compositionally restricted magmatism. It is likely that the compositional variation in igneous rocks across sVL reflect differences in magma sources, degrees of melting, and differentiation processes, as opposed to gross differences in tectonic setting.

Potential Magma Sources

Dispersion in the Hf isotope composition of the samples of approximately 16 εHf units (~ –12 to +4; Fig. 3.21) may be due to: 1) derivation from isotopically distinct magma sources, 2) variable degrees of crustal assimilation during magma ascent and emplacement, or 3) assimilation of crustal components with variable Hf isotope compositions. The presence of inherited Proterozoic zircons in many samples (Fig. 3.21a) indicates re-working of pre-existing crust, either as a primary magma source or a contaminant of mantle-derived magmas. A wide range in $\varepsilon Hf_{(i)}$ of inherited zircons of different ages further suggests the presence of crust of variable age and Hf isotope composition in the Precambrian basement underlying the metamorphic and igneous rocks of the Ross orogen. However, if explanation 2 and/or 3 (i.e., crustal assimilation) were the primary cause of the range in $\varepsilon Hf_{(i)}$, there should be a negative correlation between $\varepsilon Hf_{(i)}$ and the degree of differentiation of the samples: crustal assimilation would decrease the $\varepsilon Hf_{(i)}$, whereas increasing the SiO_2 and decreasing the Mg# through contamination with evolved crust and coupled fractional crystallization. No such correlation is evident on a plot of $\varepsilon Hf_{(i)}$ versus SiO_2 (Fig. 3.22). There is a broadening of the range of $\varepsilon Hf_{(i)}$ in the more evolved (high SiO_2; low Mg#) samples, and the lower $\varepsilon Hf_{(i)}$ values in these samples may reflect assimilation of (or direct derivation from) old, low-εHf crust. However, several of the most-evolved samples (> 70% SiO_2) have $\varepsilon Hf_{(i)}$ values that overlap the highest $\varepsilon Hf_{(i)}$ in the most-primitive (low SiO_2; high Mg#) samples—inconsistent with significant crustal assimilation during differentiation. Arrows connecting mafic samples with associated evolved samples (e.g., mafic enclave-host granite pairs) show moderately negative to positive trajectories that are inconsistent with the assimilation of old (low εHf) crust as the dominant cause of magma differentiation.

Additionally, the primitive samples span a range of approximately 7 εHf units (~ –4 to +3). These observations are most readily explained by the derivation of the igneous rocks in sVL from various isotopically distinct magma sources—an interpretation further supported by the petrologic and geochemical diversity of the rocks.

Samples from the DV area have a restricted range of $\varepsilon Hf_{(i)}$ (–7.2 to –0.3; Fig. 3.21b), whereas samples from the KGAS and BG areas span from −12.3 to +2.7 and −11.3 to +3.5, respectively. The higher $\varepsilon Hf_{(i)}$ in the KGAS and BG samples, even in highly evolved rocks, suggests derivation from a more isotopically depleted (high εHf) source than the DV samples. Depleted asthenospheric mantle (DM) was a plausible source given the inferred subduction setting, but none of the samples extend to depleted mantle εHf values (~ +15 at 500 Ma). Such a source is also difficult to reconcile with the alkaline and carbonatitic compositions in the KGAS. This is because: 1) the very low degrees of partial melting required to extract such melts from primitive or depleted mantle are considered unlikely for a subduction zone setting, and 2) the persistence of alkaline magmatism for ca. 50 million years requires a static source not in the convecting asthenospheric mantle (assuming a down-dip velocity of 20–40 km/Myr for asthenosphere convecting through corner flow; Turner & Hawkesworth, 1997). The strongly enriched trace element compositions of the most primitive samples from each area are also at odds with a DM source (Fig. 3.16). These characteristics suggest an isotopically and geochemically enriched source, potentially metasomatized sub-continental lithospheric mantle (SCLM) beneath the arc. The SCLM has been invoked as a potential source of alkaline silicate rocks and associated carbonatites in many localities (e.g., Bailey, 1987; Serri et al., 1993; Arzamastsev et al., 2001; Downes et al., 2005), and also as the source of late-stage lamprophyres and potassic granitoids in the

Ross orogen (Rocchi et al., 2009). We consider variably enriched and metasomatically altered SCLM to have been the most likely source for the alkaline of the KGAS. The metasomatism likely occurred, at least partially, through infiltration of carbonate fluids—explaining the carbonatites in the KGAS and the negative Nb anomalies on normalized trace element plots (Fig. 3.16; Ionov et al., 1993). Plots of the ratios of conservative elements (those that are not introduced to the mantle wedge from slab-derived fluids) and nonconservative elements (introduced to the mantle wedge from a slab-derived fluid) provide further information about the mechanism of mantle wedge metasomatism (Pearce & Peate, 1995). Primitive samples show enrichments in both conservative (Zr/Yb and Nb/Yb) and nonconservative (Th/Yb) element ratios (Fig. 3.23), suggesting that slab-derived fluids were not the only metasomatic agents acting on the mantle wedge beneath the arc. Enrichment in the nonconservative elements may have been ancient (i.e., may have occurred prior to the Ross orogeny) or may have been the result of continental material being introduced into the wedge through sediment subduction or tectonic erosion of the upper plate (Behn et al., 2011; Hacker et al., 2011). Alternatively, the enriched compositions of the most primitive samples may have been derived from interaction of DM-derived melts (very small degree partial melts for the alkaline and carbonatitic rocks of the KGAS) with SCLM or recycled crust with lower εHf and much higher concentrations of trace elements. In this case, the isotopic and trace element composition of DM-derived melts may have been significantly altered through minor contamination while retaining a primitive major element composition.

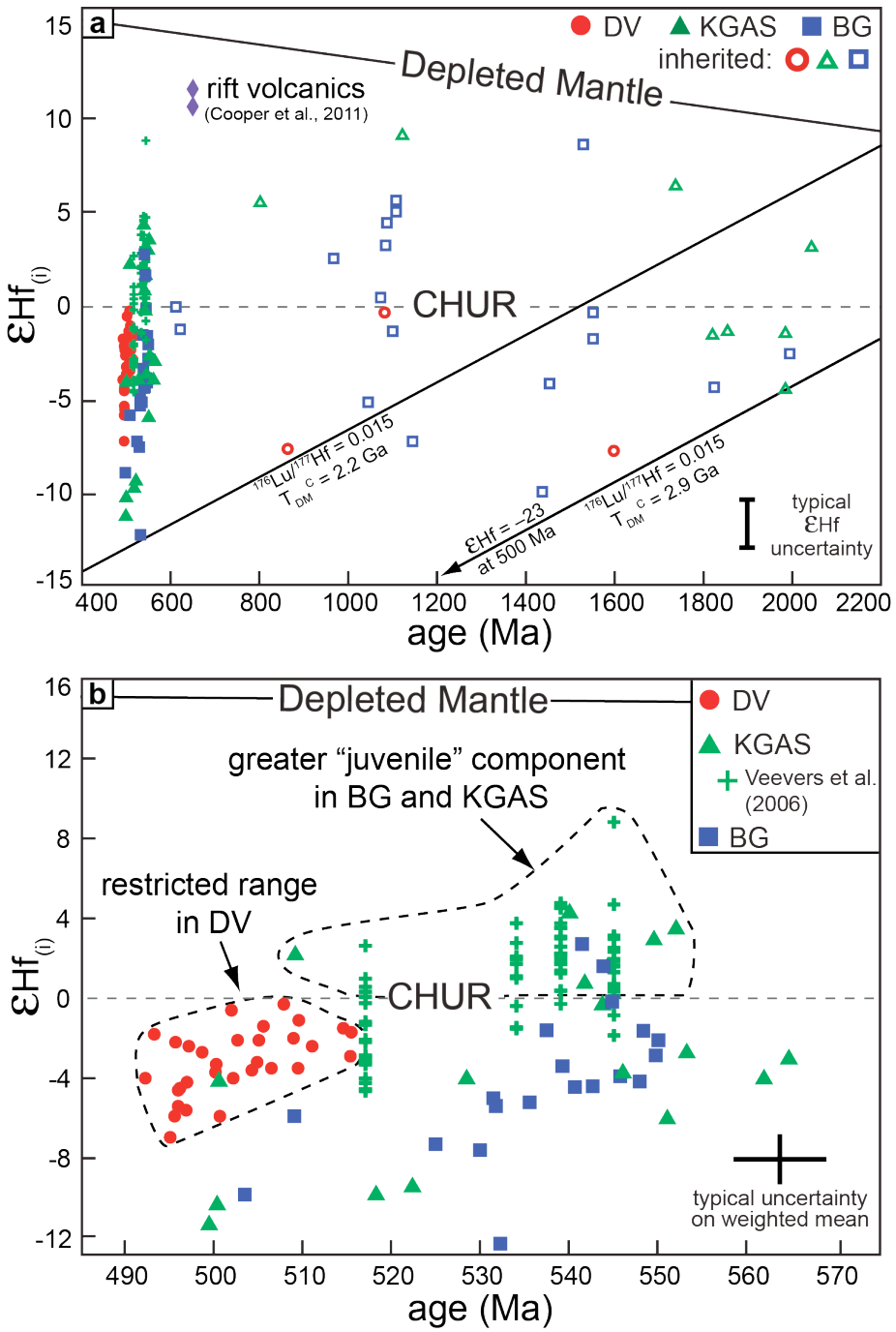

Figure 3.21 Diagrams showing $\varepsilon Hf_{(i)}$ versus age of (a) Ross-age igneous rocks and inherited zircons and (b) only Ross-age igneous rocks. The closed symbols are the weighted-mean $^{206}Pb/^{238}U$ ages and $\varepsilon Hf_{(i)}$ of samples. Purple diamonds are new Hf data for rift-related rhyolite clasts dated by Cooper et al. (2011). The open symbols and green crosses (data from Veevers et al., 2006) are the ages and εHf values of individual zircon analyses. The bottom curve in a shows the Hf isotope evolution of crust extracted at 2.2 Ga (the oldest TDMC of the samples) with an "average crust" $^{176}Lu/^{177}Hf = 0.015$ (Griffin et al., 2000). This curve does not envelope all of the inherited zircon values.

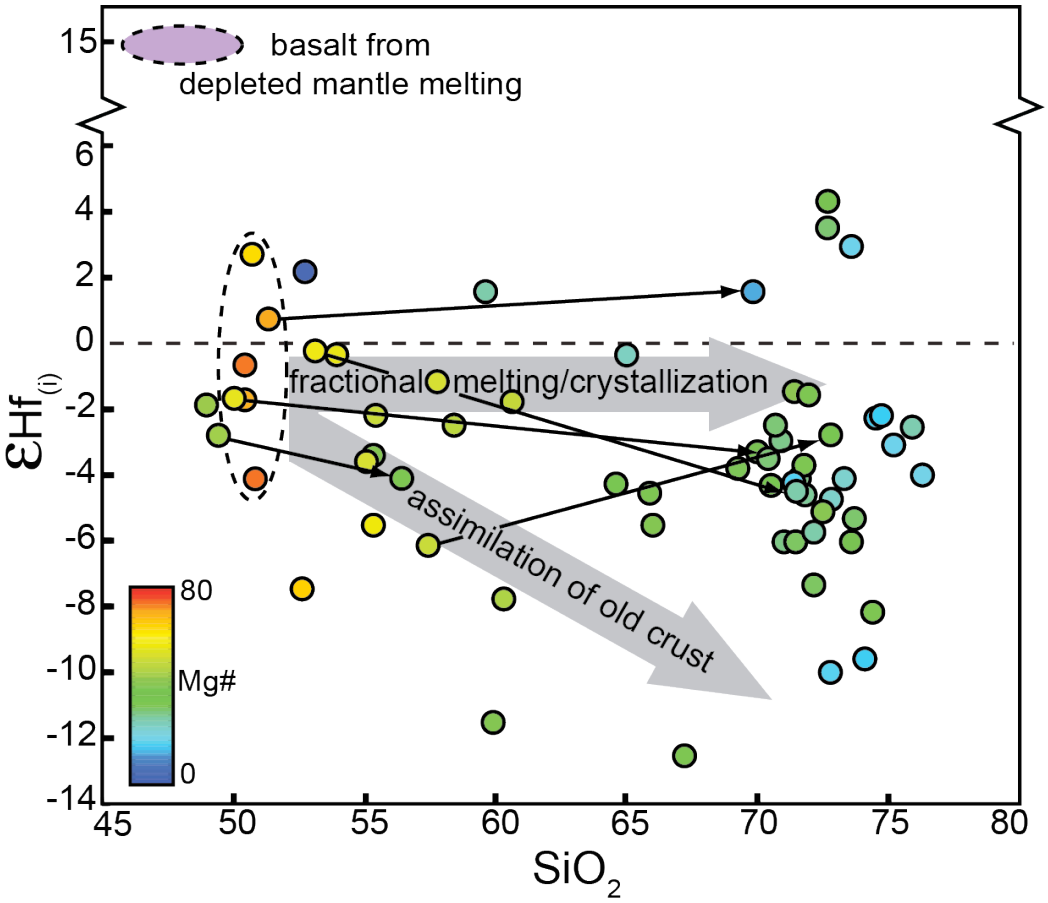

Figure 3.22 Diagram showing $\varepsilon Hf_{(i)}$ versus SiO_2, color-scaled by Mg#. Grey arrows show conceptual trajectories of primitive melts that evolve through fractional melting/ crystallization versus assimilation of old, low-εHf crust. Primitive samples with low SiO_2 and high Mg# have $\varepsilon Hf_{(i)}$ that range from –4 to +3. Evolved samples have a greater range in $\varepsilon Hf_{(i)}$ and lower values, suggesting some degree of crustal reworking. Some evolved samples with $\varepsilon Hf_{(i)}$ up to +4 were potentially derived primarily from juvenile mantle melts with minor degrees of crustal contamination. Small black arrows connect associated mafic and evolved rocks (e.g., enclave-host pairs).

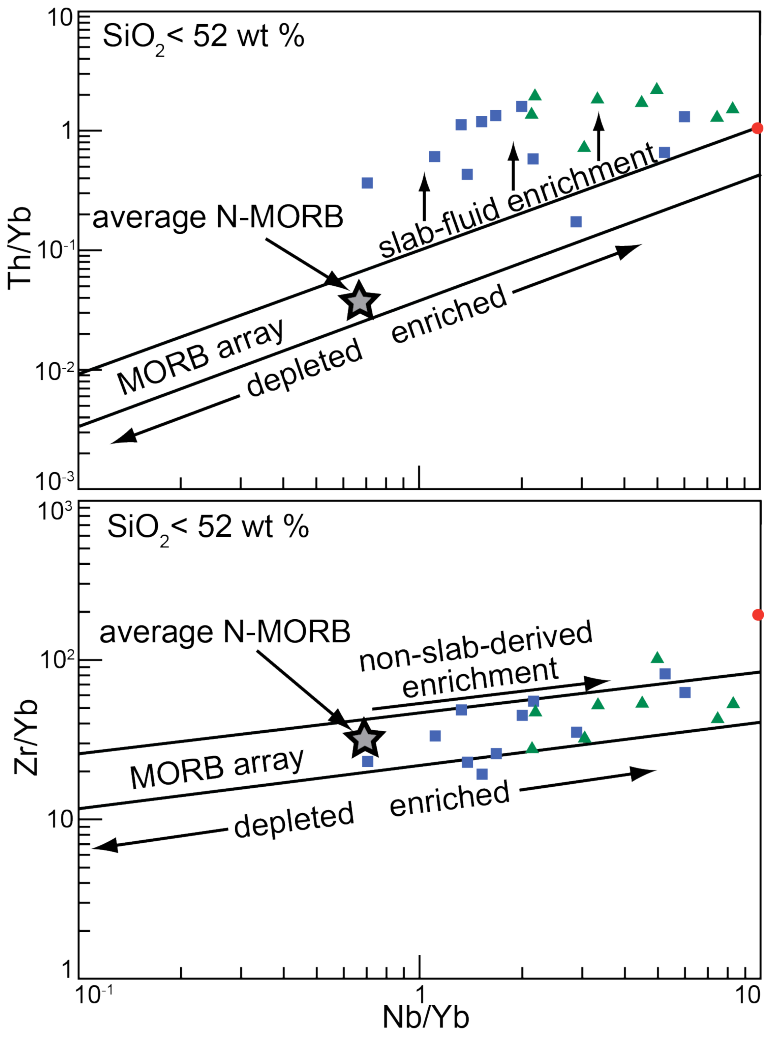

Figure 23. Diagrams of a non-conservative element ratio (Th/Yb) and conservative element ratio (Zr/Yb) plotted against a conservative element ratio (Nb/Yb) (after Pearce & Peate, 1995). Elevation of the Th/Yb off the MORB array is indicative of a contribution from a slab-derived fluid (either directly from the slab or leached from the overriding mantle wedge; Pearce & Peate, 1995). Elevation of the Zr/Yb and Nb/Yb within the mantle array indicates another mode of enrichment independent of slab-derived fluids. Average N-MORB and MORB array from Pearce and Peate (1995).

Crustal Growth Versus Recycling

The $\varepsilon Hf_{(i)}$ distribution of the samples from this study has a peak at ~ $\varepsilon Hf_{(i)}$ = –3 (Fig. 3.24); the $\varepsilon Nd_{(i)}$ distribution is broad (albeit with fewer samples) with predominantly negative values. A first-order interpretation of the negative $\varepsilon Hf_{(i)}$ and $\varepsilon Nd_{(i)}$ values is that the igneous rocks in sVL were derived primarily from reworking of preexisting continental crust of ages yielded by the depleted-mantle model ages of the samples (T_{DM}^{Hf} = 1.3–2.2 Ga; T_{DM}^{Nd} = 1.2–2.0 Ga). Although inherited zircons in the samples do not fall on the DM curve in that range, it is possible that they record earlier episodes of reworking of crust separated at T_{DM}^{Hf} and T_{DM}^{Nd}. This is consistent with the interpretation of Kemp et al. (2006) who observed linear arrays (in εHf versus age) of detrital and inherited zircons from Ordovician and Silurian sedimentary and igneous rocks from the paleo-Pacific margin of Australia (an extension of the Antarctic margin in Gondwana). They interpreted these arrays to represent multiple episodes of zircon crystallization during closed-system reworking of crust generated at the time yielded by the intersections of the arrays with the depleted mantle curve (Fig. 1 of Kemp et al., 2006). Zircons of Pan-African age (contemporaneous with the Ross orogeny) from Kemp et al. (2006) have a wide range of $\varepsilon Hf_{(i)}$, similar to the samples from this study (although several extend to lower $\varepsilon Hf_{(i)}$ of ~ –30). However, the absence of any obvious arrays in the inherited zircons from our study (Fig. 3.21a) precludes closed-system reworking of juvenile crust. Additionally, many of the inherited zircons fall below the T_{DM}^{Hf} trajectory of the lowest $\varepsilon Hf_{(i)}$ Ross-age sample, indicating the presence of lower-εHf crust not directly represented by the Ross-age granitoids. The inherited zircon with the oldest T_{DM}^{Hf} (2.9 Ga) would evolve to an εHf value of ~ –23 at 500 Ma if projected along a crustal evolution curve with $^{176}Lu/^{177}Hf$ = 0.015 (Griffin et al., 2002). Juvenile crust of ca. 3 Ga is exposed in the

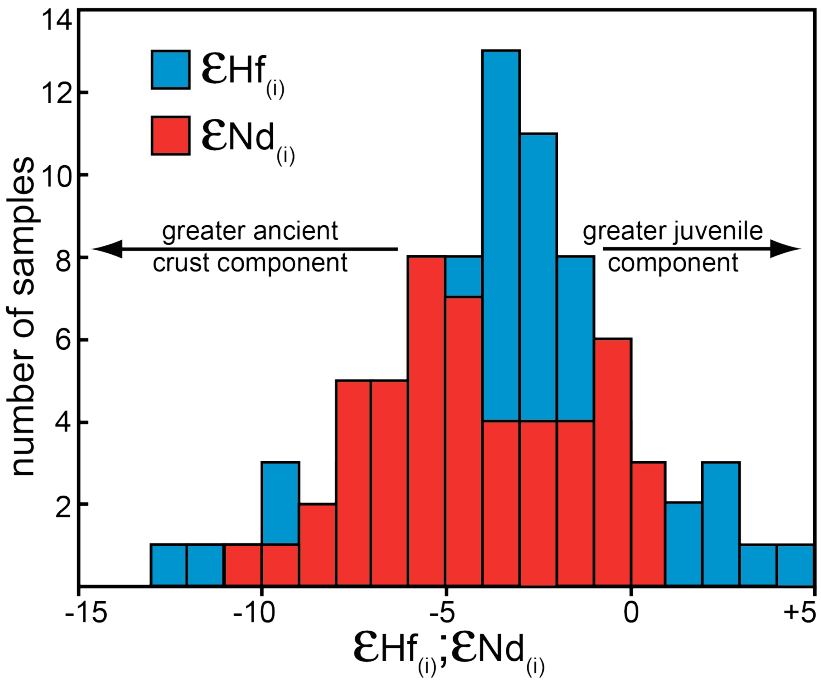

Figure 3.24 Histogram of the $\varepsilon Hf_{(i)}$ and $\varepsilon Nd_{(i)}$ of the igneous rocks from southern Victoria land shows peaks at ~ $\varepsilon Hf_{(i)} = -3$ and ~ $\varepsilon Nd_{(i)} = -5$. Greater degrees of reworking of ancient (low εHf and εNd) crust would shift the distributions to lower epsilon values. The Nd data are from this study and the following sources: Borg and DePaolo (1994); Hall et al. (1995); Cooper et al. (1997); Cox et al. (2000); Mellish et al. (2002); Cottle and Cooper (2006b).

Miller Range in cTAM (Goodge & Fanning, 1999), and it is plausible that there is crust of this age in the basement beneath the magmatic arc in sVL. None of the Ross-age igneous rocks from this study approach such negative εHf values, ruling out closed-system reworking of an ancient crust. Instead, mixing between juvenile (high εHf) and ancient crust (low εHf) components is most likely the cause of the range in isotope composition observed in the sVL igneous rocks. Binary-mixing and assimilation-fractional crystallization (AFC; DePaolo, 1981) models between juvenile and crustal end-members compare a range of mixing scenarios to the observed Hf data. The juvenile end-member, intended to represent a DM-derived basalt, was set at εHf = +14.9 (DM at 500 Ma) with a Hf concentration of 1.6 ppm (the average of the most primitive samples). This end-member was held fixed whereas other parameters were varied in the model with the intention of determining the maximum permissible amount of crustal contamination—i.e., if the juvenile end-member were more isotopically enriched than DM (εHf < +14.9), less crustal contamination would be required to reproduce the observed $\varepsilon Hf_{(i)}$ compositions of the samples. The Hf concentration of the crustal end-member was varied between 1.9 ppm, 3.7 ppm (lower and average crust from Rudnick & Gao, 2003), and 7.4 ppm—the average Hf concentration of four samples from the Skelton Group in the vicinity of the Walcott Glacier (see Chapter 1). The εHf of the crustal end member was varied between –12.3 and –23. The former value is considered the upper limit of the range, as it would require total fusion of this source—with no juvenile contribution—to generate the lowest εHf observed in the samples. The lower limit of the crustal range (εHf = –23) is derived from the crustal evolution projection through the inherited zircon with the oldest T_{DM}^{Hf} (Fig. 3.21a). The presence of numerous inherited

zircons that project below the lowest εHf sample (–12.3) along reasonable crustal evolution trajectories is evidence of ancient crust with εHf < –12.3 at 500 Ma.

Mixing hyperbolae on plots of εHf versus Hf concentration are shown in Figure 3.25. It is important to keep in mind that the samples plotted on the diagrams in Figure 3.14 do not represent cogenetic magma series, and therefore are not expected to fall along clearly defined mixing hyperbolae. However, feasible hyperbolae should envelop the range of data. It is clear in binary mixing hyperbolae between the defined end-members do not explain the range in data, in particular the high Hf concentration of many of the samples (Fig. 3.25). Samples with relatively low Hf concentrations could potentially be explained by these models with crustal contributions (for crust with εHf = –12.3) of ~30–60% required to reach εHf = –3 (the peak of the distribution in Fig. 3.23). Binary mixing hyperbolae with the εHf = –23 crustal end-member (not shown in Fig. 3.25) require only ~ 15–30% crustal contribution to reach εHf = –3 and ~35–70% to reach εHf = –12.3 (the lowest-εHf sample). The binary mixing models assume total fusion of the crustal end-member, whereas contributions from crustal partial melts are perhaps more likely. Some amount of zircon is predicted to survive partial melting of different types of crustal rocks (especially in systems with high Zr content; Kelsey et al., 2008; Yakymchuk & Brown, 2014). If any zircon was retained in the restite, the Hf concentration of the partial melt would have been lower (and more radiogenic) than in the bulk crustal end-member. Therefore, there may have been greater degrees of crustal contamination than is evident from the simple Hf binary mixing models. Inherited zircon are direct evidence for incomplete dissolution of zircon during assimilation. However, the high Hf concentrations of many of the samples suggest a high-Hf crustal end-member. Additionally, the samples plot close to the εHf-εNd “Terrestrial Array” (Fig. 3.19; Vervoort

et al., 1999), whereas residual zircon would likely decouple these two isotopic systems.

Bulk Hf partition coefficients (D_{Hf}) in the AFC models were calculated using mineral/liquid D_{Hf} for mafic bulk compositions from the GERM database (earthref.org/GERM) with fractionation of 45% plagioclase, 20% amphibole, 20% clinopyroxene, 5% olivine, 5% orthopyroxene, 5% biotite, and variable amounts of zircon. Because of the low D_{Hf} for the typical rock-forming minerals, reasonable changes the proportion of major minerals has relatively little effect on the bulk D_{Hf}. Different zircon modes were calculated from the range of zirconium concentrations in the samples—assuming that all of the zirconium resides in zircons. Models with exponentially decreasing D_{Hf} (after 10% assimilation) were intended to simulate zircon saturation followed by decreasing modal abundance of fractionating zircon. These parameters are very difficult to constrain, but they were varied widely to explore a range of permissible scenarios.

Assimilation-fractional crystallization models with equal assimilation and fractional crystallization rates (r = 1; DePaolo, 1981) are able to reproduce a range of data with relatively low Hf concentrations (Fig. 3.25). These models, with a range of end-member compositions and bulk Hf partition coefficients, reach $\varepsilon Hf = -3$ (the mode of the samples; Fig. 3.24) with 15–35% recycled crust, demonstrating that that the crustal component may be subordinate to the juvenile component in producing compositions that may interpreted as reworked ancient crust. Models with r = 1 do not explain the samples with higher εHf and Hf concentrations. Models with r < 1 (fractional crystallization outpaces assimilation) evolve to shallower trajectories which overlap with these samples but involve greater degrees of crustal assimilation. However, for r < 1, the increasing increments of crustal assimilation are relative to incrementally *decreasing* masses of magma (fractional crystallization outpaces

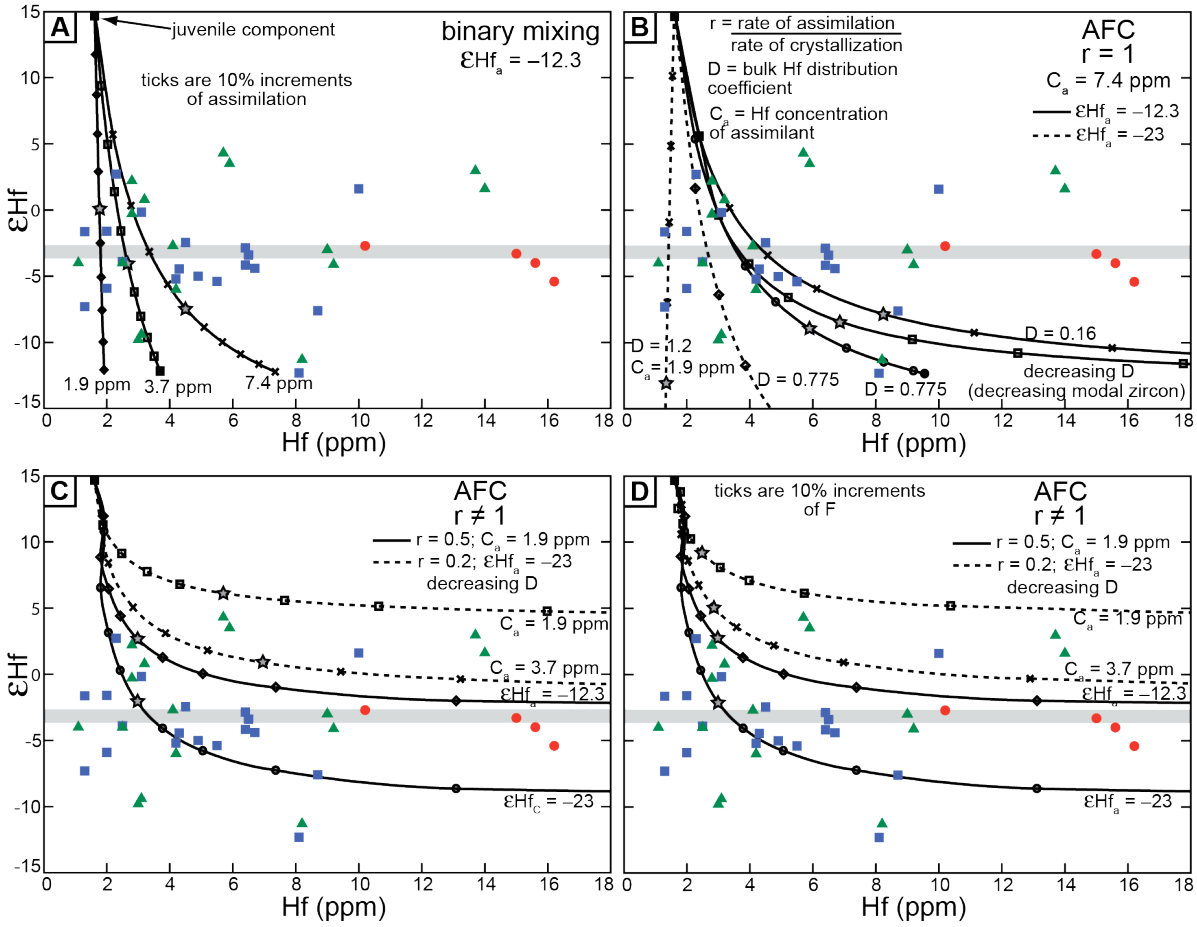

Figure 3.25 (A) Binary mixing models with the defined end-members (see text for explanation) can potentially explain the a range of samples with low Hf concentrations but do not adequately explain samples with high Hf concentrations and a range of εHf. (B) Similarly, AFC models with an equal rate of assimilation and fractional crystallization (r = 1) do not reproduce the samples with high Hf concentrations. (C) AFC models with r < 1 can reproduce the samples with relatively high εHf and Hf concentrations and εHf, though these curves essentially mimic pure fractional crystallization (horizontal) trajectories after early decreases in εHf. (D) The same mixing curves as in C, but with tick marks representing 10% increments of F (remaining mass/original mass; M/M_0). Tick marks for A–C represent 10% increments of assimilated mass relative to the remaining magma mass. The grey bars represents the mode of the εHf distribution of the samples (Fig. 3.24). Values with subscript "a" are for the crustal assimilant end-member. Only samples with Hf isotope and concentration data are plotted here.

assimilation). For example, in the case of r = 0.2, a melt that reaches 70% assimilation is already 90% crystallized—i.e., the mass of assimilated crust is only ~23% of the starting mass of the magma. These trajectories are essentially dominated by fractional crystallization (near-horizontal) after an initial decrease in εHf.

SUMMARY AND CONCLUSIONS

Igneous rocks with gross petrographic and geochemical compositions occur along a ~500 km segment of the Ross orogen in southern Victoria Land. Large complexes of dominantly sub-alkaline granitoids in the Dry Valleys and Byrd Glacier area bound a suite of alkaline silicate rocks and carbonatites, more commonly associated with intraplate and continental-rift tectonic settings, though the boundaries between the complexes are not clearly delineated. Extensive geochronology on greater than 70 samples confirms that the alkaline and carbonatitic magmatism was at least partially contemporaneous with large-scale subduction-related magmatism, though the onset and duration of magmatism was transient along the arc. Despite the significant petrographic and major-element differences between rocks, the most primitive samples from each area have broadly similar and strongly enriched trace element compositions. The most primitive samples also have relatively *enriched* Hf isotope compositions (low εHf). A broadening of the range of εHf values in more evolved samples suggests some degree of crustal assimilation during differentiation, but similar εHf in associated mafic and felsic rocks is consistent with essentially closed-system differentiation with little crustal contamination. Binary mixing and assimilation-fractional crystallization models—accounting for a range of possible scenarios—support the interpretation that crustal assimilation may have been subordinate to fractional crystallization in the differentiation of

the magmas. The estimates of crustal assimilation may also be too high if the juvenile component had lower εHf than the depleted-mantle-derived end-member used in the calculations. These results suggest that igneous rocks with negative εHf values, which resemble ancient crust, may actually be differentiates of juvenile magmas with less than 50% crustal contamination, and therefore represent significant additions of continental crust through arc magmatism.

References

Abratis, M., & Wörner, G. (2001). Ridge collision, slab-window formation, and the flux of Pacific asthenosphere into the Caribbean realm. *Geology*, *29*, 127–130.

Ague, J. J., & Baxter, E. F. (2007). Brief thermal pulses during mountain building recorded by Sr diffusion in apatite and multicomponent diffusion in garnet. *Earth and Planetary Science Letters*, *9*, 500−516.

Ague, J. J., & Carlson, W. D. (2013). Metamorphism as garnet sees it: the kinetics of nucleation and growth, equilibration, and diffusional relaxation. *Elements*, *9*, 439–445.

Ahrens, L.H., & Erlank, A.J. (1969). Hafnium. In: Wedapohl, K.H. (Ed.), *Handbook of Geochemistry, Vol. 2.* New York: Springer-Verlag.

Aleinikoff, J. N., Schenck, W. S., Plank, M. O., Srogi, L., Fanning, C. M., Kamo, S. L., & Bosbyshell, H. (2006). Deciphering igneous and metamorphic events in high-grade rocks of the Wilmington Complex, Delaware: Morphology, cathodoluminescence and backscattered electron zoning, and SHRIMP U-Pb geochronology of zircon and monazite. *Geological Society of America Bulletin*, *118*, 39–64.

Allibone, A. H. (1992). Low pressure/high temperature metamorphism of Koettlitz group schists, Taylor Valley and upper Ferrar Glacier area, South Victoria Land, Antarctica. *New Zealand journal of geology and geophysics*, *35*, 115−127.

Allibone, A. H., & Norris, R. J. (1992). Segregation of leucogranite microplutons during syn-anatectic deformation: an example from the Taylor Valley, Antarctica. *Journal of Metamorphic Geology*, *10*, 589−600.

Allibone A.H., Cox, S.C., Graham, I.J., Smillie, R.W., Johnstone, R.D., Ellery, S.G., and Palmer, K. (1993a). Granitoids of the Dry Valleys area, southern Victoria Land, Antarctica; plutons, field relationships, and isotopic dating. *New Zealand Journal of Geology and Geophysics*, *36,* 281–297.

Allibone, A.H., Cox, S.C., and Smillie, R.W. (1993b). Granitoids of the Dry Valleys area, southern Victoria Land: Geochemistry and evolution along the early Paleozoic Antarctic Craton margin. *New Zealand Journal of Geology and Geophysics*, *36*, 299–316.

Allibone, A., & Wysoczanski, R. (2002). Initiation of magmatism during the Cambrian-Ordovician Ross orogeny in southern Victoria Land, Antarctica: *Geologic Society of America Bulletin*, *114*, 1007–1018.

Armienti, P., Ghezzo, C., Innocenti, F., Manetti, P., Rocchi, S., & Tonarini, S. (1990). Isotope geochemistry and petrology of granitoid suites from Granite Harbour intrusives of the Wilson Terrane, North Victoria Land, Antarctica: *European journal of mineralogy*,

p. 103–124.

Arzamastsev, A. A., Bea, F., Glaznev, V. N., Arzamastseva, L. V., & Montero, P. (2001). Kola alkaline province in the Paleozoic: evaluation of primary mantle magma composition and magma generation conditions. *Russian Journal of Earth Sciences*, *3*, 3–24.

Aslund, T.A. (1990). Magmatism and metamorphism of mafic intrusives of the Dromedary massif, Antarctica. *Unpublished PhD thesis, University of Otago, Dunedin, New Zealand*.

Bailey, D.K. (1987). Mantle metasomatism—perspective and prospect. In: Fitton, J.G., & Upton, B.G.J. (Eds.). *The Alkaline Rocks, Oxford: Blackwell Scientific, 1–13.*

Barrett, P. J. (1981). History of the Ross Sea region during the deposition of the Beacon Supergroup 400-180 million years ago. *Journal of the Royal Society of New Zealand*, *11*, 447−458.

Barton, M.D. (1996). Granitic magmatism and metallogeny of southwestern North America. *Transaction of the Royal Society of Edinburgh: Earth Sciences*, *87*, 261–280.

Barton, M.D., Battles, D.A., Debout, G.E., Capo, R.C., Christensen, J.N., Davis, S.R., Hanson, R.B., Michelsen, C.J., & Trim, H.E. (1988) Mesozoic contact metamorphism in the western United States. In: Ernst, W.G. (Ed.), *Metamorphism and crustal evolution of the western United States*. Englewood Cliffs, New Jersey: Prentice Hall, 110–178.

Baxter, E. F., & Scherer, E. E. (2013). Garnet geochronology: timekeeper of tectonometamorphic processes. *Elements*, *9*, 433–438.

Behn, M. D., Kelemen, P. B., Hirth, G., Hacker, B. R., & Massonne, H. J. (2011). Diapirs as the source of the sediment signature in arc lavas. *Nature Geoscience*, *4*, 641–646.

Belousova E.A., Griffin, W.L., & O'Reilly, S.Y. (2005). Zircon crystal morphology, trace element signatures and Hf isotope composition as a tool for petrogenetic modeling: Examples from eastern Australian granitoids. *Journal of Petrology*, *47*, 329–353.

Belousova, E.A., Kostitsyn, Y.A., Griffin W.L., Begg G.C., O'Reilly S.Y., & Pearson N.J. (2010). The growth of the continental crust: Constraints from zircon Hf-isotope data. *Lithos*, *119*, 457–466.

Bizzarro, M., Baker, J.A., Haack, H., Ulfbeck, D., & Rosing, M. (2003). Early history of Earth's crust-mantle system inferred from hafnium isotopes in chondrites. *Nature*, *421*, 931–933.

Black, L. P., & Sheraton, J. W. (1990). The influence of Precambrian source components on the U-Pb zircon age of a Palaeozoic granite from northern Victoria Land, Antarctica. *Precambrian Research*, *46*, 275–293.

Blichert-Toft, J., Chauvel, C., & Albarède, F. (1997). Separation of Hf and Lu for high-precision isotope analysis of rock samples by magnetic sector-multiple collector ICP-MS. *Contributions to Mineralogy and Petrology*, *127*, 248–260.

Blichert-Toft, J. (2008). The Hf isotopic composition of zircon reference material 91500. *Chemical Geology*, *253*, 252–257.

Bloch, E., Ganguly, J., Hervig, R., & Cheng, W. (2015). ^{176}Lu–^{176}Hf geochronology of garnet I: experimental determination of the diffusion kinetics of Lu^{3+} and Hf^{4+} in garnet, closure temperatures and geochronological implications. *Contributions to Mineralogy and Petrology*, *169*, 1–18.

Bomparola, R. M., Ghezzo, C., Belousova, E., Griffin, W. L., & O'Reilly, S. Y. (2006). Resetting of the U–Pb Zircon System in Cambro-ordovician intrusives of the deep freeze range, Northern Victoria Land, Antarctica. *Journal of Petrology*, *48*, 327–364.

Bonin, B. (1990). From orogenic to anorogenic settings: evolution of granitoid suites after a major orogenesis. *Geological Journal*, *25*, 261–270.

Bonin, B., Azzouni-Sekkal, A., Bussy, F., & Ferrag, S. (1998). Alkali-calcic and alkaline post-orogenic (PO) granite magmatism: petrologic constraints and geodynamic settings. *Lithos*, *45*, 45–70.

Borg, S.G., & DePaolo, D.J. (1991). A tectonic model of the Antarctic Gondwana margin with implications for southeastern Australia: Isotopic and geochemical evidence. *Tectonophysics*, *196*, 339–358.

Borg, S.G., & DePaolo, D.J. (1994). Laurentia, Australia, and Antarctica as a Late Proterozoic supercontinent: Constraints from isotopic mapping. *Geology*, *22*, 307–310.

Borg, S.G., Stump, E., Chappell, B.W., McCulloch, M.T., Wyborn, D., Armstrong, R.L., & Holloway, J.R. (1987). Granitoids of Northern Victoria Land, Antarctica: Implications of chemical and isotopic variations to regional crustal structure and tectonics. *American Journal of Science*, *287*, 127–169.

Borg, S. G., DePaolo, D. J., Wendlandt, E. D., & Drake, T. G. (1989). Studies of granites and metamorphic rocks, Byrd Glacier area. *Antarctic Journal of the United States*, *24*, 19–21.

Borg, S.G., DePaolo, D.J., & Smith, B.M. (1990). Isotopic structure and tectonics of the central Transantarctic Mountains. *Journal of Geophysical Research*, *95*, 6647–6667.

Bouvier, A., Vervoort, J. D., & Patchett, P. J. (2008). The Lu–Hf and Sm–Nd isotopic composition of CHUR: constraints from unequilibrated chondrites and implications for the bulk composition of terrestrial planets. *Earth and Planetary Science Letters*, *273*, 48−57.

Caddick, M. J., Konopásek, J., & Thompson, A. B. (2010). Preservation of garnet growth zoning and the duration of prograde metamorphism. *Journal of Petrology*, *51*, 2327–2347.

Carlson, W. D. (2006). Rates of Fe, Mg, Mn, and Ca diffusion in garnet. *American Mineralogist*, *91*, 1–11.

Carlson, W. D. (2012). Rates and mechanism of Y, REE, and Cr diffusion in garnet. *American Mineralogist*, *97*, 1598–1618.

Carmichael, I. S. E., Lange, R. A., & Luhr, J. F. (1996). Quaternary minettes and associated volcanic rocks of Mascota, western Mexico: a consequence of plate extension above a subduction modified mantle wedge. *Contributions to Mineralogy and Petrology*, *124*, 302–333.

Carosi, R., Giacomini, F., Talarico, F., & Stump, E. (2007). Geology of the Byrd Glacier discontinuity (Ross Orogen): new survey data from the Britannia Range, Antarctica. *U.S. Geological Survey and The National Academies Short Research Paper*, 030, 7 p.

Cawood, P. A. (2005). Terra Australis Orogen: Rodinia breakup and development of the Pacific and Iapetus margins of Gondwana during the Neoproterozoic and Paleozoic. *Earth-Science Reviews*, *69*, 249–279.

Cawood, P. A., & Buchan, C. (2007). Linking accretionary orogenesis with supercontinent assembly. *Earth-Science Reviews*, *82*, 217–256.

Cawood, P. A., Leitch, E. C., Merle, R. E., & Nemchin, A. A. (2011). Orogenesis without collision: Stabilizing the Terra Australis accretionary orogen, eastern Australia. *Geological Society of America Bulletin*, *123*, 2240–2255.

Cherniak, D. J., Watson, E. B., Grove, M., & Harrison, T. M. (2004). Pb diffusion in monazite: a combined RBS/SIMS study. *Geochimica et Cosmochimica Acta*, *68*, 829–840.

Chu, N. C., Taylor, R. N., Chavagnac, V., Nesbitt, R. W., Boella, R. M., Milton, J. A., German, C.R., Bayon, G, & Burton, K. (2002). Hf isotope ratio analysis using multi-collector inductively coupled plasma mass spectrometry: an evaluation of isobaric interference corrections. *Journal of Analytical Atomic Spectrometry*, *17*, 1567–1574.

Connolly, J. A. D. (2005). Computation of phase equilibria by linear programming: a tool for geodynamic modeling and its application to subduction zone decarbonation. *Earth and Planetary Science Letters*, *236*, 524–541.

Connolly, J. A. D. (2009). The geodynamic equation of state: what and how. *Geochemistry, Geophysics, Geosystems*, *10*, 1–19.

Cook, Y.A. (1997). The Skelton Group and the Ross Orogeny. *Unpublished PhD thesis, University of Otago, Dunedin, New Zealand*.

Cook, Y. A., & Craw, D. (2001). Amalgamation of disparate crustal fragments in the Walcott Bay-Foster Glacier area, South Victoria Land, Antarctica. *New Zealand Journal of Geology and Geophysics*, *44*, 403–416.

Cooper, A.F., Worley, B.A., Armstrong, R.A., & Price, R.C. (1997). Synorogenic alkaline and carbonatitic magmatism in the Transantarctic Mountains of South Victoria Land, Antarctica. In: Ricci, C.A. (Ed.), *The Antarctic Region; Geological Evolution and Processes, 7th International Symposium on Antarctic Earth Sciences*. Siena: Terra Antartica Publication, 245–252.

Cooper, A. F., Maas, R., Scott, J. M., & Barber, A. J. (2011). Dating of volcanism and sedimentation in the Skelton Group, Transantarctic Mountains: Implications for the Rodinia-Gondwana transition in southern Victoria Land, Antarctica. *Geological Society of America Bulletin*, *123*, 681–702.

Cottle, J.M. (2002). Evolution of a convergent margin. *Unpublished PhD thesis, University of Otago, Dunedin, New Zealand*.

Cottle, J. M., & Cooper, A. F. (2006a). Geology, geochemistry, and geochronology of an A-type granite in the Mulock Glacier area, southern Victoria Land, Antarctica. *New Zealand Journal of Geology and Geophysics*, *49*, 191–202.

Cottle, J. M., & Cooper, A. F. (2006b). The Fontaine Pluton: An early Ross Orogeny calc-alkaline gabbro from southern Victoria Land, Antarctica. *New Zealand Journal of Geology and Geophysics*, *49*, 177–189.

Cottle, J. M., Burrows, A. J., Kylander-Clark, A., Freedman, P. A., & Cohen, R. S. (2013). Enhanced sensitivity in laser ablation multi-collector inductively coupled plasma mass spectrometry. *Journal of Analytical Atomic Spectrometry*, *28*, 1700–1706.

Cox, S. C. (1992). Garnet-biotite geothermometry of Koettlitz Group metasediments, Wright Valley, South Victoria Land, Antarctica. *New Zealand journal of geology and geophysics*, *35*, 29−40.

Cox, S.C. (1993). Inter-related plutonism and deformation in South Victoria Land, Antarctica. *Geological Magazine*, *130*, 1–14.

Cox, S.C., Parkinson, D.L., Allibone, A.H., & Cooper, A.F. (2000). Isotopic character of Cambro-Ordovician plutonism, southern Victoria Land, Antarctica. *New Zealand Journal of Geology and Geophysics*, *43*, 501–520.

Cox, S.C., Turnbull, I.M., Isaac, M.J., Townsend, D.B., & Smith Lyttle, B., compilers

(2012). Geology of southern Victoria Land, Antarctia: New Zealand Institute of Geological and Nuclear Sciences geologic map, 22, scale 1:250,000.

Davidson, J. P., & Arculus, R. J. (2005). The significance of Phanerozoic arc magmatism in generating continental crust. In: Brown, M. & Rushmer, T. (Eds.), *Evolution and Differentiation of the Continental Crust, Cambridge: Cambridge University Press*, 135–172.

Dalziel, I.W.D., & Elliot, D.H. (1982). West Antarctica: Problem child of Gondwanaland. *Tectonics*, *1*, 3–19.

Dalziel, I.W.D. (1992). Antarctica: a tale of two supercontinents. *Annual Review of Earth and Planetary Science*, *20*, 501–526.

Davies, J.H. & Bickle, M.J. (1991). A physical model for the volume and composition of melt produced by hydrous fluxing above subduction zones. *Philosophical Transactions of the Royal Society of London, 335,* 355–364.

DeCelles, P. G., Ducea, M. N., Kapp, P., & Zandt, G. (2009). Cyclicity in Cordilleran orogenic systems. *Nature Geoscience*, *2*, 251–257.

DePaolo, D. J. (1981). Trace element and isotopic effects of combined wallrock assimilation and fractional crystallization. *Earth and planetary science letters*, *53*, 189−202.

DePaolo, D. J., Linn, A. M., & Schubert, G. (1991). The continental crustal age distribution: Methods of determining mantle separation ages from Sm - Nd isotopic data and application to the southwestern United States. *Journal of Geophysical Research: Solid Earth (1978–2012)*, *96*, 2071−2088.

Di Vincenzo, G., Palmeri, R., Talarico, F., Andriessen, P.A.M., & Ricci, C.A. (1997). Petrology and geochronology of eclogites from the Lanterman Range, Antarctica. *Journal of Petrology*, *38***,** 1391−1417.

Di Vincenzo, G., & Rocchi, S. (1999). Origin and interaction of mafic and felsic magmas in an evolving late orogenic setting: the Early Paleozoic Terra Nova Intrusive Complex, Antarctica. *Contributions to mineralogy and petrology*, *137*, 15−35.

D'Orazio, M., Innocenti, F., Tonarini, S., & Doglioni, C. (2007). Carbonatites in a subduction system: the Pleistocene alvikites from Mt. Vulture (southern Italy). *Lithos*, *98*, 313–334.

Downes, H., Balaganskaya, E., Beard, A., Liferovich, R., & Demaiffe, D. (2005). Petrogenetic processes in the ultramafic, alkaline and carbonatitic magmatism in the Kola Alkaline Province: a review. *Lithos*, *85*, 48–75.

Ducea, M. (2001). The California Arc: Thick granitic batholiths, eclogite residues, lithospheric-scale thrusting, and magmatic flare-ups. *GSA Today*, *11*, 4–10.

Ducea, M. N., Ganguly, J., Rosenberg, E. J., Patchett, P. J., Cheng, W., & Isachsen, C. (2003). Sm–Nd dating of spatially controlled domains of garnet single crystals: a new method of high-temperature thermochronology. *Earth and Planetary Science Letters*, *213*, 31–42.

Ducea, M.N., & Barton, M.D. (2007). Igniting flare-up events in Cordilleran arcs. *Geology*, *35*, 1047–1050.

Encarnación, J., & Grunow, A. (1996). Changing magmatic and tectonic styles along the paleo-Pacific margin of Gondwana and the onset of early Paleozoic magmatism in Antarctica. *Tectonics*, *15*, 1325–1341.

Encarnación, J., Fleming, T. H., Elliot, D. H., & Eales, H. V. (1996). Synchronous emplacement of Ferrar and Karoo dolerites and the early breakup of Gondwana. *Geology*, *24*, 535−538.

Field, D., & Råheim, A. (1979). Rb-Sr total rock isotope studies on Precambrian charnockitic gneisses from South Norway: evidence for isochron resetting during a low-grade metamorphic-deformational event. *Earth and Planetary Science Letters*, *45*, 32−44.

Findlay, R. H., Craw, D., & Skinner, D. N. B. (1984). Lithostratigraphy and structure of the Koettlitz group, McMurdo sound, Antarctica. *New Zealand journal of geology and geophysics*, *27*, 513−536.

Finn, C. A., Goodge, J. W., Damaske, D., & Fanning, C. M. (2006). Scouting craton's edge in Paleo-Pacific Gondwana. In: Fütterer, D.K., Damaske, D., Kleinschmidt,G., Miller, H., and Tessensohn, F (Eds), *Antarctica: Contributions to global earth sciences*. Berlin: Springer, 165−173.

Fioretti, A. M., Capponi, G., Black, L. P., Varne, R., & Visona, D. (2005). Surgeon island granite SHRIMP zircon ages: a clue for the Cambrian tectonic setting and evolution of the Palaeopacific margin of Gondwana (northern Victoria Land, Antarctica). *Terra Nova*, *17*, 242–249.

Fisher, C. M., Hanchar, J. M., Samson, S. D., Dhuime, B., Blichert-Toft, J., Vervoort, J. D., & Lam, R. (2011). Synthetic zircon doped with hafnium and rare earth elements: a reference material for in situ hafnium isotope analysis. *Chemical Geology*, *286*, 32–47.

Fitton, J.G., & Upton, G.J. (1987). *Alkaline Igneous Rocks*. London: Blackwell Scientific Publications, 568 p.

Foden, J., Elburg, M. A., Dougherty-Page, J., & Burtt, A. (2006). The timing and duration of the Delamerian Orogeny: correlation with the Ross Orogen and implications for Gondwana assembly. *The Journal of Geology*, *114*, 189–210.

Frost, B. R., Barnes, C. G., Collins, W. J., Arculus, R. J., Ellis, D. J., & Frost, C. D. (2001).

A geochemical classification for granitic rocks. *Journal of petrology*, *42*, 2033–2048.

Forsyth, P.J., Mortimer, N., & Turnbull, I.M. (2002). Plutonic Rocks from the Cape Roberts Hinterland: Wilson Piedmont Glacier, Southern Victoria Land, Antarctica. *Terra Antartica*, *9*, 57–72.

Gibson, G. M., & Wright, T. O. (1985). Importance of thrust faulting in the tectonic development of northern Victoria Land, Antarctica. *Nature*, *315***,** 480–483.

Gill, J.B. (1981). *Orogenic Andesites and Plate Tectonics.* New York: Springer-Verlag.

Gleadow, A. J. W., & Fitzgerald, P. G. (1987). Uplift history and structure of the Transantarctic Mountains: new evidence from fission track dating of basement apatites in the Dry Valleys area, southern Victoria Land. *Earth and Planetary Science Letters*, *82*, 1-–14.

Goodge, J. W. (1997). Latest Neoproterozoic basin inversion of the Beardmore Group, central Transantarctic Mountains, Antarctica. *Tectonics*, *16*, 682–701.

Goodge, J. W. (2007). Metamorphism in the Ross orogen and its bearing on Gondwana margin tectonics. *Geological Society of America Special Papers*, *419*, 185–203.

Goodge, J. W., & Fanning, C. M. (1999). 2.5 b.y. of punctuated Earth history as recorded in a single rock. *Geology*, *27*, 1007–1010.

Goodge, J. W., & Fanning, C. M. (2010). Composition and age of the East Antarctic Shield in eastern Wilkes Land determined by proxy from Oligocene-Pleistocene glaciomarine sediment and Beacon Supergroup sandstones, Antarctica. *Geological Society of America Bulletin*, *122*, 1135–1159.

Goodge, J. W., & Finn, C. A. (2010). Glimpses of East Antarctica: Aeromagnetic and satellite magnetic view from the central Transantarctic Mountains of East Antarctica. *Journal of Geophysical Research: Solid Earth (1978–2012)*, *115*.

Goodge, J. W., Borg, S. G., Smith, B. K., & Bennett, V. C. (1991). Tectonic significance of Proterozoic ductile shortening and translation along the Antarctic margin of Gondwana. *Earth and Planetary Science Letters*, *102*, 58−70.

Goodge, J. W., Hansen, V. L., & Peacock, S. M. (1992). Multiple petrotectonic events in high-grade metamorphic rocks of the Nimrod Group, central Transantarctic Mountains, Antarctica. In: Yoshida, Y., Kaminuma, Y., and Shiraishi, K. (Eds.), *Recent Progress in Antarctic Earth Science*. Tokyo: Terra Scientific, 203−209.

Goodge, J. W., Hansen, V. L., Peacock, S. M., Smith, B. K., & Walker, N. W. (1993a). Kinematic evolution of the Miller Range shear zone, central Transantarctic Mountains, Antarctica, and implications for Neoproterozoic to early Paleozoic tectonics of the East Antarctic margin of Gondwana. *Tectonics*, *12*, 1460–1478.

Goodge, J.W., Walker N.W., & Hansen, V.L. (1993b). Neoproterozoic- Cambrian basement-involved orogenesis within the Antarctic margin of Gondwana. *Geology*, *21*, 37–40.

Goodge, J.W., Fanning, M.C., & Bennett, V.C. (2001). U-Pb evidence of ~1.7 crustal tectonism during the Nimrod Orogeny in the Transantarctic Mountains, Antarctica: Implications for Proterozoic plate reconstructions. *Precambrian Research*, *112*, 261–288.

Goodge, J. W., Myrow, P., Williams, I. S., & Bowring, S. A. (2002). Age and provenance of the Beardmore Group, Antarctica: constraints on Rodinia supercontinent breakup. *The Journal of geology*, *110*, 393–406.

Goodge, J. W., Myrow, P., Phillips, D., Fanning, C. M., & Williams, I. S. (2004). Siliciclastic record of rapid denudation in response to convergent-margin orogenesis, Ross Orogen, Antarctica. In: Bernet, M., and Spiegel, C. (Eds.*), Detrital Thermochronology—Provenance Analysis, Exhumation, and Landscape Evolution of Mountain Belts, Geological Society of America Special Papers*, *378*, 105–126.

Goodge, J. W., Vervoort, J. D., Fanning, C. M., Brecke, D. M., Farmer, G. L., Williams, I. S., Myrow, P.M., & DePaolo, D. J. (2008). A positive test of East Antarctica–Laurentia juxtaposition within the Rodinia supercontinent. *Science*, *321*, 235–240.

Goodge, J. W., Fanning, C. M., Norman, M. D., & Bennett, V. C. (2012). Temporal, isotopic and spatial relations of early Paleozoic Gondwana-margin arc magmatism, central Transantarctic Mountains, Antarctica. *Journal of Petrology*, *53*, 2027–2065.

Griffin, W.L., Pearson, N.J., Belousova, E., Jackson, S.E., van Achterbergh, E., O'Reilly, S.Y., & Shee, S.R. (2000). The Hf isotope composition of cratonic mantle: LAM-MC-ICPMS analysis of zircon megacrysts in kimberlites. *Geochimica et Cosmochimica Acta*, *64*, 133–147.

Griffin, W.L., Wang, X., Jackson, S.E., Pearson, N.J., O'Reilly, S.Y., Xu, X., & Zhou, X. (2002). Zircon chemistry and magma mixing, SE China: In-situ analysis of Hf isotopes, Tonglu and Pingtan igneous complexes. *Lithos*, *61*, 237–269.

Grindley, G. W., & McDougall, I. (1969). Age and correlation of the Nimrod Group and other Precambrian rock units in the central Transantarctic Mountains, Antarctica. *New Zealand journal of geology and geophysics*, *12*, 391−411.

Gunn, B.M., & Warren, G. (1962). Geology of Victoria Land between the Mawson and Mullock glaciers, Antarctica. *New Zealand Geological Survey Bulletin*, *71*, 157.

Hagen-Peter, G., Cottle, J. M., Tulloch, A. J., & Cox, S. C. (2015). Mixing between enriched lithospheric mantle and crustal components in a short-lived subduction-related magma system, Dry Valleys area, Antarctica: Insights from U-Pb geochronology, Hf isotopes, and whole-rock geochemistry. *Lithosphere*, *7*, 174–188.

Hacker, B. R., Kylander-Clark, A. R., Holder, R., Andersen, T. B., Peterman, E. M., Walsh, E. O., & Munnikhuis, J. K. (2015). Monazite Response to Ultrahigh-Pressure Subduction from U-Pb dating by Laser Ablation Split Stream. *Chemical Geology*, *409*, 28–41.

Hawkesworth, C.J., & Kemp, A.I.S. (2006). Using hafnium and oxygen isotopes in zircons to unravel the record of crustal evolution. *Chemical Geology*, *226*, 144–162.

Hall, C.E., Cooper, A.F., & Parkinson, D.L. (1995). Early Cambrian carbonatite in Antarctica. *Journal of the Geological Society*, *152*, 721–728.

Heimann, A., Fleming, T. H., Elliot, D. H., & Foland, K. A. (1994). A short interval of Jurassic continental flood basalt volcanism in Antarctica as demonstrated by $^{40}Ar/^{39}Ar$ geochronology. *Earth and Planetary Science Letters*, *121*, 19−41.

Henry, D. J., Guidotti, C. V., & Thomson, J. A. (2005). The Ti-saturation surface for low-to-medium pressure metapelitic biotites: implications for geothermometry and Ti-substitution mechanisms. *American Mineralogist*, *90*, 316–328.

Hermann, J., & Rubatto, D. (2003). Relating zircon and monazite domains to garnet growth zones: age and duration of granulite facies metamorphism in the Val Malenco lower crust. *Journal of Metamorphic Geology*, *21*, 833–852.

Holder, R. M., Hacker, B. R., Kylander-Clark, A. R., & Cottle, J. M. (2015). Monazite trace-element and isotopic signatures of (ultra) high-pressure metamorphism: Examples from the Western Gneiss Region, Norway. *Chemical Geology*, *409*, 99–111.

Holland, T. J. B., & Powell, R. (2011). An improved and extended internally consistent thermodynamic dataset for phases of petrological interest, involving a new equation of state for solids. *Journal of Metamorphic Geology*, *29*, 333–383.

Hoskin, P.W.O., & Schaltegger, U. (2003). The composition of zircon and igneous and metamorphic petrogenesis. In: Hanchar, J.M., and Hoskin, P.W.O. (Eds.), *Zircon*. Washington DC: Mineralogical Society of America, 27–62.

Iizuka, T., & Hirata, T. (2005). Improvements of precision and accuracy in in situ Hf isotope microanalysis of zircon using the laser ablation-MC-ICPMS technique. *Chemical Geology*, *220*, 121–137.

Ionov, D. A., Dupuy, C., O'Reilly, S. Y., Kopylova, M. G., & Genshaft, Y. S. (1993). Carbonated peridotite xenoliths from Spitsbergen: implications for trace element signature of mantle carbonate metasomatism. *Earth and Planetary Science Letters*, *119*, 283−297.

Jackson, S.E., Pearson, N.J., Griffin, W.L., & Belousova, E.A. (2004). The application of laser ablation-inductively coupled plasma-mass spectrometry to in situ U-Pb zircon

geochronology. *Chemical Geology*, *211*, 47–69.

Jacobsen, S.B., & Wasserburg, G.J. (1979). Nd and Sr isotopic studies of the Bay of Islands ophiolite complex and the evolution of the source of midocean ridge basalts. *Journal of Geophysical Research*, *84*, 7429–7445.

Jochum, K. P., Nohl, U., Herwig, K., Lammel, E., Stoll, B., & Hofmann, A. W. (2005). GeoReM: a new geochemical database for reference materials and isotopic standards. *Geostandards and Geoanalytical Research*, *29*, 333–338.

Kelemen, P. B. (1995). Genesis of high Mg# andesites and the continental crust. *Contributions to Mineralogy and Petrology*, *120*, 1–19.

Kellett, D. A., Cottle, J. M., & Smit, M., (2014). Eocene deep crust at Ama Drime, Tibet: Early evolution of the Himalayan orogen. *Lithosphere*, *6*, 220–229.

Kelsey, D. E., Clark, C., & Hand, M. (2008). Thermobarometric modelling of zircon and monazite growth in melt-bearing systems: Examples using model metapelitic and metapsammitic granulites. *Journal of Metamorphic Geology*, *26*, 199–212.

Kemp, A. I. S., Hawkesworth, C. J., Paterson, B. A., & Kinny, P. D. (2006). Episodic growth of the Gondwana supercontinent from hafnium and oxygen isotopes in zircon. *Nature*, *439*, 580–583.

Kemp, A. I. S., Hawkesworth, C. J., Collins, W. J., Gray, C. M., & Blevin, P. L. (2009). Isotopic evidence for rapid continental growth in an extensional accretionary orogen: The Tasmanides, eastern Australia. *Earth and Planetary Science Letters*, *284*, 455–66.

Kleinschmidt, G., & Tessensohn, F. (1987). Early Paleozoic westward directed subduction at the Pacific margin Of Antarctica, *in*: Mckenzie, G.D. (Ed.), *Gondwana six: Structure, tectonics, and geophysics*. Washington D.C.: American Geophysical Union, 89−105.

Kohn, M. J. (2009). Models of garnet differential geochronology. *Geochimica et Cosmochimica Acta*, *73*, 170–182.

Kohn, M. J., & Malloy, M. A. (2004). Formation of monazite via prograde metamorphic reactions among common silicates: implications for age determinations. *Geochimica et Cosmochimica Acta*, *68*, 101–113.

Kretz, R. (1983). Symbols for rock-forming minerals. *American mineralogist*, *68*, 277–279.

Kylander-Clark, A. R., Hacker, B. R., & Cottle, J. M. (2013). Laser-ablation split-stream ICP petrochronology. *Chemical Geology*, *345*, 99–112.

Lagos, M., Scherer, E. E., Tomaschek, F., Münker, C., Keiter, M., Berndt, J., & Ballhaus, C. (2007). High precision Lu–Hf geochronology of Eocene eclogite-facies rocks from Syros,

Cyclades, Greece. *Chemical Geology*, *243*, 16–35.

Lapen, T. J., Johnson, C. M., Baumgartner, L. P., Mahlen, N. J., Beard, B. L., & Amato, J. M. (2003). Burial rates during prograde metamorphism of an ultra-high-pressure terrane: an example from Lago di Cignana, western Alps, Italy. *Earth and Planetary Science Letters*, *215*, 57–72.

Lee, H. Y., Chung, S. L., Ji, J., Qian, Q., Gallet, S., Lo, C. H., Lee, T.Y., & Zhang, Q. (2012). Geochemical and Sr–Nd isotopic constraints on the genesis of the Cenozoic Linzizong volcanic successions, southern Tibet. *Journal of Asian Earth Sciences*, *53*, 96–114.

Liati, A., & Gebauer, D. (1999). Constraining the prograde and retrograde P-T-t path of Eocene HP rocks by SHRIMP dating of different zircon domains: inferred rates of heating, burial, cooling and exhumation for central Rhodope, northern Greece. *Contributions to Mineralogy and Petrology*, *135*, 340–354.

Liu, D., Jian, P., Kröner, A., & Xu, S. (2006). Dating of prograde metamorphic events deciphered from episodic zircon growth in rocks of the Dabie–Sulu UHP complex, China. *Earth and Planetary Science Letters*, *250*, 650–666.

Ludwig, K.R. (2003). *Isoplot / Ex, Version 2.49: A Geochronolog ical Toolkit for Microsoft Excel*. Special Publication 1a, Berkeley Geochronology Center, Berkeley, CA.

Maniar, P. D., & Piccoli, P. M. (1989). Tectonic discrimination of granitoids. *Geological society of America bulletin*, *101*, 635–643.

Martin, A.P., Cooper, A.F., Price, R.C., Turnbull, R.E., & Roberts, N.M.W. (2014). The petrology, geochronology, and significance of Granite Harbour Intrusive Complex xenoliths and outcrop sampled in western McMurdo Sound, Southern Victoria Land, Antarctic: *New Zealand Journal of Geology and Geophysics*, *58*, 33–51.

McDonough, W. F., & Sun, S. S. (1995). The composition of the Earth. *Chemical geology*, *120*, 223–253.

McKelvey, B. C., Webb, P. N., Gorton, M. P., & Kohn, B. P. (1970). Stratigraphy of the Beacon supergroup between the Olympus and Boomerang ranges, Victoria Land, Antarctica. *Nature*, *227*, 1126−1128.

Mellish, S.D., Cooper, A.F., & Walker, N.W. (2002). Panorama Pluton: a composite gabbro-monzodiorite early Ross Orogeny intrusion in southern Victoria Land, Antarctica. *Royal Society of New Zealand Bulletin*, *35*, 129–141.

Morel, M. L. A., Nebel, O., Nebel-Jacobsen, Y. J., Miller, J. S., & Vroon, P. Z. (2008). Hafnium isotope characterization of the GJ-1 zircon reference material by solution and laser-ablation MC-ICPMS. *Chemical Geology*, *255*, 231–235.

Moorbath, S., Whitehouse, M. J., & Kamber, B. S. (1997). Extreme Nd-isotope heterogeneity in the early Archaean—fact or fiction? Case histories from northern Canada and West Greenland. *Chemical Geology*, *135*, 213−231.

Münker, C., Weyer, S., Scherer, E., & Mezger, K. (2001). Separation of high field strength elements (Nb, Ta, Zr, Hf) and Lu from whole-rock samples for MC-ICPMS measurements. *Geochemistry, Geophysics, Geosystems, 2***.**

Nowell, G.M., Kempton, P.D., Noble, S.R., Fitton, J.G., Saunders, A.D., Mahoney, J.J., & Taylor, R.N. (1998). High precision Hf isotope measurements of MORB and OIB by thermal ionization mass spectrometry: Insights into the depleted mantle. *Chemical Geology*, *149*, 211–233.

Palmeri, R., Ghiribelli, B., & Ricci, C.A. (2003). Ultra-high pressure metamorphism in felsic rocks: The garnet-phengite gneisses and quartzites from Lanterman Range, Antarctica. *European Journal of Mineralogy*, *15***,** 513−525.

Patchett, P. J. (1983). Importance of the Lu-Hf isotopic system in studies of planetary chronology and chemical evolution. *Geochimica et Cosmochimica Acta*, *47*, 81–91.

Patchett, P. J., & Tatsumoto, M. (1980a). A routine high-precision method for Lu-Hf isotope geochemistry and chronology. *Contributions to Mineralogy and Petrology*, *75*, 263–267.

Patchett, P. J., & Tatsumoto, M. (1980b). Hafnium isotope variations in oceanic basalts. *Geophysical Research Letters*, *7*, 1077–1080.

Patchett, J.P., Kouvo, O., Hedge, C.E., & Tatsumoto, M. (1981). Evolution of continental crust and mantle heterogeneity: Evidence from Hf isotopes. *Contributions to Mineralogy and Petrology*, *78*, 279–297.

Paton, C., Woodhead, J.D., Hellstrom, J.C., Hergt, J.M., Greig, A., & Maas, R. (2010). Improved laser ablation U-Pb zircon geochronology through robust downhole fractionation correction. *Geochemistry, Geophysics, Geosystems: An Electronic Journal of the Earth Sciences*, *11*, 1–36.

Paton, C., Hellstrom, J., Paul, B., Woodhead, J., & Hergt, J. (2011). Iolite: Freeware for the visualisation and processing of mass spectrometric data. *Journal of Analytical Atomic Spectrometry*, *26*, 2508–2518.

Paulsen, T. S., Encarnación, J., Grunow, A. M., Layer, P. W., & Watkeys, M. (2007). New age constraints for a short pulse in Ross orogen deformation triggered by East–West Gondwana suturing. *Gondwana research*, *12*, 417–427.

Paulsen, T., Encarnación, J., Valencia, V. A., Roti Roti, J. M., & Rasoazanamparany, C. (2011). Detrital U–Pb zircon analysis of an Eocene McMurdo Erratic sandstone, McMurdo Sound, Antarctica. *New Zealand Journal of Geology and Geophysics*, *54*, 353–360.

Paulsen, T. S., Encarnación, J., Grunow, A. M., Valencia, V. A., Pecha, M., Layer, P. W., & Rasoazanamparany, C. (2013). Age and significance of 'outboard'high-grade metamorphics and intrusives of the Ross orogen, Antarctica. *Gondwana Research*, *24*, 349–358.

Pearce, J.A. (1983). Role of the sub-continental lithosphere in magma genesis at active continental margins. In: C.J. Hawkesworth, C.J. & M.J. Norry, M.J. (Eds.), *Continental Basalts and Mantle Xenoliths, Cheshire: Shiva Publishing Limited*, 230−249.

Pearce, J.A. & Peate, D.W. (1995). Tectonic implications of the composition of volcanic arc magmas. *Annual Review of Earth and Planetary Sciences, 23,* 251–285.

Pearce, J. A., Harris, N. B., & Tindle, A. G. (1984). Trace element discrimination diagrams for the tectonic interpretation of granitic rocks. *Journal of petrology*, *25*, 956–983.

Petrone, C. M., Francalanci, L., Carlson, R. W., Ferrari, L., & Conticelli, S. (2003). Unusual coexistence of subduction-related and intraplate-type magmatism: Sr, Nd and Pb isotope and trace element data from the magmatism of the San Pedro–Ceboruco graben (Nayarit, Mexico). *Chemical Geology*, *193*, 1–24.

Plank, T. & Langmuir, C.H. (1993). Tracing trace elements from sediment input to volcanic output at subduction zones. *Letters to Nature, 362,* 739–742.

Pollington, A. D., & Baxter, E. F. (2010). High resolution Sm–Nd garnet geochronology reveals the uneven pace of tectonometamorphic processes. *Earth and Planetary Science Letters*, *293*, 63–71.

Pollington, A. D., & Baxter, E. F. (2011). High precision microsampling and preparation of zoned garnet porphyroblasts for Sm–Nd geochronology. *Chemical Geology*, *281*, 270–282.

Powell, R., & Holland, T. J. B. (1988). An internally consistent dataset with uncertainties and correlations: 3. Applications to geobarometry, worked examples and a computer program. *Journal of Metamorphic Geology*, *6***,** 173–204.

Ramos, F. C., Wolff, J. A., & Tollstrup, D. L. (2005). Sr isotope disequilibrium in Columbia River flood basalts: Evidence for rapid shallow-level open-system processes. *Geology*, *33*, 457−460.

Read, S.E., Cooper, A.F., & Walker, N.W. (2002). Geochemistry and U-Pb geochronology of the Neoproterozoic-Cambrian Koettlitz Glacier Alkaline Province, Royal Society Range, Transantarctic Mountains, Antarctica, *in* Gamble J.A., Skinner, D.N.B, Henry, S. (Eds.), *Antarctica at the close of a millennium*. The Royal Society of New Zealand Bulletin, *35*, 143–151.

Read, S.E. (2010). Koettlitz Glacier Alkaline Province: Late Neoproterozoic extensional magmatism in southern Victoria Land, Antarctica. *Unpublished PhD thesis, University of Otago, Dunedin*, 595 p.

Ricci, C. A., Talarico, F., Palmeri, R., Di Vincenzo, G., & Pertusati, P. C. (1996). Eclogite at the Antarctic paleo-Pacific active margin of Gondwana (Lanterman Range, northern Victoria Land, Antarctica). *Antarctic Science*, *8*, 227–230.

Rocchi, S., Tonarini, S., Armienti, P., Innocenti, F., & Manetti, P. (1998). Geochemical and isotopic structure of the early Paleozoic active margin of Gondwana in northern Victoria Land, Antarctica. *Tectonophysics*, *284*, 261–281.

Rocchi, S., Di Vincenzo, G., Ghezzo, C., & Nardini, I. (2009). Granite-lamprophyre connection in the latest stages of the early Paleozoic Ross Orogeny (Victoria Land, Antarctica). *Geological Society of America Bulletin*, *121*, 801–819.

Rocchi, S., Bracciali, L., Di Vincenzo, G., Gemelli, M., & Ghezzo, C. (2011). Arc accretion to the early Paleozoic Antarctic margin of Gondwana in Victoria Land. *Gondwana Research*, *19*, 594−607.

Rogers, G. & Hawkesworth, C.J. (1989). A geochemical traverse across the North Chilean Andes: Evidence for crust generation from the mantle wedge. *Earth and Planetary Science Letters, 91,* 271–285.

Rowell, A.J., Rees, M.N., Duebendorfer, E.M., Wallin, E.T., Van Schmus, W.R., & Smith, E.I. (1993). An active Neoproterozoic margin: evidence from the Skelton Glacier area, Transantarctic Mountains. *Journal of the Geological Society, London*, *150*, 677–682.

Rubatto, D., Williams, I. S., & Buick, I. S. (2001). Zircon and monazite response to prograde metamorphism in the Reynolds Range, central Australia. *Contributions to Mineralogy and Petrology*, *140*, 458–468.

Rubatto, D., Hermann, J., & Buick, I. S. (2006). Temperature and bulk composition control on the growth of monazite and zircon during low-pressure anatexis (Mount Stafford, central Australia). *Journal of Petrology*, *47*, 1973–1996.

Rudnick, R. L., & Gao, S. (2003). Composition of the continental crust. In: Rudnick, R.L., and Gao, S. (Eds.), *The Crust: Treatise on geochemistry, Volume 3*. New York, Elsevier, 1–64.

Saleeby, J. B., Ducea, M. N., Busby, C. J., Nadin, E. S., & Wetmore, P. H. (2008). Chronology of pluton emplacement and regional deformation in the southern Sierra Nevada batholith, California. In: Wright, J.E., and Shervais, J.W. (Eds.), *Ophiolites, Arcs, and Batholiths: A Tribute to Cliff Hopson.* Geological Society of America Special Paper 438, 397−427.

Scherer, E. E., Cameron, K. L., & Blichert-Toft, J. (2000). Lu–Hf garnet geochronology: closure temperature relative to the Sm–Nd system and the effects of trace mineral inclusions. *Geochimica et Cosmochimica Acta*, *64*, 3413–3432.

Scherer, E., Münker, C., & Mezger, K. (2001). Calibration of the lutetium-hafnium clock. *Science*, *293*, 683–687.

Scherer, E. E., Mezger, K., & Münker, C. (2003). The ^{176}Lu decay constant discrepancy: terrestrial samples vs. meteorites. *Meteoritics and Planetary Science Supplement*, *38*, 5263.

Serri, G., Innocenti, F., & Manetti, P. (1993). Geochemical and petrological evidence of the subduction of delaminated Adriatic continental lithosphere in the genesis of the Neogene-Quaternary magmatism of central Italy. *Tectonophysics*, *223*, 117–147.

Siddoway, C. S., Baldwin, S. L., Fitzgerald, P. G., Fanning, C. M., & Luyendyk, B. P. (2004). Ross Sea mylonites and the timing of intracontinental extension within the West Antarctic rift system. *Geology*, *32*, 57–60.

Simpson, A.L. (2002). Felsic magmatism in the Darwin Glacier Region, southern Victoria Land, Antarctica. *Unpublished PhD thesis, University of Otago, Dunedin, New Zealand*.

Simpson, A.L., & Cooper, A. F. (2002). Geochemistry of the Darwin Glacier region granitoids, southern Victoria Land. *Antarctic Science*, *14*, 425–426.

Simpson, G., & Aslund, T. (1996). Diorite and gabbro of the Dromedary mafic complex, South Victoria Land, Antarctica. *New Zealand Journal of Geology and Geophysics*, *39*, 403–414.

Sláma, J., Kosler, J., Condon, D.J., Crowley, J.L., Gerdes, A., Hanchar, J.M., Horstwood, M.S., Morris, G.A., Nasdala, L., Norberg, N., Schaltegger, U., Schoene, B., Tubrett, M.N., & Whitehouse, M.J. (2008). Plešovice zircon—A new natural reference material for U-Pb and Hf isotopic microanalysis. *Chemical Geology*, *249*, 1–35.

Smillie, R.W. (1992). Suite subdivision and petrological evolution of granitoids from the Taylor Valley and Ferrar Glacier region, south Victoria Land. *Antarctic Science*, *4*, 71–87.

Smit, M.A., Scherer, E.E., Bröcker, M., & van Roermund, H.L.M. (2010). Timing of eclogite facies metamorphism in the southernmost Scandinavian Caledonides by Lu-Hf and Sm-Nd geochronology. *Contributions to Mineralogy and Petrology*, *159*, 521–539.

Smit, M. A., Scherer, E. E., & Mezger, K. (2013). Lu–Hf and Sm–Nd garnet geochronology: Chronometric closure and implications for dating petrological processes. *Earth and Planetary Science Letters*, *381*, 222–233.

Söderlund, U., Patchett, P. J., Vervoort, J. D., & Isachsen, C. E. (2004). The ^{176}Lu decay constant determined by Lu–Hf and U–Pb isotope systematics of Precambrian mafic intrusions. *Earth and Planetary Science Letters*, *219*, 311–324.

Sørenson, H. (1974). *The Alkaline Rocks*. London: John Wiley & Sons, 602 p.

Sprung, P., Scherer, E. E., Upadhyay, D., Leya, I., & Mezger, K. (2010). Non-nucleosynthetic heterogeneity in non-radiogenic stable Hf isotopes: Implications for early solar system chronology. *Earth and Planetary Science Letters*, *295*, 1–11.

Stump, E. (1995). *The Ross Orogen of the Transantarctic Mountains*. Cambridge: Cambridge University Press, 284 p.

Stump, E., Laird, M. G., Bradshaw, J. D., Holloway, J. R., Borg, S. G., & Lapham, K. E. (1983). Bowers graben and associated tectonic features cross northern Victoria Land, Antarctica. *Nature*, *304*, 334–336.

Stump, E., Gootee, B., & Talarico, F. (2006). Tectonic model for development of the Byrd Glacier discontinuity and surrounding regions of the Transantarctic Mountains during the Neoproterozoic- Early Paleozoic. In: Kleinschmidt G, Miller H, Tessensohn F (Eds.), *Antarctica: Contributions to Global Earth Sciences*. New York: Springer-Verlag, 181–190.

Stump, E., Gehrels, G., Talarico, F. M., & Carosi, R. (2007). Constraints from detrital zircon geochronology on the early deformation of the Ross orogen, Transantarctic Mountains, Antarctica. *U.S. Geological Survey and The National Academies Extended Abstract*, 166, 4 p.

Talarico, F.M., Findlay, R.H., & Rastelli, N. (2005). Metamorphic evolution of the Koettlitz Group in the Koettlitz-Ferrar Glaciers region (southern Victoria Land, Antarctica). *Terra Antartica*, *12*, 3–23.

Tanaka, T., Togashi, S., Kamioka, H., Amakawa, H., Kagami, H., Hamamoto, T., Masaki, Y., Orihashi, Y., Yondeda, S., Shimizu, H., Takanori, K., Takahashi, K., Yanagi, T., Nakano, T., Fujimaki, H., Shinjo, R., Asahara, Y., Tanimizu, M., & Dragusanu, C. (2000). JNdi-1: a neodymium isotopic reference in consistency with LaJolla neodymium. *Chemical Geology*, *168*, 279–281.

Thirlwall, M. F., & Anczkiewicz, R. (2004). Multidynamic isotope ratio analysis using MC–ICP–MS and the causes of secular drift in Hf, Nd and Pb isotope ratios. *International Journal of Mass Spectrometry, 235*, 59–81.

Tiepolo, M., & Tribuzio, R. (2008). Petrology and U–Pb zircon geochronology of amphibole-rich cumulates with sanukitic affinity from Husky Ridge (Northern Victoria Land, Antarctica): insights into the role of amphibole in the petrogenesis of subduction-related magmas. *Journal of Petrology*, *49*, 937–970.

Tonarini, S., & Rocchi, S. (1994). Geochronology of Cambro–Ordivician intrusives in northern Victoria Land: a review. *Terra Antartica*, *1*, 46–50.

Tulloch, A. J., & Kimbrough, D. L. (2003). Paired plutonic belts in convergent margins and the development of high Sr/Y magmatism: Peninsular Ranges batholith of Baja-California and Median batholith of New Zealand. *Special paper-Geological Society of America*, *374*, 275–295.

Turner, S., & Hawkesworth, C. (1997). Constraints on flux rates and mantle dynamics beneath island arcs from Tonga–Kermadec lava geochemistry. *Nature*, *389*, 568–573.

Veevers, J. J., Belousova, E. A., Saeed, A., Sircombe, K., Cooper, A. F., & Read, S. E. (2006). Pan-Gondwanaland detrital zircons from Australia analysed for Hf-isotopes and trace elements reflect an ice-covered Antarctic provenance of 700–500 Ma age, T DM of 2.0–1.0 Ga, and alkaline affinity. *Earth-Science Reviews*, *76*, 135–174.

Vervoort, J.D., & Blichert-Toft, J. (1999). Evolution of the depleted mantle: Hf isotope evidence from juvenile rocks through time. *Geochimica et Cosmochimica Acta*, *63*, 533–556.

Vervoort, J. D., Patchett, P. J., Blichert-Toft, J., & Albarède, F. (1999). Relationships between Lu–Hf and Sm–Nd isotopic systems in the global sedimentary system. *Earth and Planetary Science Letters*, *168*, 79–99.

Vervoort, J. D., Patchett, P. J., Söderlund, U., & Baker, M. (2004). Isotopic composition of Yb and the determination of Lu concentrations and Lu/Hf ratios by isotope dilution using MC-ICPMS. *Geochemistry, Geophysics, Geosystems*, *5*, 1–15.

Weaver, S. D., Bradshaw, J. D., & Laird, M. G. (1984). Geochemistry of Cambrian volcanics of the Bowers Supergroup and implications for the Early Palaeozoic tectonic evolution of northern Victoria Land, Antarctica. *Earth and Planetary Science Letters*, *68***,** 128–140.

Wiedenbeck, M., Allé, Corfu, F., Griffin, W.L., Meier, M., Oberli, F., von Quadt, A.V., Roddick, J.C., & Spiegel, W. (1995). Three natural zircon standards for U-Th-Pb, Lu-Hf, trace element and REE analyses. *Geostandards Newsletter*, *19*, 1–23.

Wiedenbeck, M., Hanchar, J.M., Peck, W.H., Sylvester, P., Valley, J., Whitehouse, M., Kronz, A., Morishita, Y., Nasdala, L., Fiebig, J., Franchi, I., Girard, J.-P., Greenwood, R.C., Hinton, R., Kita, N., Mason, P.R.D., Norman, M., Ogasawara, M., Piccoli, P.M., Rhede, D., Satoh, H., Schulz-Dobrick, B., Skår, Ø., Spicuzza, M.J., Terada, K., Tindle, A., Togashi, S., Venneman, T., Xie, Q., & Zheng, Y.-F. (2004). Further characterization of the of the 91500 zircon crystal. *Geostandards and Geoanalytical Reasearch*, *28*, 9–39.

Wendt, I., & Carl, C. (1991). The statistical distribution of the mean squared weighted deviation. *Chemical Geology (Isotope Geoscience Section)*, *86*, 275–285.

Whalen, J. B., Currie, K. L., & Chappell, B. W. (1987). A-type granites: geochemical characteristics, discrimination and petrogenesis. *Contributions to mineralogy and petrology*, *95*, 407–419.

White, W. M., & Patchett, J. (1984). Hf-Nd-Sr isotopes and incompatible element abundances in island arcs: implications for magma origins and crust-mantle evolution. *Earth and Planetary Science Letters*, *67*, 167–185.

Wooley, A.R. (1989). The spatial and temporal distribution of carbonatites. In: Bell (Ed.). *Carbonatites*. London: Unwin Hyman Ltd, 15–37.

Wysoczanski, R. J., & Allibone, A. H. (2004). Age, correlation, and provenance of the Neoproterozoic Skelton Group, Antarctica: Grenville age detritus on the margin of East Antarctica. *The Journal of geology*, *112*, 401–416.

Yakymchuk, C., & Brown, M. (2014). Behaviour of zircon and monazite during crustal melting. *Journal of the Geological Society*, *171*, 465–479.

Yakymchuk, C., Brown, M., Clark, C., Korhonen, F. J., Piccoli, P. M., Siddoway, C. S., Taylor, R.J.M., & Vervoort, J. D. (2014). Decoding polyphase migmatites using geochronology and phase equilibria modelling. *Journal of Metamorphic Geology*, *33*, 203–230.

Young, D.J., & Kylander-Clark, A.R.C. (2015). Does continental crust transform during eclogite-facies metamorphism? *Journal of Metamorphic Geology*, *33*, 331–357.

Appendices:

Appendix Figure 1: Chapter 1- False color element X-ray maps of garnet grains not shown in the text. Black scale bars are 0.5 mm.

Appendix Figure 2: Chapter 1- False color element X-ray maps of monazite grains not shown in the text. Scale bars and relative concentration scales are shown on each map.

Appendix Text 1: Chapter 2- Detailed description of analytical methods and calculations.

Appendix Table 1: Chapter 1- Excel® file with mineral compositions from EPMA.

Appendix Table 2: Chapter 1- Excel® file with garnet trace element concentrations from laser-ablation transects.

Appendix Table 3: Chapter 1- Excel® file with monazite U-Pb and REE LASS data.

Appendix Table 4: Chapters 2 and 3- Excel® file with whole-rock major- and trace-element data.

Appendix Table 5: Chapters 2 and 3- Excel® file with zircon U-Pb isotope data.

Appendix Table 6: Chapters 2 and 3- Excel® file with zircon Hf isotope data.

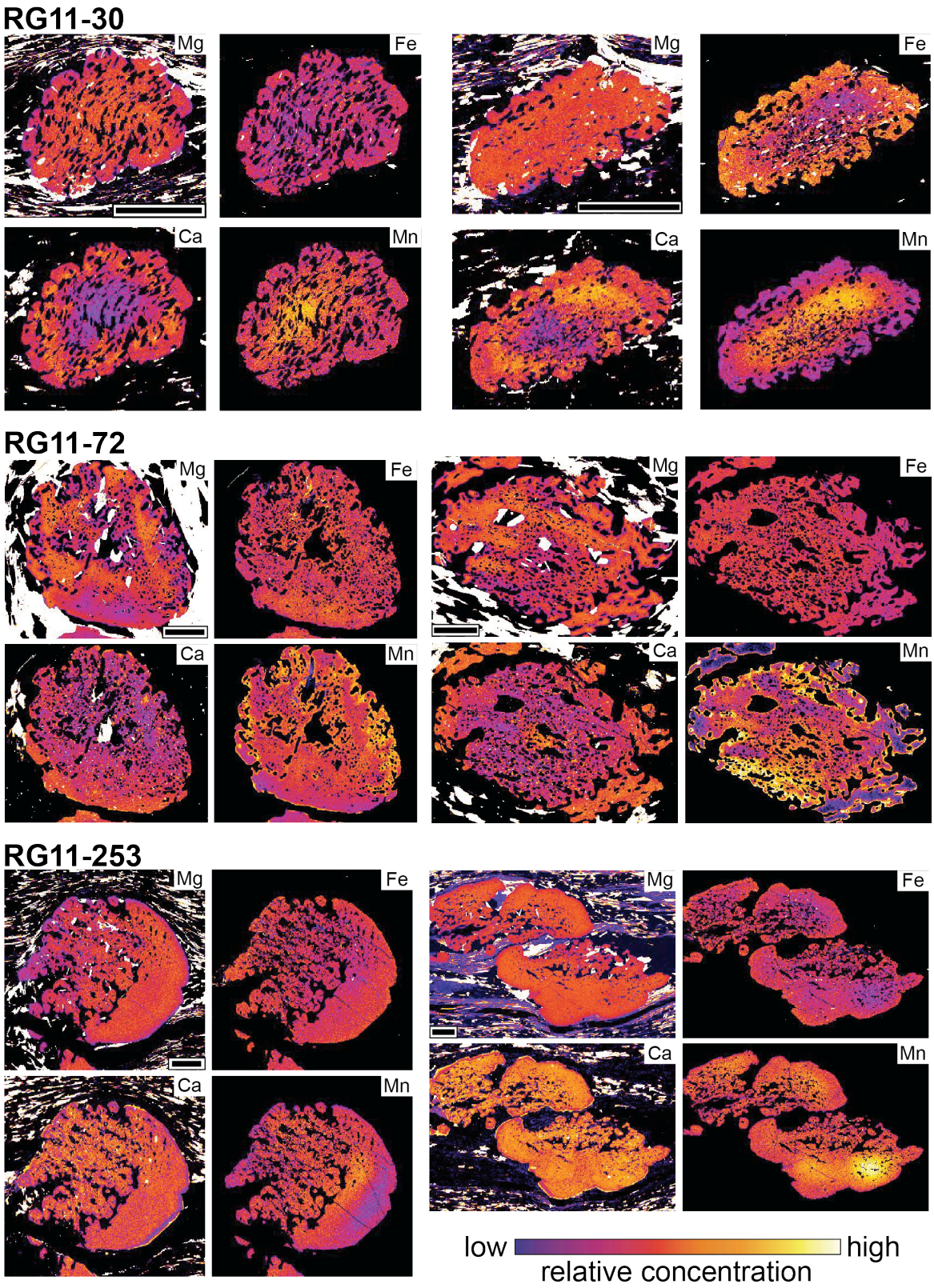

Appendix Figure 1 False color element X-ray maps of garnet grains not shown in the text. Black scale bars are 0.5 mm.

RG11-13

La

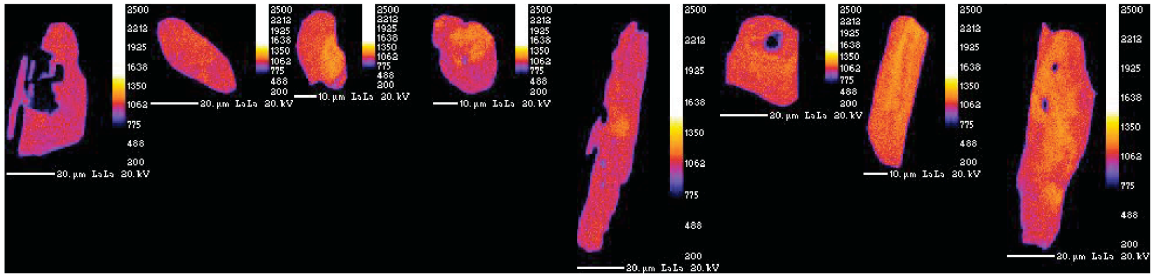

Nd

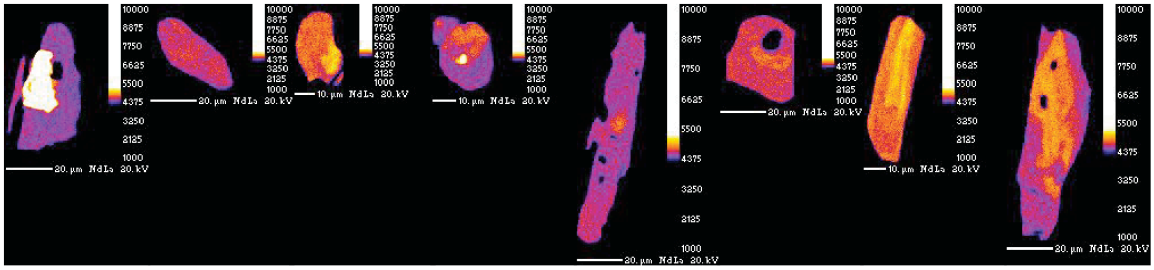

Th

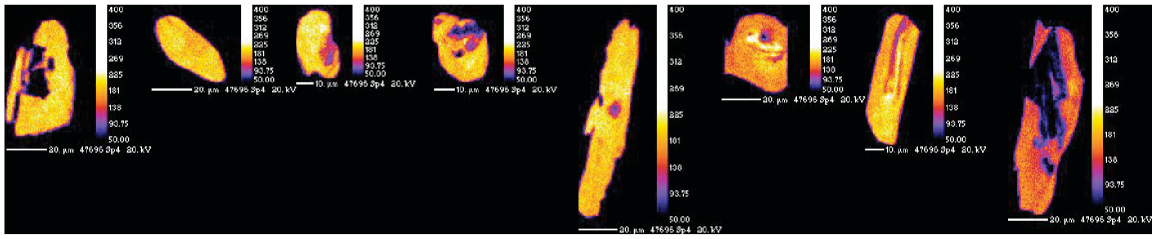

U

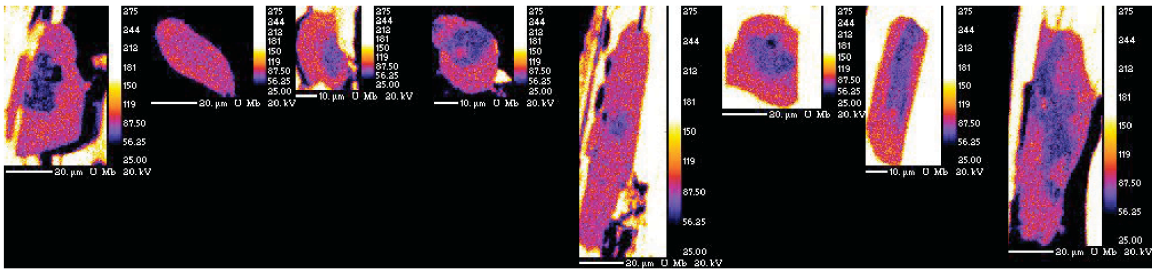

Y

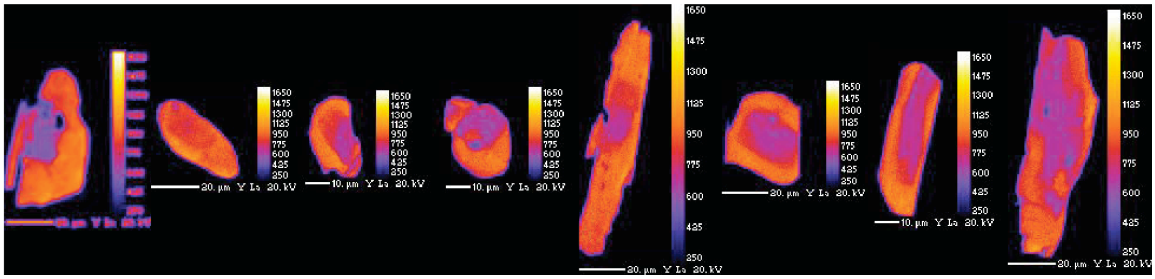

RG11-30

La

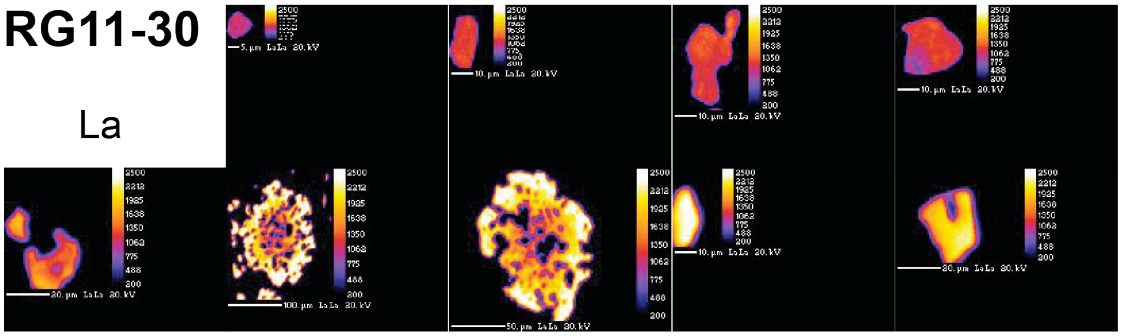

Nd

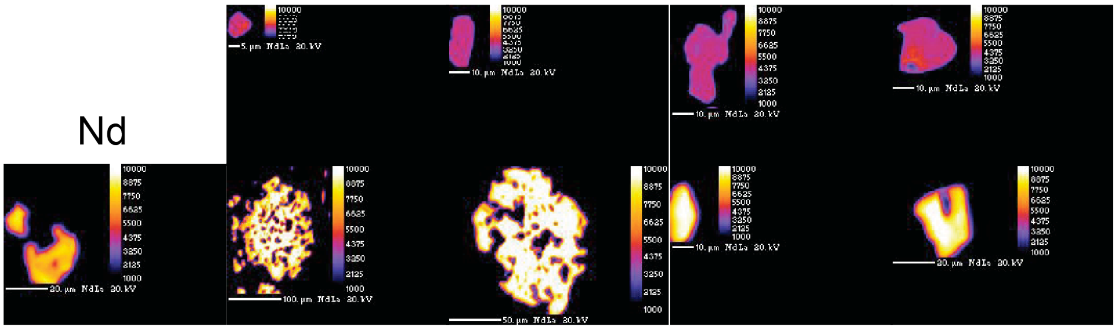

Th

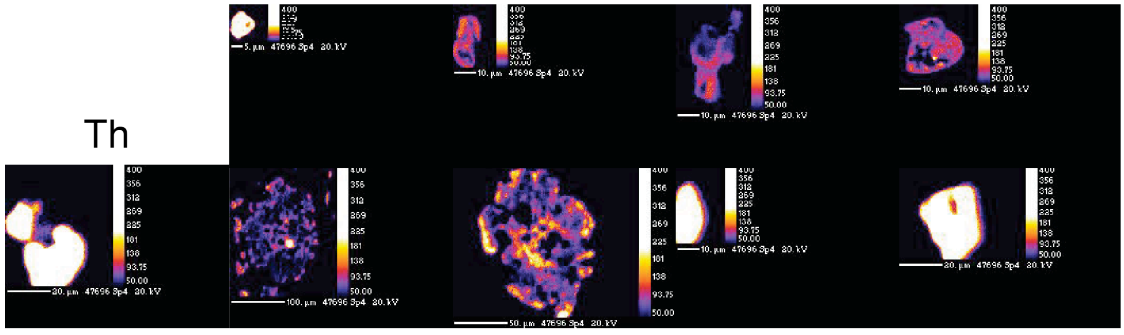

U

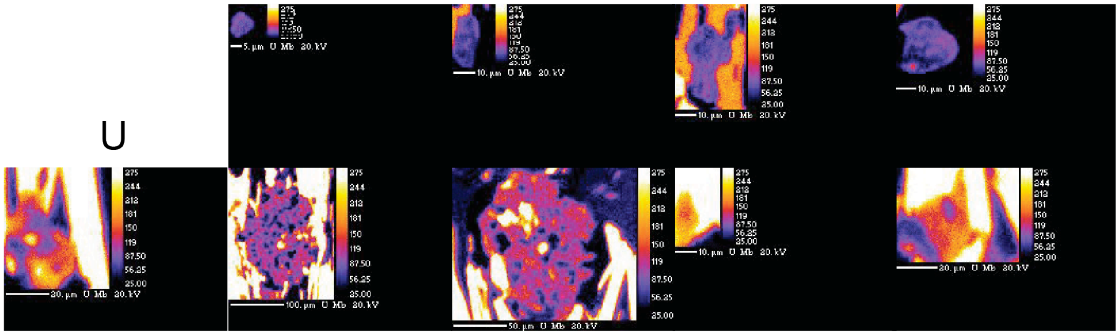

Y

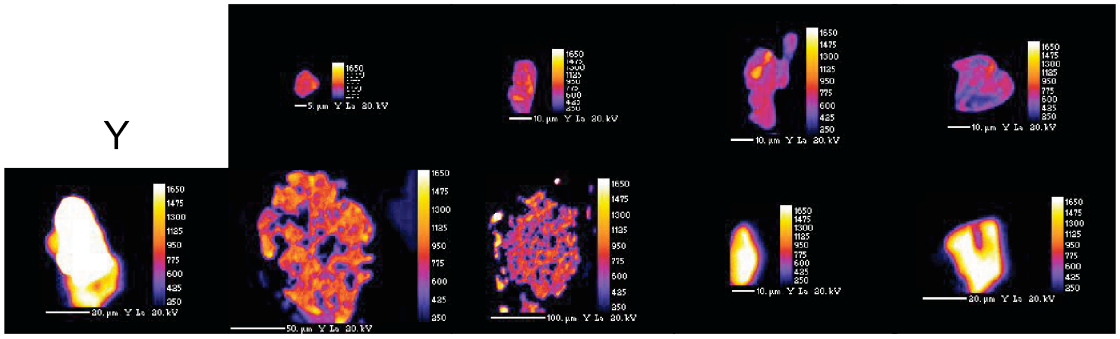

RG11-135

La

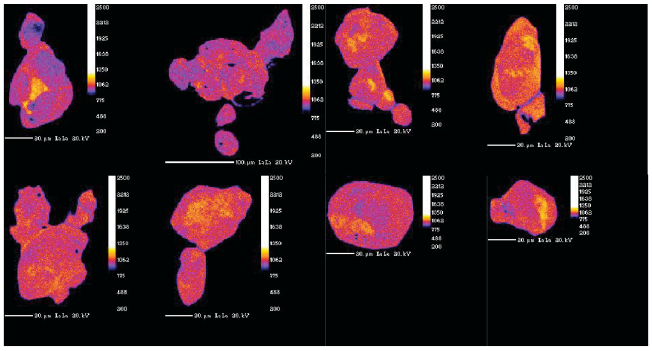

Nd

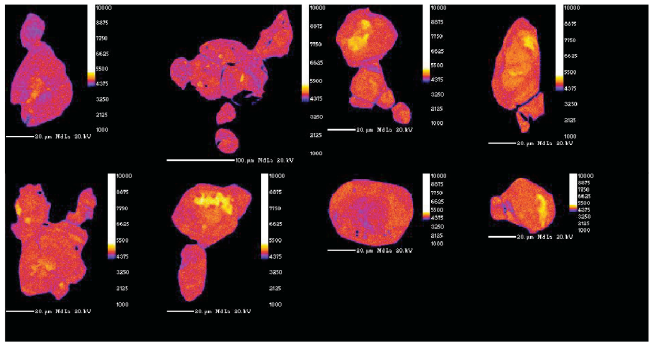

Th

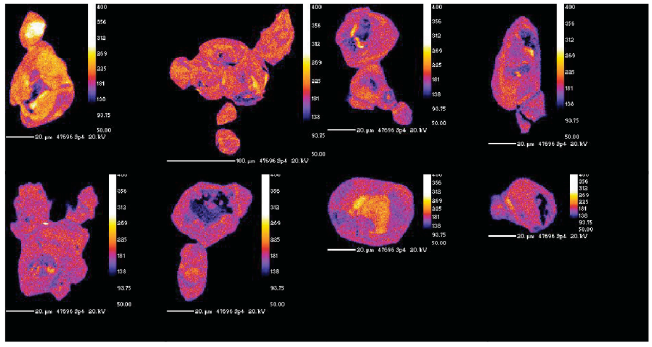

U

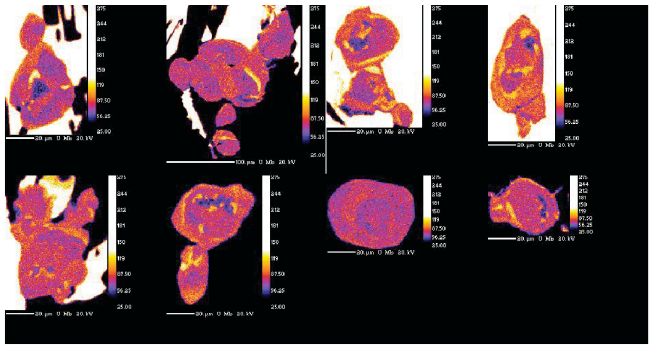

Y

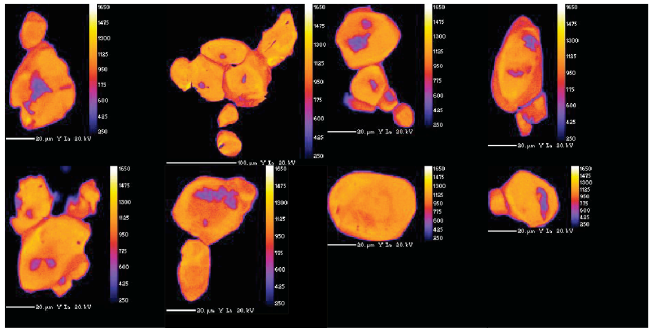

RG11-253

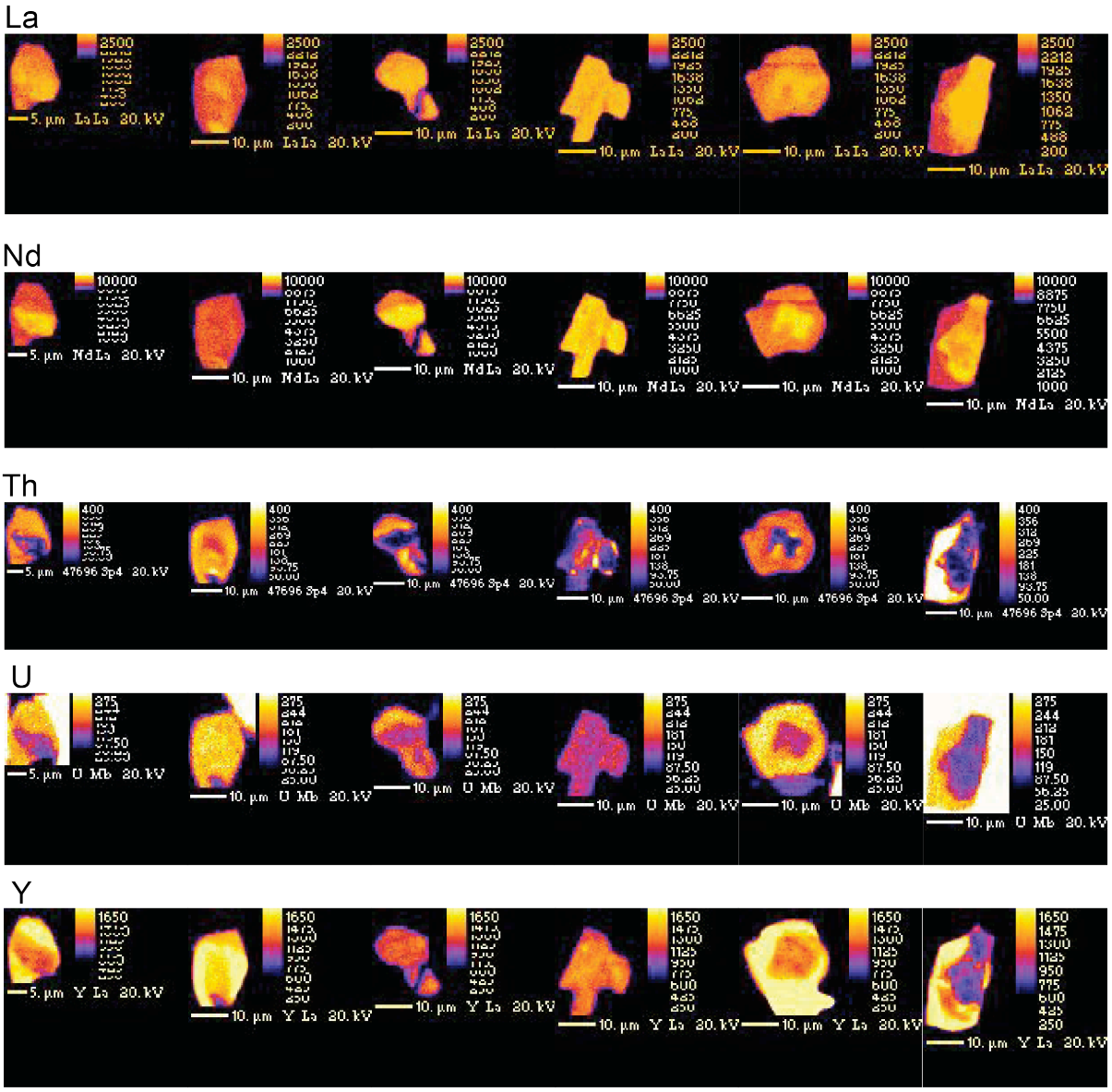

Appendix Figure 2 False color element X-ray maps of monazite grains not shown in the text. Scale bars and relative concentration scales are shown on each map.

Appendix Text 1: Chapter 2- Detailed description of analytical methods and calculations.

Whole rock geochemistry

Whole-rock samples with the prefix "P" were analyzed for 10 major oxides and 19 trace elements by X-ray fluorescence spectrometry (XRF) at the Spectrachem Analytical laboratories in Lower Hutt, New Zealand (www.crl.co.nz/services/analysis/spectrachem.htm). Samples selected for XRF analysis were crushed using a TEMA swing mill fitted with a WC head. Fused disks were produced for major element analyses and pressed powders for trace elements. Loss on ignition (LOI) was determined after heating to 1000° C. The lower limit of detection is better than 0.004 wt% oxide (for Al_2O_3) and better than 1–3 ppm for trace elements.

Samples with the prefix "RG" were analyzed at ALS Minerals in Reno, NV (www.alsglobal.com). Samples were powdered, fluxed with lithium borate, and fused into beads. The homogenized and fused beads were dissolved in a 4% HNO_3 – 2% HCL mixture for solution analysis. Thirteen oxides and 38 trace elements were analyzed by inductively-coupled plasma (ICP) atomic emission spectrometry (AES) and ICP- mass spectrometry (MS), respectively. Reference materials, duplicate samples, and blank were measured with each batch of samples to assess accuracy and reproducibility. Whole-rock data can be found Appendix Table 4.

Zircon U-Pb geochronology

Zircons were separated from whole-rock samples using standard crushing, sieving, hydrodynamic, density, and isodynamic techniques. For most samples, this step resulted in relatively pure zircon separates. Roughly 50–120 zircons from each sample were hand

selected using a binocular microscope, care taken to select grains without large cracks, inclusions, or extensive metamictization. Selected zircons were mounted in epoxy resin disks and polished to expose median cross sections through the zircons.

Polished zircon mounts were carbon coated and imaged with a Cathodoluminescence (CL) detector attached to a FEI Quanta400F scanning electron microscope using a 20 kV accelerating voltage and a beam current of 5 nA. CL images of zircons were used to guide the placement of in-situ U-Pb and Hf isotope analyses, avoiding overlapping compositional domains apparent in CL (Fig. 2).

U-Pb measurements were made on a Nu Plasma high-resolution multi collector-inductively-coupled plasma- mass spectrometer (MC-ICP-MS) (Nu Instruments, Wrexham, UK) at the University of California, Santa Barbara. A 193 nm ArF excimer laser (Photon Machines, San Diego, USA) was used to ablate domains 24 or 31 μm in diameter. Laser energy was typically 3–4 mJ and the ablation repetition rate 4 Hz. Analyses were conducted over 25 or 30 second ablation periods with 20 second washout periods between measurements to return the signal to background. Isotopes ^{204}Pb, ^{206}Pb, ^{207}Pb, and ^{208}Pb were measured on secondary electron multipliers, while ^{232}Th and ^{238}U were measured on Faraday cups equipped with 10^{11}-ohm resistors.

U-Th-Pb data were collected during seven analytical sessions. A primary reference material, '91500' zircon (1065.4 ± 0.3 Ma ^{207}Pb/^{206}Pb ID-TIMS age and 1062.4 ±0.4 Ma ^{206}Pb/^{238}U ID-TIMS age, Wiedenbeck et al., 1995; 2004) was employed to monitor and correct for mass bias as well as Pb/U fractionation. To assess data accuracy, two secondary reference zircons 'GJ-1' (608.5 ± 0.4 Ma ^{207}Pb/^{206}Pb ID-TIMS age; Jackson et al., 2004 and 601.7 ± 1.3 Ma ^{206}Pb/^{238}U ID-TIMS age; Condon, personal communication) and 'Plešovice'

(337.13 ± 0.37 Ma $^{206}Pb/^{238}U$ ID-TIMS age Sláma et al., 2008) were analyzed concurrently (typically once every 5 unknowns) and mass bias- and fractionation-corrected based on measured isotopic ratios of the primary reference material. Analyses of the GJ-1 secondary reference zircon over all of the analytical sessions yield a mean $^{206}Pb/^{238}U$ age of 601.9 ± 6.8 Ma (2 s.d.; n = 395; MSWD = 0.96). Analyses of the Plešovice secondary reference zircon over all of the analytical sessions yield a mean $^{206}Pb/^{238}U$ age of 339.7 ± 4.3 Ma (2 s.d.; n = 257; 2 points rejected; MSWD = 1.05). Data reduction, including corrections for baseline subtraction, instrumental drift, mass bias, down-hole fractionation, and primary-reference normalization was carried out using Iolite version 2.31. Full details of the data reduction methodology can be found in Paton et al. (2010; 2011).

Uncertainties on individual analyses are quoted at the 95% confidence or 2σ level and include contributions from the external reproducibility of the secondary reference material for the $^{207}Pb/^{206}Pb$ and $^{206}Pb/^{238}U$ ratios. Weighted $^{206}Pb/^{238}U$ averages were calculated using Isoplot version 3.00 (Ludwig, 2003). Uncertainties on weighted mean ages are quadratic additions of the internal precision on the measurements and the long-term external reproducibility of GJ-1 and Plešovice (~1.2%; Fig. 4).

Zircon Hf isotopes

The zircons targeted for U-Pb dating were analyzed for Hf isotope composition by laser-ablation MC-ICP-MS. In an effort to obtain Hf compositions corresponding to a specific age domains in the zircon, ablation spots were placed directly over spots previously used for U-Pb age determination. When possible, spots from analyses used in the final age determination for each sample were re-analyzed for Hf.

A 53 μm beam diameter, 4–6.5 mJ energy, and an 6–8 Hz repetition rate were used for all ablations. Analyses were conducted over a 40–60 second ablation period with 20-second washout periods between measurements. Masses 171–180 were measured simultaneously on an array of 10 Faraday cups at 1-amu spacing. Data were collected and analyzed in time-resolved mode so that any changes in ^{176}(Hf+Yb+Lu)/^{177}Hf corresponding to ablation though different growth zones could be identified. Data reduction was performed using Iolite version 2.31 (Paton et al., 2011).

There are three isobars of mass 176: ^{176}Yb, ^{176}Lu, ^{176}Hf. Zircons typically have Lu/Hf ratios of < 0.001 (Hawkesworth and Kemp, 2006), therefore the ^{176}Lu isobar generally has little effect on the corrected ^{176}Hf/^{177}Hf ratio. However, ^{176}Yb routinely contributes ~10% of the total mass 176 signal (Iizuka and Hirata, 2005), therefore, a ^{176}Yb correction is crucial to an accurate ^{176}Hf/^{177}Hf ratio. Natural ^{173}Yb/^{171}Yb = 1.123575 (Thirwall and Anczkiewicz, 2004) was used to calculate the Yb mass bias factor; this factor was used to correct for both Yb and Lu mass bias. Natural ^{179}Hf/^{177}Hf = 0.7325 (Patchett and Tatsumoto, 1980a; 1980b) was used to calculate the Hf mass bias factor. Natural ^{176}Yb/^{173}Yb = 0.786847 (Thirwall and Anczkiewicz, 2004) and ^{176}Lu/^{175}Lu = 0.02656 (Chu et al., 2002) were used for the subtraction of isobaric interferences on ^{176}Hf. Reference zircons '91500' (Blichert-Toft; 2008), 'GJ-1' (Morel et al., 2008), and 'Plešovice' (Sláma et al., 2008) were analyzed between every five to ten unknowns in order to assess the accuracy of the correction scheme. The reproducibility of the reference zircons was as follows: GJ-1: ^{176}Hf/^{177}Hf = 0.28202 ± 0.00010 (2 S.D.); Plešovice: ^{176}Hf/^{177}Hf = 0.28248 ± 0.00011 (2 S.D.); 91500: ^{176}Hf/^{177}Hf = 0.28232 ± 0.00013 (2 S.D.), corresponding to external reproducibility of ~3.5–4.5 εHf units. Internal 2 S.E. uncertainties calculated in Iolite range from ~4.5 to as high as 8.5 εHf units,

and are apparently overestimated in the Iolite data reduction scheme. This is evidenced by MSWD<<1 and more precise external reproducibility (3.5–4.5 εHf units; 2 S.D.) on populations of standards. Therefore, it was necessary to take an empirical approach to estimating the internal uncertainty on individual analyses to avoid obscuring possible geological complexity in our samples (i.e., a set of unknown analyses with an MSWD >>1 might appear as a single population if uncertainty is overestimated). To address this issue, we scaled the internal uncertainties on individual analyses by a factor of 0.7, such that the populations of standards had MSWDs = 1. This same scaling factor was then applied to the uncertainties on the sample analyses; we take this to be a more robust estimate on internal uncertainty. The data with and without this additional correction can be found in the supplementary material of Hagen-Peter et al. (2015).

Samples with the prefix "RG11" were measured during a different analytical session when conditions resulted in more precise measurements (in-run statistics of approximately 1−1.5 εHf units at the 2σ level). For these samples, the "estimated uncertainty" column in Table DR3 from Hagen-Peter et al. (2015) includes additional propagated uncertainty based on the external reproducibility of secondary reference zircons.

The $\varepsilon Hf_{(i)}$ values were calculated relative to CHUR (present-day $^{176}Hf/^{177}Hf$ = 0.282785 and $^{176}Lu/^{177}Hf$= 0.0336; Bouvier et al., 2008) for each analysis using the corresponding $^{206}Pb/^{238}U$ age for the spot and $\lambda^{176}Lu=1.867 \times 10^{-11}$ yr^{-1} (Scherer et al., 2001; 2003; Söderlund et al., 2004). Uncertainties on the corrected $^{176}Hf/^{177}Hf$ and $^{176}Lu/^{177}Hf$ (for age correction) were propagated into the $\varepsilon Hf_{(i)}$ calculations, though the contribution of the $^{176}Lu/^{177}Hf$ uncertainties are typically negligible, due to the very low Lu/Hf ratios in zircons.

The complete data set can be found in the supplementary material of Hagen-Peter et al. (2015).

Depleted-mantle model ages (T_{DM}) were calculated using the corrected present-day $^{176}Hf/^{177}Hf$ and $^{176}Lu/^{177}Hf$ for each sample. For depleted-mantle parameters, we used present-day $^{176}Hf/^{177}Hf$= 0.28325, a value similar to average MORB (Nowell et al., 1998; Griffin et al., 2000; Griffin et al., 2002), and present-day $^{176}Lu/^{177}Lu$= 0.0384 (Griffin et al., 2000). Two-stage depleted-mantle model ages (T_{DM}^{C}) were calculated using the same depleted mantle parameters and a crustal average $^{176}Lu/^{177}Hf$ = 0.015 (Griffin et al., 2002) for the evolution of the crustal magma source after it separated from the depleted mantle.